

TECHNISCHE UNIVERSITÄT MÜNCHEN
INSTITUT FÜR LUFT- UND RAUMFAHRT

Lehrstuhl für Flugantriebe

**Design and Experimental Study of Injection
Systems in a Supersonic Combustion Chamber**

Sara Rocci Denis

Vollständiger Abdruck der von der Fakultät für Maschinenwesen der Technischen Universität München zur Erlangung des akademischen Grades eines

Doktor-Ingenieurs

genehmigten Dissertation.

Vorsitzender: Univ.-Prof. Dr. rer. nat. U. Walter

Prüfer der Dissertation:

1. Univ.-Prof. Dr.-Ing. H.-P. Kau
(schriftliche Beurteilung)
Univ.-Prof. Dr.-Ing. Th. Sattelmayer
(mündliche Prüfung)
2. Univ.-Prof. Dr.-Ing. Chr. Mundt
Universität der Bundeswehr München

Die Dissertation wurde am 27.05.2011 bei der Technischen Universität München eingereicht und durch die Fakultät für Maschinenwesen am 15.10.2011 angenommen.

**Design and Experimental Study
of Injection Systems
in a Supersonic Combustion Chamber**

Thesis by Sara Rocci Denis

Träume sind die Treibfeder für neue Visionen. Träume geben Dir den Mut, immer wieder neu aufzubrechen. Sie verleihen Dir die Kraft, alles zu geben, um das Ziel zu erreichen.

Alexander Huber

The question is not whether or how the limits of flight will be extended, but when.

William Heiser and David Pratt

And by whom.

Sara Rocci Denis

Zusammenfassung

Ziel dieser Arbeit ist die Konstruktion von Einspritzsystemen für die Anwendung in einer Überschallmodellbrennkammer, wobei der Fokus für die konzipierten Injektoren auf der Flammenstabilisierung bei möglichst geringen aerodynamischen Druckverlusten liegt. Im Rahmen der Arbeit wurden experimentelle Untersuchungen in einer kontinuierlich betriebenen, modularen Modellbrennkammer bei einer Eintrittsmachzahl von 2,2 und einer Totaltemperatur von 1000 K durchgeführt.

Zu Beginn wurden das Zünd- und Stabilisierungsverhalten eines Zentralkörper-Injektors, der im Brennkammermodul konstanten Querschnitts positioniert wurde, untersucht. Drei verschiedene Injektorgeometrien wurden bezüglich der Stabilisierung einer Pilotflamme in deren Nachlauf verglichen. Einer der Injektoren (Strut 2) erwies sich als nicht geeignet, die Pilotflamme zu stabilisieren, da für diese Konfiguration die Strahlen des Brennstoffs und des Oxidationsmittels im Nachlauf sich nicht in einem Punkt treffen. Für die weiteren zwei Injektoren (Strut 1 und Strut 3) erwiesen sich nahe-stöchiometrische Bedingungen im Pilotflammenbereich als optimal, um eine Selbststabilisierung der Pilotflamme unabhängig der Luftmenge aus der dem Nachlauf benachbarten Überschallströmung zu gewährleisten. Die neuen Injektoren mindern die aerodynamischen Druckverluste im Vergleich mit den vorherigen Einspritzsystemen [11] und unterstützen die Pilotflammenstabilisierung ohne weiteren Flammhalter.

Beide Injektoren wurden bezüglich der Stabilisierung einer Methan-Überschallflamme mit positivem Ergebnis weiter untersucht. Allerdings blieb das gesamte Mischniveau in der Brennkammer gering. Verschiedene Strömungsschichten wurden nachgewiesen und das Äquivalenzverhältnis der Brennkammer blieb ebenfalls begrenzt. Während Strut 1 hinsichtlich verbesserter Gemischbildung ausgelegt wurde, wurde für Strut 3 eine Geometrie mit ausgeprägtem Flammhaltereigenschaften gewählt. Für die untersuchten Brennstoffzufuhr-Konfigurationen erwies sich Strut 3 als geeigneter Injektor, da bei diesem die Verbrennung stabiler und die benötigte Brennstoffmenge geringer ist. Die Kombination beider Injektoren mit einem Kavitätswandinjektor brachte kein positives Ergebnis. Das eingespritzte Methan mischte sich nicht mit der Überschallströmung, sodass der Brennstoff nicht gezündet werden konnte.

Abstract

The design of fuel injection systems for a subscale scramjet combustor has been addressed in this study, with particular attention to achieve good flame stabilization while minimizing the aerodynamic losses introduced by the injectors. Experimental investigations have been conducted in a subscale, direct connected, modular combustor at an entrance Mach number of 2.2 and a total temperature of 1000K.

The ignition and stabilization behaviour of a strut injector positioned in the constant cross-area section of the combustor has been studied first, and three strut geometries have been compared with respect to their capability of stabilizing a pilot flame in their wake. One of the three struts (Strut 2) did not support mixture ignition due to the fact that the pilot fuel and oxidizer were not foreseen to converge into one spot. For the other two struts (Strut 1 and Strut 3) pilot conditions close to stoichiometric have been identified as optimal to guarantee self-sustainment of the pilot flame without depending on the entrainment of air into the wake from the main supersonic flow. The new strut geometries reduced the aerodynamic losses compared to previous injector versions [11] and supported flame stabilization without introducing additional flame holders.

Both struts have been further investigated with respect to stabilization of supersonic methane combustion and both successfully supported it. However, the overall level of mixing remained low and led to a stratification of the combustor flow and to limited combustor equivalence ratios. Strut 1 and Strut 3 have been designed to promote mixing and flame holding, respectively. Strut 3 was found superior to Strut 1 for the fuelling configurations studied as the combustion process was more stable and required a lower amount of pilot fuel, while the other performance was comparable for both struts. The combination of both struts with the wall-mounted cavity injector did not provide the expected performance improvement. The injected methane did not mix with the supersonic flow and no successful ignition of the second stage fuel could be achieved.

List of Publications

S. Rocci Denis, D. Maier and H.-P. Kau

Staged Injection in a Dual-Mode Combustor for an Airbreathing Engine

26th International Symposium on Shock Waves, Volume 2, Springer Berlin Heidelberg, pp. 1123-1128, 2009

S. Rocci Denis, D. Maier and H.-P. Kau

Staged Injection in a Dual-Mode Combustor for an Airbreathing Engine

15th AIAA International Space Planes and Hypersonic Systems and Technologies Conference, Dayton, Ohio, USA; AIAA-2008-2632

D. Maier, S. Kirstein, T. Fuhrmann, S. Rocci Denis, A. Hupfer, H.-P. Kau

Scramjet Research Activities at the Institute of Flight Propulsion of the Technische Universitaet Muenchen

6th European Symposium on Aerothermodynamics for Space Vehicles, Versailles, France, 2008

S. Rocci Denis, D. Maier and H.-P. Kau

Experimental Investigations on Staged Injection in a Dual-Mode Combustor

26th International Symposium on Shock Waves, Göttingen, Germany; ISSW 2007-3781

K. Hannemann, H.K. Ciezki, O.J. Haidn, J. von Wolfersdorf, S. Rocci Denis

German Test Facilities for High Speed Air Breathing Propulsion

2nd European Conference for Aerospace Sciences, Brussels, Belgium; EUCASS 2007-5.05

S. Rocci Denis, A. Brandstetter, D. Rist and H.-P. Kau

Combustion Stability of a Dual-Mode Scramjet Configuration with Strut Injector

Chapter 5.3.1 in Basic Research and Technologies for Two-Stage-to-Orbit Vehicles - Wiley-VCH and DFG, Ed. D. Jacob, G. Sachs and S. Wagner, 2005

S. Rocci Denis, D. Maier, W. Erhard and H.-P. Kau

Catalytic Pre-Heating of Air for Free Stream Investigations on Combustion Stability for a Specific Scramjet Configuration

17th International Symposium on Air-Breathing Engines, Munich, Germany; ISABE 2005-1234

S. Rocci Denis, D. Maier, W. Erhard and H.-P. Kau

Free Stream Investigations on Methane Combustion in a Supersonic Air Flow

13th AIAA/CIRA International Space Planes and Hypersonic Systems and Technologies Conference, Capua, Italy; AIAA-2005-3314

S. Rocci Denis, A. Brandstetter and H.-P. Kau

Experimental Study on Transition between Ramjet and Scramjet Modes in a Dual-Mode Combustor

12th AIAA International Space Planes and Hypersonic Systems and Technologies Conference, Norfolk, VA, USA; AIAA-2003-7048

S. Rocci Denis, A. Brandstetter and H.-P. Kau

Transition between Ramjet and Scramjet Modes in a Combustor for an Air-Breathing Launcher

10th Australian International Aerospace Congress incorporating the 14th National Space Engineering Symposium 2003, Brisbane, Queensland, Australia; AIAC-2003-054

S. Rocci Denis, A. Brandstetter and H.-P. Kau

Stability of a Supersonic Model Combustion Chamber

Seminar des Sonderforschungsbereichs 255, Technische Universität München, 12.12.2002, Teilprojekt B12, S. 75-87

A. Brandstetter, S. Rocci Denis, D. Rist and H.-P. Kau

Experimental Investigation on Supersonic Combustion with Strut Injection

11th AIAA/AAAF International Space Planes and Hypersonic Systems and Technologies Conference, Orléans, France; AIAA-2002-5242

A. Brandstetter, S. Rocci Denis, D. Rist and H.-P. Kau

Flame Stabilization in Supersonic Combustion

11th AIAA/AAAF International Space Planes and Hypersonic Systems and Technologies Conference, Orléans, France; AIAA-2002-5224

Acknowledgements

It's always good when you finally come to the "Acknowledgements" section of a thesis! Particularly for me now, after all the time that passed since I performed the last measurements on October 26th 2007...it's a great feeling, I cannot stop smiling! And yet it's also a melancholic moment, for I gave this work and the test facility at LFA a 100%. Well, if I weren't an engineer I'd say even more than that: vacations, weekends and nights. In all these years, and especially the last one and a half, two things remained constant: my determination to finish the thesis and the people who supported me along the way, in the most different manners. Each of them unique and so important to me. I am sure I will forget somebody here and now and I apologize for it: blame me when we meet next time and I will feel so guilty that I will want to make it up with some Italian food!

My first "THANK YOU!" goes to Prof. Dr. Hans-Peter Kau, my supervisor. For the freedom and the trust he gave me to conduct my own research. For always finding somebody else than the only female engineer at the Institute to cook coffee – even when we finally were two! For the regular emails to ask about the status of the writing and for always accepting the standard answer: "I will submit soon"! I suppose it wasn't as clear as for me that indeed I will submit one day, so thank you for believing that I will not give up.

Thank you to Prof. Dr. Christian Mundt, who made me very proud and happy one day in the Wright Patterson Air Force Museum in Dayton by asking whether he could be my second supervisor and correct this work! It was highly motivating to hang in it and keep the level high when the time I could dedicate to the thesis became less!

Thank you also to Prof. Dr. Thomas Sattelmayer and to Prof. Dr. Ulrich Walter to speed up the organisation of my exam such that I could still do it in 2011, in the breaks between Himalayan climbing and engine testing in the birthplace of Aviation. I can hardly tell how much I appreciated it!

Thank you to Dr. Alexander Simpson for making my English almost Cambridge-like! I still have to understand how he could return me the thesis with the comment: "Sara, congratulations: it's really good, you write very well!", since he didn't leave a

single paragraph without red marks or comments...Well, I guess I'll just take the compliment! And of course thank you to my second proof-reader, Dr. Thomas Fuhrmann, also for the fruitful discussions during the time at LFA, for programming THE control system to filter the compressor oscillations and for finding the CO₂!

Thanks to my colleagues at LFA: I had quite a few over the years...Dr. Wolfgang Erhard, Dr. Armin Brandstetter, Dr. Andreas Hupfer, Dr. Ingo Wilke, Dr. Sebastian Soller, Dr. Giovanni Brignole, Dr. Daniel Waldner, Dr. Klaus Spyra, Sirka Fuhrmann, Florian Danner, Sebastian Lang, Christoph Kirchberger, Gregor Schlieben, Udo Busse, Bernhard Ritter, Roland Grubert, Regine Brammer and Angi Heining. And a special thanks to my favourite office mate, Dr. "da Alex" Stumvoll, for the macros, the Word formatting, the sun and his friendship! And thanks to their partners and families, for making our engineers-life so colourful every time we met for whatever else than technology!

Thank you to my colleagues at GE and especially to Dr. William Antel, Dr. Marion Menzel, Dr. Stefan Kern, Dr. Christian Vogel, Dr. Silke Lechner-Greite, Dr. Tiziana Bertocelli, Dr. Mathilde Bieber, Dr. Thierry Maeder, Dr. Christian Aalburg, Dr. Yarú Mendez, Simon Schoewel, Rodrigo Rodriguez, Miguel Gonzalez, Karin Bornemann, Guido Fustagni. Special thanks to Dr. Jorge Carretero for the Ph.D. comics I invariably recognized myself in! And more than that, for the compass and the guidance! Thank you also to those who left our GE crew and yet continued pushing me to write: Dr. Thomas Frey, Dr. Matthias Finkenrath, Gabor Ast, Dr. Emad Gharabah. And to my best friend, Dr. Herbert Kopecek, who can always say the right thing at the right moment when I am about to give up...and again, to your wonderful families for the time together!

Thank you to the Italian side of the world: to Silvia, Fabio, Erika, Cristina, Daniela, Rosaria, Cristiano and all the people who never let our friendship fall only because I crossed the Alps and did not come back! And thanks to the scramjet friends Down Under, for all inputs and the few beers together over the years: Dr. Judy Odam, Dr. Allan Paull, Dr. Russell Boyce, Dr. Andrew Neely, Dr. Neil Mudford, and to Peter Montgomery as an honorary member of Down Under!

Last but actually first, thank you to my family. For being there with their unconditioned love and support and for bearing with me during the hard times. I guess I could do nothing but peel potatoes and my grandma Rosa would still think I am the most clever girl in the world!

Nomenclature

| | | |
|------------|--------------------|---|
| a | [-] | Empirical Exponent in Equation 2.8 |
| a_A | [m/s] | Speed of Sound of the Air Stream (Section 2.4.1) |
| a_F | [m/s] | Speed of Sound of the Fuel Stream (Section 2.4.1) |
| a_1 | [m/s] | Speed of Sound Upstream of the Reaction Front |
| A | [-] | Cavity Aspect Ratio |
| A | [-] | Experimental Constant in Equation 2.8 |
| A^* | [m ²] | Total Area of the Injection Holes |
| A_0 | [cm ²] | Area of the Focal Spot |
| A_{21} | [s ⁻¹] | Einstein Coefficient for Spontaneous Emission |
| b | [m] | Scale of Segregation |
| b | [-] | Empirical Exponent in Equation 2.8 |
| B_{21} | [s ⁻¹] | Einstein Coefficient for Stimulated Emission |
| c_p | [-] | Specific Heat at Constant Pressure |
| c_{pAir} | [-] | Specific Heat at Constant Pressure (Main Air) |
| c_{pCH4} | [-] | Specific Heat at Constant Pressure (Injected Methane) |
| c_{pin} | [-] | Specific Heat at Constant Pressure (Combustor Entrance) |
| c_{pout} | [-] | Specific Heat at Constant Pressure (Combustor Exit) |
| C_{Dsf} | [N] | Skin Friction Drag Coefficient |
| d | [mm] | Diameter of the Gas Sampling Probe |
| D | [mm] | Cavity Depth |
| D^* | [m] | Sonic Round Hole Diameter |
| D_{CAT} | [mm] | Diameter of the Pt-Pd Catalyst |
| D_l | [mm] | Diameter of the Laser Beam at the Focal Lens |

| | | |
|------------------|--------------------|---|
| D_{las} | [mm] | Diameter of the Laser Beam for PLIF Measurements |
| D_{sf} | [N] | Skin Friction Drag |
| Da^* | [-] | Critical Damköhler Number in Section 3.4.2 |
| Da_{Probe} | [-] | Damköhler Number of the Gas Sampling Probe |
| ΔD_{sf} | [%] | Skin Friction Drag Difference |
| ΔH | [J] | Static Enthalpy Variation across the Combustor |
| ΔH_{tot} | [J] | Total Enthalpy Variation across the Combustor |
| Δp | [MPa] | Static Pressure Difference |
| Δp_{tot} | [MPa], [%] | Total Pressure Loss |
| Δu | [m/s] | Velocity Difference |
| ΔWA | [cm ²] | Wetted Area Difference |
| E | [J] | Overall Activation Energy |
| ER | [-] | Equivalence Ratio |
| f | [mm] | Focal Length |
| F | [-] | Fluorescence |
| h | [km] | Altitude in Figure 2.1 |
| H_{in} | [J] | Static Enthalpy of the Flow at the Combustor Entrance |
| H_{out} | [J] | Static Enthalpy of the Flow at the Combustor Exit |
| H_{tot_in} | [J] | Total Enthalpy of the Flow at the Combustor Entrance |
| H_{tot_out} | [J] | Total Enthalpy of the Flow at the Combustor Exit |
| I_{sp} | [s] | Specific Impulse |
| J' | [-] | Rotational Level in the Excited Electronic State |
| J'' | [-] | Rotational Level in the Ground Electronic State |
| k | [-] | Gladstone-Dale Constant |
| K | [-] | Proportionality Factor for Jet Penetration Height |
| L | [mm] | Cavity Length |
| L_{CN} | [m] | Distance between catalyst end and Laval nozzle |

| | | |
|------------------|--------|--|
| L_m | [m] | Distance at which the Mixing Layer Reaches the Duct Walls |
| m_{in} | [kg] | Amount of Flow at the Combustor Entrance |
| m_{out} | [kg] | Amount of Flow at the Combustor Exit |
| \dot{m} | [kg/s] | Air Mass Flow Rate Supplied to the Combustor |
| \dot{m}_{in} | [kg/s] | Mass Flow at the Combustor Entrance |
| \dot{m}_{out} | [kg/s] | Mass Flow at the Combustor Exit |
| \dot{m}_{CH_4} | [kg/s] | Methane Mass Flow Rate Supplied to the Combustor |
| M_1 | [-] | Mach Number upstream of the Reaction Front |
| M_{CC} | [-] | Combustor Entrance Mach Number |
| M_{CA} | [-] | Air Convective Mach Number (Section 2.4.1) |
| M_{CF} | [-] | Fuel Convective Mach Number (Section 2.4.1) |
| M_{Exit} | [-] | Mach Number at the Combustor Exit |
| M_F | [-] | Flight Mach Number |
| M_M | [-] | Measured Mach Number (Section 3.4.3) |
| M_{nom} | [-] | Nominal Mach Number in Figure 2.11 |
| M_T | [-] | True Mach Number (Section 3.4.3) |
| n | [-] | Index of Refraction |
| N_2 | [-] | Population of Photons in the Excited Electronic State |
| p | [atm] | Static Pressure in Equation 2.7 |
| p_{tot} | [MPa] | Total Pressure |
| p_{totM} | [MPa] | Measured Total Pressure (Section 3.4.3) |
| p_{totT} | [MPa] | True Total Pressure (Section 3.4.3) |
| p_B | [MPa] | Static Pressure Upstream of the Electric Heater (Basement) |
| p_C | [MPa] | Static Pressure on the Cavity Floor |
| p_M | [MPa] | Measured Static Pressure (Section 3.4.3) |
| p_T | [MPa] | True Static Pressure (Section 3.4.3) |
| p_0 | [MPa] | Static Pressure Upstream of the Catalyst |

| | | |
|-------------------|--------------------|--|
| p_1 | [MPa] | Static Pressure at the Laval Nozzle |
| p_2 | [MPa] | Static Pressure at the Laval Nozzle Throat |
| p_3 | [MPa] | Static Pressure at the Laval Nozzle Exit |
| p_4 | [MPa] | Wall Static Pressure in the Combustor, after the Leading Edge of the Strut Injector |
| p_5 | [MPa] | Wall Static Pressure in the Combustor, after the Trailing Edge of the Strut Injector |
| $p_{6,\dots,11}$ | [MPa] | Wall Static Pressures in the Constant Cross-Area Section of the Combustor |
| $p_{12,\dots,16}$ | [MPa] | Wall Static Pressures in the Diverging Section of the Combustor |
| p_{20} | [MPa] | Injection Pressure of the Pilot Oxidizer |
| p_{CC} | [MPa] | Static Pressure at the Combustor Entrance |
| p_{Wall} | [MPa] | Wall Static Pressure |
| P | [MPa] | Pressure in the Gas Sampling Probe |
| P_1 | [MPa] | Pressure of Initial State in Figure 2.17 |
| q | [J/kg] | Specific Heat of Reaction |
| Q | [J] | Heat of Reaction |
| Q_{21} | [s ⁻¹] | Collisional Quenching Coefficient |
| q_A | [Pa] | Air Dynamic Pressure |
| q_{cr} | [J/kg] | Critical Specific Heat of Reaction |
| q_F | [Pa] | Fuel Dynamic Pressure |
| q_R | [-] | Fuel-to-Air Dynamic Pressure Ratio |
| r | [-] | Fuel-to-Air Velocity Ratio |
| R | [J/kg-K] | Universal Gas Constant |
| s | [-] | Fuel-to-Air Density Ratio |
| S_f | [s ⁻¹] | Fluorescence Signal |
| T | [K] | Static Temperature in Equation 2.7 |

| | | |
|-----------------------------------|--------------------|--|
| T_{CH_4} | [K] | Static Injection Temperature of Methane |
| $T_{\text{CH}_4_{\text{Cavity}}}$ | [K] | Static Injection Temperature of Methane through Cavity |
| $T_{\text{tot_P_Air}}$ | [K] | Total Injection Temperature of Pilot Air |
| $T_{\text{tot_CH}_4}$ | [K] | Total Injection Temperature of Methane |
| $T_{\text{tot_P_H}_2}$ | [K] | Total Injection Temperature of Pilot Hydrogen |
| $T_{\text{tot_P_O}_2}$ | [K] | Total Injection Temperature of Pilot Oxygen |
| T_{in} | [K] | Static Temperature of the Flow at the Combustor Entrance |
| T_{out} | [K] | Static Temperature of the Flow at the Combustor Exit |
| $T_{\text{tot_in}}$ | [K] | Total Temperature of the Flow at the Combustor Entrance |
| $T_{\text{tot_out}}$ | [K] | Total Temperature of the Flow at the Combustor Exit |
| T_{tot} | [K] | Total Temperature |
| T_1 | [K] | Static Temperature Upstream of the Catalyst |
| T_3 | [K] | Burner Entry Static Temperature (Section 2.2.2) |
| T_4 | [K] | Burner Exit Static Temperature (Section 2.2.2) |
| u_2 | [m/s] | Flow Velocity Downstream of the Reaction Front |
| u_A | [m/s] | Velocity of the Air Stream (Section 2.4.1) |
| u_c | [m/s] | Convective Velocity |
| u_F | [m/s] | Velocity of the Fuel Stream (Section 2.4.1) |
| U_∞ | [km/s] | Cruise Speed in Figure 2.1 |
| v' | [-] | Vibrational Level in the Excited Electronic State |
| v'' | [-] | Vibrational Level in the Ground Electronic State |
| v_1 | [m ³] | Volume of Initial State in Figure 2.17 |
| V | [m/s] | General Flow Velocity |
| WA | [cm ²] | Wetted Area |
| x_M | [m] | Mixing Transition Distance |
| Y | [m] | Fuel Penetration Height |

Greek Symbols

| | | |
|--------------|----------------------|----------------------------|
| α | [°] | Cavity Ramp Angle |
| β | [°] | Oblique Shock Angle |
| χ_i | [-] | Mole Fraction of Species i |
| δ | [m] | Shear Layer Thickness |
| δ_m | [m] | Mixing Layer Thickness |
| Φ_p | [-] | Pilot Equivalence Ratio |
| γ | [-] | Ratio of Specific Heats |
| θ | [°] | Wedge Angle |
| λ | [nm] | Wavelength |
| ρ | [kg/m ³] | Density of a Medium |
| ρ_A | [kg/m ³] | Air Density |
| ρ_F | [kg/m ³] | Fuel Density |
| τ_c | [ms] | Total Combustion Time |
| τ_i | [ms] | Ignition Delay Time |
| τ_r | [ms] | Reaction Time |
| τ_{res} | [ms] | Combustor Residence Time |
| ω_0 | [μm] | Radius of the Focal Spot |

Abbreviations and Acronyms

| | |
|------------------|--|
| ADFA | Australian Defence Force Academy |
| AOTV | Aeroassisted Orbital Transfer Vehicle |
| ARV | Ascent and Re-entry Vehicle |
| CFD | Computational Fluid Dynamics |
| COM | Combustion Measurements |
| CV | Cruise Vehicle |
| DFG | Deutsche Forschungsgemeinschaft - German Research Foundation |
| FCU | Frequency Conversion Unit |
| FOFF | Fuel-Off Measurements |
| FON | Fuel-On Measurements |
| HTSM | Hypersonic Transport System Munich |
| ICCD | Intensified Charge-Coupled Device |
| LEO | Low Earth Orbit |
| LFA | Lehrstuhl für Flugantriebe (Institute for Flight Propulsion) |
| LIF | Laser-Induced Fluorescence |
| M | Third Body |
| NASP | National Aero-Space Plane |
| P_Air | Pilot Air |
| PF | Pilot Flame |
| P_H ₂ | Pilot Hydrogen |
| P_O ₂ | Pilot Oxygen |
| PLIF | Planar Laser-Induced Fluorescence |
| R&D | Research and Development |

| | |
|------|--------------------------------|
| RLV | Reusable Launch Vehicle |
| RV | Re-entry Vehicle |
| S1 | Strut 1 |
| S2 | Strut 2 |
| S3 | Strut 3 |
| SSTO | Single-Stage-To-Orbit |
| TSTO | Two-Stage-To-Orbit |
| TUM | Technische Universität München |
| UNSW | University of New South Wales |
| UV | Ultraviolet |

Contents

| | | |
|------------|---------------------------------|-----|
| 1 | Introduction..... | 1 |
| 2 | Technical Background | 6 |
| 3 | Experimental Testing..... | 42 |
| 4 | Results | 77 |
| 5 | Conclusion..... | 117 |
| Appendix A | Technical Drawings | 120 |
| Appendix B | Experimental Runs Summary | 135 |

List of Figures

| | |
|---|----|
| Figure 1.1 Airbreathing propulsion performance for H_2 (red) and C_xH_y (blue), versus rocket (grey), adapted from [13] & [71]. | 1 |
| Figure 2.1 Four major classes of hypersonic space transport vehicles, and major aerothermodynamic effects, adapted from [31]. | 7 |
| Figure 2.2 Engine issues for hypersonic airbreathing propulsion systems [71]. | 11 |
| Figure 2.3 Schematic diagram of a two-dimensional ramjet engine [30]. | 12 |
| Figure 2.4 Schematic of a two-dimensional scramjet engine [30]. | 13 |
| Figure 2.5 Scramjet engine reference station numbers and related terminology [30]. | 14 |
| Figure 2.6 Schematic of the Brayton cycle T-s diagram, adapted from [30]. | 14 |
| Figure 2.7 Schematic of external compression ramjet (left) and scramjet (right) inlets [70]. | 17 |
| Figure 2.8 Schematic drawing of the flow pattern of a complete normal shock train (left) and of a complete oblique shock train (right) [30]. | 18 |
| Figure 2.9 Different configurations of wall injectors: a) Port hole b) Wall step c) Ramp injector, adapted from [54] & [66]. | 23 |
| Figure 2.10 Cavity injector configuration [54]. | 24 |
| Figure 2.11 Comparison of open (left) and closed (right) cavity flow at a M_{nom} of two [56]. | 26 |
| Figure 2.12 Strut injector configuration [54]. | 26 |
| Figure 2.13 Formation of vortex structures in a transitional shear layer and growth of both the shear layer thickness δ and the mixing layer thickness δ_M , adapted from [30]. | 29 |
| Figure 2.14 Schematic of the flowfield for the case of normal fuel injection [30]. | 30 |
| Figure 2.15 Static temperature distribution inside the combustor with Strut 1 [40], [73]. | 34 |
| Figure 2.16 Mach number distribution (left) and combustion heat release (right) for different hydrogen-hydrocarbon mixtures reacting with air [23]. | 35 |
| Figure 2.17 Rankine-Hugoniot curve for $q=q_1$ with origin A at (P_1, v_1) . Dashed lines passing through A are Rayleigh lines [69]. | 39 |

| | |
|---|----|
| Figure 3.1 Schematic diagrams of three pulsed flow ground test facilities; shock tunnel (top), free piston shock tunnel (middle), expansion tube (bottom) [30]. | 43 |
| Figure 3.2 Schematic diagram of the direct connected testing facility of the LFA. | 45 |
| Figure 3.3 Schematic diagram of the supply lines in the test cell of the LFA. | 46 |
| Figure 3.4 Control panel of the Labview module. | 47 |
| Figure 3.5 3D section of the combustion chamber with strut and cavity injector. | 50 |
| Figure 3.6 Tested strut geometries; Strut 1 (left), Strut 2 (middle) and Strut 3 (right). | 51 |
| Figure 3.7 Detail of the gases supply lines to the combustion chamber. | 52 |
| Figure 3.8 Section of Strut 1 with suggested fuelling strategy for methane (A), pilot fuel (B) and pilot oxidizer (C). | 53 |
| Figure 3.9 Section of Strut 2 with possible fuelling strategy for methane (A), pilot fuel (B1, B2) and pilot oxidizer (C). | 54 |
| Figure 3.10 Section of Strut 3 with possible fuelling strategy for methane (A), pilot fuel (B) and pilot oxidizer (C). | 54 |
| Figure 3.11 3D view (left) and section (right) of the cavity injector. | 55 |
| Figure 3.12 Focused laser beam photographed with a CCD camera. | 56 |
| Figure 3.13 Bottom wall of the combustion chamber with pressure taps. Strut 1 is mounted in the first module of the combustor. | 60 |
| Figure 3.14 Mach number contours for a probe with a 0.6mm long straight section (left) and for a probe with no straight section (right) [46]. | 62 |
| Figure 3.15 3D section of the gas sampling probe. | 63 |
| Figure 3.16 Detail of the gas sampling arrangement. | 64 |
| Figure 3.17 Gas sampling probe during free stream tests with an older injector [59]. | 65 |
| Figure 3.18 Aft-looking-forward view of the combustor with supersonic methane flame. | 65 |
| Figure 3.19 Schematic of a Pitot tube in a supersonic stream. | 66 |
| Figure 3.20 Schlieren image of a M_T measurement using the shock and apex angles. | 67 |
| Figure 3.21 Total conditions measurement sequence. Gas sampling and total pressure (left), total temperature (middle), Mach number (right). | 68 |
| Figure 3.22 Schlieren optic setup in the test cell. | 69 |

| | |
|---|----|
| Figure 3.23 Schematic of LIF excitation between two rotovibronic states of OH and subsequent relaxation [63]. | 71 |
| Figure 3.24 Schematic and specifications of the LFA laser system for PLIF measurements. | 73 |
| Figure 3.25 Optical path to the test section. | 74 |
| Figure 3.26 Generation of the illumination plane. | 74 |
| Figure 4.1 Comparison of the old injection system (left) to Strut 1 (right). | 77 |
| Figure 4.2 Wall static pressure distribution without combustion for the configuration without injector and for both versions of the previous strut [11]. | 78 |
| Figure 4.3 Numerical prediction of the Mach number distribution in the first portion of the combustor with Strut 1 [40]. | 79 |
| Figure 4.4 Superposition of the Injector1 (3mm, red) to Strut 1, with laser sparks locations. | 80 |
| Figure 4.5 Wall static pressure distribution for the three struts (S1, S2 and S3) under Fuel-Off conditions. | 83 |
| Figure 4.6 Ignition probability for injection of pilot hydrogen as a function of the fuel mass flow rate. | 84 |
| Figure 4.7 Ignition probability for the pilot H ₂ -Air mixture as a function of the pilot equivalence ratio. | 85 |
| Figure 4.8 Ignition probability for the pilot H ₂ -O ₂ mixture as a function of the pilot equivalence ratio. | 85 |
| Figure 4.9 Comparison of the wall static pressure distribution for combustion of the H ₂ -Air (triangles) and H ₂ -O ₂ (diamonds) pilot flames, each at $\Phi_p = 7$. | 86 |
| Figure 4.10 Top view of the H ₂ -Air (left) and H ₂ -O ₂ (right) pilot flames behind Strut 1. | 86 |
| Figure 4.11 Wall static pressure distribution in the combustor for a H ₂ -O ₂ flame at $\Phi_p = 1.48$; comparison of the Fuel-Off, Fuel-On and Combustion distributions. | 89 |
| Figure 4.12 Comparison of the combustion heat release for H ₂ -O ₂ pilot flames at different Φ_p (ER in the graphics). | 89 |
| Figure 4.13 Combustion heat release for the pilot flame at increasing Φ_p . | 90 |
| Figure 4.14 Comparison of the wall static pressure distribution for H ₂ -O ₂ pilot flames at different Φ_p (ER in the graphics). | 90 |
| Figure 4.15 Total pressure drop across the combustion chamber at different Φ_p . | 91 |

| | |
|--|-----|
| Figure 4.16 Section of Strut 2 with possible fuelling strategy for methane (A), pilot fuel (B1, B2) and pilot oxidizer (C)..... | 92 |
| Figure 4.17 Wall static pressure distribution for pilot flames stabilized at different Φ_p (ER in the graphics) using Strut 3 and compared to the Fuel-Off condition. | 93 |
| Figure 4.18 Illumination plane and camera setup for the PLIF measurements in the combustor. | 94 |
| Figure 4.19 OH \cdot PLIF of the H $_2$ -O $_2$ pilot flame at $\Phi_p = 0.97$ in the first (left) and second (right) window downstream of Strut 3. | 94 |
| Figure 4.20 Wall static pressure distribution for combustion of a near stoichiometric pilot flame with Strut 1 (squares) and with Strut 3 (triangles). | 95 |
| Figure 4.21 Near stoichiometric pilot flames stabilized with Strut 1 (left) and with Strut 3 (right). | 95 |
| Figure 4.22 OH \cdot PLIF downstream of the injector for a near stoichiometric pilot flame with Strut 1 (top) and with Strut 3 (bottom)..... | 95 |
| Figure 4.23 Supersonic flame stabilization with Strut 1 at $\Phi_p = 0.99$ with 1.5g/s (top), 3g/s (middle) and 4.5g/s (bottom) methane injected through the strut sides. | 99 |
| Figure 4.24 Total pressure drop across the combustor with Strut 3 for increasing amount of injected methane. | 99 |
| Figure 4.25 Mach number at the combustor exit with Strut 3 for increasing amount of injected methane. | 100 |
| Figure 4.26 Wall static pressure distribution for injection of 4.5g/s methane with Strut 1. Φ_p is equal to 1.45..... | 101 |
| Figure 4.27 Wall static pressure distribution for combustion of a near stoichiometric pilot flame and of a lean supersonic methane flame using Strut 1 (1.5g/s CH $_4$). | 102 |
| Figure 4.28 Wall static pressure distribution for supersonic combustion of 1.5g/s stabilized using Strut 1 with a near stoichiometric and with a rich pilot flame, respectively..... | 103 |
| Figure 4.29 Wall static pressure distribution for supersonic methane flames stabilized with Strut 1 using a near stoichiometric pilot flame and for increasing amount of injected CH $_4$ | 104 |
| Figure 4.30 Wall static pressure distribution for supersonic methane flames stabilized with Strut 1 using a rich pilot flame and for increasing amount of injected CH $_4$ | 104 |

| | |
|---|-----|
| Figure 4.31 PLIF imaging of the near stoichiometric pilot flame (left) and of the supersonic flames stabilized with Strut 1 at $\text{CH}_4 = 1.5\text{g/s}$ (middle) and $\text{CH}_4 = 3\text{g/s}$ (right). From top to bottom: imaging through the four windows downstream of the strut on an illumination plane aligned with the central streamline. Image resolution: 1000. | 105 |
| Figure 4.32 PLIF imaging of the rich pilot flame (left) and of the supersonic flames stabilized with Strut 1 at $\text{CH}_4 = 1.5\text{g/s}$ (middle) and $\text{CH}_4 = 3\text{g/s}$ (right). From top to bottom: imaging through the four windows downstream of the strut on an illumination plane aligned with the central streamline. Image resolution: 512..... | 105 |
| Figure 4.33 Left: Visualization fields for the direct and PLIF imaging. Right, top: Direct imaging of the near stoichiometric pilot flame (top left), of the rich pilot flame (top right) and of the corresponding supersonic flame stabilized with Strut 1 at $\text{CH}_4 = 1.5\text{g/s}$. Bottom: PLIF imaging of both methane flames through the first two windows downstream of the strut on an illumination plane aligned with the central streamline. Image resolution: 512..... | 106 |
| Figure 4.34 Wall static pressure distribution for combustion of a near stoichiometric pilot flame and of a lean supersonic methane flame using Strut 3 (1.5g/s CH_4)..... | 108 |
| Figure 4.35 Supersonic flame stabilization with Strut 3 at $\Phi_p = 0.73$ (left) and at $\Phi_p = 0.97$ (right) with 1.5g/s (top), 3g/s (middle) and 4.5g/s (bottom) methane injected through the strut sides. | 109 |
| Figure 4.36 Comparison of the wall static pressure distribution for a supersonic flame at 1.5g/s methane stabilized at near stoichiometric pilot conditions with Strut 1 (circles) and Strut 3 (triangles), respectively..... | 110 |
| Figure 4.37 Wall static pressure distribution for supersonic methane flames stabilized with Strut 3 using a lean pilot flame and for increasing amount of injected CH_4 | 111 |
| Figure 4.38 Wall static pressure distribution for supersonic methane flames stabilized with Strut 3 using a near stoichiometric pilot flame and for increasing amount of injected CH_4 | 111 |
| Figure 4.39 Wall static pressure distribution for staged injection with Strut 1 using a rich pilot flame and for increasing amount of CH_4 injected through the cavity. | 114 |
| Figure 4.40 Side view of a $\text{CH}_4 = 1.5\text{g/s}$ supersonic methane flame with additional injection of methane through the cavity. Left: $\text{CH}_4_{\text{Cavity}} = 2\text{g/s}$; right $\text{CH}_4_{\text{Cavity}} = 8.6\text{g/s}$ | 115 |
| Figure 4.41 Wall static pressure distribution for staged injection with Strut 1 using a rich pilot flame and for increasing amount of CH_4 injected through the cavity. | 115 |

List of Tables

| | |
|--|-----|
| Table 2.1 Ignition delay correlations and τ_i for H ₂ and CH ₄ in air, adapted from [14]. | 33 |
| Table 2.2 Lower heating value and stoichiometric air-fuel ratio for the reactions considered. | 38 |
| Table 3.1 Conditions of the airflow entering the combustor and corresponding M_F . | 58 |
| Table 3.2 Labelling of the experimental data. | 59 |
| Table 3.3 List of measured static pressures. | 61 |
| Table 4.1 Comparison of Injector1 [11], Strut 1, Strut 2 and Strut 3 in terms of aerodynamic performance. | 82 |
| Table 4.2 Combustion heat release for the H ₂ -Air and H ₂ -O ₂ pilot flames at $\Phi_p = 7$. | 88 |
| Table 4.3 Performance comparison of the near stoichiometric flames stabilized with Strut 1 and Strut 3. | 96 |
| Table 4.4 Summary of the testing conditions for main flame stabilization with Strut 1 and Strut 3. | 98 |
| Table 4.5 Performance comparison of the supersonic methane flames stabilized with a near stoichiometric and with a rich pilot flame using Strut 1. | 103 |
| Table 4.6 Performance comparison of the supersonic methane flames stabilized with a near stoichiometric and with a rich pilot flame using Strut 3. | 108 |
| Table 4.7 Performance comparison of the supersonic methane flames stabilized with a near stoichiometric pilot flame using Strut 1 and Strut 3. | 110 |
| Table 4.8 Performance comparison of the supersonic methane flames stabilized with a rich pilot flame using Strut 1 and with a near stoichiometric pilot flame using Strut 3. | 112 |
| Table 4.9 Summary of the testing conditions for staged injection with Strut 1. | 113 |
| Table 4.10 Summary of the testing conditions for staged injection with Strut 3. | 116 |

1 Introduction

1.1 Overview

Technological advances throughout the history of aviation have always been driven by a desire to reach higher speeds and altitudes and to further extend the flight range. Airbreathing ramjet and scramjet engines first attracted attention during the 1950' and the 1970' due to their potential to sustain high speed atmospheric flight. More recently, they have been considered as possible means of providing safe and affordable access to space. Third-generation reusable launch vehicle systems with airbreathing or combined-cycle propulsion are envisioned to reduce the cost and enhance the reliability of transporting payloads to Earth orbits. Dual-mode scramjets are at the core of concepts for both single-stage-to-orbit and two-stage-to-orbit systems that aim to take advantage of the potential performance gains over conventional rocket-propelled vehicles. Figure 1.1 illustrates the relative performance levels in terms of specific impulse (I_{sp}) for airbreathing engine cycles against rockets.

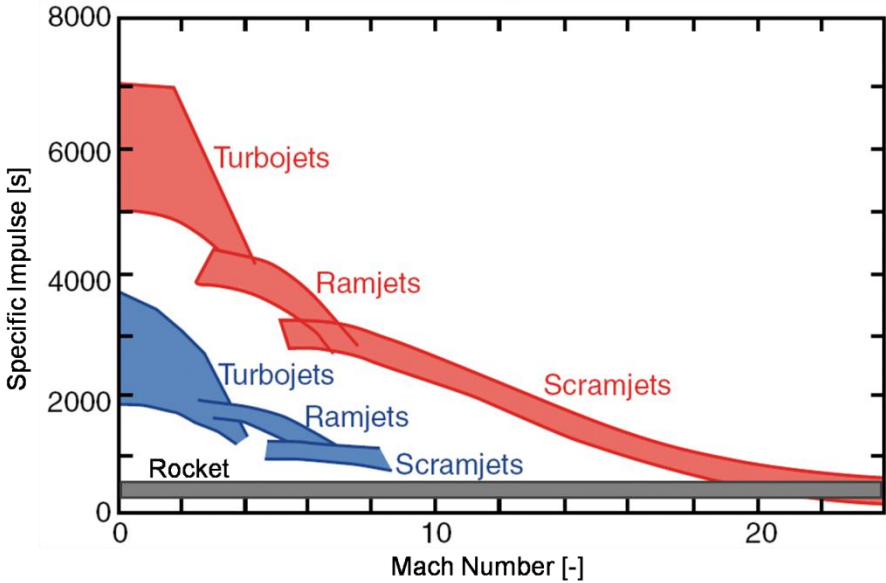


Figure 1.1 Airbreathing propulsion performance for H_2 (red) and C_xH_y (blue), versus rocket (grey), adapted from [13] & [71].

As airbreathing engines exploit the oxygen available in the atmosphere the division of the total take-off weight of the system is more effective than for rockets

[30]. The lower the oxygen weight fraction, the greater the fraction of the take-off weight available for the payload and the empty weight. Importantly, the empty weight can be used for increasing robustness, safety, flexibility and productivity of the system. The reduced propellant weight leads to a significant increase of the theoretical specific impulse for airbreathing propulsion over rockets both at lower flight Mach numbers, where it is typically a factor of ten higher, and at hypersonic speeds [36].

The trend in performance data shown in Figure 1.1 suggests conventional turboaccelerators should be replaced by subsonic combustion ramjets and by supersonic combustion ramjets, or scramjets, with increasing flight speed. Even chemical rockets may perform better than conventional engines at hypersonic speeds due to the constant level of I_{sp} they can produce. Thus, a combination of these three basic engine classes (turbojets, ramjets and rockets) will be required to cover the range of typical space access missions.

The use of supersonic combustion in non-conventional airbreathing engines becomes necessary at flight Mach numbers of approximately five. At those speeds the deceleration of the incoming airflow to subsonic conditions is accompanied by prohibitive losses leading to a drop in performance. Firstly, the viscous and shock wave losses in the inlet-isolator duct significantly impact the overall total pressure losses. Secondly, the increase in static temperature across the shock structure promotes molecular dissociation and endothermic reactions are initiated, reducing the conversion rate of thermochemical energy into kinetic energy (thrust). Finally, the significant internal pressures and heat loads to be contained and absorbed by the structure increase the weight of the engine [37]. The revolutionary nature of this type of propulsion presents considerable challenges. Technology breakthroughs are necessary for issues like engine-vehicle integration, engine stability and dependability over a broad operative range, structural integrity, materials, intake/nozzle efficiency, weight reduction, mixing and combustion stability and efficiency within a combustor of reasonable size.

Over the last twenty years considerable efforts have been undertaken, which aim to provide more extensive knowledge and appropriate design tools for airbreathing hypersonic propulsion systems. Recent advancements in the development of analytical tools and extensive ground testing in different facilities led to the first successful flight experiments demonstrating the feasibility of supersonic combustion.

Nevertheless, the conversion of the chemical energy of the propellant into thermal energy within the combustor is still challenging and the design of suitable fuel injection and flame stabilization systems remains a key challenge. This is further complicated by the fact that, unlike for the inlet and for the nozzle, existing computational and empirical techniques are not sophisticated enough to support the full design of the combustor.

Additional research is also required to gain a deeper insight into the basic physical processes governing fuel injection, mixing and combustion and to extend the predictive capabilities of computational fluid dynamics. A synergistic development of numerical tools, ground testing and flight testing demonstration is required for the development of operational hypersonic airbreathing propulsion.

1.2 Aim of the thesis

The experimental work described within this thesis continues previous efforts made at the Institute for Flight Propulsion (LFA) of the Technische Universität München (TUM), concentrating on the stabilization of combustion in a supersonic airstream [10], [11], [32], [33], [57]. This investigation focused on exploring the potential of liquid hydrocarbons for application to scramjet engines, on reducing the aerodynamic losses associated with the fuel injection and on enhancing both the mixture homogeneity and the overall equivalence ratio. Gaseous methane has been used to simulate cracked hydrocarbon fuels and the feasibility of supersonic combustion has been investigated under a broad range of conditions.

A reduction of the aerodynamic losses has been achieved by designing new strut injection geometries and developing innovative fuelling strategies. Particular emphasis has been placed on the development of struts that provide combustion stabilization without requiring additional flame holding devices.

The best performing strut geometries have been combined with a wall-mounted cavity injector positioned further downstream in the combustion chamber. This preliminary study of staged injection investigated the possibility of enhancing the overall mixing level and equivalence ratio in the combustor with a fuelling strategy that allows the control of the combustion process by varying the amount of fuel injected at each stage.

1.3 Experimental Approach

The investigations have been performed in the direct-connected test facility at the Institute for Flight Propulsion of the TUM. The majority of the experiments have been carried out at a stagnation temperature of 1000K, a stagnation pressure of 0.94MPa and a combustor entrance Mach number of 2.2. These conditions correspond to a flight Mach number of approximately 4.25, i.e. within the flight regime generally referred to as the "mid-speed" regime [9], [13]. Within this range the combustor operation is expected to undergo transition from the subsonic to the supersonic mode. The flow is highly distorted and characterized by the presence of subsonic and supersonic regions.

The first objective of these experiments was to assess whether flame ignition and stabilization are possible under the aforementioned conditions. The second objective was to investigate the combustor behaviour as a function of the geometry of the injection system, the fuelling strategy and the quantity of fuel injected.

The third objective of this study was to demonstrate the feasibility of supersonic combustion with the newly devised injection systems under conditions that are more severe in relation to flame ignition and stabilization. To achieve this, tests have been performed at lower stagnation temperature (650K) and pressure (0.75MPa) whilst maintaining the inlet Mach number (M_{CC}). The corresponding flight Mach number ($M_F \approx 3.25$) lies at the bottom end of the mid-speed regime.

Finally, tests were performed continuously varying the stagnation temperature from 1000K to 650K and stagnation pressure from 0.94MPa to 0.75MPa, to investigate the flame stability during transition from a simulated flight Mach number of 4.25 to 3.25.

1.4 Thesis Structure

The thesis is composed of five chapters and two appendices.

Chapter 2 introduces the typical issues encountered in the development of non-conventional hypersonic airbreathing engines and presents an overview of the different engine types and components. Particular attention is paid to the injection systems and to the analysis of the basic physical processes of fuel mixing and combustion. Finally, a

brief discussion of different kinds of fuel for application to airbreathing hypersonic propulsion and a review of the existing types of ground testing facilities is presented.

Chapter 3 describes the supersonic combustion testing facility of the Institute for Flight Propulsion, the experimental methodology and the test conditions. The novel fuel injection systems and configurations are detailed and the measurement techniques applied are introduced.

Chapter 4 presents the experimental results, beginning with those related to stabilization of a pilot flame in the wake of strut injectors. The data on supersonic methane combustion for single-stage injection are then discussed and the different strut geometries and fuelling strategies are compared in detail. The results of the two-stage injection through strut and cavity conclude the analysis.

Chapter 5 summarizes the most important findings of the investigation and the major conclusions are outlined.

Appendix A includes the technical drawings of the components and Appendix B summarizes the conditions for the different experimental runs.

2 Technical Background

The interest of the international aerospace community in hypersonic vehicles for application to space transport has increased over the last few decades and different vehicle classes have been defined depending on the mission requirements. Along with the vehicle size and configuration, different mission profiles determine the aerothermodynamic environment in which the system will operate and thus the aspects that will be critical to the design.

This chapter provides a background on supersonic combustion. The chapter starts with a brief description of hypersonic vehicles. This is followed by a focussed discussion on the specific features of airbreathing hypersonic propulsion and the associated engine components. Finally, different injector types are detailed in relation to the mixing, ignition and combustion processes.

2.1 Hypersonic Flight and Systems

The re-entry of the WAC Corporate rocket on February 24, 1949 and Yuri Gagarin's safe return to Earth onboard the Vostok 1 on April 12, 1961 were the first successful achievements of hypersonic flight (unmanned and manned respectively). Since then, milestones such as the Mach 7 flight of the experimental hypersonic airplane X-15 in 1963 and the development of the Space Shuttle, with a re-entry speed up to Mach 25, have been key milestones in the field of hypersonic flight. Nevertheless such missions are far from commonplace with sustained hypersonic flight representing a significant challenge for the aerospace community.

The definition of the term *hypersonic* is not trivial. Unlike for the sonic border, there is no clear delineation between supersonic and hypersonic conditions. Perhaps the best way is to define the hypersonic regime in terms of flow phenomena that become progressively more important as the Mach number increases [2]. The relevant flow phenomena are thin shock layers, entropy layer, viscous interaction, high-temperature and low-density effects. However, this still does not identify any Mach number threshold from where the flight regime can be referred to as hypersonic. In fact, no clear definition of the aerothermodynamic environment is available to

characterize the hypersonic flow during the flight through the atmosphere and the hypersonic environment must be determined depending on the mission requirements and the vehicle size constraints.

A re-entry vehicle like the Space Shuttle, for instance, requires high drag coefficients and small initial flight path angles. The hypersonic deceleration occurs at high altitudes and viscous or inviscid interactions, non-equilibrium thermochemistry and non-continuum flow models must be accounted for in the design. On the contrary, a low-drag, slender vehicle entering the atmosphere at large initial flight path angles experiences hypersonic deceleration at much lower altitudes and has to withstand high heating rates and dynamic pressures.

Four major classes of hypersonic space transport vehicles can be identified [7], [31]. Figure 2.1 summarizes the important aerothermodynamic phenomena for each class. These include aeroassisted orbital transfer vehicles (AOTV), winged re-entry vehicles (RV), ascent and re-entry vehicles (ARV) and hypersonic cruise vehicles (CV). The latter is the subject of the present study.

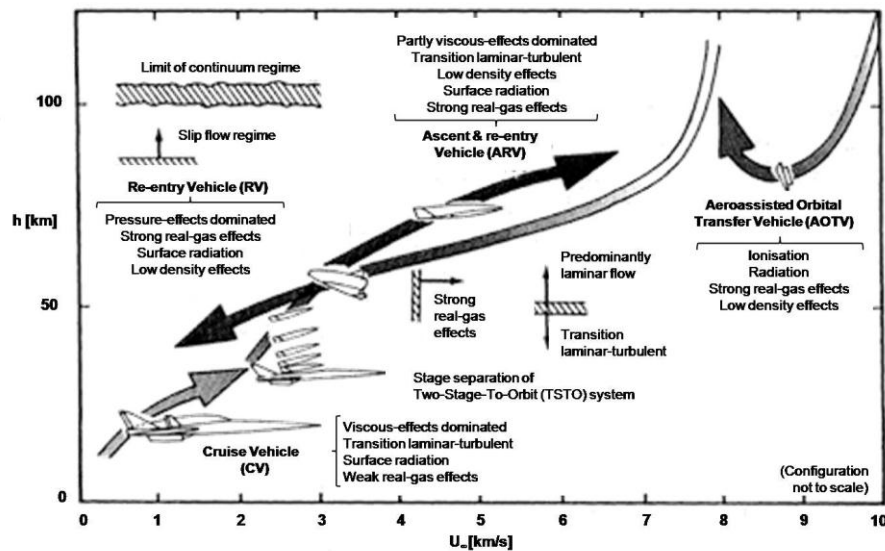


Figure 2.1 Four major classes of hypersonic space transport vehicles, and major aerothermodynamic effects, adapted from [31].

Airbreathing hypersonic cruise vehicles fly for extended time periods within the atmosphere at relatively low altitudes and very high speeds. As highlighted in Figure 2.1, the aerodynamic loads due to the high free stream Reynolds numbers and dynamic pressures and the severe thermal loads are key aspects for the system design.

Because of the potential for reducing the delivery cost to Low Earth Orbit (LEO), several nations initiated research programs in the mid 1980s to develop an aerospace vehicle exploiting airbreathing propulsion to accomplish payload transfer to a LEO. The broad requirements for such a transatmospheric vehicle were based on the analysis of a rocket propelled space transport system [30]. It was envisaged that similar to a conventional airplane the system would be equipped with wings, control surfaces and wheels to increase its dependability, robustness and productivity. The vehicle was also intended to be reusable and compatible with a variety of payloads and the fuel was envisaged to provide the cooling expected to be necessary for the structures. It was estimated that manufacturing, assembly, transportation and launching facilities would be much smaller than for rockets, reducing the costs of space access by a factor of ten.

Over time two groups of airbreathing space transport concepts, the Single-Stage-To-Orbit (SSTO) and the Two-Stage-To-Orbit (TSTO), emerged. These will be outlined here based on two key development programs.

The USA National Aero-Space Plane (NASP) program started in 1986 as a joint initiative between NASA and the Department of Defence. The purpose of the program was to develop a SSTO transatmospheric vehicle, the X-30, capable of flying into a LEO. This manned aerospace plane was envisaged to be enhanced with scramjet propulsion and would perform horizontal takeoff and landing from, and to, a conventional runway. The vehicle would accelerate to hypersonic speeds, fly and deliver a payload into orbit and return to Earth with propulsive capability. These features would make its operability, flexibility and productivity comparable with those of a conventional airplane [13], [30]. The main advantage of a SSTO system, the utilization of a single vehicle to perform the whole mission, is reduced by its higher complexity and development costs, as well as its increased sensitivity to design parameters such as dry mass and propulsion system performance [38].

A flight test of the X-30 has not been carried out in the NASP program, but the technology contributions accomplished encouraged NASA to initiate the "Hyper-X" flight research program in 1995. The objective of the latter was to demonstrate the performances of an airframe-integrated scramjet at flight Mach numbers of 5, 7 and 10. The Hyper-X program has been renamed "X-43A" as it evolved into a more comprehensive research project, the NASA's Advanced Space Transportation Program, which also includes the X-43B and X-43C. The former aims to develop a reusable flight demonstrator integrating either rocket thrusters or gas turbine engines with a dual-mode scramjet (DMSJ) in a dual-flowpath configuration. The latter is designed to

perform flight tests of a hydrocarbon-fuelled DMSJ. The ultimate goal of the overall program is the development of third-generation reusable launch vehicles with airbreathing or combined-cycle propulsion.

The Two-Stage-To-Orbit solution for a launcher was extensively investigated in the German Hypersonic Technology Program between 1988 and 2003. Parallel studies on fully reusable TSTO space transport systems were carried out from 1989 to 2003 at the "Collaborative Research Centres" 253, 255 and 259 at the Aachen, Munich and Stuttgart Universities. The baseline concept consisted of a manned, airbreathing-propelled lower stage and of a rocket-powered upper stage. The upper stage would be released at an altitude of about 30km and a flight Mach number of 7 during the 0-g phase of a parabolic flight manoeuvre [38].

While the two stages cannot be designed independently, the critical aerothermodynamic aspects of each stage (cf. CV and ARV of Figure 2.1, respectively) differ due to the different vehicle trajectories and configurations. The higher development and operational costs compared to a SSTO system would be balanced by the lower technology level required for the design of each stage and by the increased robustness and safety. Projections indicated a potential cost reduction for orbital payload delivery of an order of magnitude compared to rockets [30].

The Collaborative Research Centre 255 in Munich focussed on the development of an airbreathing, hypersonic space plane performing horizontal takeoff and landing referred to as the "Hypersonic Transport System Munich" (HTSM). The vehicle was anticipated to have wings, control surfaces and wheels and would use a combined cycle engine integrating a conventional turbojet with ramjet and scramjet propulsion.

The design of the airbreathing hypersonic unit of the HTSM represented one of the major challenges of the program. A range of research groups were involved in different aspects of the design. The experimental study at the Institute for Flight Propulsion (LFA) converged on the feasibility of hydrogen combustion in supersonic flows.

Following the conclusions of the HTSM program, the work on supersonic combustion at the LFA continued with two distinct efforts. The first was a self-funded, fundamental research (this thesis). The second, started in April 2005, was a new collaborative program on a national level supported by the German Research Foundation (DFG). The aim of the Graduate School 1095 is to investigate the aerothermodynamic design of a scramjet for future space transportation systems and

the work at LFA focuses on the application of different fuels to scramjet propulsion [22], [72].

2.2 Airbreathing Engines

As this thesis is focussed on supersonic combustion, from this point on the term *airbreathing* will be used to indicate only the non-conventional airbreathing system whose main element is the ramjet engine. Furthermore, the terms *ramjet engine* or *ramjet propulsion* will generally refer to an engine performing subsonic and/or supersonic combustion, while *ramjet*, *scramjet* and *dual-mode* will be used to refer to the specific configurations.

Three features make airbreathing propulsion unique and are critical to the design process. First, ramjet engines capture the oxygen they require directly from the atmosphere. Second, at supersonic and hypersonic flight speeds, mechanical air compression is no longer required and the system exploits the compression inherent in capturing and decelerating the flow. Third, the engine is completely integrated with the airframe as opposed to being attached to the wings or aft control surfaces, to avoid prohibitive external drag levels and narrow internal passages that would cause the flow to be dominated by wall effects [26], [27], [30].

The engine utilizes an inlet to capture and compress the air, which is then ducted to the combustion chamber. A component generally referred to as isolator may be required to control the interaction between the inlet and the combustion chamber. Finally, the fuel-air mixture burned in the combustor passes through a nozzle and is accelerated. Due to the absence of rotating machinery, the engine does not need to be axially symmetric about a centreline and the bottom surface of the vehicle can be used as an inside surface for the engine.

The engine-airframe integration has the major drawback that only one duct is available for the engine. However, the enthalpy increase along the flowpath must be sufficient to generate positive thrust and to propel the vehicle. At low speeds or within a very thin atmosphere ramjet engines cannot process enough airflow to meet this requirement, making it necessary to combine with another engine type.

A number of technical challenges are encountered in the design of hypersonic airbreathing propulsion. Examples are the broad ranges of operative flight Mach numbers and altitudes, the high degree of system integration with regard to both the

performances and the aerodynamics and the limited time intervals to accomplish stable and efficient mixing and combustion. The technical challenges associated with such a demanding design are summarized in Figure 2.2. A more detailed description of the specific issues lies outside the scope of this thesis and can be found in the mentioned references.

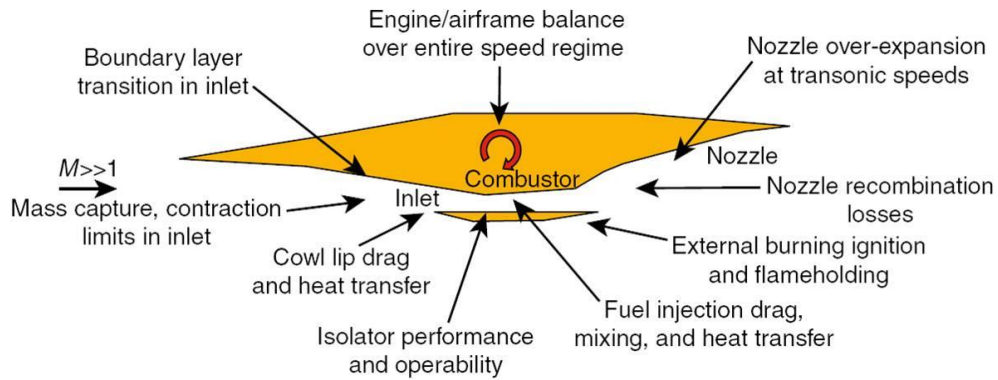


Figure 2.2 Engine issues for hypersonic airbreathing propulsion systems [71].

The fundamental differences between ramjet, scramjet and dual-mode engines will be examined in the following sections before a short description of the individual engine components is presented.

2.2.1 Ramjet Engines

The ramjet cycle is typically chosen for flight Mach numbers (M_F) between three and six. The operation in this engine is characterized by the fact that the captured airflow is decelerated to subsonic speeds prior to entry to the combustion chamber. Below $M_F=3$ the volume of processed flow is not enough to guarantee sufficient air compression, while above $M_F=6$ the losses associated with the deceleration of the flow become prohibitive and the engine performance drops.

As mentioned above, the cycle pressure ratio is achieved by exploiting the compression inherent in the flow deceleration, which is accomplished in a multi-step process. The captured flow first passes through the bow shock at the vehicle forebody and then flows into a convergent duct, reducing its speed. A strong shock system and a divergent duct further decelerate the airflow and increase the overall pressure level. In the combustor, fuel is mixed with the subsonic, high pressure air and the mixture reacts. The hot combustion products leave the burner and are accelerated to

supersonic speeds through a convergent-divergent nozzle before being exhausted into the atmosphere. Figure 2.3 schematically depicts a planar geometry ramjet engine.

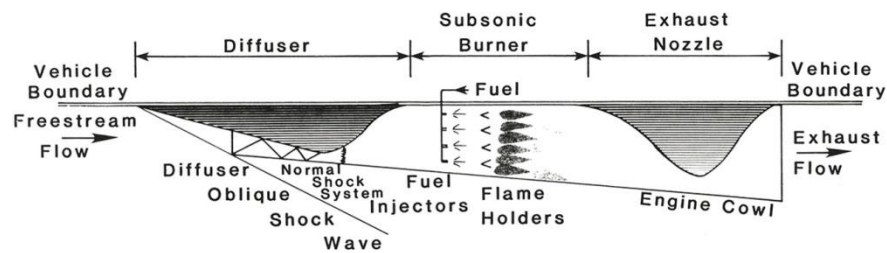


Figure 2.3 Schematic diagram of a two-dimensional ramjet engine [30].

Two physical throats are required to stabilize ramjet operation. The first throat is positioned before the outlet of the diffuser and is needed to stabilize the normal shock wave. The flow is not choked in the first throat and reaches subsonic conditions only across the final shock wave. The second throat is located downstream of the combustor and is necessary to accelerate the hot subsonic flow to supersonic conditions (the flow is choked in the second throat). The section between the two throats is referred to as the transition section. The static pressure at the combustor entry is fixed by the choking condition in the second throat and it appears as a subsonic back pressure to the transition section [1], [30].

In order to minimize the total pressure losses associated with the normal shock system and to maximize the installed engine thrust, the ramjet engine operates at a high inlet contraction ratio. This increases the risk of engine unstart and complicates the stabilization of the inlet shock system. Mechanisms to control the boundary layer, such as bleeding, become necessary with negative implications for the inlet total pressure losses. However, the other major source of losses, the Rayleigh losses associated to the combustion process, are relatively low, since the process takes place in a subsonic flow. Balancing the inlet pressure recovery and the combustion losses governs the fuel specific impulse levels shown in Figure 1.1 and is essential to achieve efficient design of a ramjet engine [1].

2.2.2 Scramjet Engines

As the flight speed exceeds Mach numbers of six the pressure, temperature and density of the flow entering the combustor after deceleration to subsonic conditions are considerably higher than in the freestream. The heat loads and the internal pressure

levels to be absorbed and contained by the structures are significant and the engine size and weight become unacceptable. The performance of the ramjet system drops due to the pressure losses associated with the strong shock system and the initiation of endothermic dissociation reactions that reduce the amount of chemical energy available for thrust generation [1], [30], [37].

At these conditions it is more advantageous to decelerate the incoming airflow to a Mach number above one. The combustion process thus takes place in a supersonic flow and the corresponding engine is the "supersonic combustion ramjet", or "scramjet". A planar geometry scramjet engine is sketched in Figure 2.4.

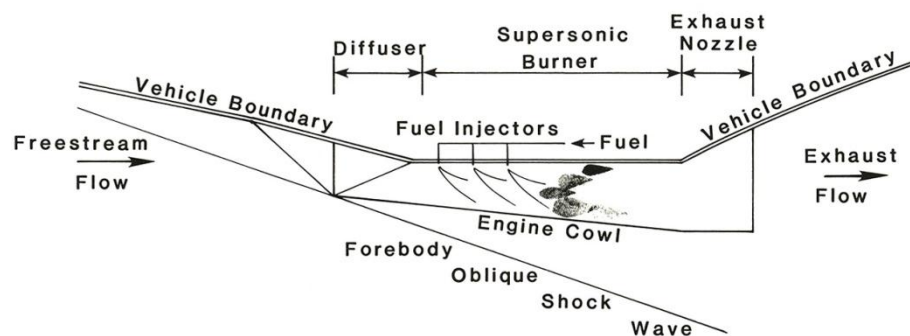


Figure 2.4 Schematic of a two-dimensional scramjet engine [30].

The fact that the flow is supersonic throughout the engine allows for a simpler geometry of the inlet and the nozzle. The inlet is entirely convergent in order to decelerate the flow and contributes only partially to the cycle pressure ratio increase, which is now mostly accomplished by the oblique shock waves from the vehicle forebody upstream of the engine. The nozzle, on the contrary, is entirely divergent to accelerate the supersonic high-temperature flow from the combustor. Both the compression and the expansion are accomplished partially on the vehicle boundary (external contributions) and partially inside the engine (internal contributions). This last point emphasizes the importance of proper engine-airframe integration.

The reference stations at different axial positions along the engine flowpath are defined in Figure 2.5 according to the notation of reference [30], which omits several station numbers to be consistent with conventional airbreathing engine analysis and to allow the inclusion of other engine components such as the fuel injectors and mixers.

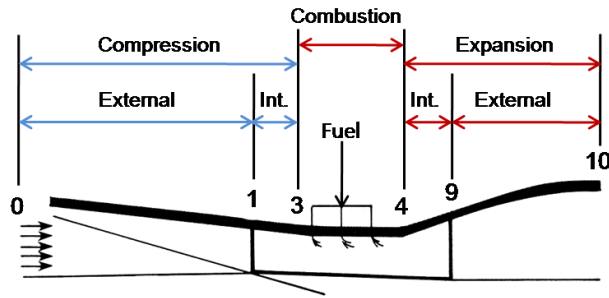


Figure 2.5 Scramjet engine reference station numbers and related terminology [30].

Because of the extremely short flow residence time available, the most specific challenge is to achieve stable and efficient fuel mixing and combustion within a burner of reasonable size. Additionally, the combustor experiences severe heat loads due to three factors. First, the significant kinetic energy of the incoming flow is converted into internal energy and thus the static temperature of the flow increases. Second, the air compression through the shock system leads to a local high gas density. Third, the combustion process inherently increases the gas temperature.

As for the factors governing the specific impulse of the propulsion cycle, the situation is the converse of that for the ramjet. The inlet pressure recovery losses are relatively low, as scramjet operation does not require a normal shock wave and typically occurs at low inlet contraction ratios. Unfortunately, the Rayleigh losses associated with the combustion process are high [1], [37].

For completeness the scramjet thermodynamic reference cycle, i.e. the Brayton cycle, is presented in Figure 2.6 for the engine stations shown in Figure 2.5.

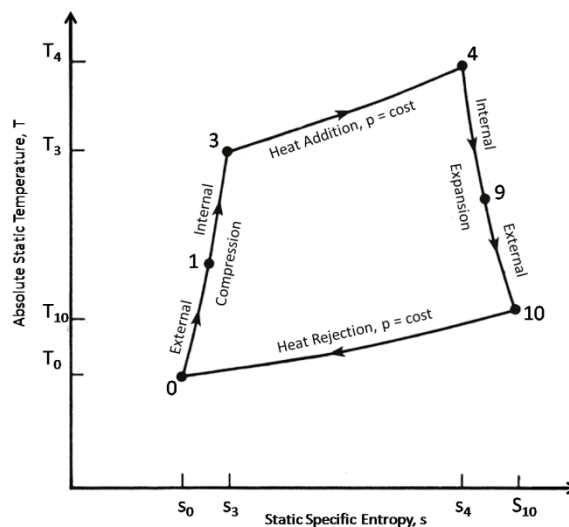


Figure 2.6 Schematic of the Brayton cycle T-s diagram, adapted from [30].

The air flow undergoes adiabatic compression from undisturbed freestream conditions to the combustor entry conditions (Points 0 to 3). The higher level of the specific entropy at station 3 is due to the irreversibilities caused by the presence of skin friction and shock waves in the inlet.

The combustion process is represented by a heat addition process supplying the same amount of thermal energy, but with no mass addition and chemical change of the air constituents. This assumption relies on considering the processed air as a pure substance for thermodynamic analysis purposes and is reasonably realistic for the expected values of the fuel-to-air ratio. The process is modelled as a constant static pressure, frictionless heat addition increasing the static temperature of the flow across the burner from T_3 to T_4 . The hot flow is then adiabatically expanded to the pressure of the surrounding atmosphere. The expansion process is also irreversible and takes into account the associated skin friction and shock wave losses.

The process between point 10 and 0 is an imaginary, constant static pressure and frictionless process through which heat is rejected by the flow that exits the vehicle and returns to the initial conditions. The rejected heat represents the amount of heat added to the flow that is not converted into useful cycle work [30].

2.2.3 Dual-Mode Engines

The typical space transport mission profiles suggest that either two different engines for ramjet and scramjet operation or one engine with variable-throat geometry will be necessary to cover the range of foreseeable flight conditions. The latter solution, although possible, is highly impractical, while the former obviously increases the system complexity, weight and cost, making airbreathing propulsion less appealing as an alternative to rockets.

A more elegant solution, the dual-mode combustion system, was conceptualized in 1963 and demonstrated experimentally for the first time in 1966 [8], [9], [30]. The dual-mode engine is capable of operating in both subsonic and supersonic modes without the area constrictions that limit the mass flow rate at flight Mach numbers higher than six.

The concept is realized by the use of thermal choke rather than mechanical choke, which allows a single engine designed with the no-throat scramjet geometry. The transition between the engine modes is accomplished by the implementation of an isolator as described in Section 2.2.5.

Thermal choking of the flow downstream of the combustor generates a high back pressure upstream of station 3. The back pressure, in turn, causes a shock train in the isolator, which behaves like a variable-area diffuser and adapts to the back pressure level, as long as the latter remains under a critical value exceeding the isolator's ability to contain the normal shock train. Thus, control of the total temperature distribution along the engine axis enables ramjet operation without requiring physical throats. The thermal throat downstream of the combustor is provided by a suitable axial area distribution along the engine flowpath combined with controlled fuel-air mixing and combustion. With increasing flight speed, choking of the flow is no longer required and the engine operation changes to the scramjet mode to effectively reduce the internal static pressure by keeping the flow supersonic throughout the engine path.

The discussion of the dual-mode operation engine concluded the survey of the typology of airbreathing engines, which are classified depending on the combustion regime. The following four sections present the engine components, the major requirements inherent in their design and the most important specific losses.

2.2.4 Inlet

The inlet is the component responsible for air capture and compression. At the examined flight speeds (M_F above three), the aerodynamic compression in the inlet entirely removes the need for conventional mechanical compressors. Thus, the inlet must guarantee the necessary cycle static pressure ratio with a minimum-weight, maximum-performance geometry under the entire range of vehicle operation [30], [70].

A number of aerodynamic and mechanical challenges face the inlet designer. These include boundary layer separation, starting limits, variable geometry and structural cooling. Deceleration of the flow must be achieved whilst providing efficient compression, low drag and uniform profiles of the flow to be further processed by the combustor.

Besides these general guidelines, specific requirements arise depending on whether the inlet is designed for a ramjet or for a scramjet application. The ramjet primarily relies on external compression on the inlet portion integrated with the vehicle forebody. The inlet requires a high degree of forebody turning and boundary layer bleed to achieve the necessary pressure recovery. Unless the engine is designed for dual-mode operation, a diffuser with a physical throat is necessary to stabilize the

normal shock system that decelerates the flow to subsonic conditions and, again, boundary layer bleeding may be required to stabilize the shock wave-boundary layer interaction and to trap terminal shock systems.

Conversely, scramjet inlets can operate at a higher compression ratio for they require a lower degree of forebody turning; the internal performance is not negated by the external drag on the engine cowl and bleed is no longer required because the hypersonic, turbulent boundary layer is more resistant to separation. Finally, in a scramjet inlet the operative conditions influence the structure of the flow. At high speeds and/or low heat release rates in the combustor the flow is supersonic throughout the inlet while lower speeds and/or higher heat release levels cause thermal blockage of the combustion process and a pre-combustion shock train appears in the inlet. The shock train can be sufficiently strong to decelerate the flow to a subsonic state.

The manner in which the aspects discussed above influence the design of ramjet and scramjet inlets is summarized in Figure 2.7.

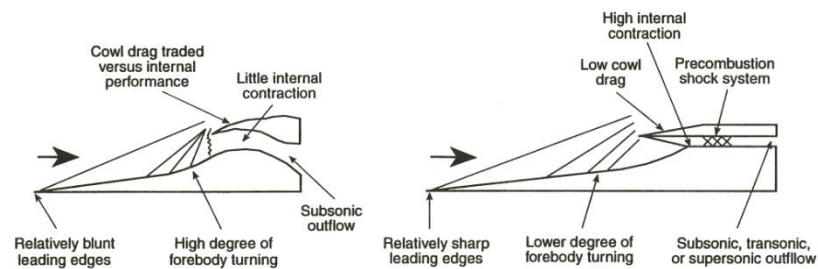


Figure 2.7 Schematic of external compression ramjet (left) and scramjet (right) inlets [70].

2.2.5 Isolator

The discussion in the previous sections highlighted the strong aerodynamic coupling between the inlet and the combustor. The reasons for this coupling are the viscous flow and the shock and expansion waves originating in the inlet and propagating downstream. The subsonic portion of the boundary layer allows the transmission of information upstream even in a supersonic flow and the shock-boundary layer interactions intensify the process. As a result, a pressure rise in the combustor due to fuel injection and/or combustion could lead to separation of the inlet flow and degrade the overall engine performance. The isolator, a constant area diffuser, is used to aerodynamically decouple the supersonic inlet from the combustor [1], [30].

Particularly susceptible to aerodynamic coupling is the performance of a dual-mode engine at low flight speeds and with thick inlet boundary layers. In this case, aerodynamic isolation is required between the supersonic inlet and the subsonic combustor. The back pressure level forces a normal shock train in the isolator, as shown in Figure 2.8. The theoretical maximum static pressure rise through the shock train approaches the value that would be reached behind a single normal shock wave. In reality, distortion of the inlet flow influences the viscous interaction and lowers the level of the static pressure rise achievable over the shock train. This inhibits the isolator's ability to contain the shock train without disgorging it and causing inlet unstart.

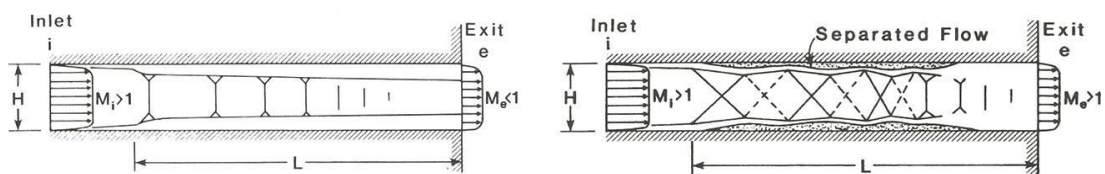


Figure 2.8 Schematic drawing of the flow pattern of a complete normal shock train (left) and of a complete oblique shock train (right) [30].

At higher flight speeds and with thinner inlet boundary layers the engine operates in scramjet-mode, a lower static pressure rise is required and the back pressure level induces an oblique shock train in the isolator. As in the case of ramjet mode, the isolator must be sufficiently long to contain the entire shock train, otherwise upstream migration of its leading edge will cause engine unstart. It is important to note that the total isolation length is shorter than in ramjet-mode operation, as the flow is only locally subsonic.

Finally, at hypersonic speeds an isolator is not required as the flow is highly supersonic throughout the engine. In this case the inclusion of an isolator negatively impacts the engine performance. The trade-off between providing an isolator at low flight Mach numbers and maintaining high performances at hypersonic speeds is critical to the design of dual-mode engines for operation over a broad range of flight conditions.

2.2.6 Combustion Chamber

The design of a combustion chamber for an airbreathing engine is a considerably more complicated task than simply optimizing the geometry of the duct for a specific operation range. Problems including flame stabilization, efficient energy conversion

and thermal management are further complicated by fuel injection, mixing and ignition. At supersonic and hypersonic flight Mach numbers the combustion heat release contributes to the increase in the total energy of the working fluid, which is already high due to the dependence of the kinetic energy on the square of the flight velocity. Thus, minimizing losses becomes critical to the successful design of the engine [30], [71].

Aerodynamic losses associated with hypersonic flows and relevant to the combustor design are determined by friction drag and heat transfer. The friction drag is proportional to the flow velocity squared, whilst the heat transfer shows a velocity-cubed dependence [2]. Studies have demonstrated that combustor skin friction is the major contribution to the total drag and a range of techniques have been proposed to reduce its magnitude [52], [54]. Heat loads on the engine walls have to be managed either through heat radiation from the vehicle, which reduces the propulsion efficiency, or through capitalizing on the cooling capability inherent in the fuel, which increases both the weight and complexity of the engine.

When combustion occurs, thermal issues further complicate the aerodynamic environment. The static pressure rise associated with supersonic combustion in a constant-area duct may induce boundary layer separation and subsequent choking of the combustor. To avoid separation, the combustor is designed with either divergent walls, to counteract the pressure increase with an expansion, or with a step. In addition to accommodating the pressure rise with an increase of the cross-sectional area, the latter also provides a barrier to the upstream migration of a potential separation bubble [37].

It is important to note that the contribution of the chemical energy of the reactants to the total enthalpy of the working fluid is a function of flight speed. At flight Mach numbers equal or lower than eight the potential combustion heat release and the kinetic energy of the oncoming flow are approximately the same. At M_F of around 25 the kinetic energy is approximately 90% of the total energy of the working fluid with the remainder due to gradual, diffusive mixing and combustion that take place in the burner [1].

Thus, the manner in which the combustion process alters the flow characteristics depends on the flight regime. At flight Mach numbers above eight, the flow deflections due to heat release are minimal and the flow boundaries are contoured for adapting to the pressure distribution and preventing the formation of strong shocks. The Mach

number variations along the combustor flowpath are significant and flowfield analysis requires full three-dimensional modelling. At Mach eight and below, where transition between ramjet and scramjet modes occurs, the combustor is characterized by a highly distorted flow with a mixture of subsonic and supersonic zones. The heat release due to combustion leads to a significant pressure rise, high flow deflections and boundary layer separation. The bulk Mach number is above one along the flowpath and one-dimensional modelling delivers a realistic analysis of the flowfield.

The fuel injection, ignition and mixing phenomena are key to a robust design. These physical processes have to be accomplished within an extremely limited time, while also minimizing aerodynamic losses. Fuel, injection configuration and fuelling strategy have to be carefully optimized in order to guarantee that the mixture ignition and reaction times are compatible with the residence time of the flow in the combustion chamber.

Finally, the interactions between the internal and the external flowpaths and amongst the different engine components must be included in the energy analysis to optimize the overall system design. As the combustor is the component that most significantly affects the overall enthalpy loss because of the distorted flowfield and of the combustion inefficiencies, the combustor becomes the component from which to start the analysis of the flowpath as a whole. Moreover, the combustor design directly influences the vehicle volume, wetted area and drag and this further justifies the choice of the combustion chamber as the central component of the flowpath.

The common features of supersonic combustion and the physical processes of fuel injection, mixing and ignition will be detailed in Section 2.4.

2.2.7 Nozzle

The nozzle is the component that expands and accelerates the high pressure and temperature combustion gases to produce the net thrust. For thermal management purposes alone the nozzle might be integrated with the combustion chamber, however for weight reduction considerations it is always integrated with the vehicle afterbody to form a single-sided or free expansion nozzle. The achievement of high performance is not only a matter of either maximizing the expansion efficiency or minimizing the entropy rise, but also includes control of the direction of the exhaust flow [1], [30], [48].

Besides the net thrust, the airframe integrated nozzle of an airbreathing engine generates lift and sidewall forces, their associated moments and potentially torque. Therefore, aerodynamic balance is crucial to guarantee a dynamically stable flight over the whole operation range.

The major challenge associated with the design of the nozzle is to establish the internal flowpath in order to accommodate the pressure gradient along the axis and to determine the shape of the nozzle contour. The chemically reactive and distorted nature of the entry flow further complicates the problem. The classical approach to two-dimensional expansion processes based on the method of characteristics is used to develop a hypersonic expansion system. In order to minimize the length of the nozzle, the majority of the flow turning and the static pressure removal occur on an initial expansion fan centred on a sharp corner at the nozzle entry. The remaining expansion is achieved by imposing a convenient slope to the nozzle boundary to absorb each characteristic upon its incidence at the surface.

As nozzle operation mostly takes place at off-design conditions, performance degradation must be taken into account. The principal loss mechanisms to be aware of are underexpansion, flow divergence, viscous and shock wave losses, chemical kinetics effects and skin friction. A detailed description of the loss mechanisms and of the way in which they influence the nozzle design goes beyond the scope of the present thesis and can be found in the literature [1], [30], [48].

2.3 Overview of Types of Fuel Injectors

Though not classical, main engine components, fuel injection systems are of critical importance in the development of airbreathing propulsion engines. This is because they are the instrumental in achieving a homogeneous mixture in addition to flame holding. Moreover, the survey of the previous sections highlighted the influence that fuel injection has on both the flow aerodynamics and the overall engine performance. Accurate design of injection becomes less a matter of efficiency than of the feasibility of the whole engine concept.

In the conventional approach, fuel is supplied to the combustion chamber, where it reacts to energise the cycle working fluid. This injection strategy is applied in the present study. A promising, alternative approach is to perform fuel injection in the intake. In this scenario mixing of fuel and air occurs upstream of the burner, enhancing

the efficiency of the process and allowing the utilization of shorter combustion chambers [52].

For given inlet flow conditions the net heat release in the combustion chamber is governed by the mixing efficiency. The former is proportional to the degree of fuel-air mixing achieved, while the latter is a measure of the stream thrust losses associated with the fuel injection and the mixing processes [37]. Both are determined, to a large extent, by the injection configuration.

Several key issues have to be considered in the design of a suitable fuel injection system. First, the injector must guarantee fast and homogeneous fuel distribution in order to minimize the length of the combustion chamber. Second, it must provide a certain degree of flame holding to support fuel ignition and to anchor the flame over the whole operation range. Third, the total pressure losses introduced must be minimized to avoid excessive reduction of the stream thrust. In addition, the aerodynamic disturbance increases the static pressure and temperature in the combustor, which results in higher friction and heat transfer losses. Fourth, the system must allow the adjustment of the amount of fuel injected at a specific location, in order to control the combustion heat release process, to avoid excessive thermal loads on the walls and to prevent thermal choking during scramjet operation. Fifth, the flow distortion due to the injectors must be minimized to guarantee a uniform flow profile and an efficient expansion in the nozzle [25], [66].

The different systems that have been proposed to fulfil these requirements can be classified in two major groups: wall jets and central injectors. Several variations and combinations of these two basic types have been investigated worldwide and a selection of the most common geometries is presented in the following section. Emphasis is placed on their advantages and disadvantages, while the peculiarities of the physical mixing process are addressed in Section 2.4.1.

2.3.1 Wall Injectors

For the purpose of this discussion three configurations will be classed as wall injectors, i.e. port holes, steps and ramps. Figure 2.9 presents a schematic of the three configurations.

The simplest way to deliver fuel to the combustor consists of transverse injection through holes in the chamber walls. Fast, near-field mixing of fuel and air proceeds via a penetration mechanism governed by the momentum flux ratio between the jet and

the airstream. The flow field close to the injection port is highly three-dimensional due to the interaction of the jet with the crossflow. The resulting local shocks and flow separation generate low-speed regions in which radical pools can be stabilized and subsequently support fuel ignition and combustion. Unfortunately, the extreme temperatures in the radical pools increase the thermal loads and the skin friction drag on the combustor walls. The total pressure losses associated with the shocks also degrade the aerodynamic performance [54], [70].

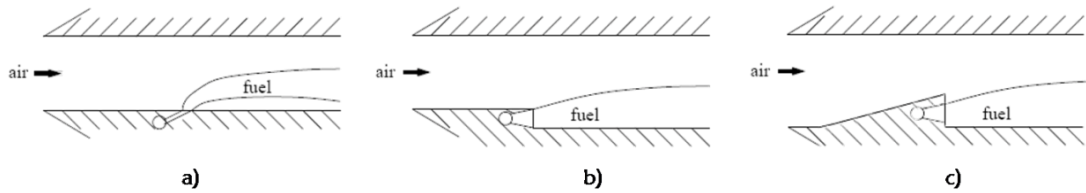


Figure 2.9 Different configurations of wall injectors: a) Port hole b) Wall step c) Ramp injector, adapted from [54] & [66].

The number, geometry, spatial resolution between two holes and the injection angle influence the efficiency of port injectors. Injection through multiple ports increases the mixing level and the energy release. A minimum hole diameter and spatial resolution should be provided in order that homogeneous mixing be achieved. Elliptical or wedge-shaped holes produce weaker shocks than circular ones and thus reduce the aerodynamic losses. Unfortunately, this has a negative impact on jet penetration. Jet penetration is relatively insensitive to the injection angle, at angles higher than 15° . This allows the designer to leverage the axial component of the fuel momentum to increase the stream thrust at high speeds.

Step injectors achieve mixing through a diffusion mechanism. Fuel is injected at the base of the step in the axial direction and the fuel stream adds to the main stream momentum. Additionally, a low-speed, high-temperature recirculation zone is generated behind the step and provides flame holding. Unfortunately, the implementation of this injection technique requires long combustion chambers to accommodate both the mixing and combustion processes, resulting in increased skin friction and heat transfer losses. Should losses reach a critical level it may be necessary to include mixing enhancing devices such as vortex generators, which in turn increase the aerodynamic losses.

Ramp injectors also exploit a diffusive mixing mechanism, but additionally enhance the mixing using the streamwise vorticity produced by the ramp and the

shock structure initiated at the ramp leading edge. Again, fuel is injected at the blunt base of the ramp and the axial component of the fuel momentum contributes to the generation of additional thrust. A recirculation zone facilitates flame holding and supports fuel ignition at static temperatures below the fuel self-ignition temperature. While the positive effect of the streamwise vortices on fuel entrainment into the main airstream is intuitive, the manner in which the shock interaction influences the mixing process is worth explanation. The shock generated on the leading edge of the ramp is reflected on the combustor walls and impinges on the fuel-air interface producing a twofold advantage. First, it enhances the level of vorticity and the fuel-air mass exchange. Second, the static pressure and temperature rise behind the shock wave provides improved conditions for fuel ignition and reaction. Unfortunately, the shock structure depends on the flight speed and systems relying on shock-induced ignition face issues at off-design [32], [33].

The level of vorticity and the aerodynamic losses associated with the use of an intrusive body such as a ramp are influenced by its size and geometry. Unswept ramps, like the one of Figure 2.9c, are the simplest ramp configuration. A swept ramp is similar, but further enhances the streamwise vorticity and the mixing level. Finally, aero-ramps generate vorticity without the need of an intrusive wedge, thus reducing the total pressure losses [18], [66].

All the types of wall injectors discussed herein provide film cooling of the combustor walls and can reduce the heat transfer losses. However, most of the fuel is confined for an extended axial length either in the boundary layer or in a region relatively close to the wall, where the lower temperature inhibits both diffusion and burning of the fuel. In addition, if combustion occurs in the low-speed boundary layer, the thermal loads on the walls drastically increase.

2.3.2 Cavity Injectors

For the purposes of this discussion cavity injectors are treated separately to wall injectors. The simplest cavity geometry is the wall recess of Figure 2.10.

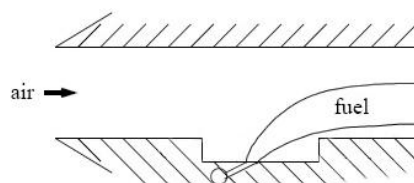


Figure 2.10 Cavity injector configuration [54].

Fuel can be injected either upstream of the cavity or in the cavity itself, either from the floor or from the front or rear walls. Injection upstream is referred to as "passive injection" because the flow is entrained into the cavity from the freestream. Injection from within the cavity is known as "direct injection". It should be noted that passive fuel injection proved not to promote homogeneous mixing and stable combustion [24].

Cavity injectors have two key advantages. First, they deliver fuel to the combustor and second they act as a flameholder to anchor the ignition point and to stabilize the flame. The recirculation region inside a cavity is characterized by high static temperatures and residence times. This renders cavities particularly useful for stabilizing supersonic combustion of hydrocarbons, whose kinetic rates are otherwise too low for ignition and reaction to occur within the typical flow residence times [50].

The three main mechanisms of interaction of a cavity with the surrounding flow are mass exchange, shear layer instabilities and drag generation [6]. In the case of mass exchange, cavities entrain oxidizer from the main airflow and, if fuel is injected inside the cavity, ignition and reaction can occur. The radicals produced leave the cavity and mix with the main airflow, further accelerating the combustion process.

Shear layer instabilities arise due to the airflow separation from the upstream lip of the cavity and subsequent reattachment at some position downstream. The point of reattachment is a function of the geometry. The interaction of the shear layer with the rear wall can cause fluctuations and pressure wave propagation inside the cavity which is then termed "unstable". This type of cavity provides high mass exchange rates with the surrounding flow and is therefore used to support fuel-air mixing. Shear layer control can inhibit the fluctuations and thus the vortices trapped inside the cavity are not disturbed by oscillating pressure waves. Such a cavity is known as "stable" and is primarily used as a flameholder as a result of the long residence times of the fuel in the recirculation region.

Cavities are furthermore classified into "open" and "closed" depending on their geometrical aspect ratio, or length-to-depth ratio. For aspect ratios below ten the cavity is referred to as open; the shear layer separates at its leading edge and reattaches to the rear wall. For aspect ratios above 10 the cavity is closed; the shear layer still separates at its leading edge, but reattaches to the cavity floor. The difference between the two is visible in the Schlieren images shown in Figure 2.11 [56].

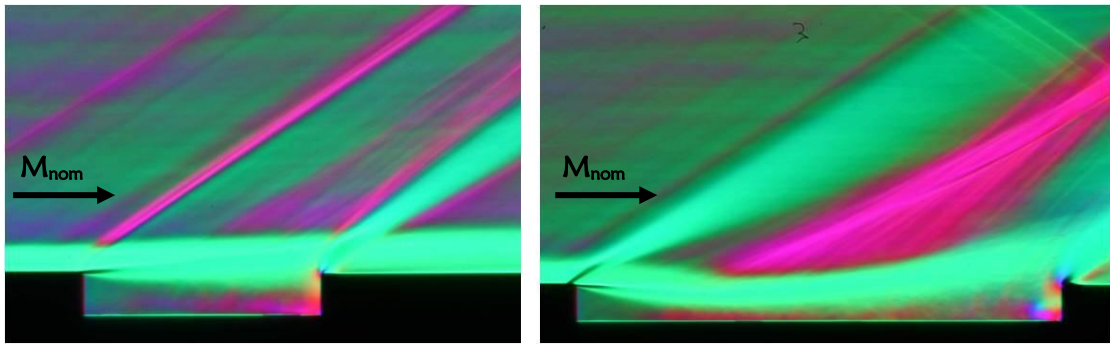


Figure 2.11 Comparison of open (left) and closed (right) cavity flow at a M_{nom} of two [56].

Shear layer separation and reattachment are also responsible for the generation of "cavity drag" due to the pressure difference between the front and the rear faces of the cavity. One technique to reduce the cavity drag is to incline the cavity rear face. Ramp angles between 16° and 30° have been found to minimize this type of drag [42], [61], [74].

The design of a cavity fuel injector is therefore a trade-off between the mixing and flame holding enhancement, drag reduction and optimization of the fuel injection inside the cavity (i.e. location and shape of the injection ports).

2.3.3 Central Injectors

Central injectors use a combination of penetration and diffusion mechanisms to achieve fuel-air mixing. They consist of struts in a central position in the combustion chamber, as depicted schematically in Figure 2.12.

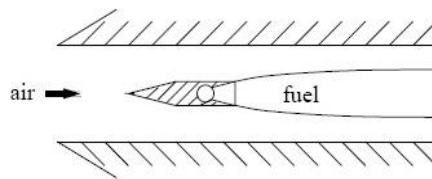


Figure 2.12 Strut injector configuration [54].

Struts require a shorter combustor length than wall injectors to accommodate the mixing process because they use a penetration mechanism. Further, struts provide flame holding capabilities, as their wake generates a recirculation zone in which radical pools can be stabilized and guarantee an ignition source for the remainder of the mixture. Finally, the fact that mixing and combustion of the fuel occur in the middle of the airstream reduces the thermal loads on the combustor walls.

The main disadvantages of strut injection are the high aerodynamic losses due to obstruction, the total pressure losses associated with the shock structure they produce and the significant thermal loads that the injector has to withstand. Cooling will be required at least at high speeds, in order to guarantee structural integrity.

The configuration shown in Figure 2.12 performs fuel injection in only the streamwise direction, i.e. into the wake of the strut. It should be noted that a combination of central and port injection would allow an increase in the amount of fuel delivered and enhance the penetration of the fuel jets into the main airflow. Based on this consideration, the injectors designed for the present study all introduce fuel via injection into the wake and transverse port injection by means of a series of holes on each side of the strut.

The efficiency of strut injection, both for axial and for normal injection, is dependent on the size and geometry of the injector itself, on the number of injection holes, the hole diameter and the spacing between two ports. Investigations have confirmed that there is considerable potential of strut injection for flight at Mach numbers up to eight. Above this threshold, the heat loads and cooling requirements render this injection configuration unviable [54].

2.4 Combustion System Processes

The physical processes occurring in the combustion chamber will be introduced in the following sections. Following a description of the sequence of events that take place, the discussion will begin with the mixing, continue with the fuel ignition and conclude with the combustion. The latter will be analysed separately from the point of view of the reactions and of the process of heat addition.

2.4.1 Fuel-Air Mixing

Combustion can occur in a gas-phase only if the reactants are mixed to near-stoichiometric proportions, as the molecular collisions promote the exchange of atoms between fuel and air molecules. Fuel-air mixing is based on mass transport on two different scales, i.e. the macroscale and the microscale. The scale of segregation b is defined as the average distance between the molecules of fuel and air. A mixture which is homogeneous at the molecular level has a scale of segregation equal to zero. Both

the macroscale and the microscale mass transport contribute to reduce the magnitude of \mathbf{b} [30].

Macromixing, or near field mixing, is based on the mechanical work accomplished by vorticity. Micromixing, or far field mixing, is the molecular diffusion due to concentration gradients. Both processes take place at the mixant interface and must be complete in order to allow the chemical reaction of fuel and air. The effect of macromixing is to extend the fuel-air interfacial area, which in turn increases the rate of molecular diffusion. The thickness of the corresponding mixing layer, δ_m , is defined as the region within which the mole fractions of fuel and air differ by at least one percent from their values in the unmixed streams. The mixing layer and its thickness are shown in the comprehensive schematic of Figure 2.13.

Mixing with Axial Fuel Injection

In the case of two uniform gaseous streams flowing in a straight duct at the same convective velocity u_c , shear stresses do not arise between the streams and neither momentum nor vorticity lateral transport occurs. If the two streams have different molecular identities, as in the case of fuel and air, lateral mass transport occurs at the mixant interface. In accordance with Ficks' law the time rate is proportional to the product between the interfacial area and the local concentration gradient [69]. The total length required to approach complete micromixing via molecular diffusion is approximately twice the distance required for the mixing layer to reach the duct walls, L_m . Thus, micromixing alone is not a viable choice to guarantee efficient and rapid mixing within a combustor of reasonable size.

To increase the mixing rate, gaseous fuel could be injected at a lower speed than the surrounding air, so that shear stresses arise and promote momentum exchange between the streams. If $u_A > u_F$, a velocity difference and a velocity ratio can be defined as $\Delta u = u_A - u_F$ and $r = u_F / u_A$, respectively. The convective velocity u_c is defined as the average between the velocities of the two streams, $u_c = \frac{1}{2}(u_A + u_F)$. As the streams have different molecular compositions, the shear layer is also the mixing layer and whilst the flow in it remains laminar, its thickness δ_m grows at the same rate than for the zero-shear mixing layer discussed above. In this case all lateral transport is achieved by diffusive processes.

If Δu is further increased and the flow undergoes transition from laminar to turbulent, large scale vortices form periodically between the two streams as a result of

the Kelvin-Helmholtz instability [30]. This process is shown in Figure 2.13. The vortices entrain the slower fluid, i.e. the fuel, and contribute to a reduction of both the mixing length and the convective time. Via these processes the mixant interface is stretched, the scale of segregation is reduced and the local concentration gradients are increased. This latter effect has a positive impact on molecular diffusion.

Nevertheless, micromixing only begins to occur at a certain axial distance x_M downstream of the trailing edge of the splitter plate shown in Figure 2.13 (represents an axial fuel injector). Behind the mixing transition point, the thickness of the mixing layer grows as a constant fraction of the shear layer thickness. The axial growth rate of the mixing layer, δ_m/x , can be determined as a function of both the velocity and density ratio of the two streams.

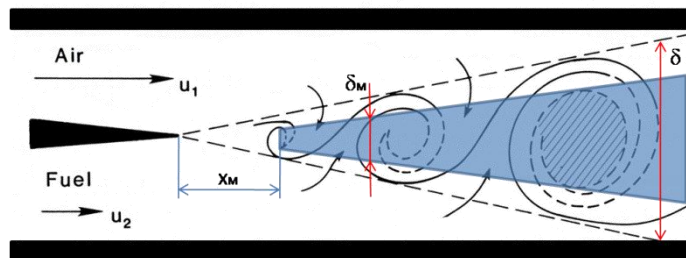


Figure 2.13 Formation of vortex structures in a transitional shear layer and growth of both the shear layer thickness δ and the mixing layer thickness δ_m , adapted from [30].

It should be noted that the positive impact of turbulence on the mixing process between air and fuel are counteracted by higher losses due to the viscous dissipation of mechanical energy. The increased level of entropy and the higher total pressure losses reduce the overall cycle efficiency. Hence, mixing enhancement by energizing the shear layer can only be applied to a limited extent before the losses become prohibitive.

Mixing with Normal Fuel Injection

Fuel injection from a jet normal to a supersonic air flow can improve mixing as it reduces the velocity ratio to zero and maximizes the velocity difference between the air and fuel streams. The flowfield close to the point of fuel injection is sketched in Figure 2.14.

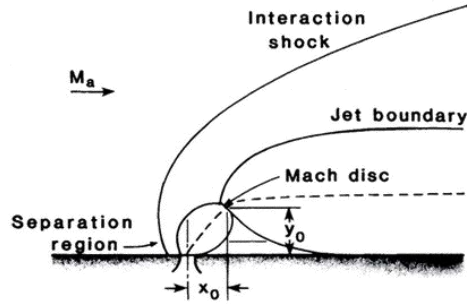


Figure 2.14 Schematic of the flowfield for the case of normal fuel injection [30].

The fuel jet generates a local normal shock wave, which leads to boundary layer separation upstream of the jet. In turn, this allows the fuel to extend upstream of the injection hole where it mixes with the air, thus reducing the aforementioned mixing transition distance x_M to a negative value. Importantly, a subsonic wake forms behind the jet core and provides a flame holding region that anchors the mixing layer to the jet. Unfortunately, the cycle efficiency is affected by the losses associated with the shock wave and the separation of the boundary layer.

A study has suggested that normal fuel injection drastically improves the near-field mixing, but does not result in a significant reduction in the total required mixing length [30]. More recent investigations confirmed the potential of transverse injection in enhancing the overall mixing level compared to the case of axial injection [4].

An important parameter to characterize the normal fuel injection is the jet penetration height. An empirical relation has been defined to correlate the results of tests with different injection hole geometry and jet speeds [37], [55]. The penetration height Y is nondimensionalized by the sonic round hole diameter D^* and is expressed as a function of the ratio of the dynamic pressure of the fuel and air streams, q_R

$$\left(\frac{Y}{D^*}\right)^2 = Kq_R \quad \text{Equation 2.1}$$

The penetration characteristics from different investigations have shown good agreement for K equal to 16. D^* and q_R are defined as

$$D^* = \left(\frac{4\Sigma A^*}{\pi}\right)^{1/2} \quad \text{Equation 2.2}$$

$$q_R = \frac{q_F}{q_A} = \frac{\rho_F u_F^2}{\rho_A u_A^2} \quad \text{Equation 2.3}$$

where A^* is the total area of all injection holes, ρ_F and ρ_A are the fuel and air densities, and u_F and u_A the fuel and air speeds, respectively.

Effects Influencing the Shear and Mixing Layers Growth

To complete the review on fuel-air mixing three factors that influence the development of the shear and mixing layers should be mentioned, namely the density, the compressibility and the heat release. Density differences between the two streams necessitate a correction to the expression for the convective velocity u_c , which is no longer equal to the simple average of the fuel and air speeds. Instead, u_c becomes a function of the density ratio $s = \rho_F / \rho_A$, and for incompressible flows can be defined as

$$u_c = \frac{u_A + \sqrt{s}u_F}{1 + \sqrt{s}} \quad \text{Equation 2.4}$$

For compressible flows, the convective velocity must be determined iteratively using the convective Mach numbers of the fuel and air streams

$$M_{CA} = \frac{u_A - u_c}{a_A} \quad \text{Equation 2.5}$$

$$M_{CF} = \frac{u_c - u_F}{a_F} \quad \text{Equation 2.6}$$

where a_A and a_F are the speeds of sound of the two streams. Once u_c is known, the axial growth rate of the shear layer can be expressed as a function of r , s and of a fit parameter which is determined empirically [30].

The convective Mach number introduced above characterizes the behaviour of compressible shear layers, whose spread rate decreases with increasing Mach number. Increasing compressibility effectively reorganizes the turbulence field and inhibits the formation of the vortical structures involved in the mixing processes. As a result, the shear stresses are suppressed and the lateral transport of momentum is reduced. The compressibility effects can be accounted for by multiplying the incompressible shear layer growth rate by an empirical correction factor that depends on M_{CA} [17], [18].

The heat release influences the development of the shear and mixing layers as it results in gas dilatation which causes both layers to occupy a greater volume fraction of the duct. However, an increase in the growth rate of both layers is inhibited by an outward displacement velocity component that can be observed as a second and

predominant effect of heat release. Due to compressibility, the turbulent shear stresses are suppressed by the outward displacement to such an extent that it counteracts the effect of gas dilatation. This effect is mild at higher Mach numbers, where the contribution of heat release to the total enthalpy of the flow is small compared with the portion due to the kinetic energy [17], [30].

2.4.2 Ignition

For a generic fuel-air mixture, the combustion process is organized in a series of sequential elementary reactions involving many intermediate species. The chain reactions are initiated when the energy of the colliding reactants overcomes the activation energy limit and sufficient radicals are formed to start the reaction mechanism. This step of the combustion process is termed ignition and the time interval between the establishment of a combustible mixture and the onset of a flame is referred to as the ignition delay time (τ_i). The ignition delay time is a function of the initial pressure, temperature and composition of the mixture [14].

The ignition delay time is commonly defined as the time required to increase the temperature of the mixture by 5% of the overall reaction temperature rise [34], [47]. According to this definition, for hydrogen-air mixtures it follows that

$$\tau_i = \frac{8 \cdot 10^{-4} \cdot e^{\frac{9600}{T}}}{p} \quad \text{Equation 2.7}$$

where p is pressure in [atmospheres], T is temperature in [Kelvin] and τ_i in milliseconds. This relation is valid for temperatures above 1000K.

For mixtures of air and hydrocarbons and for the comparison of candidate scramjet fuels it is more convenient to express τ_i using the Arrhenius correlation

$$\tau_i = A \cdot e^{\frac{E}{RT}} \cdot [C_x H_y]^a \cdot [O_2]^b \quad \text{Equation 2.8}$$

where the constant A and the exponents a and b are determined empirically, E is equivalent to the overall activation energy, R is the universal gas constant and T is the initial temperature. The molar concentrations in Equation 2.8 are a function of the initial pressure and temperature and of the mole fraction of each species, χ_i

$$[\dots]_i = \frac{\chi_i \cdot p}{RT} \quad \text{Equation 2.9}$$

The experimental data from several studies have been reviewed and compared by Colket and Spadaccini [14] for different hydrocarbon fuels and for hydrogen, using Equation 2.8. The results for hydrogen and methane at two different temperatures and for two equivalence ratios are listed in Table 2.1 along with the empirical parameters and exponents valid for initial temperatures between 1100K and 1500K.

The equivalence ratio has been varied by decreasing the molar concentration of oxygen instead of increasing the fuel concentration. This is because changes in the fuel concentration have only a weak influence on τ_i while the dependence on the oxidizer concentration is relatively strong. The observation of longer ignition delay times for a stoichiometric than for a lean mixture, hence, is due to the experimental procedure. As expected, due to the strong C-H bond of the methane molecule the ignition delay time for the hydrocarbon is always longer than for hydrogen.

| Ignition Delay Correlations | | | | | Ignition Delay Times [ms] | | | |
|-----------------------------|----------|--------|-------|------|---------------------------|-------|------------|-------|
| | | | | | $p = 7\text{atm}$ | | | |
| Fuel | A | E | a | b | $\Phi = 0.5$ | | $\Phi = 1$ | |
| | | | | | 1300K | 1400K | 1300K | 1400K |
| Hydrogen | 1.60E-14 | 19,700 | -1 | 0 | 0.024 | 0.013 | 0.027 | 0.023 |
| Methane | 2.21E-14 | 45,000 | -1.05 | 0.33 | 9.996 | 2.774 | 13.401 | 6.616 |

Table 2.1 Ignition delay correlations and τ_i for H_2 and CH_4 in air, adapted from [14].

Although this data refers to a relatively high static pressure compared to that expected for scramjet combustors, they highlight the significant effect of temperature changes on the ignition delay time. For instance, at the equivalence ratios recommended for scramjet operation in order to limit the compressibility effects on mixing, i.e. $\Phi \approx 0.45$, a temperature reduction from 1400K to 1300K increases the ignition delay time of methane by a factor of three. Similarly, decreasing the initial pressure, which is linked to τ_i by the concentration terms of Equation 2.9, will extend the ignition delay time. Pressure has a smaller effect than the temperature however, because of the weaker dependence $\tau_i \propto p^{a+b}$.

When the initial conditions are below the autoignition threshold, no spontaneous ignition of the mixture takes place. This issue is encountered by airbreathing engines at flight Mach numbers below seven, where the internal energy of

the incoming flow is still too low for mixture self-ignition to occur within a combustor of reasonable length, in particular for hydrocarbon fuels.

Nevertheless, if the total temperature of the airflow is high enough, autoignition can be achieved by exploiting low-speed flow regions, like strut wakes and recirculation zones inside a cavity or behind a ramp. In such regions, the kinetic energy of the flow is converted to internal energy, with the twofold advantage of providing both a high recovery temperature and of extending the local flow residence time.

If the total temperature is too low to provide sufficient recovery even for the case of complete deceleration of the airflow, autoignition does not occur in low-speed regions either and an external ignition source is required for the reactions to be initiated. External ignition through electric sparks or plasma torches is necessary at flight Mach numbers below 5.5, i.e. during ramjet operation [14].

The experiments at the basis of the present work have been carried out in a low-enthalpy test facility. The maximum recovery temperature estimated with numerical simulations is below the self-ignition temperature for both methane and hydrogen [34]. Therefore, a Nd:YAG laser beam has been directed into the low-speed mixing region and focused through a suitable lens to ionise the gas and form a highly energetic plasma, which ignites the mixture. Further details of the laser ignition setup will be provided in Chapter 3 together with the description of the lab and the equipment. The numerical prediction of the static temperature distribution and a detailed view of the recirculation zone at the trailing edge of the strut are reported in Figure 2.15 [73].

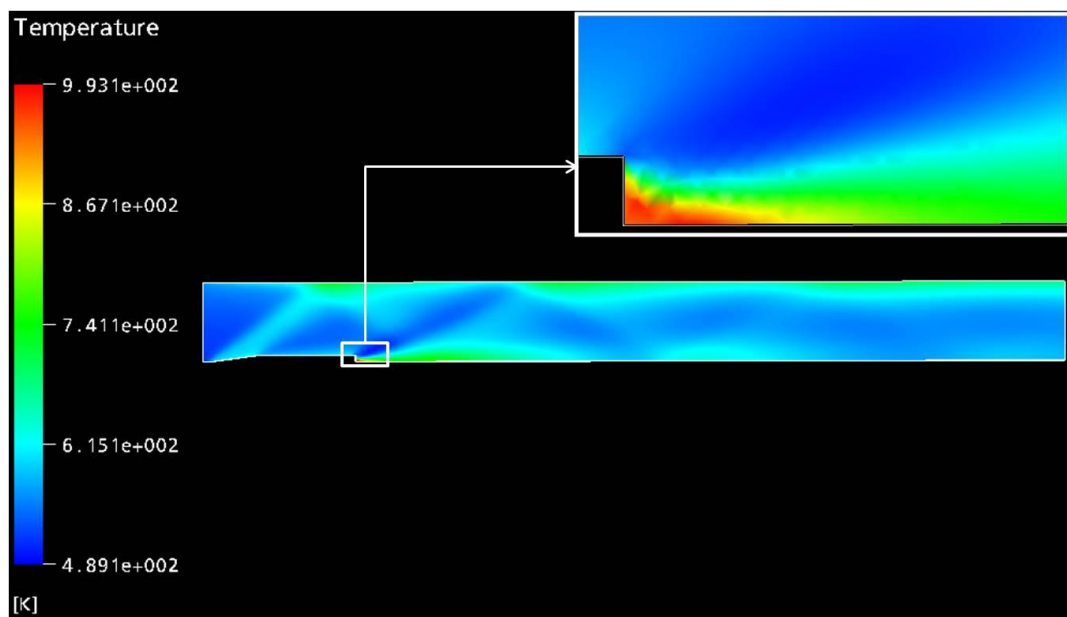


Figure 2.15 Static temperature distribution inside the combustor with Strut 1 [40], [73].

The ignition delay time is also affected by the presence of hydrocarbon contaminants, free radicals and water vapour in the mixture [14], [43]. The presence of water vapour inhibits the reactions and it is a concern mainly for engine testing in wind tunnels using vitiated air heaters, like the test facility at LFA. Free radicals generally promote the reactions and act toward reducing the ignition delay time. Again, their "artificial" presence in the vitiated air supplied to a subscale combustor can influence the ignition behaviour of the mixture and has to be accounted for.

Hydrocarbon fuels, despite the long ignition delay times compared to hydrogen, are still of interest for scramjet engines due to their high density, which makes them both easier to store and optimal media for regenerative structural cooling. The available heat sink can be increased by endothermic decomposition of higher hydrocarbons, which involves cracking the fuel into a mixture of smaller hydrocarbons and hydrogen [14]. Some of the resulting species will react easier than the original hydrocarbon, while other species, like methane, will be less reactive. Depending on the degree of cracking achieved in the heat exchanger, and on the complexity of the parent hydrocarbon, contaminants and radicals may be present in the mixture and reduce the ignition delay time. While this interaction is desired to achieve efficient combustion, it has to be controlled in order to avoid dynamic instabilities or even choking of the flow because of too rapid heat release.

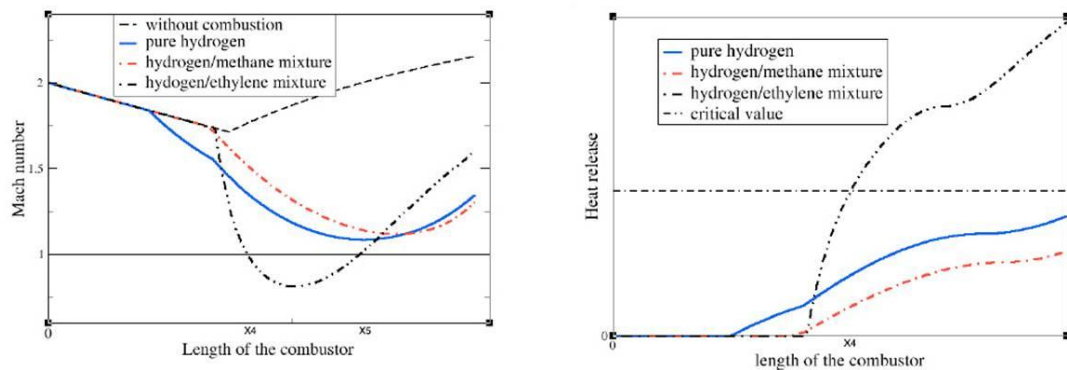


Figure 2.16 Mach number distribution (left) and combustion heat release (right) for different hydrogen-hydrocarbon mixtures reacting with air [23].

Figure 2.16 reports the results of a one-dimensional analysis of the interaction among flow confinement, mixture self-ignition and combustion heat release for different hydrogen-hydrocarbon mixtures reacting with air [23]. The plots for the hydrogen-ethylene mixture confirm thermal choking after rapid mixture autoignition, as discussed above. Due to the abrupt reaction, the heat release overcomes the critical

value for the combustor, i.e. the horizontal line in the right plot, and the Mach number distribution on the left indicates subsonic conditions in the combustor.

2.4.3 Reaction

Once the chain reactions are initiated, the combustion process continues following the reaction mechanism until complete consumption of the reactants is achieved. The reaction time, τ_r , is defined as the time required from ignition to increase the mixture temperature by 95% of the overall combustion temperature increase [35].

As following mixture ignition free radicals are available to support the chain reactions, the exponential dependence of the reaction time on temperature is weaker than it is for the ignition delay time. For hydrogen-air mixtures the analytic expression for τ_r is

$$\tau_r = \frac{3.32 \cdot 10^{-4} \cdot e^{\frac{-1.12T}{1000}}}{p^{1.7}} \quad \text{Equation 2.10}$$

where p is in [atmospheres], T in degrees Kelvin and τ_i in milliseconds [43].

The total time required for complete combustion of the mixture is the sum of the ignition delay time and the reaction time

$$\tau_c = \tau_i + \tau_r \quad \text{Equation 2.11}$$

Thus, for fixed mixture and flow speed, the combustion chamber must be sufficiently long in order that the flow residence time, τ_{res} , be on the same order of τ_c .

Since practical constraints limit the maximum length of a scramjet combustor, the residence time of the high-speed combustor flow is shorter than the overall combustion time and the chemical reactions typically do not reach equilibrium. The net combustion heat release is reduced below the level expected for complete combustion.

Whether supersonic combustion is mixing-rate or reaction-rate limited hinges on several factors, the selected fuel being only the most intuitive. Previous studies have proven that the reaction-rate completion times for hydrogen-air mixtures are between $1\mu s$ and $1000\mu s$ under a broad range of pressures and temperatures [37]. Since such τ_r are compatible with the typical τ_{res} for a scramjet combustor the process will be mixing-controlled.

More recently investigations have been carried out [47] to better define the operation range in which hydrogen combustion is mixing-controlled and reaction-controlled. Tests carried out with a subscale engine at entry flow Mach numbers of 4, 6 and 8 identified a transition from reaction-controlled combustion to mixing-controlled combustion with increasing Mach number.

Unfortunately, no such detailed study was available on supersonic combustion of methane to support the preliminary design of the experiments for the present work. In general, methane is characterized not only by longer ignition delay times than hydrogen, as discussed in Section 2.4.2, but also by longer reaction times due to the high number of elementary steps involved in its combustion mechanism. The typical flow residence time for the conditions and for the geometrical configuration examined is 0.36ms. Since the overall τ_c for methane is expected to be longer than for hydrogen, with the mixing being the main driver of the combustion process, a twofold approach has been followed in the investigations.

First, the ignitability¹ of pure methane in air has been assessed by axial injection in the wake of a strut with the purpose of exploiting the stabilized flame as an ignition source for additional methane injected normal to the supersonic airstream. Then, based on the ignition results of hydrocarbon mixtures reported in Section 2.4.2, methane has been replaced by hydrogen in the axial injection, to guarantee mixture ignition in the wake and a stable ignition source for the additional methane. Furthermore, the addition of hydrogen and the radicals set free in the wake of the strut are expected to support reaction-rate rather than mixing-rate controlled combustion of methane, which will improve the net heat release.

In this study three combustion reactions will be considered, i.e. hydrogen-air, hydrogen-oxygen and methane-air; the global reaction mechanisms are now presented. A first estimate of the combustion efficiency will be based on the assumption that none of the water in the products condenses to liquid; since all reactants and products are gaseous, the phase will not be specified in the combustion equations. The lower heating values are listed in Table 2.2 along with the value of the stoichiometric air-fuel ratios.

¹ As discussed in Section 2.4.2, both the static and the total temperatures of the incoming air flow are below the autoignition temperature of the mixture and the plasma generated by a focused laser beam has been used as an external ignition source.

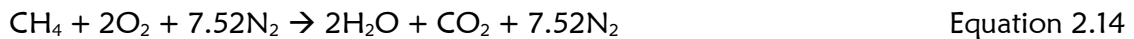
Hydrogen-Oxygen



Hydrogen-Air



Methane-Air



| Reaction | Lower Heating Value [kJ/kg] | Stoichiometric Air-Fuel Ratio [-] |
|---------------------------------|--------------------------------|--------------------------------------|
| H ₂ - O ₂ | 120100 | 7.9 |
| H ₂ - Air | 120100 | 34.5 |
| CH ₄ - Air | 50016 | 17.2 |

Table 2.2 Lower heating value and stoichiometric air-fuel ratio for the reactions considered.

2.4.4 Heat Addition to a Supersonic Flow

Once the reactions are initiated, the aerodynamic behaviour of the supersonic flow is further complicated by coupling with the thermodynamics of the combustion process. Although the flowfield in a scramjet combustor is highly three-dimensional, a one-dimensional analysis provides considerable insight into the flow processes and is used in this section under the assumption that the chemical reactions can be modelled as the amount of heat released by combustion, Q , and added to a steady airflow. Furthermore, the body forces and the heat losses to the surroundings are assumed to be negligible [5], [65], [69].

For constant area ducts and ideal-gas behaviour, the equations for the normal reaction front follow from the state relationship and the conservation of mass, momentum and energy. The relationship for the flow velocity is reported below by way of example; the subscripts 1 and 2 refer to the conditions upstream and downstream of the reaction front, respectively.

$$\frac{u_2}{a_1} = M_1 - \frac{1}{\gamma+1} \frac{1}{M_1} \left[(M_1^2 - 1) \pm \sqrt{(M_1^2 - 1)^2 - 2(\gamma + 1)M_1^2 \frac{q}{c_p T_1}} \right] \quad \text{Equation 2.15}$$

In the relationship, γ is the ratio of the specific heats, c_p the constant pressure specific heat, T_1 the static temperature upstream of the reaction front and q the specific heat released by the reactions. The expressions for the ratios of static pressures, static temperatures and densities all contain the term in the squared brackets [5].

For fixed upstream conditions, equating the radicand of Equation 2.15 to zero gives the critical amount of heat that can be released into a constant area duct with a steady process:

$$\frac{q_{cr}}{c_p T_1} = \frac{1}{2(\gamma+1)} M_1^2 \left(1 - \frac{1}{M_1^2} \right)^2 \quad \text{Equation 2.16}$$

The condition corresponding to the critical heat addition is defined as thermal choking and the flow downstream of the reaction front is characterized by the local speed of sound.

Simultaneous solution of the conservation of mass, momentum and energy equations for a certain q yields the Rankine-Hugoniot curve which is the locus of all possible thermodynamic states that can be reached from an initial state (P_1, v_1) by addition of the heat $q=q_1$:

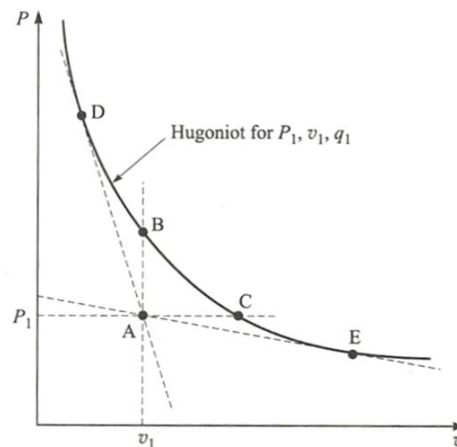


Figure 2.17 Rankine-Hugoniot curve for $q=q_1$ with origin A at (P_1, v_1) . Dashed lines passing through A are Rayleigh lines [69].

Since relationships for the conservation of mass and momentum require that pressure and density must either both increase or both decrease across the reaction, the states between the points B and C are physically inaccessible. The relationship between

pressure and density at a fixed flow speed yields the Rayleigh line, which passes through the origin A and whose intersection with the Rankine-Hugoniot determines the thermodynamic state after the reaction. The limiting Rayleigh lines are tangent to the upper and lower branches of the Rankine-Hugoniot curve at the points D and E, termed upper and lower Chapman-Jouguet point, respectively.

For solutions on the upper branch of the Rankine-Hugoniot, static pressure and density always increase while the velocity decreases. The opposite occurs for solutions on the lower branch. This defines the peculiarities of heat addition in the supersonic and in the subsonic regimes, for the upper branch corresponds to supersonic reaction fronts and the lower branch to subsonic.

In both regimes heat addition causes a drop of the total pressure and total density of the flow. This is shown from the following relationships when considering that the static temperature of a medium is always lower than its total temperature and hence T/T_{tot} is always lower than one [69].

$$\frac{1}{p_{\text{tot}}} \frac{dp_{\text{tot}}}{dx} = -\frac{\gamma}{\gamma-1} \frac{1}{c_p T} \left(1 - \frac{T}{T_{\text{tot}}}\right) \frac{dq}{dx} \quad \text{Equation 2.17}$$

$$\frac{T}{T_{\text{tot}}} = \left(1 + \frac{\gamma-1}{2} M^2\right)^{-1} \quad \text{Equation 2.18}$$

The supersonic combustion regime is identified by solutions between the points D and B on the upper branch of the Rankine-Hugoniot, i.e. by the weak supersonic solutions. They correspond to stationary heat addition to a supersonic flow, which remains supersonic downstream of the reaction front. The upper Chapman-Jouguet point is the threshold to the detonation regime; the heat of reaction reaches its critical value and a normal shock precedes and in fact initiates the reaction. The flow speed after a detonation wave is equal (solution D) or lower than the local speed of sound and supersonic conditions cannot be restored in a constant cross area duct.

The effect of heat addition can be compared to that of a change in the duct cross-sectional area. A supersonic flow in a converging channel decelerates, whereas its static pressure and density increase (the opposite occurs in a subsonic flow). Heat addition has therefore the same effect than an area contraction. Conversely, heat subtraction will result in an acceleration of a supersonic flow by decreasing pressure and density. This is similar to the effect of a diverging duct.

The heat release in a scramjet combustor of constant cross-sectional area is often further accelerated by the interaction with shock waves generated from the fuel injection devices. The associated combustion pressure rise is expected to be rather abrupt, with an initial adverse pressure gradient, and can cause both thermal choking and boundary layer separation. Since both phenomena are associated with high losses and can potentially lead to inlet unstart, the combustor has to be designed in order to accommodate the combustion pressure increase. One possible approach consists of using a divergent-area combustor to counteract the static pressure increase. The setup used for the present investigations is a combination of a constant-area and a divergent-area design and will be discussed into more detail in Section 3.2.2.

2.5 Summary

The classes of hypersonic vehicles have been introduced with particular emphasis on the development of airbreathing space transport systems. The differences between ramjet, scramjet and dual-mode operation have been highlighted and the components of an airbreathing engine described to provide a solid background on the complex interactions that influence the design of scramjet combustors. Fuel injection systems have been reviewed and compared in detail and insight has been provided into both the fuel injection mechanisms and the mixing process.

The physical processes of mixture ignition and reaction have been analysed for both hydrogen and methane from the viewpoint of the issues typically encountered in scramjet combustors. Limited data is available in the open literature on the supersonic combustion of methane, which is the focus of the present work. Finally, the process of heat addition to a supersonic airflow is discussed and completes the review on the aerothermodynamic aspects of scramjet combustor design.

3 Experimental Testing

Assessment of scramjet performance in ground-based testing facilities requires not only adequate simulation of the conditions expected in flight, but also the use of advanced measurement technologies in order to gain a deeper insight into the scramjet flow path. First, this chapter details the different typologies of hypersonic ground testing facilities. This will be followed by a description of the supersonic combustion lab of the Institute for Flight Propulsion. The strut and cavity injectors will be introduced in detail along with the experimental methodology adopted. An overview of the instrumentation and measurement techniques used in the current study will conclude the chapter.

3.1 Overview of Ground Testing Facilities

Successful development of an efficient propulsion system requires extensive testing. Although flight testing offers realistic environmental conditions, new designs are initially investigated in ground-based facilities to mitigate the risk of failure and reduce the overall development costs. The major types of hypersonic ground testing facilities are pulsed flow facilities, blowdown facilities and continuous flow facilities [30].

Because of the high stagnation temperature levels attainable, pulsed flow facilities allow testing under conditions for which real gas effects become significant. They include shock tunnels, free-piston shock tunnels and expansion tubes. All operate using a large mass of compressed driving gas whose energy is rapidly transferred to a smaller mass of working gas and further leveraged by concentrating the release of the working gas in space and time. The major drawback of pulsed flow facilities is that the high stagnation enthalpy levels can be reached only for a very short time on the order of a fraction of a millisecond to a few milliseconds.

All three types of pulsed flow facility have a primary and a secondary diaphragm. The rupture of the primary causes a shock wave to be released in the working gas, while the secondary bursts when the shock reaches it, thus allowing the compressed gas to escape to the test section. In addition to the driving and to the

working gas used in classic shock tunnels, a light compression gas is exploited in free piston shock tunnels to further increase the total enthalpy of the working fluid. Both tunnels also feature a facility nozzle to accelerate the tests gas, since this is briefly brought to rest before entering the test chamber. In the expansion tube the working gas processed by the primary shock wave can expand into an acceleration tube after rupture of the secondary diaphragm, which results in Mach numbers sufficiently high that no facility nozzle is needed. The three concepts of these pulsed flow ground test facilities are schematically depicted in Figure 3.1.

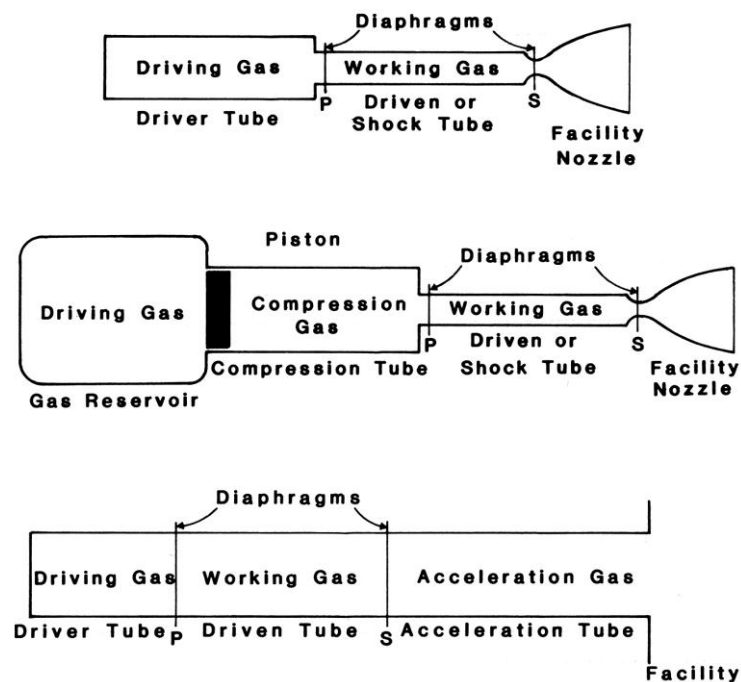


Figure 3.1 Schematic diagrams of three pulsed flow ground test facilities; shock tunnel (top), free piston shock tunnel (middle), expansion tube (bottom) [30].

Blowdown facilities allow for longer testing times than pulsed flow facilities, as the air is slowly compressed and stored in high-pressure reservoirs before being released to the test section. The required enthalpy levels are reached through air pre-heating. Common pre-heating methods to simulate flight Mach numbers up to 15 include pebble heaters, vitiated heaters, arc heaters or a combination of these devices. Although the testing times are extended up to a few minutes and aerothermodynamic equilibrium can be approached, the maximum stagnation pressure is limited to about 10MPa and true operative conditions cannot be reproduced. Additionally, air pre-heating can influence the mixing and combustion processes or affect the quality of the flow supplied to the test section. For example vitiated heaters, which include a combustor along the supply line, introduce both free radicals and water vapour that

alter the gas composition. Arc heaters have a negative effect due to debris released by the electrodes.

Continuous flow facilities are designed for long duration testing and are the best alternative when investigating components under aerothermodynamic equilibrium. However, due to practical requirements such as the power required to operate the facility, duplication of true flight parameters is not possible and full-scale engines are substituted by subscale models or engine components. The most common types of continuous flow facilities are freejet and direct connected facilities. Both comprise a high pressure source, an air heater to simulate the enthalpy level, a plenum, a facility nozzle to reproduce the required Mach number, a test article and an exhaust system to remove both the air and any combustion products.

In the case of hypersonic airbreathing propulsion, the power requirement of freejet facilities for full-scale testing becomes prohibitive and direct connected testing is performed instead as it requires both a lower stagnation pressure and less upstream flow. The air supplied to the test section corresponds to the flow downstream of all or some of the engine compression losses. Similar to blowdown facilities, the enthalpy levels are duplicated by means of one or more heaters, which entails the aforementioned issues of air contamination and fidelity of mixing and combustion processes.

3.2 Testing Facility

The supersonic combustion lab of the Institute for Flight Propulsion (LFA) is a direct connected facility and belongs to the class of R&D (research and development) facilities. This allows testing a scramjet combustion chamber in isolation from the other engine components. Although the complex interaction mechanisms between inlet, isolator and combustor cannot be resolved, the high instrumentation resolution provides valuable insight into the combustion phenomena.

A series of screw-type compressors delivers up to 0.5kg/s air to the test section at a maximum pressure of 1MPa. The air is first heated up to 650K by means of an electric heater and subsequently burnt in a vitiated heater to attain total temperatures as high as 1200K. Oxygen replenishment takes place upstream of the electric heater in order to guarantee realistic gas composition and uniform temperature distribution of the flow supplied to the test section as the oxygen is heated together with the air. The vitiated heater implemented in the LFA test bed will be the subject of Section 3.2.1.

The flow is accelerated to supersonic conditions through an interchangeable Laval nozzle. This allows different combustor entrance Mach numbers, M_{CC} , to be simulated. For the present investigations M_{CC} has been set to a value of 2.2, which is also the highest value attainable. The Laval nozzle has been designed using the method of characteristics for given flow quantities at the nozzle entrance and for a fixed pressure distribution at the end of the tube, where the velocity is assumed to be uniform. A more detailed description of the design procedure lies outside the focus of this thesis; however, the contour function and the technical drawings of the nozzle are included in Appendix A for completeness. Prior to the experimental campaign documented in this thesis, the nozzle was calibrated using static and total pressure data as well as Schlieren optic imaging to determine the exit Mach number. The static pressure is measured upstream of the nozzle, at the throat and close to the exit.

A subscale combustion chamber is connected to the Laval nozzle. It has a modular setup which allows a high degree of flexibility in choosing the fuel injection location and in implementing the instrumentation for the experimental analysis. The combustor and the fuel injection systems will be detailed in Section 3.2.2 and Section 3.2.3, respectively. An exhaust system collects air and combustion products and removes them from the test cell. A schematic of the test facility is shown in Figure 3.2.

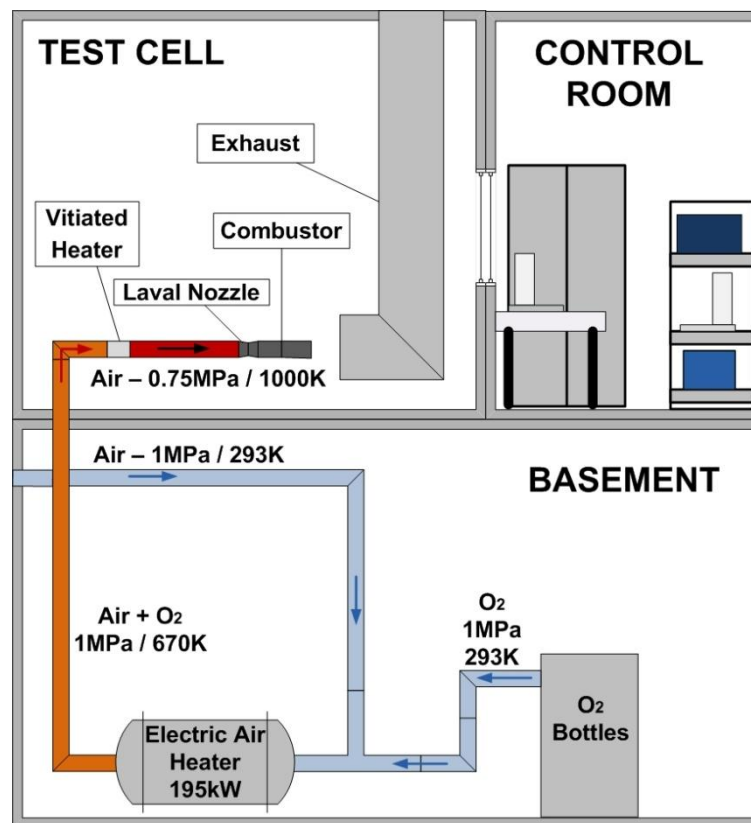


Figure 3.2 Schematic diagram of the direct connected testing facility of the LFA.

In addition to the main supply line, the test cell is equipped with several pipelines to deliver gases both to the vitiated heater and and to the combustion chamber. A plan of the supply lines is presented in Figure 3.3.

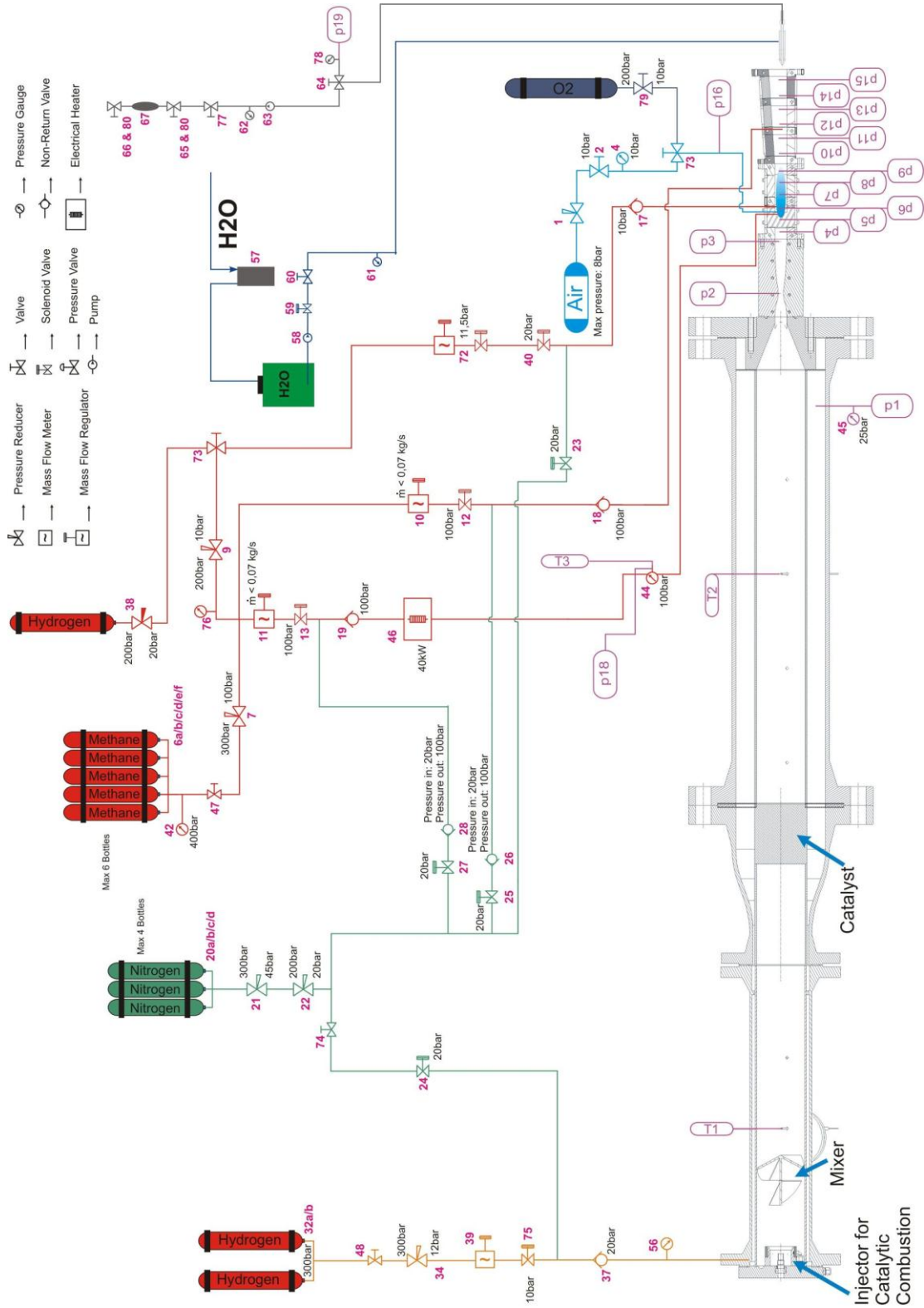


Figure 3.3 Schematic diagram of the supply lines in the test cell of the LFA.

A nitrogen supply is connected to the lines for hydrogen and methane to evacuate the piping in case of emergency and a water cooling system has been implemented to perform gas sampling of the combustion products. The most relevant components will be highlighted in the next sections along with the description of the experimental equipment.

The data acquisition and the control of the experiments have been performed from the control room using a single Labview module. The control panel is presented in Figure 3.4.

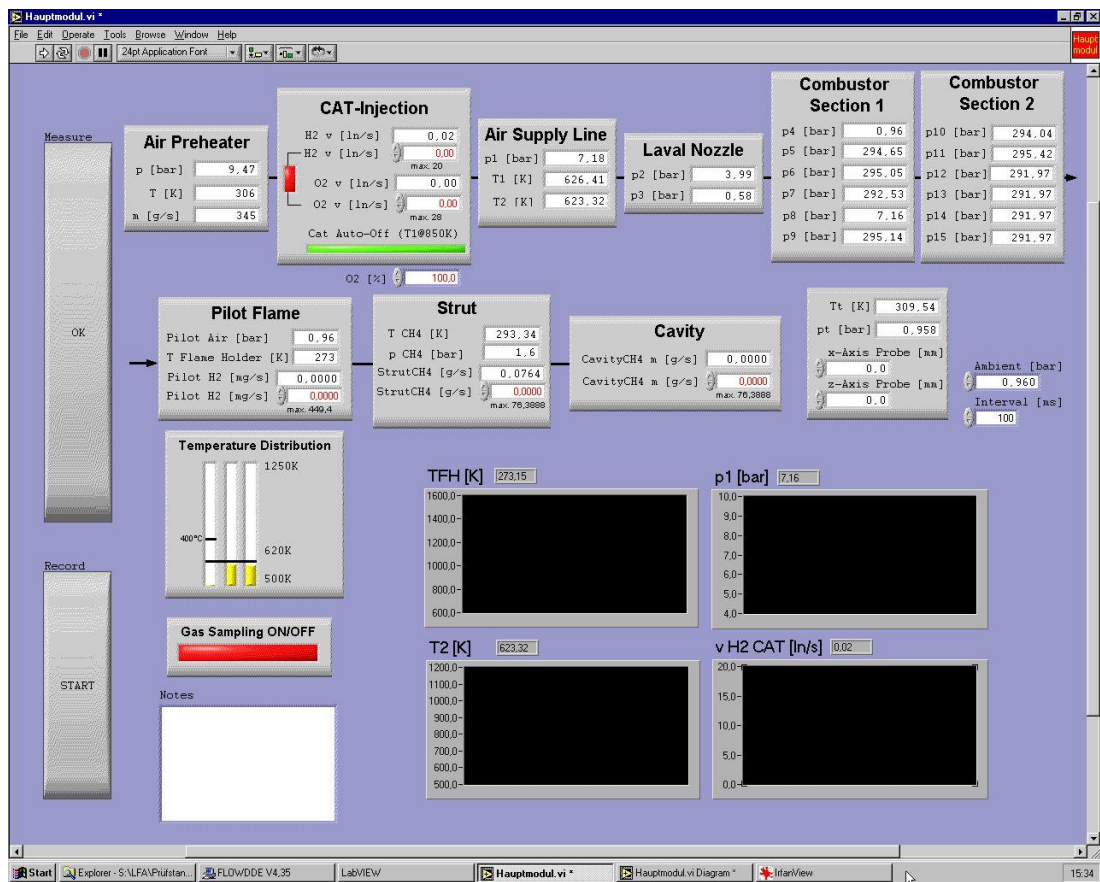


Figure 3.4 Control panel of the Labview module.

3.2.1 Air Heating Systems

The electric heater implemented along the main supply line allows continuous pre-heating of the air up to 650K without contamination of the flow. For a combustor entrance Mach number of 2.2, such temperature level corresponds to a flight Mach number of 3.25 and does not properly duplicate the conditions expected for flight in the mid-speed range [9].

To further increase the stagnation temperature of the air, a vitiated heater has been implemented along the supply line. The heater shown in Figure 3.3 consists of a hydrogen injector, a mixer and a Platinum-Palladium catalyst. Part of the oxygen contained in the air and the injected hydrogen undergo a flameless, heterogeneous reaction on the catalyst surface, thus increasing the overall temperature of the flow up to a maximum of 1200K, corresponding to a flight Mach number of 4.75. However, in order to extend the test time and preserve the experimental equipment, the present investigations have been carried out at a temperature of 1000K corresponding to a M_F of approximately 4.25.

A more extensive description of the work undertaken for designing the vitiated heater is beyond the scope of this thesis and can be found in reference [59]. Here it is sufficient to mention that the original oxygen level has been no longer re-established by injection and decomposition of nitrogen dioxide, but by direct addition of oxygen as described above and that the catalyst used featured a length of 95mm and a diameter of 110mm.

For the purposes of this thesis, though, it is important to analyse the effect of the air vitiation on the combustion process, since a deviation in the composition of the test gas from atmospheric air has the potential to affect the reliability of the extracted data. As discussed in Section 2.4.2, the presence of free radicals in the flow delivered to the test section can reduce the ignition delay time. Radicals, H and OH, can be set free during the catalytic combustion of hydrogen in air. Under certain conditions the nitrogen from the air can dissociate and produce nitric oxide, NO, which also enhances combustion [35]. However, the chemical mechanisms of NO formation become active at temperatures above 1500K or in rich combustion. In addition small concentrations of NO have been proven not to affect combustion at low pressures [28], [69]. For the experimental conditions considered in the present study, hence, the presence of NO in the test gas can be neglected.

The radicals set free during the branching steps of the hydrogen combustion can be removed from the flow if sufficient time is available for the termination step reaction



to be completed. M is a species known as the third body.

The Laval nozzle is positioned at a distance L_{CN} downstream of the catalyst. L_{CN} is expressed by the relationship

$$L_{CN} = 10 \cdot D_{CAT} = 1.1 \text{ m} \quad \text{Equation 3.2}$$

where D_{CAT} denotes the diameter of the catalyst. Gas chromatographic analysis of samples collected at the exit of the Laval nozzle was performed with a twofold purpose. First, the results of the analysis were used to assess whether the selected L_{CN} was sufficient for complete radicals recombination. Second, gas sampling was used to determine the amount of hydrogen and oxygen to be supplied to the vitiated heater in order to restore the original atmospheric level for a given temperature increase.

Since neither free radicals nor unburned hydrogen have been detected in the gas samples collected at different positions of the nozzle exit cross section, it can be assumed that all of the injected hydrogen reacted to water prior to entry into the combustion chamber. The absence of radicals excludes a reduction of the effective ignition delay time. However, the presence of water vapour results in a chemical inhibition of ignition. For instance, H_2O contamination can increase the ignition delay time of hydrogen in air by a factor of five [43].

As mentioned in Section 2.4.3, an external ignition source is required to initiate the combustion of a pilot flame in the wake of a strut injector. Thus, the inhibition effect on spontaneous ignition due to water vapour can be neglected. However, methane is also injected normally into the airstream containing water vapour. The presence of water vapour could thus retard the ignition of the main fuel further away from the wake, where the pilot flame acts as an ignition source.

3.2.2 Combustion Chamber

The uncooled subscale combustion chamber consists of two modules with an overall length of 360mm. The first module features a constant cross section of 27mm×25mm and a length of 160mm. The second module diverges on one side by four degrees over 200mm and has an exit cross section of 41mm×25mm. The walls of the combustion chamber are made of stainless steel and have quartz windows to enable optical access for non-intrusive measurement techniques. Additionally, thirteen pressure taps are implemented along the bottom wall to monitor the static pressure distribution.

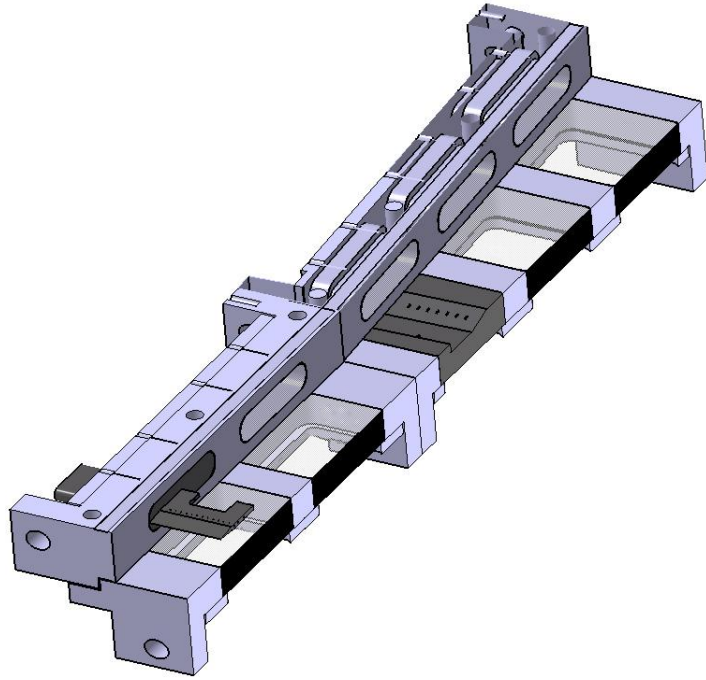


Figure 3.5 3D section of the combustion chamber with strut and cavity injector.

As shown in Figure 3.5, the slots in the walls allow flexible positioning of the different injection systems. A strut injector is implemented in the module with constant cross section, where shock reflections and friction contribute to increase the overall static pressure and thus support mixture ignition and flame stabilization. As discussed in the Sections 2.4.2 and 2.4.4, the heat released by the reactions could exceed the critical value for the combustor. Therefore, the second module is divergent to accommodate the pressure rise and avoid thermal choking.

The strut can be used as single stage injector or be combined with a cavity injector, which is placed in the diverging module. The fuel injectors will be detailed in the following Section.

3.2.3 Injection Systems

The design of the fuel injection systems for the combustion chamber described above represents the core of the work done for this thesis. The choice of a central injector is justified by the results of previous investigations carried out on ramp and strut injection at the LFA [10], [11], [32], [33], [58]. The struts designed for the present experiments aim to optimize aspects such as aerodynamic losses and fuel distribution.

A cavity has been introduced as a second stage injector to further extend the operating range by increasing the overall equivalence ratio and to assess the possibility

of controlling the combustion and heat release processes by tuning the amount of fuel injected at each stage.

The different geometries and fuelling configurations tested will be presented in the following sections. Detailed technical drawings of the injectors are included in Appendix A.

Strut Injectors

Three different struts have been designed and tested as a single stage injector. The different concepts are shown in Figure 3.6 and will be referred to as Strut 1, Strut 2 and Strut 3, respectively.

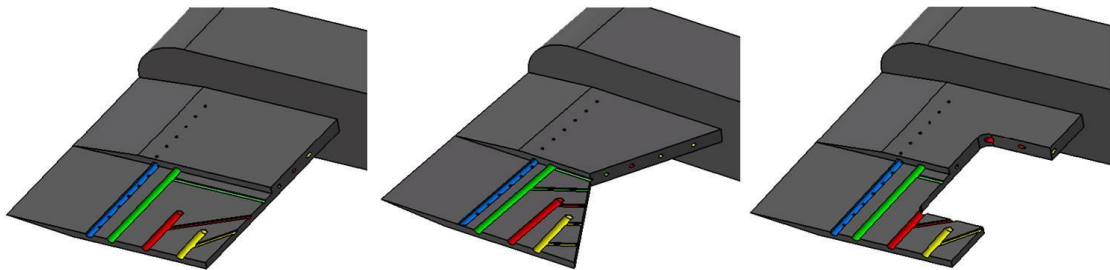


Figure 3.6 Tested strut geometries; Strut 1 (left), Strut 2 (middle) and Strut 3 (right).

All three struts are made of Alloy 800H and feature an apex half angle of 7.5° , 23mm length, 27mm width and 2mm thickness. The peculiarities of central injectors have been examined in Section 2.3.3. The devised concepts combine axial injection into the wake of the strut with transverse port injection from the sides. This combination was chosen in order to enhance fuel penetration into the supersonic airflow and promote fuel-air mixing while creating a recirculation zone for flame stabilization. The purpose is to exploit the subsonic wake of the strut to stabilize a pilot flame which is then used as an ignition source for the main supersonic flame. Fuel (hydrogen or methane) and oxidizer (air or oxygen) at sonic speed and a temperature of about 290K can be injected streamwise into the wake.

The mixture ratio of the pilot flame can be changed by varying the amount of fuel and oxidizer injected axially. The amount of fuel is adjusted by means of the mass flow controller (72 of Figure 3.7), while the amount of oxidizer is determined based on the sonic flow condition at the end of the injection holes and set through the injection pressure of the oxidizer, p_{20} . Air is delivered by the house supply (0.8MPa), and the maximum achievable mass flow rate of the pilot air limits the range of possible

pilot equivalence ratios when air is used as oxidizer. This constraint does not affect the oxygen supply. The schematic of Figure 3.7 shows both supply lines.

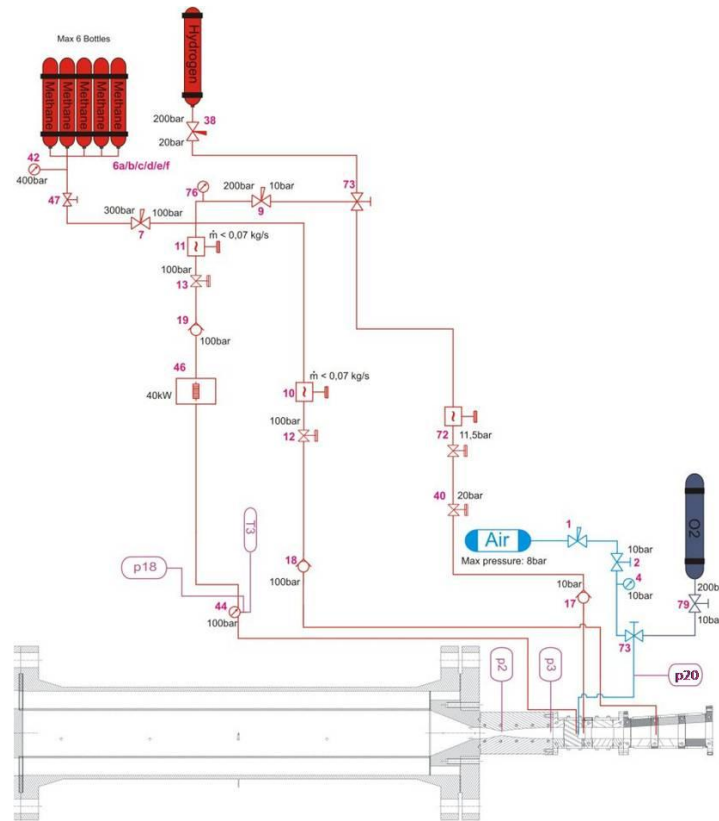


Figure 3.7 Detail of the gases supply lines to the combustion chamber.

Methane is delivered to both the strut and the cavity injectors as main fuel for the supersonic combustion; the mass flow rate can be adjusted in both cases through coriolis-type mass flow controllers up to a maximum of 0.075kg/s and the injection occurs in both cases at sonic speed.

Along one of the lines an electric heater with a power of 40kW provides pre-heating of the fuel up to 560K; the connections are interchangeable and allow supplying warm methane either to the strut or to the cavity. The strut has been preferred for these investigations since injecting methane at about 270K through the cavity provides a certain degree of cooling of the combustor wall in which the injector is implemented. Nevertheless, tests have been carried out also with injection of cold methane through the strut sides.

All struts have a series of twelve holes on each side for methane injection; the holes have a diameter of 0.3mm and the spacing between two holes is 2mm. The concepts differ in the trailing edge geometry and in the axial fuelling configuration.

Strut 1 has a straight trailing edge; the axial fuel injection system is designed to be symmetrical with respect to the centreline *a* evidenced in Figure 3.8. Oxidizer is supplied in the middle through the hole indicated by **C**, whereas fuel is injected through the four holes marked as **B**. The system is conceived in such a way that on either side of the centreline *a* two fuel jets and one oxidizer jet converge in one point; both triplets generate a combustible mixture in the area circled in red in Figure 3.8.

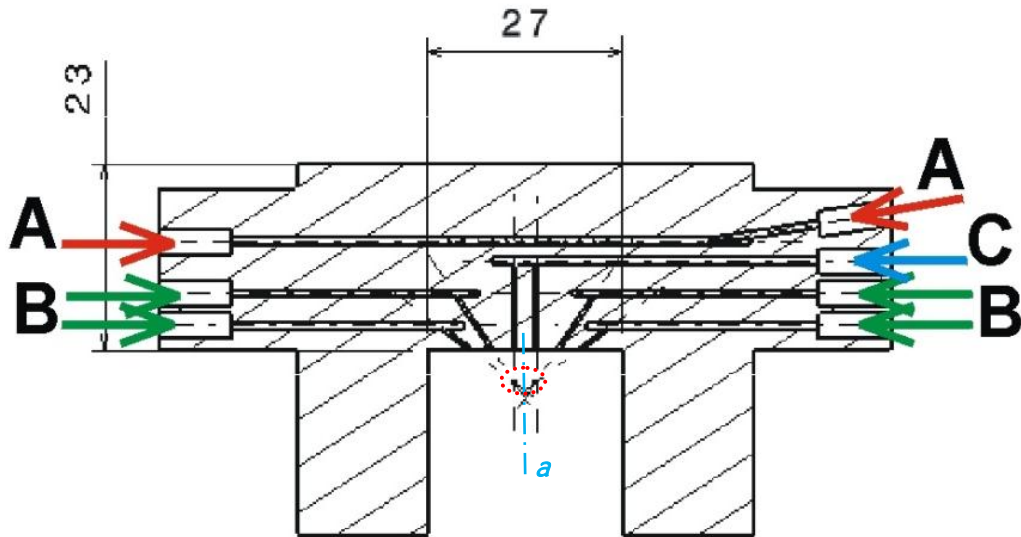


Figure 3.8 Section of Strut 1 with suggested fuelling strategy for methane (A), pilot fuel (B) and pilot oxidizer (C).

The design of the injectors aims to increase the system flexibility by allowing interchangeable supply lines for fuel and oxidizer. For instance, for Strut 1 fuel can be injected through the holes C and oxidizer through the holes B, in order to adjust the pilot equivalence ratio. The same applies to Strut 2 and Strut 3. Using Strut 2, pilot oxidizer can be supplied by means of the triplet of holes C and pilot fuel through the remaining holes B1 and B2 as depicted in Figure 3.9. A different fuelling configuration can also be adopted; oxidizer can be injected through B1 or B2, in addition to or instead of using the holes C. Using Strut 3, the same alternatives as for Strut 1 can be investigated, since these struts differ barely for the geometry of the trailing edge.

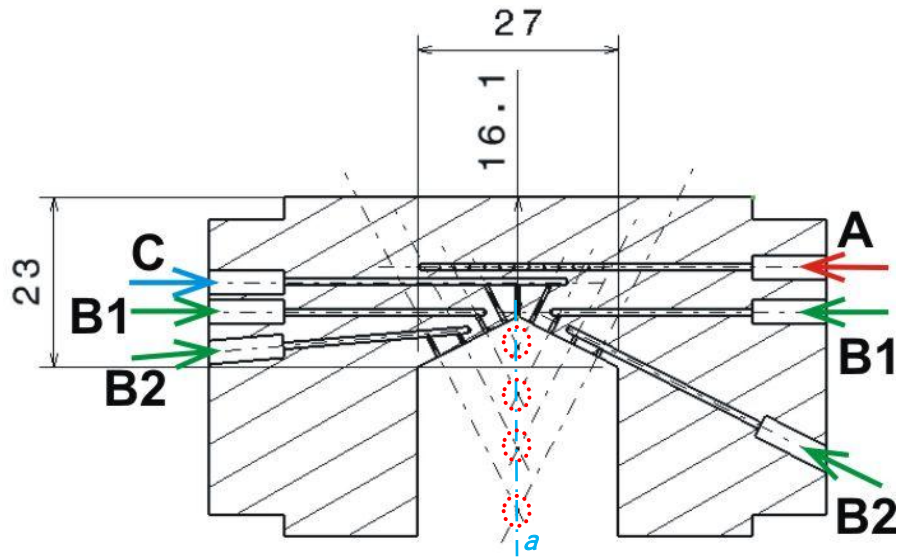


Figure 3.9 Section of Strut 2 with possible fuelling strategy for methane (A), pilot fuel (B1, B2) and pilot oxidizer (C).

The trailing edge geometry of Strut 2 is shaped such that the generated vortices shed sequentially starting from the centreline of the strut. The intention of this arrangement is to promote axial mixing of the jets impinging within the core of the wake and to support lateral entrainment of the combustion products once the reaction is initiated. Instead of converging in one or in two points belonging to the same lateral plane as for Strut 1, the jets from the central triplet and from the three sets of paired holes impinge at consecutive axial locations. The subsequent injection of fuel should mitigate the risk of thermal choking after mixture ignition and render the combustion heat release more homogeneous.

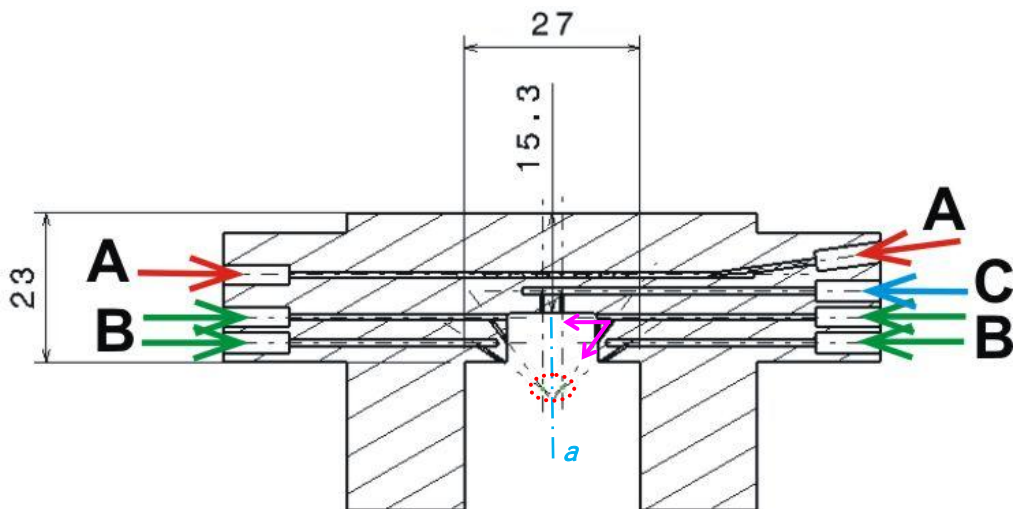


Figure 3.10 Section of Strut 3 with possible fuelling strategy for methane (A), pilot fuel (B) and pilot oxidizer (C).

A section of Strut 3 is shown in Figure 3.10. The central portion of the trailing edge is cut to form a recess to minimize the disturbance of the recirculation zone by the external flow. Although the gases supply lines are the same as described for Strut 1, the different trailing edge geometry allows injection of fuel towards the centreline through two additional ports opened in the sides of the recess; the pink arrows in Figure 3.10 highlight the bifurcation of the upper line marked as B. The design combines the main features of the other struts, i.e. a stable recirculation zone to extend the residence time of the flow and a sequential injection of fuel in the streamwise direction to control the combustion heat release.

Cavity Injector

Cavity design is a trade off between enhancing the overall equivalence ratio through injection of additional fuel and minimizing the drag penalty associated with the use of a cavity [6], [50], [61]. Figure 3.11 presents a three-dimensional view and a section of the injector. The cavity is placed in the first portion of the diverging module of the combustor to avoid further heat release in the constant cross section area and yet to be close enough to the pilot flame for the fuel to be ignited. The orientation of the injection holes is matched to the direction of the stream lines.

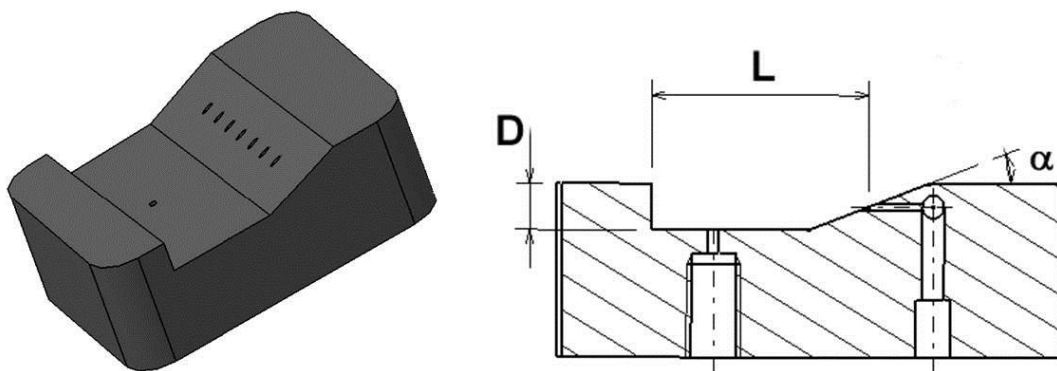


Figure 3.11 3D view (left) and section (right) of the cavity injector.

The cavity has a 4mm depth, D and a 20mm length, L , where the latter is measured from the front wall to the middle of the slanted rear wall. Since the cavity drag coefficient depends on the geometry of the rear wall, a ramp angle α of 20° has been chosen according to the results of Samimy [61] who found the cavity drag to be minimal with this angle.

A static pressure tap was positioned on the cavity floor to compare the pressure p_c to the value measured on the opposite combustor wall. Although optical access is limited when the cavity is mounted in the top combustor wall this configuration has been preferred to implementing it into the bottom wall in order to obtain exhaustive information on the wall static pressure distribution.

As discussed in Section 2.3.2, having a length-to-depth ratio ($A = L/D$) equal to five the cavity is classified as open. In this configuration the shear layer detaching at the front cavity lip will reattach at the cavity rear wall and not on its floor. An open cavity has been selected with the twofold purpose of limiting drag and total pressure losses and of promoting the mixing of fuel and air rather than to use it as a flame holder [6].

3.2.4 Laser Ignition Setup

As discussed in Section 2.4.2, the focused beam of a solid-state Nd:YAG laser has been used as external ignition source to light off the pilot flame. The ignition setup consisted of the Lab 130-10 laser by Spectra Physics, which delivers 200mJ per pulse at 532nm wavelength and at a frequency of 10Hz. The laser beam has been guided to the test section by means of two high power mirrors and focused in the pilot mixing region using a plano-convex lens made of fused silica. Although a range of focal lengths, f , generated a spark capable of igniting the mixture the optimum, i.e. the shortest time to ignition after switching on the laser, has been found with a lens of $f = 80\text{mm}$. Figure 3.12 shows a picture of the focal spot taken with the CCD camera.

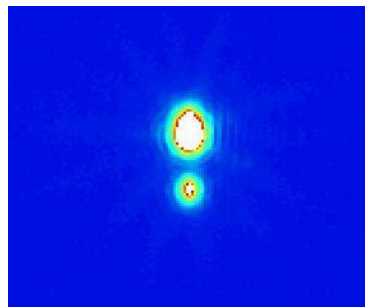


Figure 3.12 Focused laser beam photographed with a CCD camera.

Mixture ignition occurs via the non-resonant mechanism, in which the wavelength of the laser radiation is different than the absorption lines of the medium. The pilot mixture is ionized in the focal spot by the energy of the laser. Electrons are set free and accelerated through absorption of the beam energy; they collide with other molecules, and form more ions and electrons. The plasma generated by the

electron avalanche is heated by the laser radiation. Once the energy content of the spark exceeds a certain threshold, typically 10^{10} to 10^{11} W/cm² for gases, optical breakdown occurs, leading to local temperatures up to 10^6 K [40], [64]. A flame kernel develops and grows sustained by the laser spark until it reaches a critical size at which it becomes self-sustaining and the mixture is ignited.

For the $f = 80$ mm lens used, assuming that the laser beam diameter at the lens, D_l , does not change from its initial 10mm along the optical path, the radius (ω_0) and the area (A_0) of the focal spot can be determined as

$$\omega_0 \approx \frac{2}{\pi} \lambda \frac{f}{D_l} \quad \text{Equation 3.3}$$

$$A_0 \approx \pi \omega_0^2 \quad \text{Equation 3.4}$$

For an average pulse width of 7ns at 200mJ pulse energy, the resulting intensity in the focal spot can be shown to be approximately $1.22 \cdot 10^{16}$ W/cm², i.e. well above the aforementioned optical breakdown threshold. With the adopted configuration and for stoichiometrically suitable conditions, ignition was reliably achieved within one second.

3.3 Test Conditions and Experimental Methodology

Freestream Conditions

The majority of the tests have been carried out using both the electric and the vitiated heater to stabilize the total temperature of the supplied air at 1000K. A subset of experiments have been conducted to assess whether the injectors support mixture ignition and flame stabilization under more severe conditions, i.e. at a total temperature of 650K stabilized using the electric heater alone. In this case, only discrete data have been collected, recording whether ignition took place for both the pilot and main flames.

Finally, during some experiments the total temperature level has been continuously reduced from 1000K to 650K to investigate the flame stability. As for the tests at 650K, the purpose was to record whether the flames extinguished while varying the inlet temperature. Table 3.1 summarizes the conditions of the incoming air at the two total temperature levels.

| T_{tot} [K] | \dot{m} [kg/s] | P_{tot} [MPa] | p_{cc}^2 [MPa] | M_{cc} [-] | M_{F} [-] |
|-------------------------|---------------------|---------------------------|----------------------------|------------------------|-----------------------|
| 1000 | 0.345 | 0.94 | 0.060 | 2.2 | 4.25 |
| 650 | 0.345 | 0.75 | 0.077 | 2.2 | 3.25 |

Table 3.1 Conditions of the airflow entering the combustor and corresponding M_{F} .

Tested Configurations

The experiments have been structured to assess the performance of the three struts for different configurations. The struts were first tested as single-stage injectors to verify whether the geometries support mixture ignition and pilot flame stabilization without the requirement for further flame holding devices. For this purpose, varying mass flows of methane and hydrogen have been injected into the wake of the three struts while adjusting the amount of additional oxidizer to determine the optimal mixture composition.

The struts were then tested for their performance in stabilizing the supersonic combustion of methane. These investigations have been conducted using two of the most promising conditions determined for the pilot flame, i.e. a stoichiometric and a lean mixture. The amount of methane injected has been increased in a stepwise manner.

In light of the findings of the single-stage injection tests only Strut 1 and Strut 3 have been combined with the cavity in a two-stage injection configuration. Strut 2 did not meet the expected performance and further, major optimization work would have been needed, going beyond the time and budget resources available for the present study. As in the case of the single-stage tests, the amount of methane injected through the cavity has been increased progressively; additionally, the effect of the fuel injection temperature has been investigated by switching the methane supply lines of strut and cavity as briefly explained in Section 3.2.3.

Experimental Methodology

For each configuration and condition tested, the data have been acquired during "Fuel-Off", "Fuel-On" and "Combustion" measurements. The Fuel-Off measurements

² Since a static pressure tap is not available at the entrance of the combustion chamber, the value measured close to the exit of the Laval nozzle has been used for p_{cc} instead. Referring to this value also avoids overestimating the static pressure due to the influence of shocks and other aerodynamic phenomena occurring in the combustor.

represent the reference condition for each strut and a first comparison of the three different geometries. The main airstream is supplied to the combustor at the desired temperature and the pressures and temperatures are recorded.

During the Fuel-On measurements fuel and, if required, additional oxidizer have been injected into the combustor without igniting the mixture. The Fuel-On measurements were carried out for the sake of quantifying the momentum effect on the pressure variation inside the combustor.

The Combustion measurements refer to the data recorded for the different flow conditions and fuelling configurations after igniting the mixture. The contribution of the combustion to the overall pressure variation can be decoupled from the momentum since the latter is known from the Fuel-On measurements.

Data Labelling

Labelling of the experimental data aimed to reflect the following information:

| Type of injection | Type of measurement | Type of flame |
|-------------------------------|-------------------------|-------------------------|
| S1 : Strut 1 | | |
| S2 : Strut 2 | FOFF : Fuel-Off | PF : Pilot Flame |
| S3 : Strut 3 | FON : Fuel-On | CH4 : Main Flame |
| S1C : Strut 1 & Cavity | COM : Combustion | |
| S3C : Strut 3 & Cavity | | |

Table 3.2 Labelling of the experimental data.

Additionally, a consecutive numbering identifies the test conditions in terms of the amount of fuel and oxidizer injected through the different systems according to the experimental run summary reported in Appendix B. For instance, the label S1_FON_PF41 refers to a pilot flame stabilization test with Strut 1 as single-stage injector, with fuel injection but without ignition at the conditions specified by the number 41 at the end, i.e. 345g/s air, 100mg/s hydrogen and 820mg/s oxygen.

3.4 Instrumentation and Diagnostic Techniques

To gain insight into the aerothermodynamic processes occurring in the combustion chamber the testing facility has been equipped with a range of instrumentation. In addition to conventional pressure and temperature sensors a variety of non-intrusive optical systems was available for the investigation. Further, a gas sampling probe has been designed and gas chromatographic analysis of the samples has been performed. The measurement equipment applied for this study will be detailed in the following sections.

3.4.1 Static Pressure Measurements

The static pressure has been measured at three flow stations along the main supply line. The first pressure has been measured upstream of the electric heater, the second upstream of the catalyst and the third prior to the entrance of the Laval nozzle. Due to the low flow velocity in the main supply line this value can be assumed to equal the total pressure and has been used as reference for the values acquired in the Laval nozzle and in the combustion chamber.

Two static pressure taps have been implemented at the throat and at the exit of the Laval nozzle. The wall pressure distribution inside the combustor has been measured using a series of thirteen static pressure taps implemented along the bottom wall. Seven sensors are implemented into the constant cross-area section of the combustor and the other six in the divergent, as highlighted in the drawing of Figure 3.13. The tap at the exit of the Laval nozzle is also visible. All static pressure probes have a diameter of 1mm.

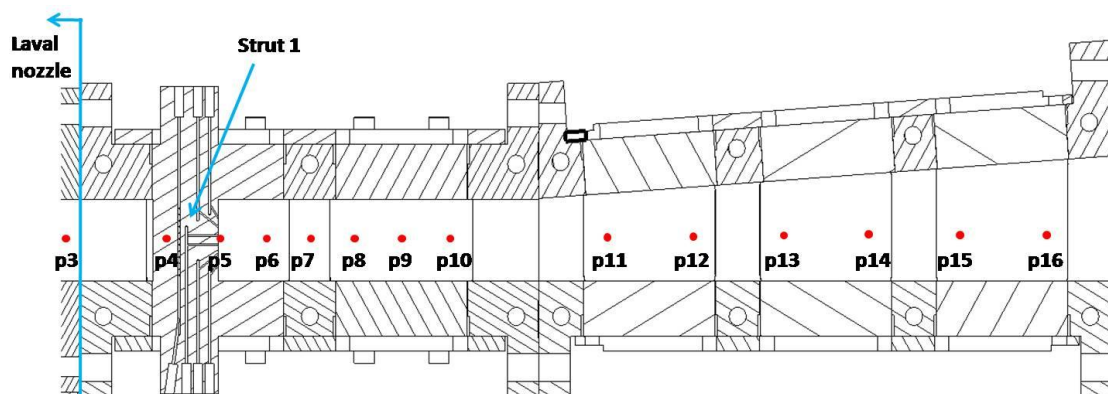


Figure 3.13 Bottom wall of the combustion chamber with pressure taps. Strut 1 is mounted in the first module of the combustor.

Table 3.3 lists the static pressure taps. For those at either at the Laval nozzle or in the combustor the distance from the chamber entrance is also indicated. For all configurations in which the cavity is implemented in the diverging section of the combustor an additional pressure tap was included to measure the static pressure on the cavity floor (see Figure 3.11).

| Pressure | Location | Distance from combustor entrance |
|----------------------|--|----------------------------------|
| p_B | Upstream of electric heater (Basement) | - |
| p_0 | Upstream of catalyst | - |
| $p_1 (\sim p_{tot})$ | Laval nozzle entrance (entrance total pressure) | - |
| p_2 | Laval nozzle throat | - |
| $p_3 = p_{cc}$ | Laval nozzle exit | -5mm |
| p_4 | Combustor, constant cross-area section, after the leading edge of the strut injectors | 31mm |
| p_5 | Combustor, constant cross-area section, after the trailing edge of the strut injectors | 48mm |
| p_6 | Combustor, constant cross-area section | 65mm |
| p_7 | Combustor, constant cross-area section | 80mm |
| p_8 | Combustor, constant cross-area section | 95mm |
| p_9 | Combustor, constant cross-area section | 112mm |
| p_{10} | Combustor, constant cross-area section | 129mm |
| p_{11} | Combustor, diverging section | 183.6mm |
| p_{12} | Combustor, diverging section | 213.5mm |
| p_{13} | Combustor, diverging section | 245.1mm |
| p_{14} | Combustor, diverging section | 274.1mm |
| p_{15} | Combustor, diverging section | 306.6mm |
| p_{16} | Combustor, diverging section | 336.5mm |
| p_c | Cavity floor | - |

Table 3.3 List of measured static pressures.

3.4.2 Gas Sampling

To complete the information on the combustion process and on the aerodynamics of the flow exiting the combustor a gas sampling probe has been designed based on the work of Mitani, Tomioka et al. [43], [45], [46], [68], who investigated quenching in gas sampling probes for application to scramjet engines. They analytically determined a critical value of the Damköhler number of the probe below which quenching of the reactions is expected:

$$Da^* < Da_{\text{Probe}} \propto (d \cdot P)^2 \quad \text{Equation 3.5}$$

As the Damköhler number is proportional to the squared product of the tip diameter of the probe and the pressure inside the probe, the tip diameter has to be small and the pressure in the probe low in order to fulfil Equation 3.5. However, for small tip diameters the Reynolds number decreases and viscous effects become relevant; friction choking can inhibit the quenching of the reaction.

Another critical phenomenon to consider when designing a probe for supersonic conditions is the shock occurring at the entrance. The shock is normal, at least in the central part of the tip and can heat the collected samples altering the measured gas composition. Further, if the shock takes place in front of the probe, lighter species can be deviated and the collected samples will be enriched with the heavier reaction products, again leading to incorrect results.

The internal and external geometry of the probe tip have to be carefully chosen to address these effects. Following Mitani et al. [46], a probe with a 30°-angle cone tip, a tip diameter of 0.3mm and a short straight section should maximize the reaction quenching. Figure 3.14 shows the results of a simulation of the viscous flow around the probe performed with an axisymmetric viscous code for two different internal tip sections [46].

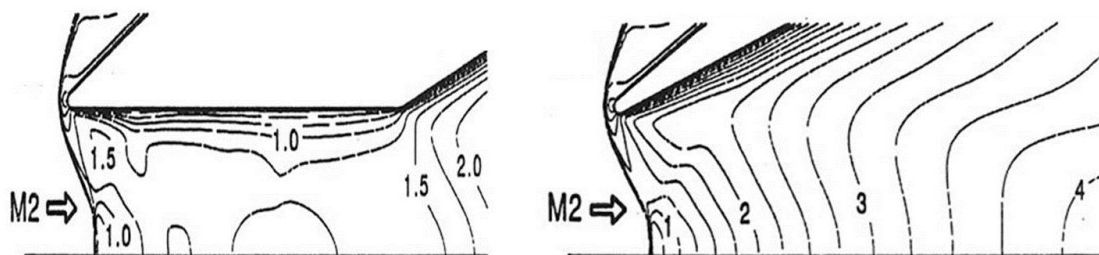


Figure 3.14 Mach number contours for a probe with a 0.6mm long straight section (left) and for a probe with no straight section (right) [46].

The shock structure is similar for both geometries. Both probes guarantee swallowing of the initial shock thus preventing preferential gas sampling of heavier reaction products. However, while for the left probe viscous effects are not negligible, the right probe expands the flow from Mach one to supersonic conditions after the normal shock. This supports quenching of the reactions by reducing pressure and temperature of the mixture.

In addition to designing the tip geometry in order to promote reaction quenching, the gas sampling probe used by Mitani et al. [46] is water cooled to further support chemical freezing of the gas composition by a combination of conduction and forced convection. Copper was selected to manufacture the probe due to its high thermal conductivity and the amount of water supplied was regulated to prevent glowing of the probe tip [67].

The probe used for the present investigations has been designed following the same principles. As schematically represented in Figure 3.15, open loop water cooling has been performed. However, as acetylene is one of the by-products of methane combustion, neither copper nor silver could be used for gas sampling in a methane flame, for both materials react with acetylene. Therefore, an austenitic nickel alloy, the Nicrofer3220H or Alloy 800H, has been used to manufacture the gas sampling probe and its support. Although the thermal conductivity of the Alloy 800H (29W/m-K at 1273K) is a factor of ten lower than that of copper at the operative temperatures, the alloy withstands temperatures up to 1670K against the 1360K of copper.

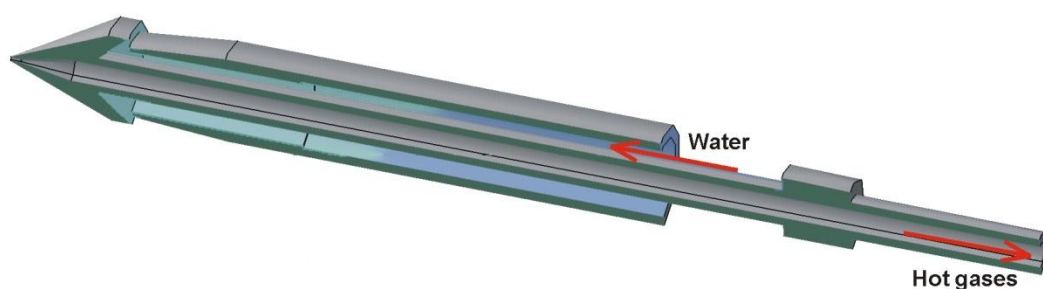


Figure 3.15 3D section of the gas sampling probe.

Due to the low thermal conductivity of the Alloy 800H, the tip of the probe has been designed with a 0.6mm long internal straight section in order to avoid excessive heat loads on a very thin wall. The drawings of both the probe and its support are provided in Appendix A. The gas samples have been collected into stainless steel

cylinders of 75cc volume which were evacuated prior to the tests. The cooling water loop and the gas sampling line are shown in Figure 3.16.

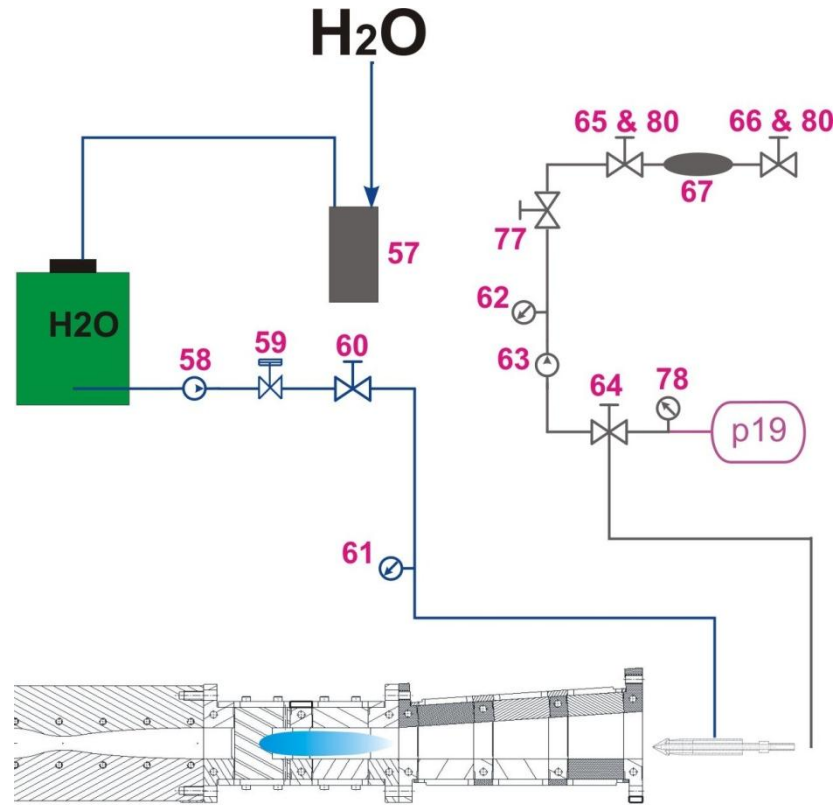


Figure 3.16 Detail of the gas sampling arrangement.

The first application of gas sampling in this study was to calibrate the catalytic combustion setup for the amount of oxygen to be added in order to recreate a realistic composition of the air supplied to the combustor. Further, these gas samples have been analysed for the presence of unburned radicals which could influence the main combustion processes. No unburned radicals were detected in any of the probes for the conditions tested. In addition, the amount of water produced by the catalytic combustion could be determined prior to each main combustion test. This allowed correction of the total amount of water measured in the samples collected during the main combustion for the effect of air vitiation.

During the supersonic combustion tests the gas sampling probe was mounted on a motorized system of transverse stages. Samples have been collected at various locations at the combustor exit and a gas chromatographic analysis has been carried out to determine the net quantity of water due to the main reactions and to detect whether any intermediate species were present. Figure 3.17 shows the water cooled

probe during free stream measurements with one of the injection systems used in previous work at LFA [60].

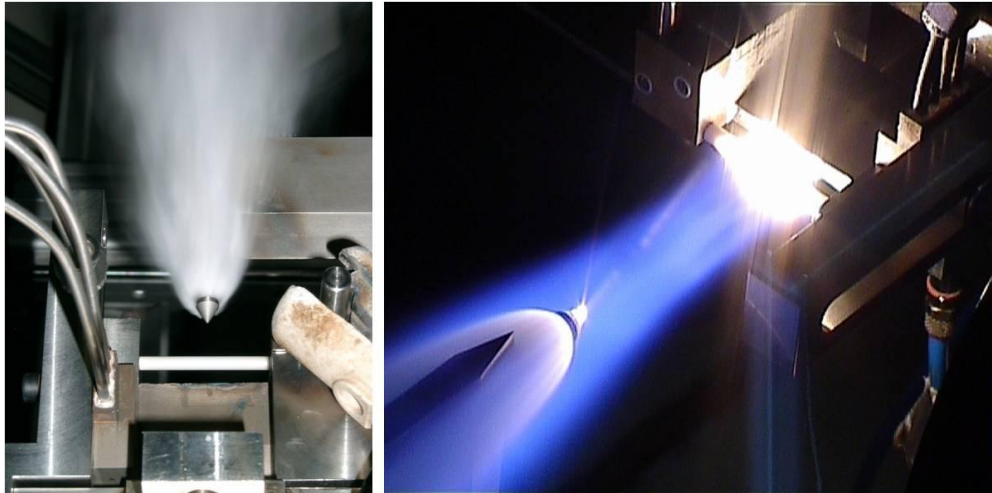


Figure 3.17 Gas sampling probe during free stream tests with an older injector [59].

3.4.3 Total Conditions at the Combustor Exit

To determine the performance of the model combustion chamber the total conditions have been measured at different locations along the vertical centreline of the exit plane. The choice of the measurement positions has been made to investigate the different flow regions observed in the combustor during the tests. In fact, the supersonic methane flame did not spread over the whole height of the combustor and different flow conditions are thus expected inside and outside the flame core, which is visible as stream core over part of the exit cross section in Figure 3.18.

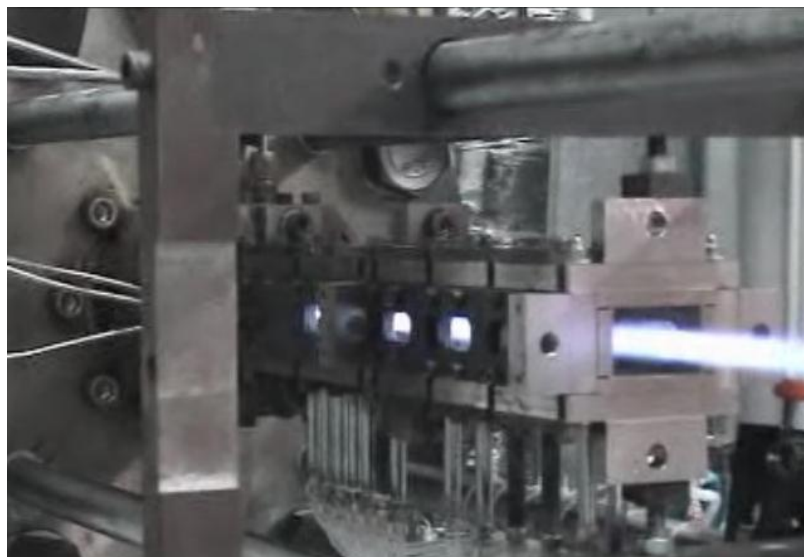


Figure 3.18 Aft-looking-forward view of the combustor with supersonic methane flame.

Given the small cross sectional area at the combustor exit (41mm x 25mm) and the size of the probes, only one sensor could be implemented at a time in order not to choke the combustor. Thus, the data have to be regarded as local values at one position, which provide a very first indication of the conditions in the different flow regions.

The probe described in the previous section has been designed with the twofold purpose of performing both gas sampling and total pressure measurements at the combustor exit. After collecting the samples in the cylinders, the line has been commuted by means of a valve to connect the probe to a pressure transducer and measure the pitot pressure. The measured values have been post-processed to take into account the effect of the shock occurring in the tip of the probe. The total pressure measured by the Pitot tube is lower than the true value at the designated location, since the Mach number of the incoming flow is reduced across the bow shock. This is exemplified in the schematic of Figure 3.19, where the subscripts M and T stand for "Measured" and "True", respectively.

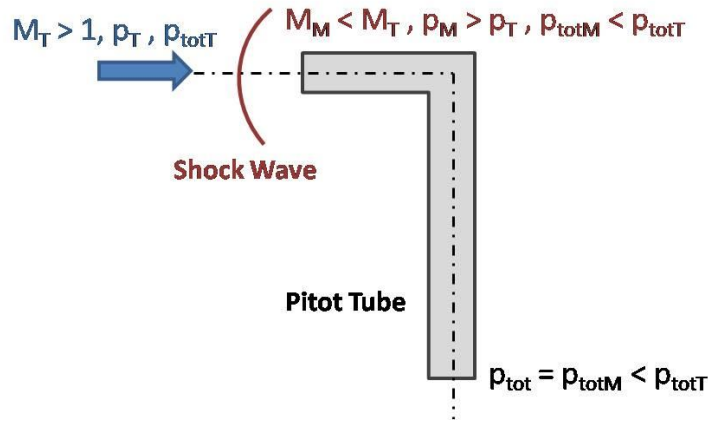


Figure 3.19 Schematic of a Pitot tube in a supersonic stream.

The Rayleigh Pitot tube formula

$$\frac{p_{totM}}{p_T} = \left(\frac{\gamma+1}{2} M_T \right)^{\frac{\gamma}{\gamma-1}} \left[\frac{2\gamma M_T^2 - (\gamma-1)}{\gamma+1} \right]^{-\frac{1}{\gamma-1}} \quad \text{Equation 3.6}$$

links the measured total pressure to the true static pressure and true Mach number. Knowing either p_T and p_{totM} or M_T and p_{totM} , the true total pressure can be obtained by manipulating the Rayleigh formula with the true isentropic ratio:

$$\frac{p_{totT}}{p_T} = \left(1 + \frac{\gamma-1}{2} M_T^2 \right)^{\frac{\gamma}{\gamma-1}} \quad \text{Equation 3.7}$$

Unfortunately the probe developed could not be modified to measure the static pressure. Therefore an additional measurement was developed to obtain the Mach number at the desired position, corresponding to M_T of Equation 3.6 and Equation 3.7. A wedge of known leading edge angle δ has been introduced into the stream at the same location in which the total pressure was first measured and a Schlieren image of the shock generated at the leading edge has been recorded (Figure 3.20). The shock angle β has been determined from the Schlieren photographs for the different conditions and both θ and β have been used to solve the implicit theta-beta-Mach relation for the M_T [3]:

$$\frac{1}{\tan \vartheta} = \left(\frac{\gamma+1}{2} \frac{M_T^2}{M_T^2(\sin \beta)^2 - 1} - 1 \right) \tan \beta \quad \text{Equation 3.8}$$

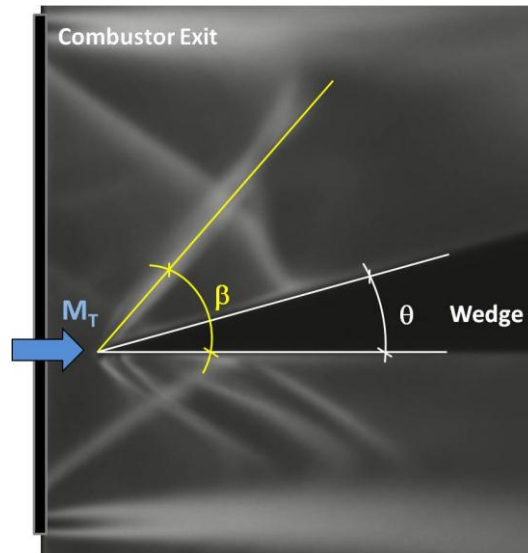


Figure 3.20 Schlieren image of a M_T measurement using the shock and apex angles.

In order to solve the three equations above the ratio of specific heats has been determined for each condition, as the value for pure air differs from that for the vitiated air or for the methane flame. Knowing the gas composition at the measurement location from the gas chromatographic analysis, the molar mass and the specific constant of the mixture have been calculated and the specific heat at constant pressure determined utilizing the Gordon-McBryde code to obtain the c_p and γ of the mixture.

The total temperature has been measured using a Type K thermocouple and a recovery factor correction. The gas sampling and total pressure probe, the

thermocouple and the wedge have been mounted on linear guides and positioned sequentially at the designated measurement positions to obtain the local values. Figure 3.21 shows images of one sequence inside the supersonic methane flame.

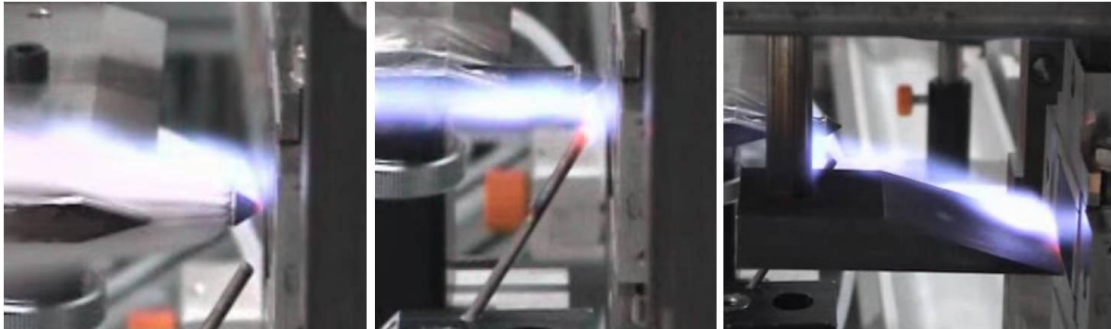


Figure 3.21 Total conditions measurement sequence. Gas sampling and total pressure (left), total temperature (middle), Mach number (right).

3.4.4 Infrared Pyrometer

Knowing the total temperature at the combustor entrance and at the exit a first estimate of the heat released by combustion can be performed for the pilot and main flames at different conditions. However, since the combustion chamber is neither cooled nor insulated, thermal losses occur by convection and possibly radiation. Therefore, an infrared pyrometer has been directed onto the metallic frame of the combustion chamber to measure the wall temperature. The Impac-IGA120 pyrometer used in the present investigations is suitable for a temperature range between 630.15K and 2073.15K and wavelengths between 1.45 μm and 1.8 μm .

3.4.5 Schlieren Optic Setup

The Schlieren method is a non-intrusive optical technique relying upon the angular deflection of light crossing a medium with inhomogeneities. The absolute index of refraction, n , quantifies the degree to which the speed of light is reduced inside a medium. If the medium is a gas, the refractive index varies with the density, ρ , according to the following relation

$$n = k\rho + 1 \quad \text{Equation 3.9}$$

where k is the Gladstone-Dale constant. A density gradient thus leads to a gradient in the refractive index. A Schlieren optic setup visualizes the deflection of light. The technique is particularly suitable for investigations of heat transfer phenomena and shock or blast waves which are characterized by high density gradients.

In the basic arrangement, a Schlieren system consists of a non-coherent light source followed by a lens to collimate the light before it reaches the test section. A second lens focuses the light on a cut-off plane, which is used to detect the angular deflections of the light. Another lens is typically used to visualize the optical field on a Schlieren plane. Additionally, a diaphragm or a filter can be used to create a homogeneous light field before collimating the rays with the first lens.

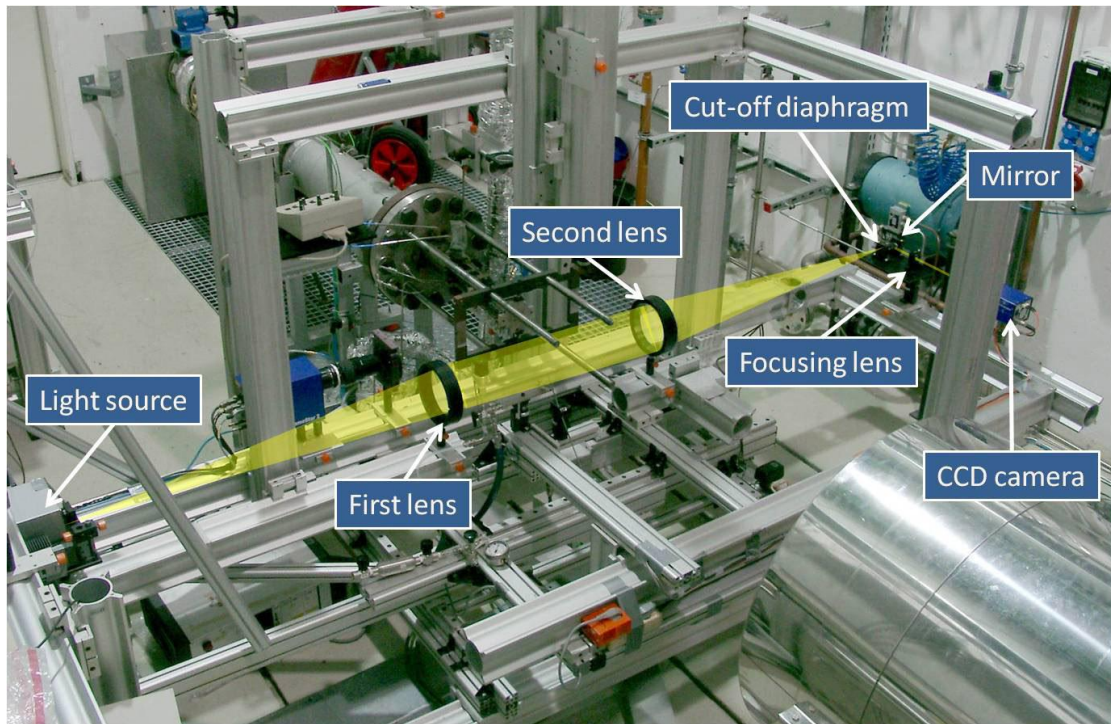


Figure 3.22 Schlieren optic setup in the test cell.

The system used for these experiments is presented in Figure 3.22. It consists of a halogen light source and a slit diaphragm, followed by an aspheric lens of 1000 mm focal length and 150 mm diameter to collimate the light. A second aspheric lens with the same focal length and diameter focuses the light onto the round diaphragm at the cut-off plane. The distance between the light source and the first lens and the distance between the second lens and the cut-off diaphragm was equal to the focal length of each lens. Due to space constraints, a mirror is implemented after the cut-off diaphragm to deflect the light by 90° towards a focusing lens and a remote controlled CCD camera, which records the images of the optical field. The setup is mounted on a two-axis system of linear guides, to allow online adjustment of the measurement position along the whole length of the combustor and in the exit region.

Besides being relatively simple and cost effective, the setup used has low sensitivity to vibrations, while providing good accuracy. However, two drawbacks

affected the present measurements. First, only integral images through the whole combustion chamber depth could be recorded inside the combustor and at its exit plane. This prevented discerning the complex flowfield generated around the different injectors in the direction normal to the imaging plane, i.e. the combustor width. Further, the shock angle on the wedge positioned at the combustion exit could be determined only within a certain accuracy (refer to Figure 3.20). Second, the inherent sensitivity of the refractive index to density variations is limited and good resolution of small density gradients can only be achieved by using a high-intensity, long-wave light source and high resolution optics. Alternatively, the sensitivity of the system can be improved by increasing the focal length of the second lens or by reducing the size of the optical field which is cut at the cut-off plane. Both approaches however have disadvantages. Improving the light source and the optics increases the cost of the system, while a greater focal length leads to space constraints. A narrower optical field allows only detection of detailed regions, increasing the possibility of missing an important feature.

For the sake of this study the resolution and size of the optical field have been sufficient to determine whether the flow conditions at the combustor exit are supersonic and to estimate the exit Mach number as detailed in Section 3.4.3. The cost of a system with higher resolution and accuracy would be justified to investigate the flowfield inside the combustor. However, since the optical accessibility of the present combustion chamber is limited to less than 40% of its height, the information gained with a better Schlieren optic setup would remain lacking and hence did not justify any of the improvement strategies described above.

3.4.6 Planar Laser-Induced Fluorescence Setup

Laser-induced fluorescence (LIF) is a process involving the absorption of a photon of light by an atom or molecule such that it is excited to a higher electronic energy state. Since the excited energy state is of non-equilibrium, the atom or molecule will return to the ground energy state either by emitting a light photon or through collisions with other molecules. If the de-excitation occurs by photon emission, the resulting fluorescence can be collected as a LIF signal. Fluorescence is isotropic, incoherent and strongly unpolarized due to the de-phasing effect of collisions. The intensity of fluorescence is a function of the absorber concentration and of the temperature, pressure and velocity of the gas. In fact, the complex dependency of the state transition on the mentioned parameters is the major disadvantage of this optical

measurement technique. In general, the absorber is excited using a pulsed laser. The laser beam can be expanded into a thin sheet with a combination of cylindrical and of spherical lenses to form an illumination plane which is directed through the region of interest. In this case, one refers to planar laser-induced fluorescence or PLIF. The fluorescence is usually recorded with an ICCD (Intensified Charge-Coupled Device) camera [20], [21], [62], [63].

Planar laser-induced fluorescence is particularly suitable to analyze high-speed combustion processes since it is a non-intrusive technique and allows species selection of over more than thirty reaction intermediate products. Further, concentrations in the range of part-per-million and sub-part-per-million can be detected, which is of interest for species like the OH, CH and NH radicals. In the experiments carried out for the present study OH radicals have been excited from the rovibronic (rotational-vibrational-electronic) ground state $X^2\Pi$ to the excited state $A^2\Sigma^+$ by means of a Q-switched, Nd:YAG-pumped dye laser. Figure 3.23 illustrates the split of the molecular electronic levels into sub-levels according to the vibrational and rotational energy [16].

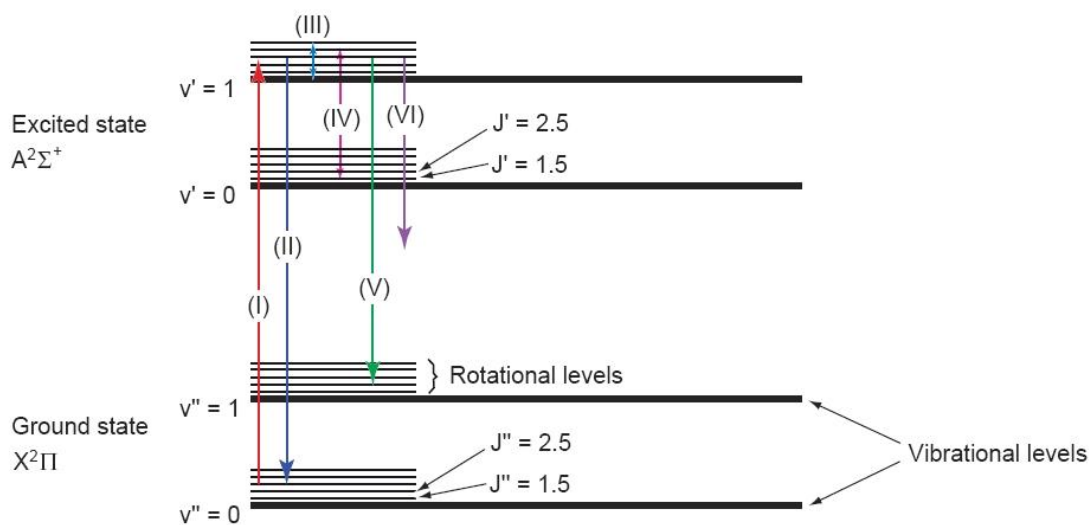


Figure 3.23 Schematic of LIF excitation between two rotovibronic states of OH and subsequent relaxation [63].

The processes that can take place when applying PLIF are also illustrated in Figure 3.23. According to the labelling, (I) corresponds to exciting a particular transition of the OH radicals by tuning the laser wavelength to be resonant with it. (II) is the stimulated emission from the excited to the ground state and does not result in a PLIF signal. It is characterized by the Einstein coefficient B_{21} . (III) and (IV) indicate the rotational and the vibrational energy transfer, respectively, i.e. the redistribution of

energy to nearby rotational and vibrational levels that occurs through collisions. (V) is the spontaneous emission, which results into a PLIF signal and occurs at a rate described by the Einstein coefficient A_{21} . (VI) represents the collisional quenching that depopulates the excited electronic state with a rate constant Q_{21} without emitting photons and hence decreases both the amplitude and lifetime of the fluorescence signal. Other processes that may take place and affect fluorescence are collisional excitation, predissociation and photoionization. However, they could be neglected in the present investigations due to energetic reasons [20], [21], [63].

The resulting fluorescence, F , is proportional to the population of photons in the excited state, N_2 , and the rate of relaxation by spontaneous emission

$$F = N_2 \cdot A_{21} \quad \text{Equation 3.10}$$

The fluorescence can be formulated explicitly by using the rate equations for the ground and excited states and expressing N_2 as a function of the Einstein coefficients for stimulated and spontaneous emission and absorption. However, the fluorescence signal, S_f , measured by the CCD camera is also a function of the properties of both the laser beam and the optics and can be expressed by the relation

$$S_f = E_{las} \frac{\Omega}{4\pi} l A_{las} C_{opt} N_1^0 \frac{B_{12}}{B_{12} + B_{21}} \frac{A_{21}}{1 + I_{v,sat}/I_v} \quad \text{Equation 3.11}$$

where E_{las} is the energy of the laser, $\Omega/4\pi$ the solid angle of the camera, l the axial extent of the fluorescent area, A_{las} the focal area of the laser beam, C_{opt} the collection efficiency of the optics and N_1^0 the initial population in the ground state. The terms denoted by I_v refer to the spectral irradiance of the laser used to excite the fluorescence. Usually the laser operates either in the linear or in the saturated regime. In the linear regime the fluorescence signal is linearly proportional to the laser irradiance, while in the saturated regime the laser irradiance is sufficient to significantly depopulate the ground electronic state and the fluorescence signal dependence on the laser excitation irradiance is non-linear. The spectral saturated irradiance is defined as the laser irradiance per unit wavelength interval required to produce a steady state for the laser-coupled system [20], [21].

In addition to the laser system, the main elements of PLIF setups for OH detection are the opto-mechanical components of the light path, an intensified charge-coupled device (ICCD) camera and the control electronics. The PLIF setup available at the LFA is schematically represented in the following pictures and will be briefly

described here. Further details can be found in the references [62]. To excite transitions in the band of the OH radicals the laser wavelength should be close to $\lambda=283\text{nm}$. The exciting laser at the LFA is a Nd:YAG-pumped dye laser using Coumarin 153 as the dye. The two lasers are mounted on top of each other on a support structure and the pumping beam is directed to the dye laser by means of two high power mirrors, Mirror 1 and Mirror 2 of Figure 3.24.

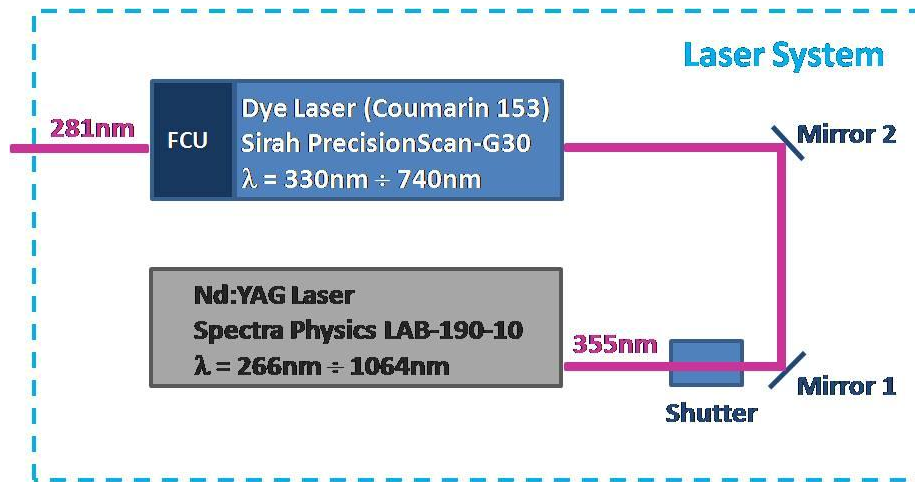


Figure 3.24 Schematic and specifications of the LFA laser system for PLIF measurements.

The fundamental resonance of the Nd:YAG laser is split into its third harmonic and filtered by dichroic mirrors to obtain a monochromatic laser output at 355 nm. This wavelength corresponds to the highest efficiency of the Coumarin 153 used in the dye laser. A remote controlled shutter opens to start pumping the dye laser, which can generate an output at wavelengths between 330nm and 740nm depending on the dye. For Coumarin 153 the wavelength lies in the range $\lambda = 517\text{nm} - 574\text{nm}$, and is reduced to a final wavelength between 258.5nm - 287nm by means of a frequency conversion unit (FCU) with a maximum output energy of 10mJ. The optimal excitation wavelength can be found by comparing the dye efficiency over the range of λ to the energy level of an OH transition band in a spectral diagram. For the present application, λ_{opt} is 281.1nm.

The laser beam leaves the laser system as an ultraviolet (UV) light beam of 4mm diameter. The optical components used to build the beam path to the test section and the windows of the combustion chamber are made of fused silica to allow transmission of the UV radiation. As illustrated in Figure 3.25, the laser beam is first deflected upwards with Mirror 3, which is necessary in order to gain space for the lenses. Mirror 4 deflects the beam towards the test section and Mirror 5 points it downwards.

A cylindrical lens featuring a focal length of 41mm expands the 4mm laser beam into one transverse direction and a subsequent plano-convex lens of 500mm focal length parallelizes the light sheet and focuses it in the middle of the test volume.

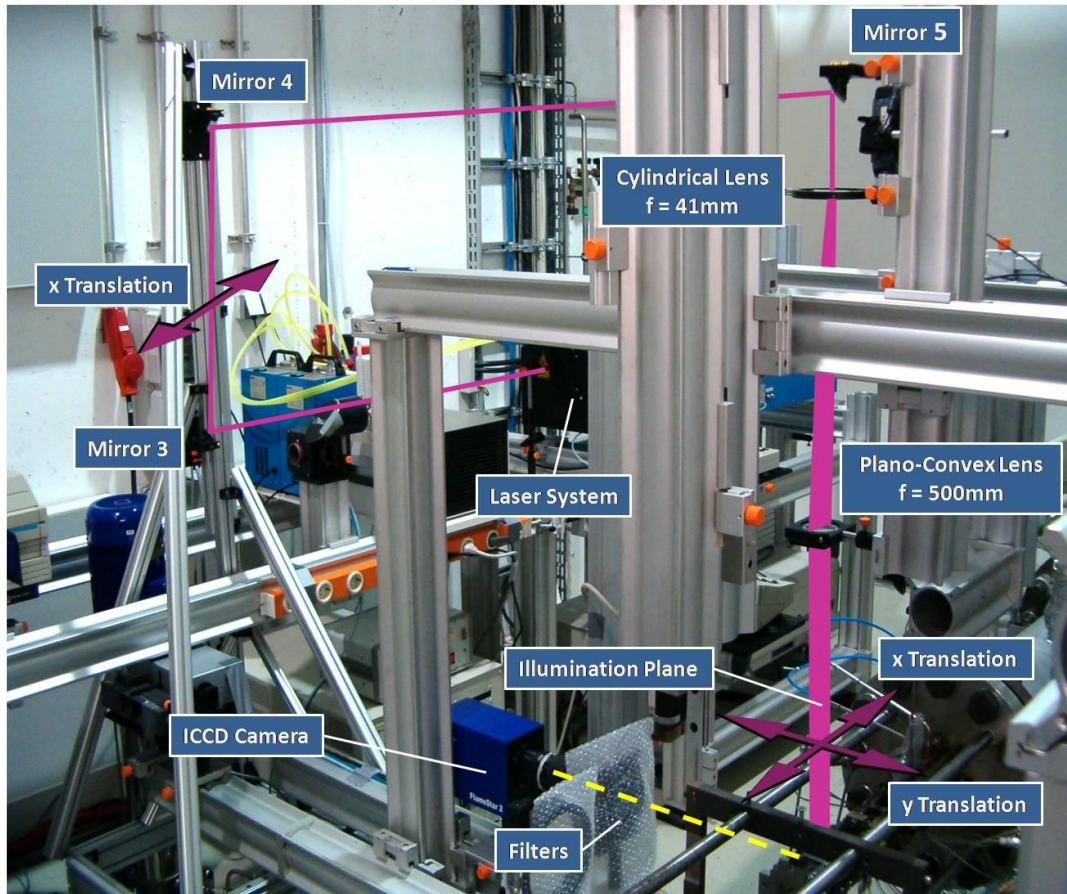


Figure 3.25 Optical path to the test section.

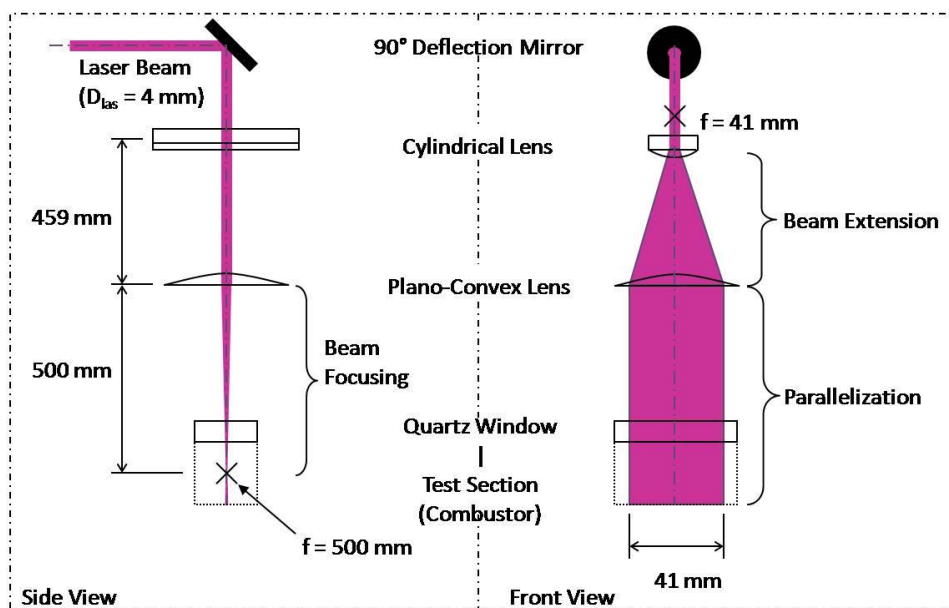


Figure 3.26 Generation of the illumination plane.

The location of the focus and the extension of the illumination plane (41mm, the same as the length of each combustor window) were achieved by tuning the distance between the lenses relative to the combustor, as illustrated in Figure 3.26. The last mirror and the two lenses were mounted on a support that can be translated in both the x and y directions to scan the length and the width of the combustion chamber. The first two mirrors are mounted on a separate support which can translate only in the axial direction, since their position in the y direction has to be fixed relative to the output of the laser system. The ICCD camera FlameStar 2 by LaVision is mounted on the motorized system of linear guides normal to the illumination plane, at the height of the combustor windows. The camera translates in both x and y directions together with the optics that generate the laser sheet and hence the optics only had to be focused at the beginning of the experiments. The distance of the camera from the test section has been set to record the images such that the axial length of a side window corresponds to 384 pixels on the CCD chip (384 x 286 pixels). The camera head is water cooled to minimize the thermal disturbance on the fluorescence signal and it contains an amplifier to intensify the photoelectric charge of each pixel. The OH fluorescence typically occurs at a wavelength between 305nm and 335nm. Since the fluorescence of other species, Rayleigh and Mie scattering and other sources of luminosity have the potential to affect the results, two Schott filters (UG11 and WG305) have been implemented in front of the ICCD camera to improve the quality of the PLIF imaging.

The ICCD camera is part of a more comprehensive measurement system by LaVision, consisting of FlameStar and of the software DaVis. The former includes the timing and control electronics for the camera, which is used to trigger the measurement to the laser pulses. The latter controls the system of linear guides and performs data acquisition and processing such as background subtraction and statistical analysis. For example, statistical interpolation provides information on the (y,z) planes from the images acquired on the (x,z) planes.

The major limitation of the PLIF setup available at the LFA is the use of Coumarin 153 as a dye instead of Rhodamine. The higher efficiency of Rhodamine in the wavelength range of interest would drastically improve the system sensitivity to the OH fluorescence and thus the accuracy of the results. However, replacing the dye would have required a new frequency conversion unit for the Sirah laser, which would have exceeded the budget allocated for the tests. The OH fluorescence results presented should therefore be regarded as complementary to the other measurements.

3.5 Summary

The test facility for supersonic combustion of the Institute for Flight Propulsion has been related to the range of facilities used for supersonic and hypersonic studies. Its components have been described and particular attention has been paid to the new injection systems that have been designed as the main focus of this thesis. The underlying design criteria have been related to the background presented in Chapter 2 to guide the reader through the results that will be discussed in the following chapter. The experimental conditions and the adopted methodology have been summarized before describing the measurement techniques that have been applied. Hereby, a detailed insight has been provided into the gas sampling system, the apparatus to measure the total conditions at the combustor exit and the new planar laser-induced fluorescence setup for OH detection. All of these measurement techniques have been developed as part of the work conducted for this study and have been applied for the first time at LFA as an integral system supporting the aerothermodynamic analysis of the mixing and combustion process.

4 Results

This chapter details the experimental results and will start with those concerning the stabilization of the pilot flame. The general results will be reviewed first, while Strut 1 will be presented in more detail and used as a reference for the discussion of the other two struts, which will be conducted mainly on aspects that are distinctive for each of them. Next, the results on flame stabilization for single-stage injection will be presented, again structured as a general overview followed by a detailed insight of the different injectors and by a comparison among them. Finally, the discussion of the results on staged injection will conclude the chapter.

4.1 Pilot Flame Stabilisation

The three strut injectors developed during this study have been conceived as an optimization of the previous injection system, which consisted of a strut coupled with a cylindrical flame holder [11], [58]. The modifications made to the strut significantly decreased the aerodynamic losses and improved the ignition behaviour, with a positive effect on combustion stabilization. The modifications and their effect will be described with reference to Figure 4.1, where the previous system is compared to Strut 1, which maintained the same trailing edge geometry.

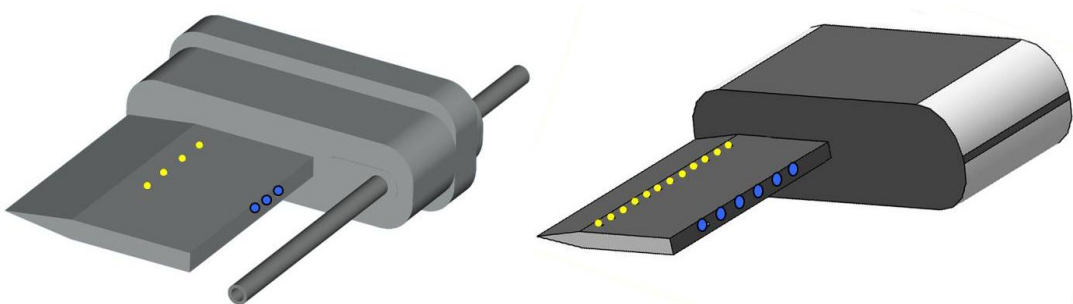


Figure 4.1 Comparison of the old injection system (left) to Strut 1 (right).

The strut geometries used in the past featured a thickness of either 3mm or 5mm. While both versions proved to be suitable to stabilize pilot and main flames with the aid of the cylindrical flameholder, they significantly obstructed the combustion

chamber. The geometric obstruction was 12% for the 3mm strut and 20% for the 5mm strut, and led to aerodynamic choking for the 5mm thick injector. This is shown in Figure 4.2 by the increase of the wall static pressure in the Laval nozzle (taps E1 and E2) for Injector2 [11].

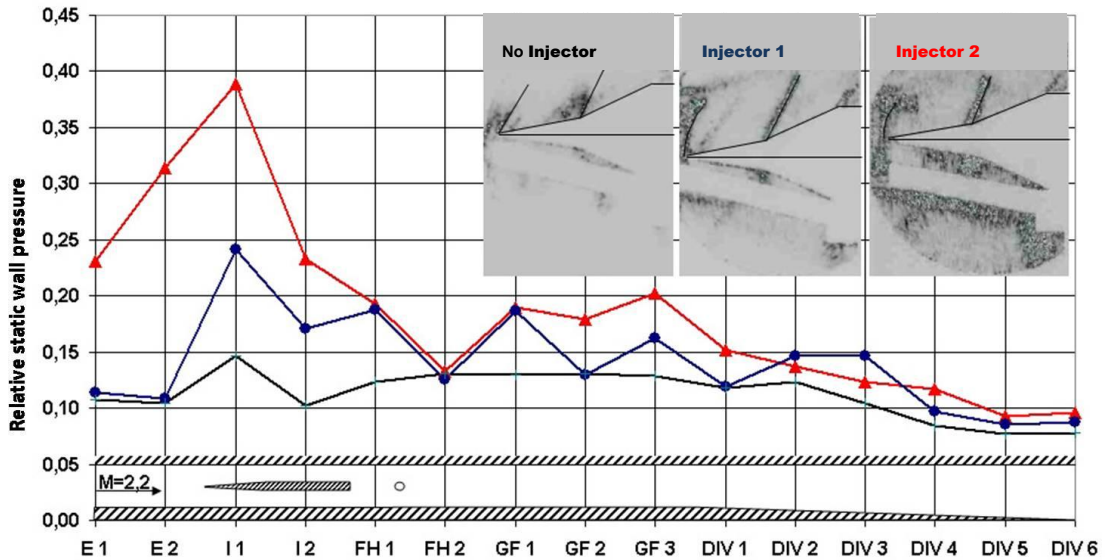


Figure 4.2 Wall static pressure distribution without combustion for the configuration without injector and for both versions of the previous strut [11].

To limit the risk of choking, all of the present struts have been designed with a thickness of 2mm, which corresponds to 8% obstruction of the combustor cross section. However, reducing the thickness of the strut also reduces the size of the recirculation zone generated in its wake and thus the region in which the pilot flame can be ignited and stabilized. Therefore, two other modifications have been introduced to achieve flame stabilization with the thinner injectors. Firstly, the overall length of the strut has been reduced from 30mm to 23mm, while maintaining the same apex half-angle. Secondly, the number and configuration of the axial injection holes has been changed to achieve a more homogeneous fuel distribution and to better tune the pilot stoichiometry of the mixture in the ignition region. The overall design proved to be successful in stabilizing the pilot flame over a broad range of pilot equivalence ratios without requiring a flame holder using Strut 1 and Strut 3. Strut 2 did not show the expected performance and did not support pilot flame stabilization or ignition. Strut 2 will be analysed separately in Section 4.1.2, while the effect of the shorter struts will be discussed in the next section.

The reduced length of the strut is a key design parameter since it is directly related to the shock structure inside the combustion chamber. Numerical simulations of

the Laval nozzle and of the combustor have been carried out at LFA for the configuration using Strut 1 without fuel injection [40]. Figure 4.3 shows the Mach number distribution in the first portion of the combustor, over a length of approximately 60mm. The shock generated at the leading edge (I) is first reflected at the wall (II) and impinges into the wake of the strut (W) at a distance of approximately 10mm from the trailing edge. The shock is reflected again on the shear layer (III), and a third reflection (IV) occurs again on the walls. By impinging into the shear layer, the shock waves break the interface between the main stream and the wake, which favours the mixing. It also affects the vortical structures shedding at the trailing edge. The simulation also resolves the boundary layers at the walls (BL), the expansion fans (E) at the trailing edge and the low speed region in the wake behind it (in blue).

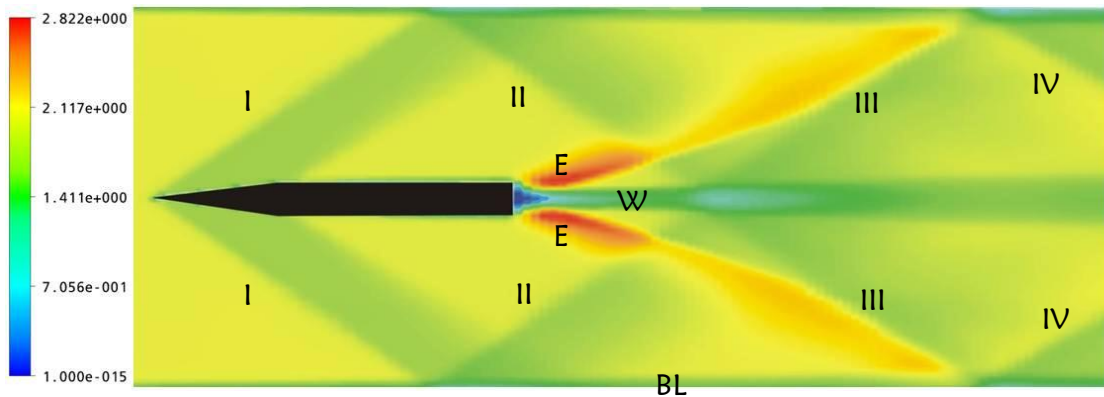


Figure 4.3 Numerical prediction of the Mach number distribution in the first portion of the combustor with Strut 1 [40].

The injection of pilot fuel and oxidizer takes place directly into the low speed recirculation region. As highlighted in Figure 3.8 of Section 3.2.3, each pilot injection triplet converges into one point at approximately 4.1mm from the trailing edge, which is also the location where the laser spark is directed to ignite the mixture. The choice of a shorter strut has a twofold, positive effect on flame stabilization due to the shifting of the pilot mixing and ignition region further upstream of the first shock reflection (II). First, the shock wave does not interfere with either the laser spark or the vortices shedding downstream in the recirculation zone at the location critical for mixture ignition. Second, the reflected shock wave further increases the static pressure and temperature and hence supports the reactions.

No numerical simulation is available for the previous system inside the combustion chamber used for the experiments, for which the shock structure has been

predicted analytically [11]. However, for the same entry Mach number, dictated by the same contour of the Laval nozzle, and the same apex half angle, a simple comparison of the struts can be done by superposing the cross section of an older strut to the simulations of Figure 4.3. While a full comparison of both flow fields cannot be supported by the suggested approach, the shock at the leading edge and its first reflection can be compared fairly well and show that the leading edge shock (I) does not reflect onto the side of the strut, as was predicted analytically. Instead, the reflected wave (II) impinges at the location where the laser spark was focused to ignite the pilot mixture (about 5.8mm downstream of the trailing edge [11]). The previous and present locations of the ignition spark have been represented as stars downstream of each strut in Figure 4.4; the red strut is the 3mm thick Injector1 used in the previous investigations.

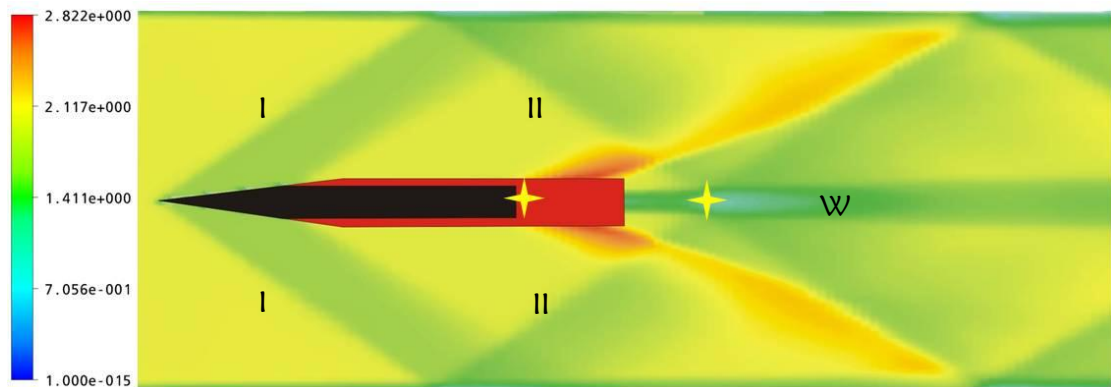


Figure 4.4 Superposition of the Injector1 (3mm, red) to Strut 1, with laser sparks locations.

For the previous configuration the reflected shock wave (II) impinges onto the focal spot in such a way that it disruptively interacts with the circular shock waves generated at the latter when the medium undergoes optical breakdown. Under such conditions, the mechanism of plasma formation becomes less effective and the growth of the flame kernels is likely disturbed by the interaction of the shock waves. Hence, the kernel is either destroyed by the impinging shock or is prevented from reaching its critical size before being entrained into, and accelerated by, the surrounding flow where the residence time and the temperature are too low to achieve ignition. The introduction of the circular flame holder in the wake confined the mixture in the region around the focal spot, allowing sufficient time for the flame kernel to grow sufficiently to initiate the reaction. Further, the presence of the flame holder may have supported mixture ignition due to the effect of small metallic particles released in the

focal spot, similar to the thermal ignition mechanism in which an ablative target absorbs the laser energy and then transfers it to the mixture [40].

Based on these considerations, the new designs have significantly shorter struts to guarantee that the focal spot for ignition is not affected by the reflected shock wave (II). This is shown for the black strut in Figure 4.4. With this configuration, optical breakdown of the mixture occurs successfully for all stoichiometrically suitable conditions with both Strut 1 and Strut 3. The plasma spark heats the sonic jets of hydrogen and oxidizer initially at ambient temperature and supports the formation, and growth, of flame kernels. Once the reaction is initiated in a small portion of the mixture inside the wake the ignition kernels move downstream, mix both within the wake and with the external flow at the interface until they cross the reflected shock wave. This further increases the static pressure and temperature and hence supports completion of the reactions. Thus a self-sustaining pilot flame can be stabilized without the aid of additional flame holders.

Although no total pressure measurements are available at the combustor exit for Injector1 and Injector2, both the lower aerodynamic blockage of the new struts and eliminating the flame holder are assumed to reduce the total pressure losses. Further, the greater wetted area (WA) of the previous injectors provided a significant contribution to the skin friction drag, and hence to the total pressure losses inside the combustor. A first-approximation comparison of the expected skin friction drag reduction has been performed assuming that the dynamic pressure and the friction coefficient are constant among the four struts and can be expressed as

$$D_{sf} = \frac{1}{2} \rho V^2 C_{Dsf} WA \quad \text{Equation 4.1}$$

the skin friction reduction will be direct proportional to the reduction of the wetted area, which is twice the side area of each injector. The results have been corroborated by comparing the total pressure losses for the three struts analysed in the course of the present study. The experimental data refer to the total pressure loss across the combustion chamber for each strut under "Fuel-Off" conditions (averaged over three tests). Lower friction drag is expected to be coupled with lower total pressure losses and vice versa. Table 4.1 summarizes the data for Injector1, Strut 1, Strut 2 and Strut 3. The variation of wetted area, skin friction drag and total pressure losses are referred to Strut 1: an increase with respect to the values for Strut 1 is denoted by a plus, a reduction by a minus.

| Strut [-] | WA [cm ²] | Δ WA [%] | Δ D _{sf} [%] | Δ p _{tot} [MPa] | Δ p _{tot} [%] |
|--------------|--------------------------|--------------------|---------------------------------|------------------------------------|----------------------------------|
| Injector1 | 16.2 | +23.5 | +23.5 | NA | NA |
| Strut 1 | 12.4 | - | - | 0.36 | - |
| Strut 2 | 10.6 | -14.5 | -14.5 | 0.12 | -67.5 |
| Strut 3 | 10.1 | -18.5 | -18.5 | 0.19 | -46.2 |

Table 4.1 Comparison of Injector1 [11], Strut 1, Strut 2 and Strut 3 in terms of aerodynamic performance.

In general, a reduction in wetted area and, thus, skin friction drag is reflected by a lower total pressure loss across the combustor, which confirms the expected trend and supports the conclusion that the total pressure losses of the new injectors are lower than the previous ones. It should be noted that this is without taking into account the contribution of the cylindrical flame holder, which would also be anticipated to increase the losses. The apparent inconsistency in the total pressure losses between Strut 2 and Strut 3 can be explained in terms of other geometric features of the injector. While the trailing edge of Strut 2 is aerodynamically shaped to promote vortex shedding and to ease the entrainment of the low speed wake into the surrounding supersonic flow, the recess at the trailing edge of Strut 3 creates a stable recirculation zone, with two bubbles at the corners that extend the flow residence time. Therefore, the flow in the wake behind Strut 2 will be accelerated quickly and recover more kinetic energy before leaving the combustor. Conversely, the flow in the wake of Strut 3 will leave the combustor at a lower speed, leading to a higher total pressure loss. Compared to Strut 1, even though the recessed trailing edge of Strut 3 still represents a penalty due to the recirculation bubbles, the positive effect of the smaller wetted area and lower skin friction drag are predominant.

Before addressing the extensive results concerning the stabilization of the pilot flame with the different struts the overall static pressure distribution is analyzed based on the "Fuel-Off" case, in order to provide an insight into the aerodynamic phenomena occurring in the combustor. Figure 4.5 shows the basic wall static pressure distribution along the combustor for the three struts; p_3 is measured in the Laval nozzle. In general, the first p_{wall} peak is caused by the shock at the strut leading edge, while the second and third peaks are due to shock reflections. In the diverging module the supersonic flow expands and p_{wall} decreases, except for p_{11} and p_{14} , again due to shock reflections. At these taps the p_{wall} rise becomes lower as the shocks weaken.

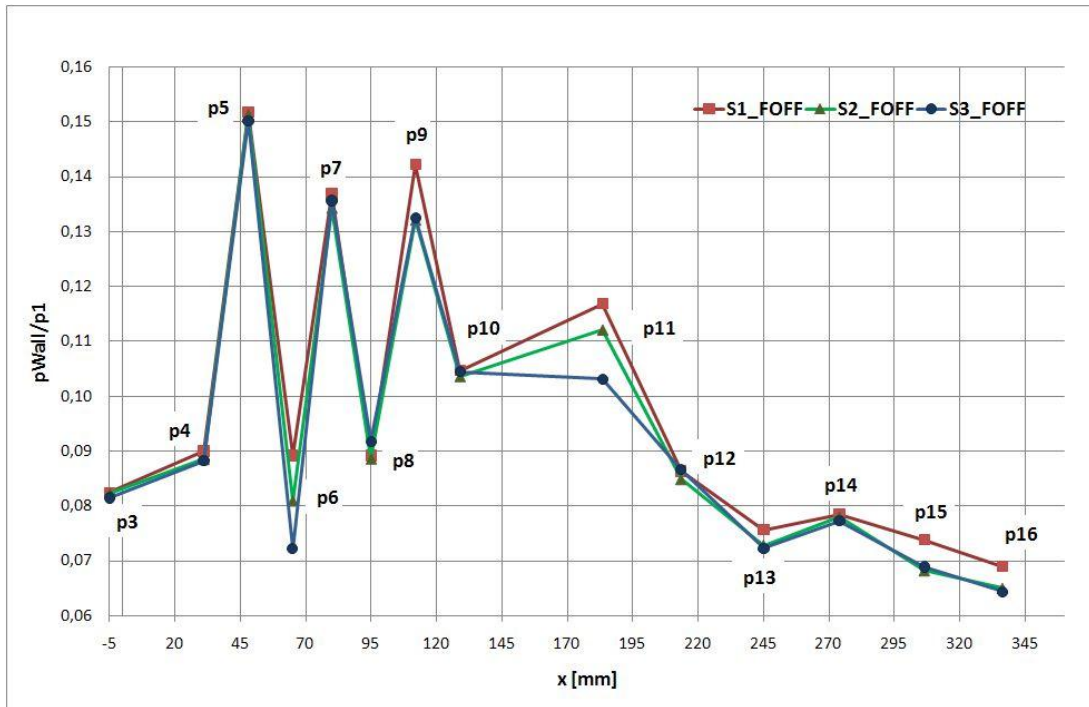


Figure 4.5 Wall static pressure distribution for the three struts (S1, S2 and S3) under Fuel-Off conditions.

The wall static pressure distribution for the three struts is similar, since the initial shock at the leading edge remains unchanged for the same inlet boundary conditions. The different readings of sensors 6, 9 and 11 are due to differences in the shock reflections downstream of the trailing edge, whose geometry influences the development of the wake. In particular, the wedge shaped and recessed trailing edge of Strut 2 and Strut 3, causes the flow to expand earlier than for the configuration with Strut 1 and, hence, p_6 is significantly lower. The expansion is at a maximum for Strut 3 and leads also to the lower value of p_{11} , since it reduces the strength of the shock reflections in the divergent.

4.1.1 Strut 1

In an early series of experiments, the ignitability of pure methane in air has been tested with Strut 1 for a pilot equivalence ratio, Φ_p , ranging between 2.6 (the lowest possible at the time) and 14.4. A successful ignition was not recorded, likely due to the combination of two factors: the mixture being too rich and the temperature of the injected methane being too low, both of which affects the growth of the flame kernels in the ignition zone. Although the intensity of the laser spark is sufficient to cause optical breakdown, the flame kernels growth is prevented by the impingement of the cold methane jets undergoing expansion to sonic conditions prior to injection. The

temperature of the methane injected axially through the series of holes B (Figure 3.8) is typically between 210K and 220K (no pre-heating system could be implemented in the pilot methane line). Investigation of leaner mixtures would have required the use of pilot oxygen, which was not available during these early experiments and further tests with methane as pilot fuel have not been carried out due to time constraints. However, the results obtained for hydrogen suggest that it might be possible to achieve successful ignition of methane if stoichiometric conditions are established in the pilot mixture. Further, pre-heating of the pilot methane should be beneficial and rig modifications are recommended to determine whether it would be possible to operate the combustor using only one type of fuel.

Next, a dedicated series of tests has been conducted with Strut 1 to assess mixture ignitability and flame stabilization for different values of Φ_p . First, hydrogen has been injected alone and then together with either air or oxygen as an oxidizer. The amount of gases injected was increased in a stepwise manner and ignitability maps have been populated.

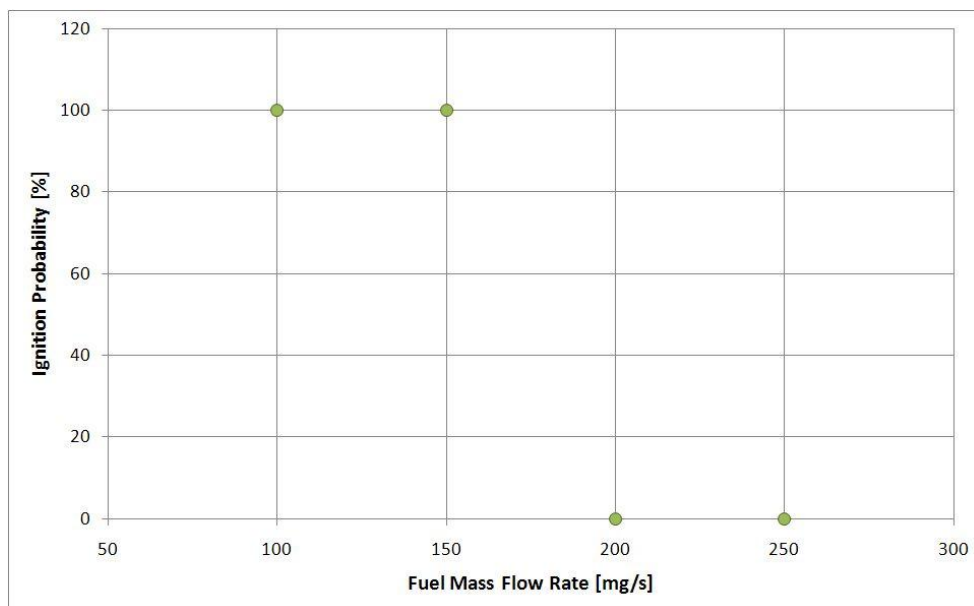


Figure 4.6 Ignition probability for injection of pilot hydrogen as a function of the fuel mass flow rate.

Figure 4.6 shows the ignition probability for the injection of pilot hydrogen alone. Successful ignition is achieved only as long as the amount of air entrained into the pilot zone from the surrounding supersonic flow is sufficient to guarantee stoichiometric conditions in the pilot region. For higher fuel mass flow rates the mixture is too rich to be ignited.

With the addition of pilot oxidizer it was possible to ignite both H₂-O₂ and H₂-Air flames in the ranges of Φ_p under investigation. However, the variation from rich to very rich conditions leads to less reliable or even to no ignition particularly for the H₂-Air case. This behavior is similar to the trend for hydrogen alone and to the results for the CH₄-Air mixture. The ignition probability for the H₂-Air and H₂-O₂ mixtures are plotted as a function of the pilot equivalence ratio in Figure 4.7 and Figure 4.8, respectively.

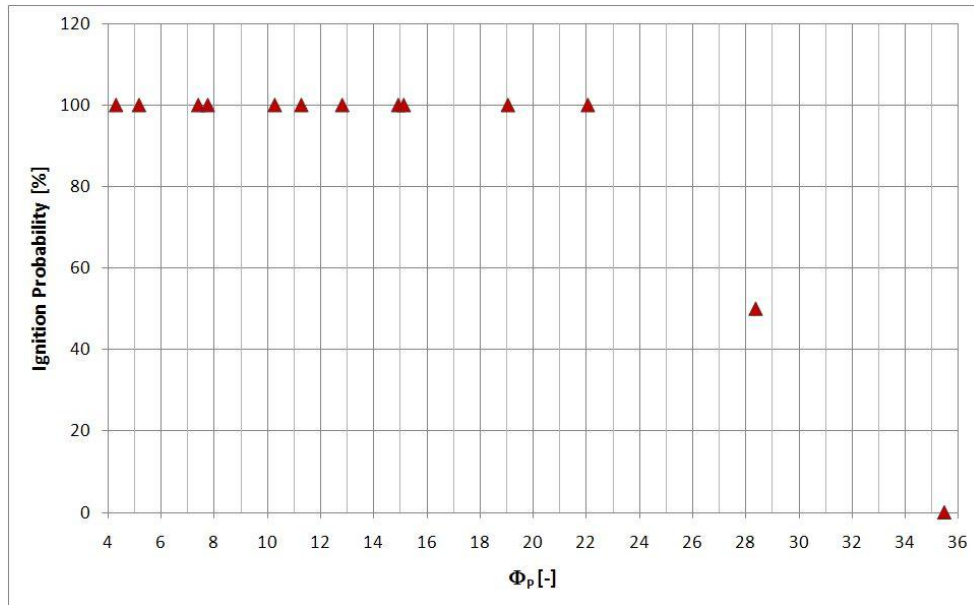


Figure 4.7 Ignition probability for the pilot H₂-Air mixture as a function of the pilot equivalence ratio.

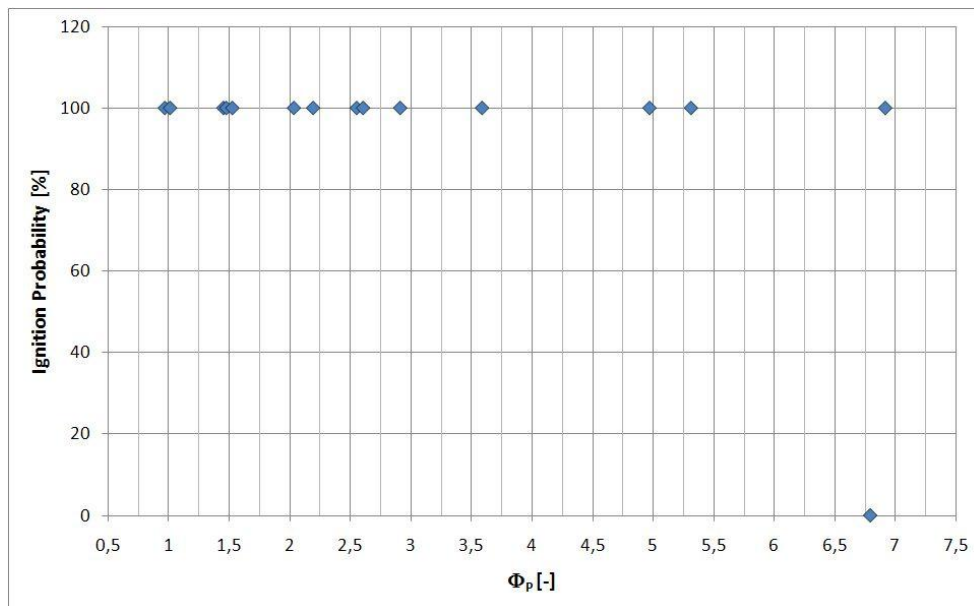


Figure 4.8 Ignition probability for the pilot H₂-O₂ mixture as a function of the pilot equivalence ratio.

Once ignited, both flames are stable over a broad operation range and the wall static pressure distributions in Figure 4.9 indicate similar combustion modalities. The exception is the somewhat higher static pressure level for the H₂-O₂ flame, which reflects a higher combustion heat release. The first portion of the two flames in the constant cross-area section of the combustor is photographed and shown from the top in Figure 4.10.

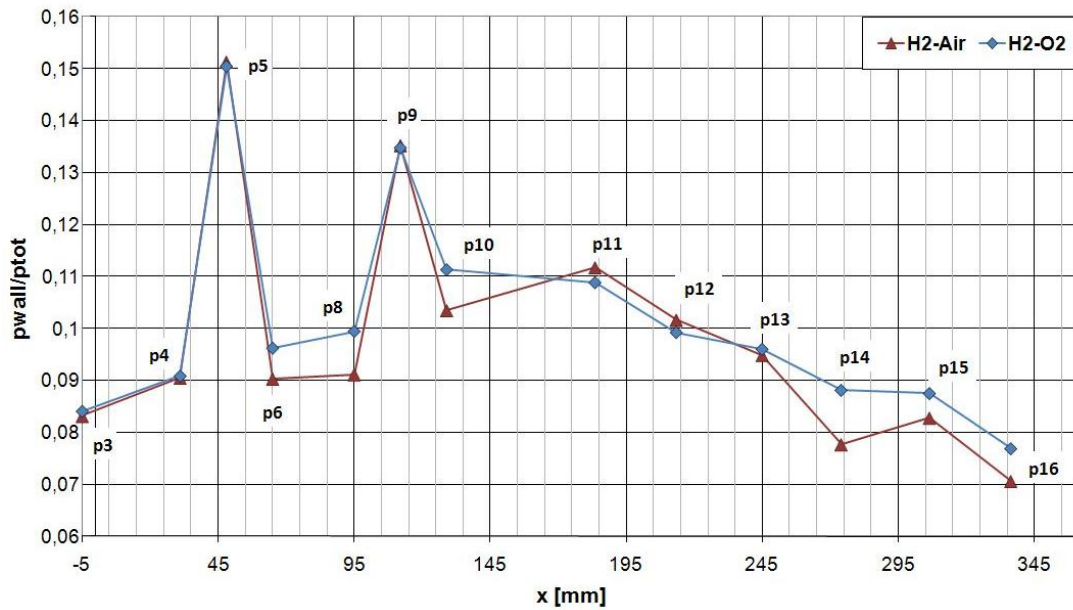


Figure 4.9 Comparison of the wall static pressure distribution for combustion of the H₂-Air (triangles) and H₂-O₂ (diamonds) pilot flames, each at $\Phi_p = 7^3$.

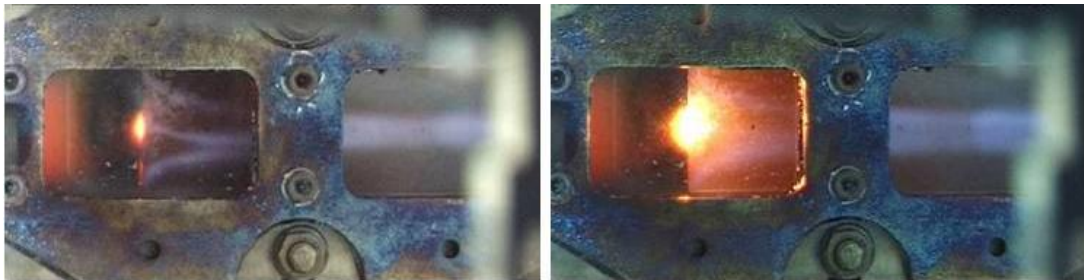


Figure 4.10 Top view of the H₂-Air (left) and H₂-O₂ (right) pilot flames behind Strut 1.

A first estimate of the heat released by combustion can be done from the gas sampling data, the exit Mach number and the total temperatures. Knowing the amount

³ Note that in this diagram p₇ is missing and thus only two pressure peaks appear in the constant cross-area section of the combustor. This is due to the fact that the combustion chamber has been modified at a later stage and the corresponding sensor has been added to increase the accuracy of the p_{wall} measurements. For consistency with the nomenclature, however, it was preferred to skip p₇ than to use a sequential labeling in Figure 4.9.

of hydrogen and oxygen supplied to the catalyst and using the results of the gas chromatographic analysis, the thermodynamic properties of the mixture have been determined at the combustor entrance prior to combustion. Similarly, the analysis of the gas samples collected during the corresponding combustion tests allowed the determination of the gas composition and the thermodynamic properties at the combustor exit for each flame. The specific heat of the mixture at constant pressure has been determined from the gas sampling data by entering the mixture composition in the Gordon-McBride code at the corresponding temperature. The static temperature can be calculated using the total-to-static relationship

$$\frac{T_{tot_in/out}}{T_{in/out}} = \left(1 + \frac{\gamma_{in/out}-1}{2} M_{in/out}^2 \right) \quad \text{Equation 4.2}$$

since the ratio of specific heats, the total temperature and the Mach number are measured at the combustor entrance and at the exit.

The energy equation has been applied to the combustion chamber considered as a closed system. The heat losses to the surroundings have been neglected due to the inaccuracy in determining the coefficients for natural convection to the surroundings from a one-point measurement of the combustor surface temperature.

The enthalpy balance across the combustor can be written as

$$\Delta H_{tot} = H_{tot_out} - H_{tot_in} = m_{out} c_{pout} T_{tot_out} - m_{in} c_{pin} T_{tot_in} \quad \text{Equation 4.3}$$

and is representative of the heat released during combustion of each pilot flame. Table 4.2 summarizes the conditions and the results for the two flames at $\Phi_p = 7$. The total temperature of the mixture before combustion can be determined using the data measured at the combustor entrance for the main air and the relationships for choked flow at the throat of a converging nozzle for the gases injected through the strut. Following this approach in presence of the pilot flames only, the abovementioned temperature is given by

$$\begin{aligned} & (\dot{m} \cdot c_p \cdot T_{tot})_{Main_Air} + (\dot{m} \cdot c_p \cdot T_{tot})_{P_H2} + (\dot{m} \cdot c_p \cdot T_{tot})_{P_Air/P_O2} = \\ & = \dot{m}_{in} \cdot c_{pin} \cdot T_{tot_in} \end{aligned} \quad \text{Equation 4.4}$$

where \dot{m}_{in} is the sum of the three mass flow rates supplied to the combustor. Note that the amount of pilot gases injected affects the total mass flow rate only to the third digit; therefore, no differentiation is done between m_{in} and m_{out} in Table 4.2, although the effective amounts are considered in the thermodynamic analysis. Also, the total

temperature of the main airflow is very close to the overall mixture temperature and is omitted in the table to favor its readability.

| Pilot Flame [-] | $m_{in/out}$ [kg] | $T_{tot_P_H2}$ [K] | $T_{tot_P_Air/P_O2}$ [K] | T_{tot_in} [K] | T_{tot_out} [K] | ΔH_{tot} [kJ] |
|--------------------------------|----------------------|-------------------------|--------------------------------|----------------------|-----------------------|--------------------------|
| H ₂ -Air | 0.35 | 363 | 351.0 | 1050.5 | 1030.6 | 15.3 |
| H ₂ -O ₂ | 0.35 | 363 | 280.5 | 1067.4 | 1131.5 | 50.0 |

Table 4.2 Combustion heat release for the H₂-Air and H₂-O₂ pilot flames at $\Phi_p = 7$.

The interaction of the aerodynamic phenomena with the thermodynamic effects due to combustion of the pilot flame is now discussed and the results are compared with those of the corresponding cold tests to quantify the effective combustion pressure rise. Figure 4.11 reports the "Fuel-Off", "Fuel-On" and "Combustion" wall static pressure distributions for a H₂-O₂ flame at $\Phi_p = 1.48$. The distributions for "Fuel-Off" and "Fuel-On" are only slightly different and it can be concluded that the effect of the momentum of fuel and oxidizer on the wall static pressure is limited. This is expected in the case of axial injection. In the presence of the combustion of the pilot flame the first sensors detect values matching those of the fuel-off case, i.e. no thermal choking occurs in the combustor. The higher level of p_6 is due to combustion heat release: the comparison to the cold test confirms only a 5% contribution of fuel injection to the total Δp . The higher level of p_{wall} and its decrease in the diverging section indicate supersonic conditions and the contribution of combustion heat release to the overall Δp_{11} and Δp_{12} is up to 96% and 95% respectively, and is about 74% for Δp_{13} . Disappearance of the p_{wall} peaks at taps 10 and 14 supports the conclusion that the combustion process now controls the shock reflections.

The combustion heat release, both its modality and its intensity, depend on the pilot equivalence ratio. Leaner mixtures than the one analyzed in Figure 4.11 show similar wall static pressure distributions, but slightly lower pressure levels. This suggests that it would be beneficial to increase Φ_p in order to increase the overall combustion efficiency. Both distributions of p_{wall} are plotted in Figure 4.12. However, an optimum value of Φ_p would be expected, which is related to both the amount of oxidizer entrained into the wake from the surrounding flow and the modality of heat release.

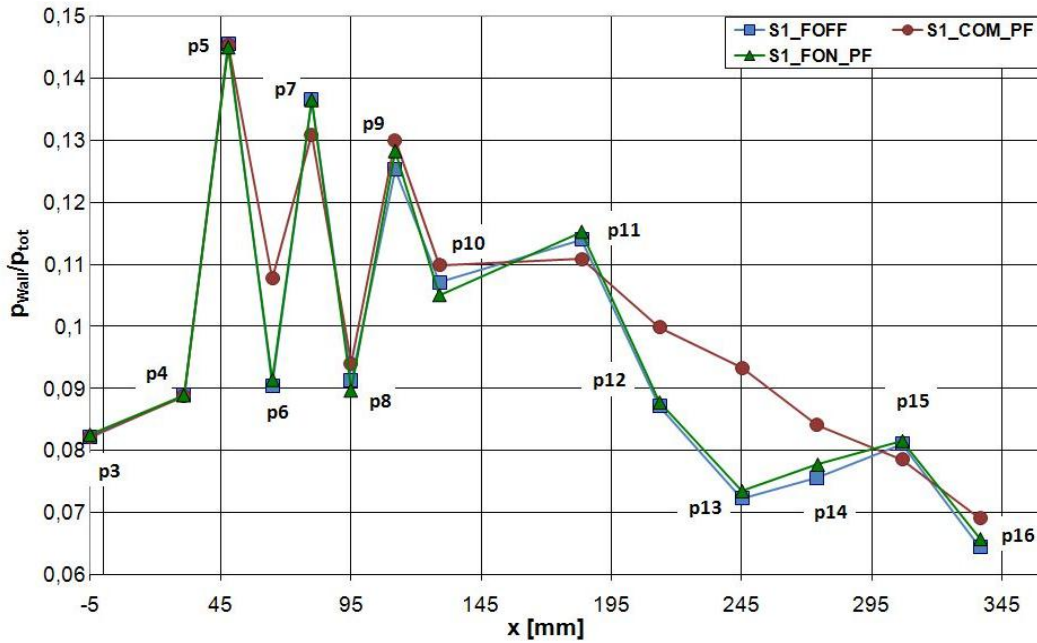


Figure 4.11 Wall static pressure distribution in the combustor for a H_2-O_2 flame at $\Phi_p = 1.48$; comparison of the Fuel-Off, Fuel-On and Combustion distributions.

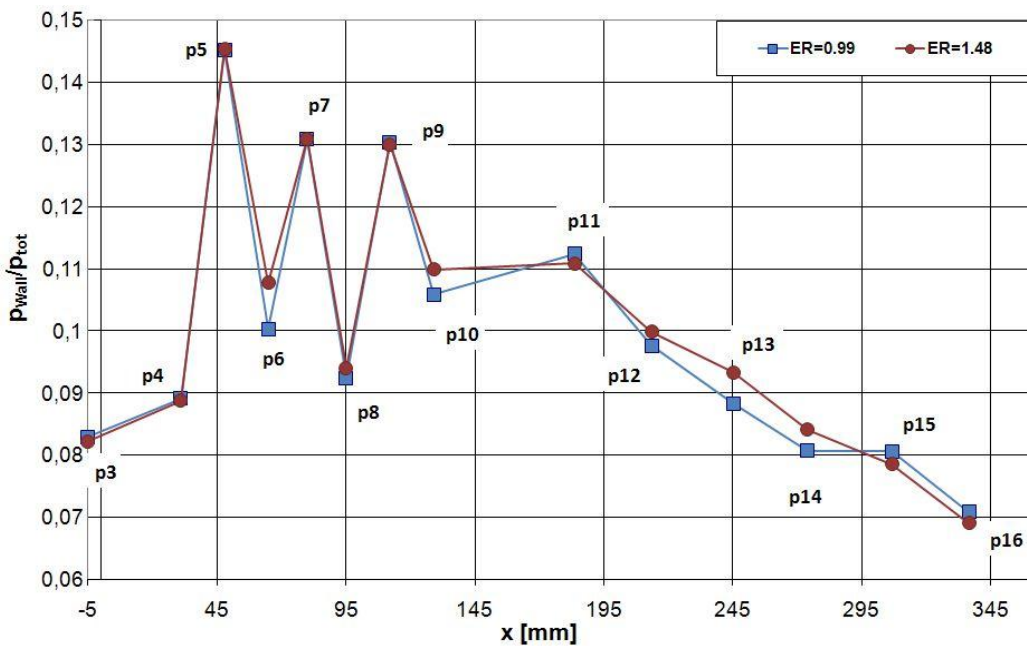


Figure 4.12 Comparison of the combustion heat release for H_2-O_2 pilot flames at different Φ_p (ER in the graphics).

Figure 4.13 shows the combustion heat release estimated from the total enthalpy difference across the combustor for increasing pilot equivalence ratio. Rich pilot flames can only burn completely if sufficient air is available from the surrounding flow to obtain stoichiometric conditions. As the maximum amount of air that can be entrained into the wake is dictated by the strut geometry and by the manner in which the wake

develops and interacts with the supersonic flow there is a limit to the amount of fuel that can be effectively burned beyond $\Phi_p = 1$, before ΔH_{tot} drops. However, for the present operating conditions the limit is not reached, and for pilot equivalence ratios greater than $4.5 \div 5$ the step increase in total enthalpy is indicative of a different combustion modality in which the heat is mainly released in the constant cross-area section of the combustor instead of in the divergent.

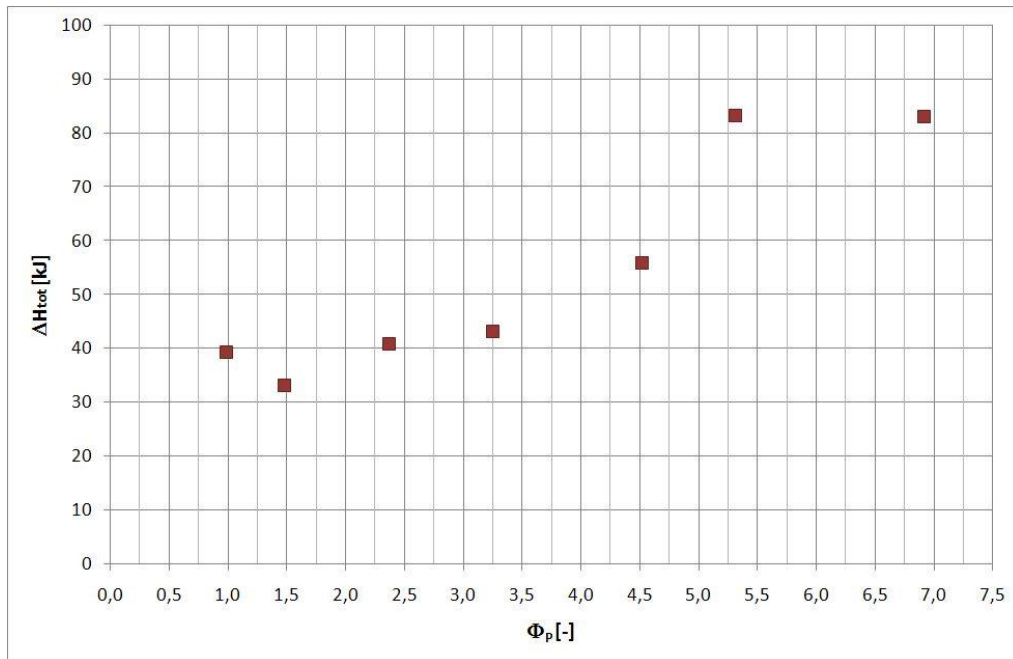


Figure 4.13 Combustion heat release for the pilot flame at increasing Φ_p .

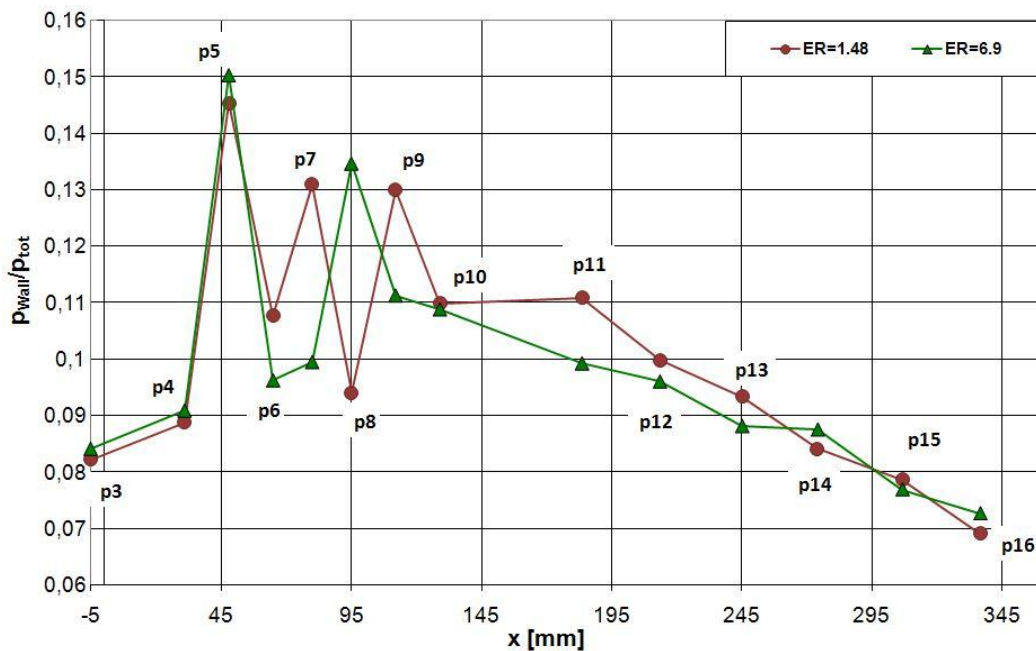


Figure 4.14 Comparison of the wall static pressure distribution for H_2-O_2 pilot flames at different Φ_p (ER in the graphics).

The wall static pressure distributions of Figure 4.14 shows a steep increase of p_8 instead of two pressure peaks at p_7 and p_9 and a lower p_{wall} level downstream of sensor 10 (where some pressure oscillations due to shock reflections again appear). More importantly, p_5 measured higher values and although the conditions in the combustor are still supersonic, the risk of thermal choking becomes higher due to the greater amount of injected fuel and oxidizer, which increases the aerodynamic obstruction and leads to more intense, abrupt combustion in the constant cross-area section.

The comparison of the different flames in terms of total pressure drop across the combustion chamber confirms substantially lower performance at higher pilot equivalence ratios. In addition the exit Mach number decreases from 1.91 for the stoichiometric flame to 1.78 for the flame at an $\Phi_p = 6.9$. Therefore, the optimal operative conditions are selected as a trade-off between obtaining a high heat release and controlling the combustion to avoid transition to subsonic conditions. This is best achieved by stabilizing the pilot flame at Φ_p between 1 and 2.5.

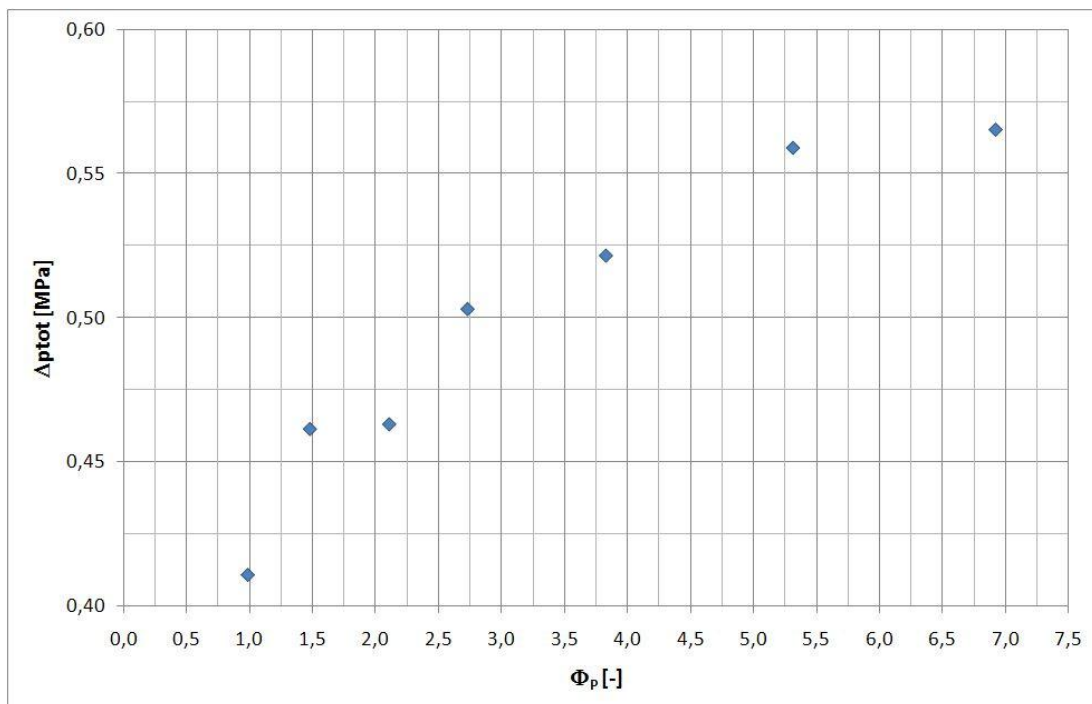


Figure 4.15 Total pressure drop across the combustion chamber at different Φ_p .

The analysis of the total pressure drop concludes the first part of the study of the H_2 -Air and H_2 - O_2 pilot flames with Strut 1. Further investigations have been carried out to assess what operative conditions of the pilot flame are best able to stabilize the

main supersonic flame. This will be presented in the chapter dedicated to the single-stage injection.

4.1.2 Strut 2

Strut 2 did not support ignition and stabilization of the pilot flame. The fuelling strategy originally foreseen and exemplified in Figure 4.16 was varied to investigate all possible combinations of fuel and oxidizer through the different holes provided for axial injection; however successful ignition has not been obtained.

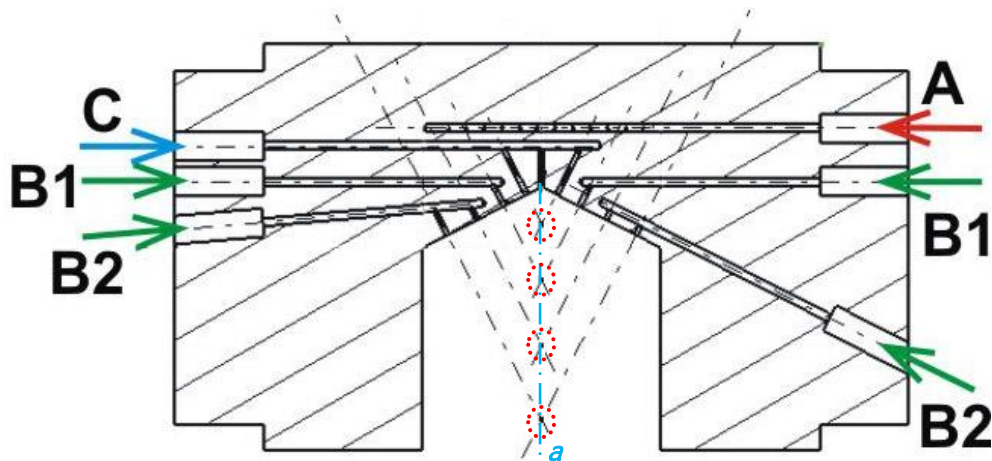


Figure 4.16 Section of Strut 2 with possible fuelling strategy for methane (A), pilot fuel (B1, B2) and pilot oxidizer (C).

The interaction of different factors led to this result. Firstly, and most importantly, none of the possible configurations allowed fuel and oxidizer to converge into a single spot. This was found to be critical to achieve mixture ignition. Ionization of non-premixed fuel or oxidizer in the laser focal spot sets free highly reactive radicals, and yet it is not sufficient to initiate combustion. The radicals are confined by the cold jets impinging behind the radical pool generated at the ignition location, which affects the mixing process. Even though the vortex shedding at the trailing edge promotes the entrainment of radicals, fuel and oxidizer into the main flow, no effective mixing occurs in the region of highest temperature and the reactions cannot be initiated. Further, the cooling effect of the injected gases freezes the radicals and inhibits the production of flame kernels. Thus, instead of favouring a homogeneous distribution of fuel and oxidizer, this injection strategy turned out not to be suitable to support stabilization of a pilot flame and has not been investigated further.

4.1.3 Strut 3

The pilot flame stabilization using Strut 3 led to similar results to those obtained using Strut 1. First, the wall static pressure distribution for a lean and a stoichiometric pilot flame stabilized with Strut 3 are analyzed and compared to the distribution at "Fuel-Off" conditions. Second, a comparison of the two struts in terms of wall static pressure distributions, combustion heat release and total pressure drop associated with a stoichiometric pilot flame is presented. Figure 4.17 shows the charts for Strut 3.

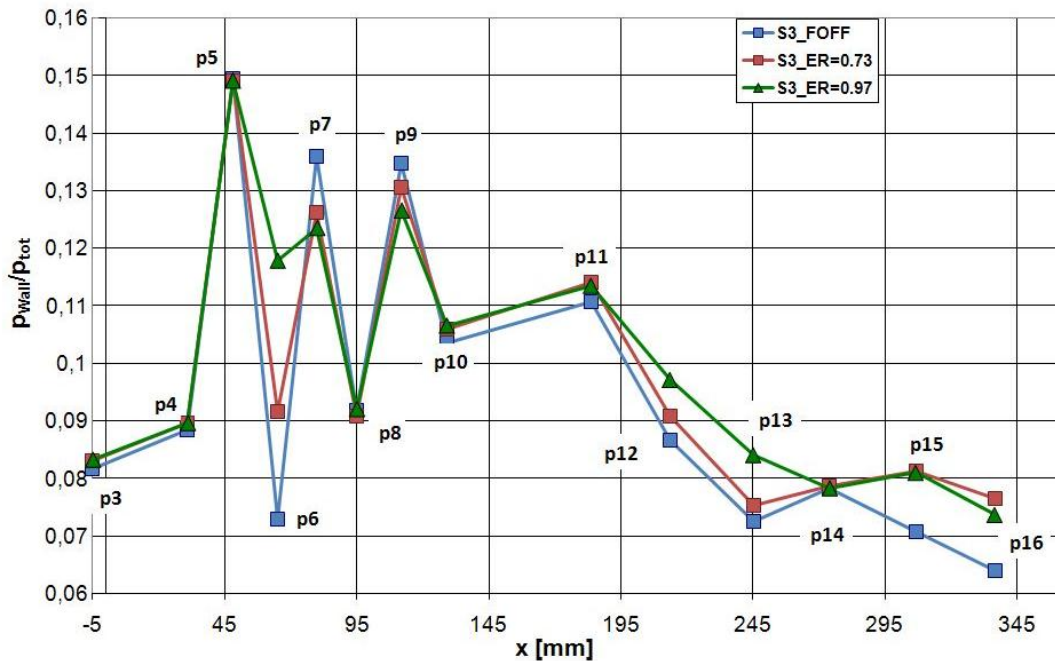


Figure 4.17 Wall static pressure distribution for pilot flames stabilized at different Φ_p (ER in the graphics) using Strut 3 and compared to the Fuel-Off condition.

The distribution for the pilot flame at $\Phi_p = 0.73$ is only slightly different than the basic aerodynamic one, with the higher p_6 indicating that the main combustion heat release occurs in the recess at the strut trailing edge. This is also corroborated by the presence of pressure peaks in the diverging section, typical indication of shock reflections, which suggests that aerodynamic effects still dominate and the flow field is not controlled by the combustion process as was the case for Strut 1. Further, analysis of the Planar Laser Induced Fluorescence measurements at the four axial stations corresponding to the combustor windows downstream of the strut confirms no detection of OH radicals downstream of the constant cross-area section. This confirms that the higher levels of pressure of p_{15} and p_{16} are not due to combustion heat release, but rather to reflected shock waves.

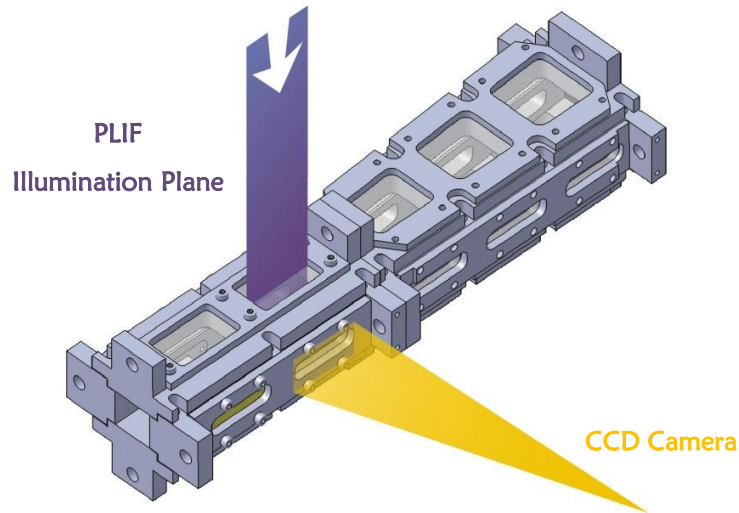


Figure 4.18 Illumination plane and camera setup for the PLIF measurements in the combustor.

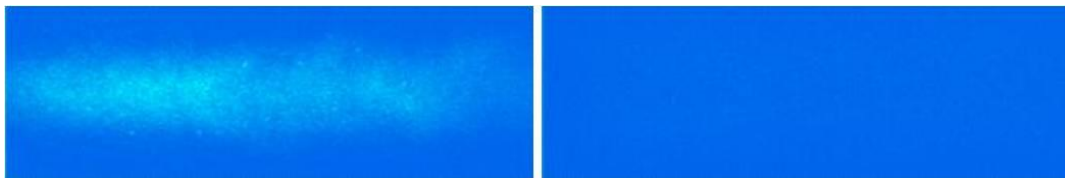


Figure 4.19 OH[·] PLIF of the H₂-O₂ pilot flame at $\Phi_p = 0.97$ in the first (left) and second (right) window downstream of Strut 3.

The last conclusion is valid also for the p_{wall} distribution of the pilot flame at $\Phi_p = 0.97$, as visible in the OH[·] PLIF of Figure 4.19. Figure 4.18 shows the illumination plane and the camera perspective with respect to the combustion chamber. In this case the static pressure increase due to combustion is significantly higher than for the leaner flame, particularly at p_6 . However, the enthalpy balance based on the temperature measurements highlights only a minor difference between the two cases, i.e. 55kJ for the richer flame against 57.2kJ for the leaner and no conclusion on which pilot condition is most suitable can be drawn so far.

The pilot flame stabilized at $\Phi_p = 0.97$ with Strut 3 is compared to the case of a near stoichiometric pilot flame stabilized with Strut 1. The corresponding wall static pressure distributions are plotted in Figure 4.20 and a view of both flames in the combustor is shown in Figure 4.21. Again, the heat release occurs further upstream for Strut 3. It is believed that the recess at the trailing edge creates a recirculation region that acts as aerodynamic flame holder for the mixture. Conversely, the straight trailing edge of Strut 1 does not provide such a stable zone and combustion takes place further

downstream, as indicated by the higher levels of p_7 and p_9 and by the slightly higher p_{wall} in the diverging section.

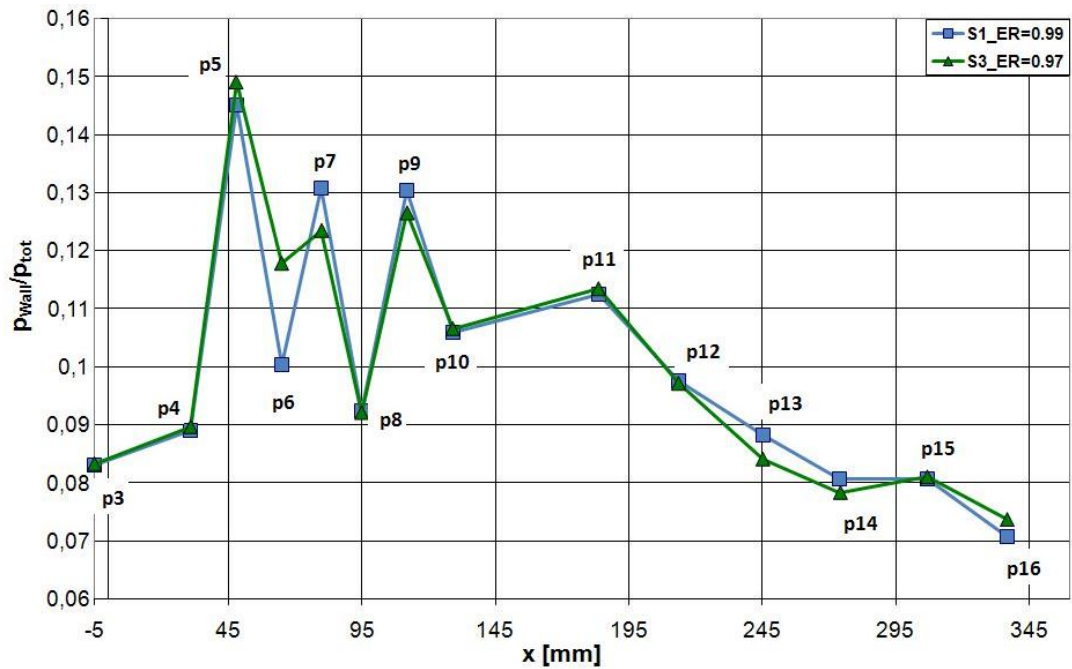


Figure 4.20 Wall static pressure distribution for combustion of a near stoichiometric pilot flame with Strut 1 (squares) and with Strut 3 (triangles).



Figure 4.21 Near stoichiometric pilot flames stabilized with Strut 1 (left) and with Strut 3 (right).

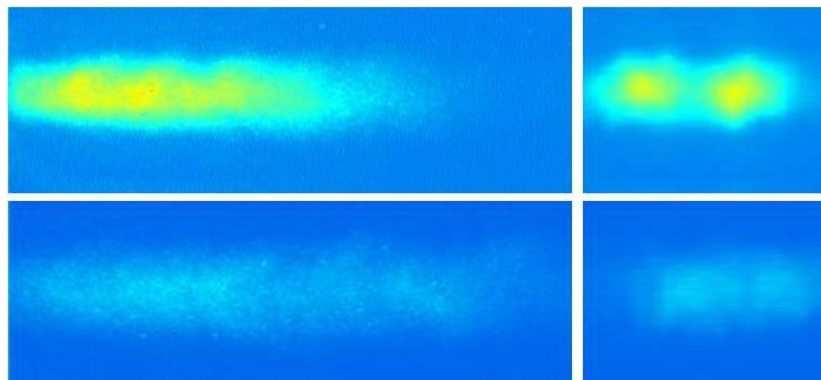


Figure 4.22 OH- PLIF downstream of the injector for a near stoichiometric pilot flame with Strut 1 (top) and with Strut 3 (bottom).

The comparison of the OH- PLIF measurements for the two flames also shows more intense combustion in the region visible behind the injector with Strut 1. It should

be noted that the highest concentration of radicals for Strut 3 will be found in the recirculation zone, which is not optically accessible for PLIF measurements. The PLIF results are compared in Figure 4.22. The images on the left are averaged over ten direct measurements on the (x,z)-plane. The pictures on the right are the corresponding images on the (y,z)-plane is interpolated by the acquisition software.

In terms of overall performance, the presence of a flame holding recirculation zone increases the total pressure drop across the combustor compared to Strut 1. However, the Mach numbers at the combustor exit are comparable, and the overall total enthalpy increase is higher for Strut 3 (Table 4.3). The next step is to assess whether both struts would be equally suitable to stabilize the main supersonic flame and under which operative conditions of the pilot flame.

| Strut [-] | Φ_p [-] | ΔH_{tot} [kJ] | Δp_{tot} [MPa] | M_{Exit} [-] |
|--------------|-----------------|--------------------------|---------------------------|-------------------|
| Strut 1 | 0.99 | 39.3 | 0.41 | 1.91 |
| Strut 3 | 0.97 | 57.2 | 0.55 | 1.97 |

Table 4.3 Performance comparison of the near stoichiometric flames stabilized with Strut 1 and Strut 3.

4.1.4 Conclusion

The stabilization of a pilot flame in the wake of a central injector has been extensively investigated for three different strut geometries. All geometries proved to improve the aerodynamic performance of the central injection system compared to the configurations used in previous studies [11]. Early investigations of a methane pilot flame did not lead to successful ignition due to test bed constraints on the maximum amount of oxidizer available and on the fuel injection temperature. Strut 1 and Strut 3 stabilized a hydrogen pilot flame using either oxygen or air as pilot oxidizer. No additional flame holder was needed to support ignition of the pilot flame, as the new injectors have been designed and succeeded to optimize the ignition location with respect to the shock structure established in the combustor. The performance of the H₂-Air and H₂-O₂ pilot flames are comparable at the same equivalence ratio; lean or stoichiometric flames with either oxidizer lead to a smooth combustion mode, thus limiting the total pressure losses. Due to Strut 1's trailing edge geometry the pilot flames are stretched further downstream in the combustor which favours mixing and increases the ignition area at the interface to the main supersonic flow. The trailing edge geometry of Strut 3 accentuates the flame holding behaviour and reduces the axial

extension of the flame. Although the total pressure drop is slightly higher, such geometry allows stabilizing leaner flames and is less sensitive to variations of the surrounding flow field. Strut 2 did not provide the expected results. A successful ignition was not obtained. This is believed to be due to the lack of a common impingement spot for fuel and oxidizer at the ignition location.

4.2 Supersonic Flame Stabilization with Single-Stage Injection

The pilot flames have been further studied as ignition and stabilization sources for the main methane flame using both Strut 1 and Strut 3. Methane has been injected after establishing stable combustion of the pilot flame at different values of the pilot equivalence ratio. Lean to rich pilot mixtures have been investigated to find the optimal operating conditions. The mixture ratio in the pilot zone turned out to be a key factor in the overall combustion stabilization process. As highlighted in the dedicated chapter, rich pilot flames require entrainment of sufficient air from the surrounding supersonic flow to burn stably. At $\Phi_p > 1$ injection and ignition of methane lead to a lack of oxidizer in the pilot flame region. Air is no longer entrained from the main airflow, and both the pilot and the supersonic flames are blown off. Thus, near stoichiometric conditions are necessary to guarantee stable combustion of the pilot and main flames. Higher air mass flow rates would be needed to reach $\Phi_p = 1$ for the H₂-Air case. However, due to the test bed constraints mentioned in Section 3.2.3, they could not be provided during the present study and further tests have been carried out only with H₂-O₂ pilot flames. Direct comparison of Strut 1 and Strut 3 has been performed using a near stoichiometric pilot flame and by increasing the amount of injected methane. In addition, the supersonic flame stabilization has been investigated for a richer pilot flame using Strut 1, which was found to promote higher mass exchange between the wake and the surrounding flow. Conversely, given the flame holding characteristics of Strut 3, the latter has been also studied using a lean pilot flame as an ignition source for the different methane flames. Table 4.4 summarizes the testing conditions for which the results will be discussed.

| Strut [-] | Φ_p [-] | \dot{m}_{CH_4} [g/s] | T_{CH_4} [K] | T_{totCH_4} [K] | Labelling [-] |
|--------------|-----------------|---------------------------|-------------------|----------------------|------------------|
| Strut 1 | 0.99 | 1.5 | 440 | 520 | S1_CH4_1 |
| | | 3 | | | S1_CH4_2 |
| | | 4.5 | | | S1_CH4_3 |
| Strut 1 | 1.48 | 1.5 | 440 | 520 | S1_CH4_4 |
| | | 3 | | | S1_CH4_5 |
| | | 4.5 | | | S1_CH4_6 |
| Strut 3 | 0.73 | 1.5 | 440 | 520 | S3_CH4_1 |
| | | 3 | | | S3_CH4_2 |
| | | 4.5 | | | S3_CH4_3 |
| Strut 3 | 0.97 | 1.5 | 440 | 520 | S3_CH4_4 |
| | | 3 | | | S3_CH4_5 |
| | | 4.5 | | | S3_CH4_6 |

Table 4.4 Summary of the testing conditions for main flame stabilization with Strut 1 and Strut 3.

In general, both struts supported stabilization of the main methane flame under different conditions. However, the amount of injected methane could not be increased over a certain threshold. As it is visible in the images of Figure 4.23, increasing the fuel mass flow rates leads to a shorter flame. Furthermore, analysis of the exhaust gases shows that a higher amount of CH_4 remains unburned. The gas sampling probe has been placed at different positions along the y-axis at the combustor exit and the results show that, depending on the operative conditions, either the combustion products or the unburned methane are confined to the middle of the supersonic stream. This indicates a low mixing level in the (y,z)-plane between the fuel and the supersonic air. All experimental data (observation of the flame structure, gas sampling results and total conditions at the combustor exit) suggest a stratification of the combustor flow. In the central layer, i.e. inside and close to the strut wake, the fuel-air mixture is homogenous and the combustion rather strong; this flow leaves the combustor at a Mach number ranging from 1.63 to 1.93, depending on the injector and on the equivalence ratio, Φ . At higher Φ the combustion process is rather incomplete, the flame is shorter and the flow behind it is easier to accelerate from the surrounding flow, which leads to higher M_{Exit} . The next layer is basically air with little or no fuel. Finally, the most external stratum consists of the boundary layer flow.

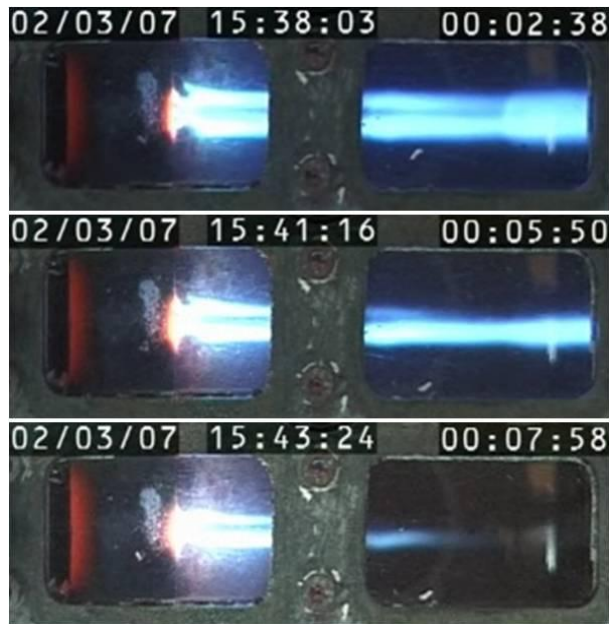


Figure 4.23 Supersonic flame stabilization with Strut 1 at $\Phi_p = 0.99$ with 1.5g/s (top), 3g/s (middle) and 4.5g/s (bottom) methane injected through the strut sides.

The central and outer layers are compared for Strut 3 in terms of total pressure drop and exit Mach number in Figure 4.24 and Figure 4.25. As discussed above, the central layer, in which combustion occurs, is characterized by a higher total pressure drop and by lower Mach numbers at the exit of the combustor. No measurement of the total conditions has been performed in the boundary layer.

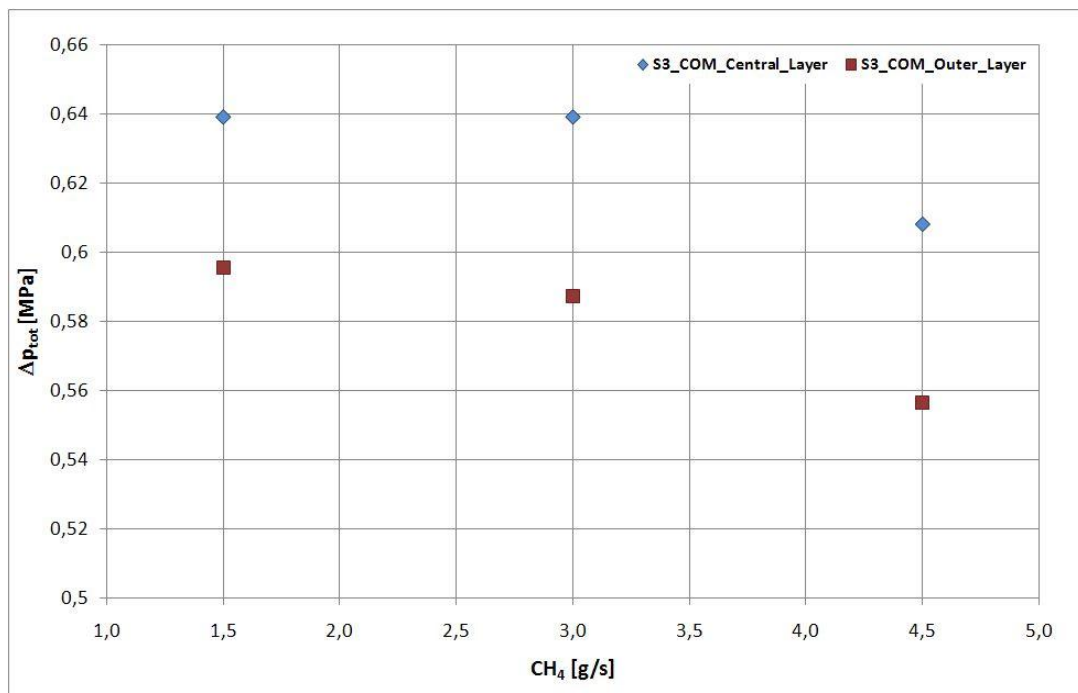


Figure 4.24 Total pressure drop across the combustor with Strut 3 for increasing amount of injected methane.

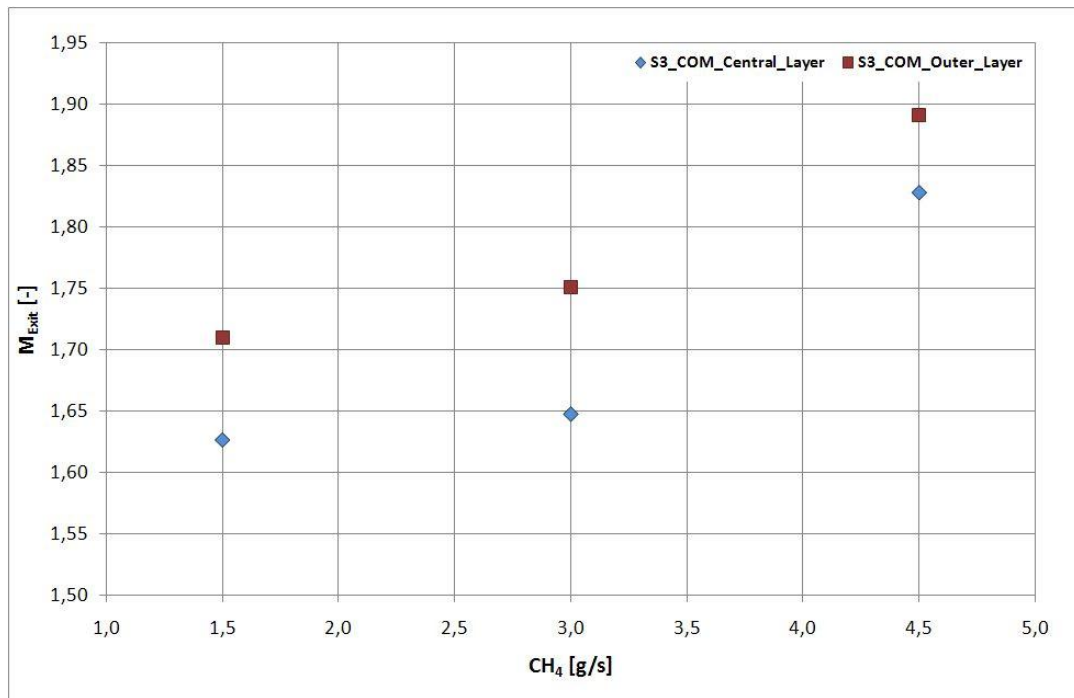


Figure 4.25 Mach number at the combustor exit with Strut 3 for increasing amount of injected methane.

A more detailed insight into the supersonic flame stabilization with each strut will be provided in the following chapters. However, the general effect of injecting fuel normal to the main airflow will be analysed first, using a comparison between the wall static pressure distribution at "Fuel-Off" and "Fuel-On" conditions. Figure 4.26 shows the corresponding diagram for injection of 4.5g/s methane using Strut 1 and the richer pilot flame, as listed in the summary of Table 4.4. The effect of fuel injection is particularly evident under such conditions, but the same behaviour is detected also when less fuel is injected. The general trend is similar for Strut 3, which will not be commented here; the differences are due to the peculiarities of the basic aerodynamic fields for each strut.

Unlike axial injection, the effect of normal fuel injection on the wall static pressure distribution is significant. In particular, the level of p_5 downstream of the injection holes is much higher due to the increased aerodynamic blockage at this location. Still, the unvaried readings of the sensors 3 and 4 indicate that the higher blockage does not cause transition to subsonic conditions. The higher level of p_{Wall} at tap 9 and in the diverging section also confirms the substantial contribution of the injected fuel mass to the overall pressure level and will be considered when analysing the effective pressure rise due to combustion of the supersonic flame.

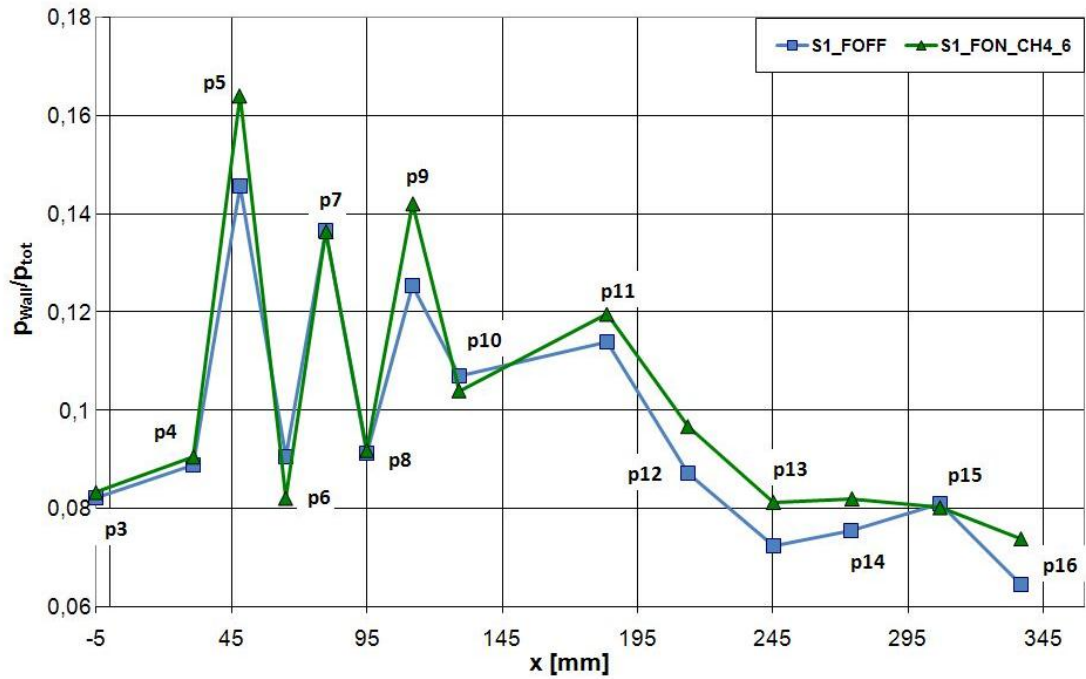


Figure 4.26 Wall static pressure distribution for injection of 4.5g/s methane with Strut 1. Φ_p is equal to 1.45.

As for the pilot flame, the energy balance can be applied to determine the heat released by combustion of the different methane flames. In this case, the contribution of the methane has to be accounted for to determine the total temperature of the mixture before combustion:

$$\begin{aligned}
 & (\dot{m} \cdot c_p \cdot T_{tot})_{Main_Air} + (\dot{m} \cdot c_p \cdot T_{tot})_{H_2} + (\dot{m} \cdot c_p \cdot T_{tot})_{O_2} + \\
 & + (\dot{m} \cdot c_p \cdot T_{tot})_{CH_4} = \dot{m}_{in} \cdot c_{pin} \cdot T_{tot_in}
 \end{aligned}
 \tag{Equation 4.5}$$

4.2.1 Strut 1

The presence of a stable pilot flame guarantees immediate ignition of the supersonic flame when methane is injected. The general differences between combustion of the pilot and the main flames are highlighted by the wall pressure distributions of Figure 4.27, where the leanest methane flame is plotted against the stoichiometric pilot flame. The curve relating to methane combustion shows a higher p_5 level. However, as explained in the previous section, this pressure peak is mainly due to mass injection and analysis of the measurements under "Fuel-On" conditions at this location confirms a contribution of less than 10% provided by the heat release to the total pressure rise. Compared to the pilot flame, for both the Φ_p considered and independent of the amount of injected methane, the combustion heat release of the

supersonic flame is shifted further downstream: p_6 is lower, while p_7 and p_8 are only slightly different. This suggests that, although the CH_4 already reacts behind the strut, combustion in this zone occurs in a weak regime and becomes stronger only further downstream in the divergent section. Thus, no thermal choking occurs and the process takes place under supersonic conditions, which is also confirmed by the Mach numbers measured at the combustor exit and reported in Table 4.5. Unlike for the pilot flame, combustion does not control the aerodynamics and the p_{wall} peaks are detected again, although shifted and weaker compared to the "Fuel-Off" case.

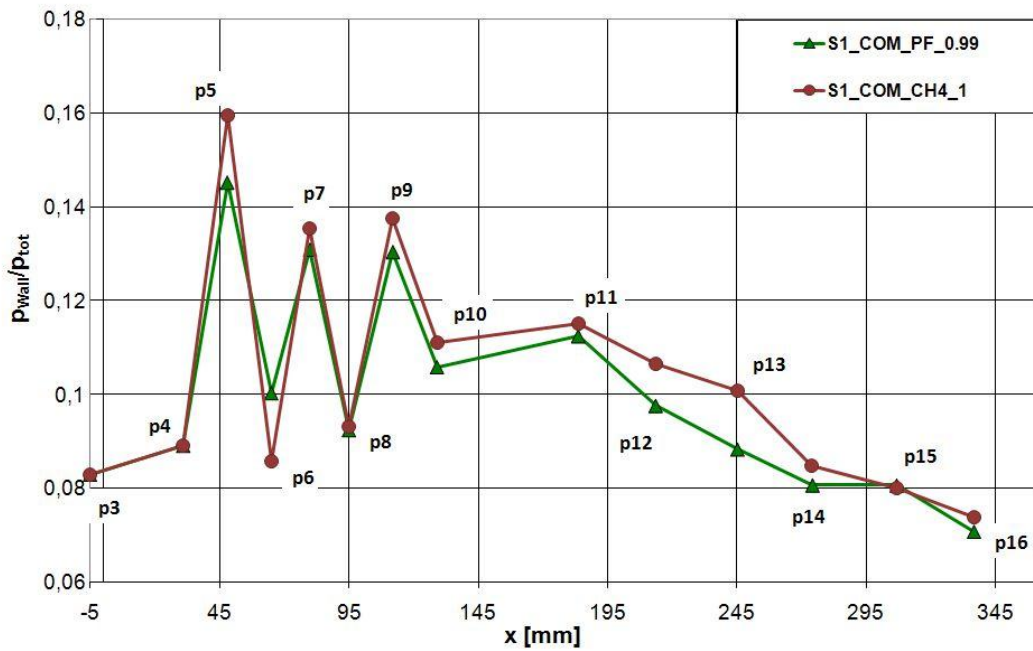


Figure 4.27 Wall static pressure distribution for combustion of a near stoichiometric pilot flame and of a lean supersonic methane flame using Strut 1 (1.5g/s CH_4).

Figure 4.28 shows the wall static pressure distribution for combustion of 1.5g/s methane, stabilized with the two different pilot flames at $\Phi_p = 0.99$ and $\Phi_p = 1.48$, respectively. The wall static pressure distributions are very close, which supports the conclusions on the general trends discussed above. However, the performance analysis indicates more effective combustion when the richer pilot flame is used as an ignition source. For comparable exit Mach numbers, the combustion heat release is higher and the total pressure drop is lower, as listed in the first two rows of Table 4.5.

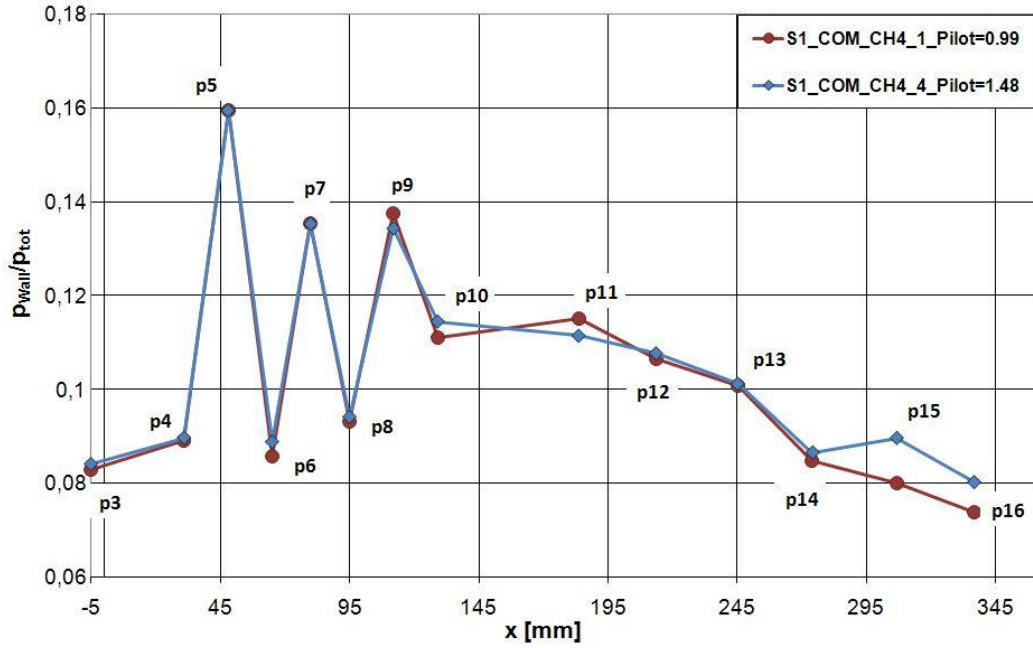


Figure 4.28 Wall static pressure distribution for supersonic combustion of 1.5g/s stabilized using Strut 1 with a near stoichiometric and with a rich pilot flame, respectively.

| Flame [-] | ϕ_p [-] | \dot{m}_{CH_4} [g/s] | ΔH_{tot} [kJ] | Δp_{tot} [MPa] | M_{Exit} [-] |
|--------------|-----------------|---------------------------|--------------------------|---------------------------|-------------------|
| S1_CH4_1 | 0.99 | 1.5 | 143.2 | 0.62 | 1.64 |
| S1_CH4_4 | 1.48 | 1.5 | 205.1 | 0.57 | 1.62 |
| S1_CH4_2 | 0.99 | 3.0 | 99.9 | 0.53 | 1.66 |
| S1_CH4_5 | 1.48 | 3.0 | 250.2 | 0.65 | 1.61 |
| S1_CH4_3 | 0.99 | 4.5 | 57.3 | 0.39 | 1.93 |
| S1_CH4_6 | 1.48 | 4.5 | 71.9 | 0.43 | 1.86 |

Table 4.5 Performance comparison of the supersonic methane flames stabilized with a near stoichiometric and with a rich pilot flame using Strut 1.

If the amount of injected methane is increased, the combustion heat release is still higher for the flames stabilized at $\Phi_p = 1.48$ than at $\Phi_p = 0.99$. However, the total pressure losses become slightly higher. With the stoichiometric pilot flame the heat release and the total pressure losses decrease steadily with increasing CH_4 mass flow rates, while the Mach number increases. Conversely, at $\Phi_p = 1.48$ a maximum of the heat release appears at 3g/s methane, then the combustion becomes weaker and analysis of the exhaust gases shows that a higher amount of CH_4 remains unburned. This is also confirmed by the wall static pressure distributions of Figure 4.29 and Figure 4.30, respectively. The pressure readings of tap 13 in the diverging section of the combustor for the supersonic flames stabilized at stoichiometric Φ_p constantly decrease for increasing CH_4 mass flow rates, which is aligned with the lower heat release

estimated with the energy balance. The curves for injection of 1.5g/s and 3g/s methane at $\Phi_p = 1.48$ show similar distributions, except for the slightly higher value of p_{10} at 1.5g/s methane. This might indicate a stronger combustion in the constant cross-area section under such condition. The wall static pressure readings in the divergent are significantly lower when the amount of injected methane is further increased to 4.5g/s, where the estimated combustion heat release is over three times lower than at 3g/s.

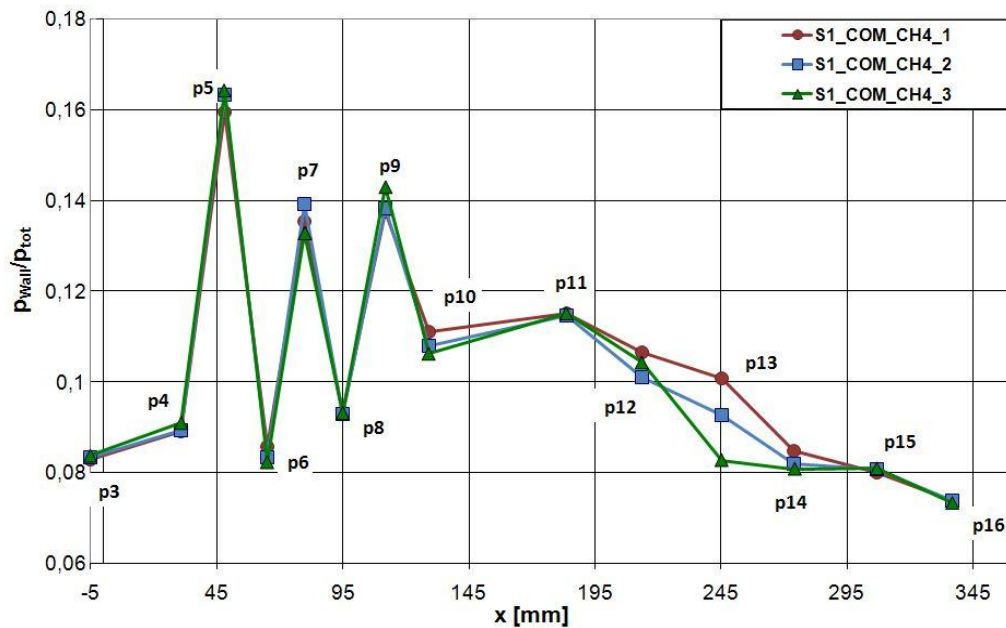


Figure 4.29 Wall static pressure distribution for supersonic methane flames stabilized with Strut 1 using a near stoichiometric pilot flame and for increasing amount of injected CH_4 .

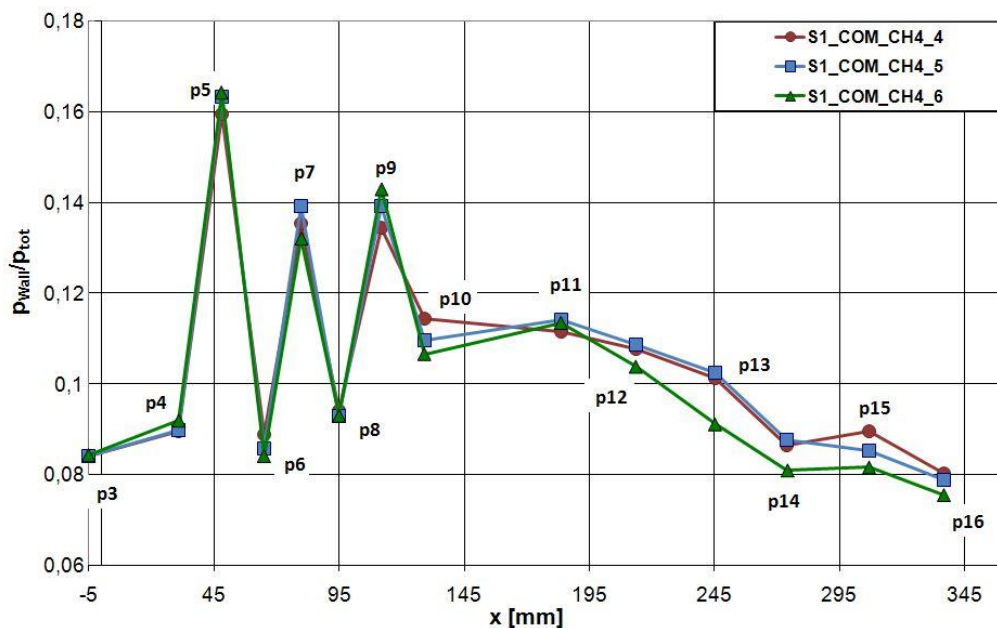


Figure 4.30 Wall static pressure distribution for supersonic methane flames stabilized with Strut 1 using a rich pilot flame and for increasing amount of injected CH_4 .

Further insight into the combustion modality can be gained by analyzing the PLIF images of Figure 4.31 and Figure 4.32, in which the supersonic flames at 1.5g/s and 3g/s methane are compared to the respective pilot flames. The resolution of the images has been adjusted in order to capture the gradients in the OH-concentrations at the different conditions while avoiding oversaturation of the detector.

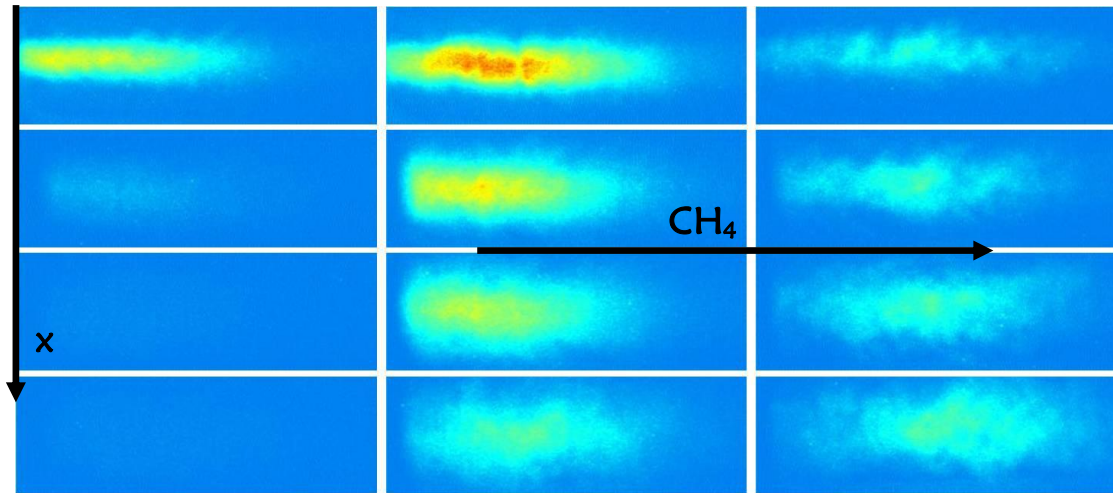


Figure 4.31 PLIF imaging of the near stoichiometric pilot flame (left) and of the supersonic flames stabilized with Strut 1 at $\text{CH}_4 = 1.5\text{g/s}$ (middle) and $\text{CH}_4 = 3\text{g/s}$ (right). From top to bottom: imaging through the four windows downstream of the strut on an illumination plane aligned with the central streamline. Image resolution: 1000.

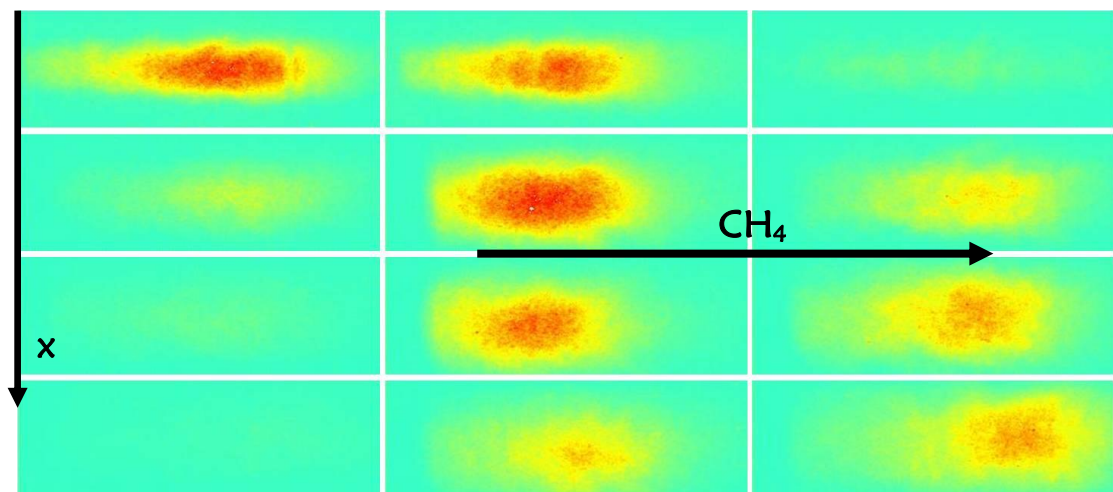


Figure 4.32 PLIF imaging of the rich pilot flame (left) and of the supersonic flames stabilized with Strut 1 at $\text{CH}_4 = 1.5\text{g/s}$ (middle) and $\text{CH}_4 = 3\text{g/s}$ (right). From top to bottom: imaging through the four windows downstream of the strut on an illumination plane aligned with the central streamline. Image resolution: 512.

For both Φ_p values, combustion occurs not only in the region immediately after the strut as it is in the case of the pilot flame alone, but it extends also into the diverging section, which confirms the wall static pressure data. However, for increasing

amount of injected methane the intensity of the reactions diminishes and is comparable for the leaner and the richer supersonic flames only in the last portion of the combustion chamber, where the effect of the pressure adaption to the ambient conditions at the exit is likely to be the promoter for the process. The effect of increasing the CH_4 mass flow rate is particularly evident for the supersonic flames stabilized at $\Phi_p = 1.48$, for which almost no radicals are detected in the first optically accessible section behind the strut (top, right picture in Figure 4.32). Weaker supersonic combustion in the constant cross-sectional area module of the combustor is peculiar under rich pilot flame conditions. Observation of the PLIF images in the first window downstream of the strut shows that while injection of 1.5g/s methane at $\Phi_p = 0.99$ leads to stronger combustion than with the pilot flame alone, at $\Phi_p = 1.48$ the reaction at this location is already slightly weaker than for the corresponding pilot flame. This is due to the pilot flame being further developed under richer conditions, which explains the initial higher OH^\cdot concentrations before ignition of the main flame, as discussed in Section 4.1.1 and as visible in the top right pictures of Figure 4.33. The short, stoichiometric pilot flame supports methane ignition immediately downstream of the strut trailing edge and a strong reaction takes place in the constant cross-sectional area portion of the combustor. Because of the greater extension of the pilot flame in the axial direction at $\Phi_p = 1.48$, the interface available as an ignition source for the methane is further stretched and a bigger amount of CH_4 is directly ignited and burns along the interface before the bulk reaction occurs further downstream.

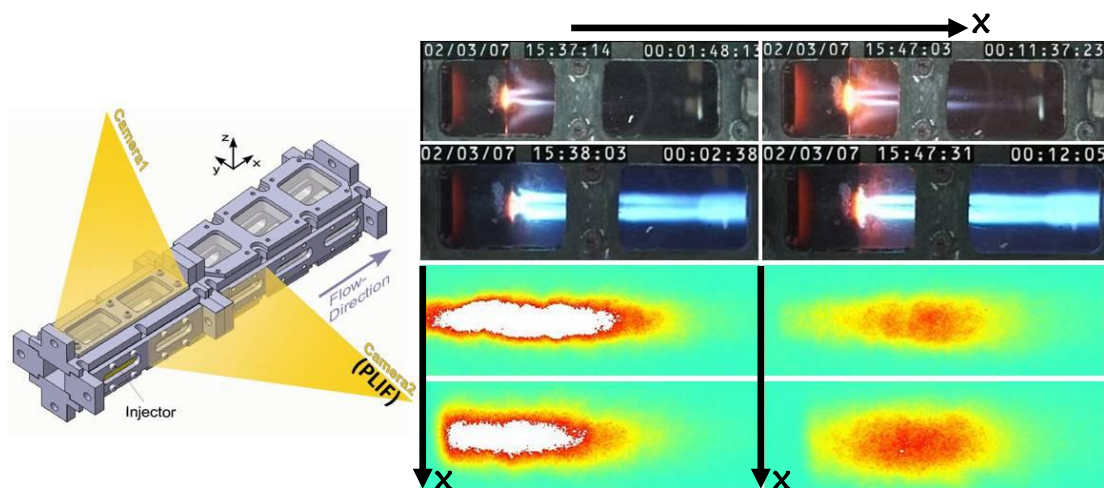


Figure 4.33 Left: Visualization fields for the direct and PLIF imaging. Right, top: Direct imaging of the near stoichiometric pilot flame (top left), of the rich pilot flame (top right) and of the corresponding supersonic flame stabilized with Strut 1 at $\text{CH}_4 = 1.5\text{g/s}$. Bottom: PLIF imaging of both methane flames through the first two windows downstream of the strut on an illumination plane aligned with the central streamline. Image resolution: 512.

In Figure 4.33, the comparison of the PLIF imaging for both flames at $\text{CH}_4 = 1.5\text{g/s}$ highlights higher OH^\cdot concentrations in the case of the stoichiometric pilot flame. However, the radicals that are set free do not have sufficient time to recombine and complete the reactions before undergoing the expansion in the diverging section. During the expansion the adverse pressure gradient further inhibits completion of the reactions. Although the gradient is not steep enough to freeze the reactions, the radicals can only partly recombine and do not release the whole heat of combustion. A longer combustor would be required for the reactions to be completed and to maximize the heat release. On the contrary, the rich pilot flame favors a more homogeneous reaction of the injected methane already in the constant cross-area section. Stabilization of the supersonic flame profits from the sustained ignition source: as visible in the direct imaging of Figure 4.33, the flame structure is more regular and symmetric than for the flame stabilized under stoichiometric pilot conditions and promotes radicals recombination such that a higher amount of heat is released during the supersonic combustion. Further, the amount of methane that can react effectively is higher in the smoother combustion modality. This is the reason for the peak of combustion heat release detected at 3g/s methane and $\Phi_p = 1.48$, while under stoichiometric pilot conditions the heat release steadily decreases with increasing CH_4 .

Thus, it can be concluded that the rich pilot flame under consideration is more suitable than the stoichiometric one to stabilize the supersonic methane combustion due its higher inherent stability and spatial extension. Further increase of the pilot equivalence ratio leads again to less stable combustion, for the pilot flame lacks oxidizer to be self-stabilizing when methane is injected. Although at higher CH_4 mass flow rates the total pressure losses are higher for the supersonic flame at $\Phi_p = 1.48$, the larger combustion heat release and the comparable Mach numbers at the combustor exit justify the choice of the rich flame as an optimal pilot for flame stabilization with Strut 1. For example, for the performance listed at $\text{CH}_4 = 3\text{g/s}$ in Table 4.5, a 22.6% greater total pressure loss is accompanied by a 2.5-time higher combustion heat release. At 4.5g/s methane mass flow rate the total pressure losses are again comparable for both pilot flame conditions and in both cases the combustion heat release sinks. A higher amount of unburned methane is detected in the gas samples collected at the combustor exit under these conditions: the combustion process becomes less effective. As already mentioned in Section 4.2, this is indicative of a major limit of the present injectors in supporting mixing of the main fuel. The methane remains confined in the central layer and cannot combine with sufficient amount of

oxidizer to complete the reaction. The overall equivalence ratio is hence very low and the performance of the combustor can be improved only with a radical modification of the injection system.

4.2.2 Strut 3

Successful ignition and stabilization of the supersonic methane flame have been achieved using Strut 3. Figure 4.34 proves that combustion of the supersonic flame does not lead to thermal choking, for the level of p_3 and p_4 remains unvaried. Compared to combustion of the pilot flame alone, the overall static pressure level is significantly higher and analysis of the overall performance listed in Table 4.6 confirms a major increase of the heat release for exit Mach numbers higher than 1.6.

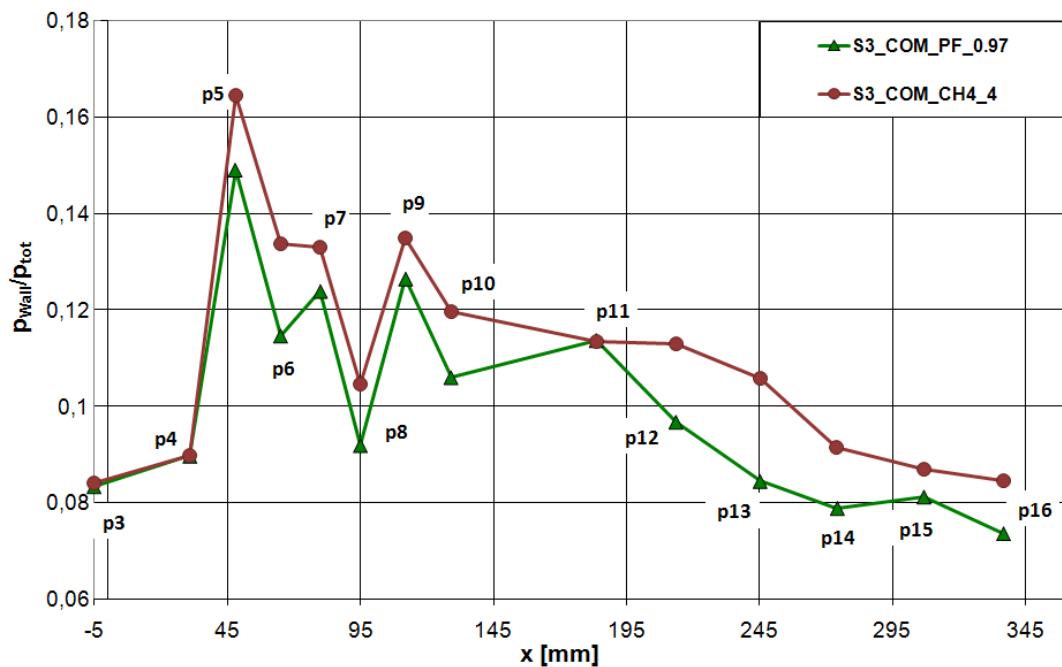


Figure 4.34 Wall static pressure distribution for combustion of a near stoichiometric pilot flame and of a lean supersonic methane flame using Strut 3 (1.5g/s CH₄).

| Flame [-] | ϕ_p [-] | \dot{m}_{CH_4} [g/s] | ΔH_{tot} [kJ] | Δp_{tot} [MPa] | M_{Exit} [-] |
|--------------|-----------------|---------------------------|--------------------------|---------------------------|-------------------|
| S3_CH4_1 | 0.73 | 1.5 | 146.3 | 0.64 | 1.63 |
| S3_CH4_4 | 0.97 | 1.5 | 171.3 | 0.64 | 1.65 |
| S3_CH4_2 | 0.73 | 3.0 | 137.5 | 0.64 | 1.65 |
| S3_CH4_5 | 0.97 | 3.0 | 245.5 | 0.65 | 1.61 |
| S3_CH4_3 | 0.73 | 4.5 | 72.2 | 0.61 | 1.83 |
| S3_CH4_6 | 0.97 | 4.5 | 113.8 | 0.63 | 1.71 |

Table 4.6 Performance comparison of the supersonic methane flames stabilized with a near stoichiometric and with a rich pilot flame using Strut 3.

Further, the recess at the trailing edge of the strut anchors the flame in such a way that the aerodynamic losses are fairly insensitive to changes in the amount of injected methane and in the pilot equivalence ratio. The total pressure losses are mainly controlled by the generated recirculation zone and remain constant at approximately 0.64MPa. While the total pressure losses and exit Mach numbers are comparable, the combustion heat release achieved when the supersonic flames are stabilized at $\Phi_p = 0.97$ is higher than for operation at leaner pilot flame conditions. Similarly to the findings for Strut 1, there is a limit to the amount of methane that can be injected and react effectively. Because the interface along which heat and mass exchanges can take place is more extended and stable, a higher degree of homogeneity of the pilot flame favors ignition and stabilization of the supersonic methane flames. For Strut 3 this is the case at near stoichiometric pilot conditions, where an effective reaction of a higher amount of CH_4 can be achieved compared to stabilization at lean pilot conditions. This conclusion is supported by the direct flame visualizations of Figure 4.35, by the PLIF results, and by the estimated combustion heat release. The latter constantly decreases for increasing methane mass flow rate at $\Phi_p = 0.73$, while a maximum is detected at $\text{CH}_4 = 3\text{g/s}$ for $\Phi_p = 0.97$.

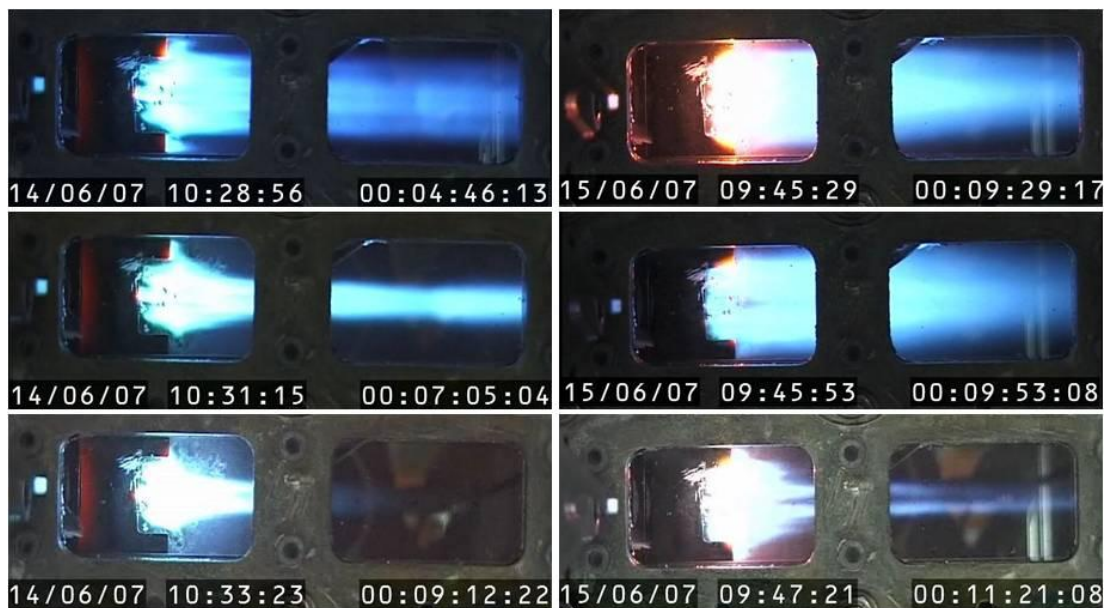


Figure 4.35 Supersonic flame stabilization with Strut 3 at $\Phi_p = 0.73$ (left) and at $\Phi_p = 0.97$ (right) with 1.5g/s (top), 3g/s (middle) and 4.5g/s (bottom) methane injected through the strut sides.

Because of the recirculation zone generated at the trailing edge of Strut 3 there is a major difference in the combustion modality compared to Strut 1. This is shown in the wall static pressure distributions of Figure 4.36. Combustion is now strong already

in the recess at the trailing edge of the strut and a pressure peak due to the reaction is detected at p_6 at both pilot equivalence ratios tested and independent of the injected amount of methane (refer also to Figure 4.37 and Figure 4.38). The overall wall static pressure is higher for Strut 3 including in the diverging section, which indicates more effective combustion and a higher combustion heat release. In fact, at near stoichiometric pilot conditions, combustion of 1.5g/s methane with Strut 1 releases about 143kW heat, against the 172kW with Strut 3. The difference is even higher ($\Delta H_{tot} = 146\text{kW}$) when 3g/s methane are injected, as reported in Table 4.7.

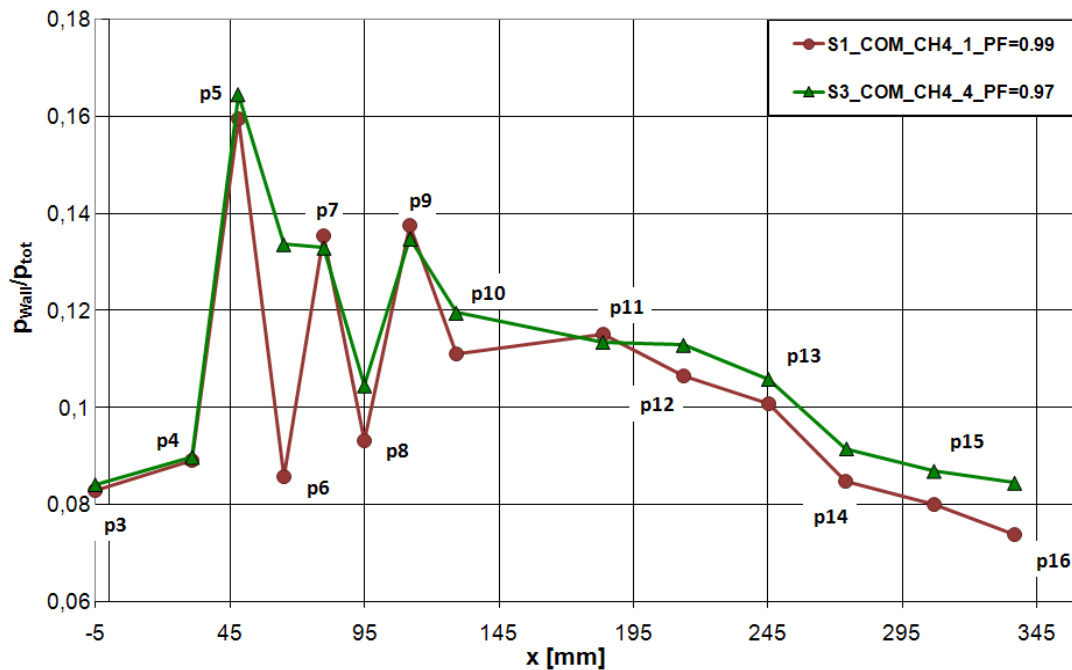


Figure 4.36 Comparison of the wall static pressure distribution for a supersonic flame at 1.5g/s methane stabilized at near stoichiometric pilot conditions with Strut 1 (circles) and Strut 3 (triangles), respectively.

| Flame [-] | ϕ_p [-] | \dot{m}_{CH_4} [g/s] | ΔH_{tot} [kJ] | Δp_{tot} [MPa] | M_{Exit} [-] |
|--------------|-----------------|---------------------------|--------------------------|---------------------------|-------------------|
| S1_CH4_1 | 0.99 | 1.5 | 143.2 | 0.62 | 1.64 |
| S3_CH4_4 | 0.97 | 1.5 | 171.5 | 0.64 | 1.65 |
| S1_CH4_2 | 0.99 | 3.0 | 99.9 | 0.53 | 1.66 |
| S3_CH4_5 | 0.97 | 3.0 | 245.5 | 0.65 | 1.61 |
| S1_CH4_3 | 0.99 | 4.5 | 57.3 | 0.39 | 1.93 |
| S3_CH4_6 | 0.97 | 4.5 | 113.8 | 0.63 | 1.71 |

Table 4.7 Performance comparison of the supersonic methane flames stabilized with a near stoichiometric pilot flame using Strut 1 and Strut 3.

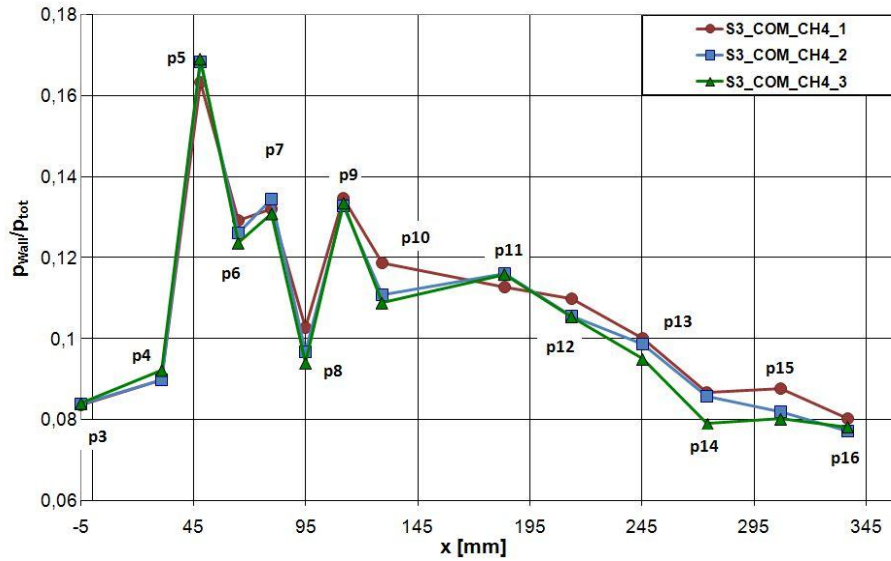


Figure 4.37 Wall static pressure distribution for supersonic methane flames stabilized with Strut 3 using a lean pilot flame and for increasing amount of injected CH₄.

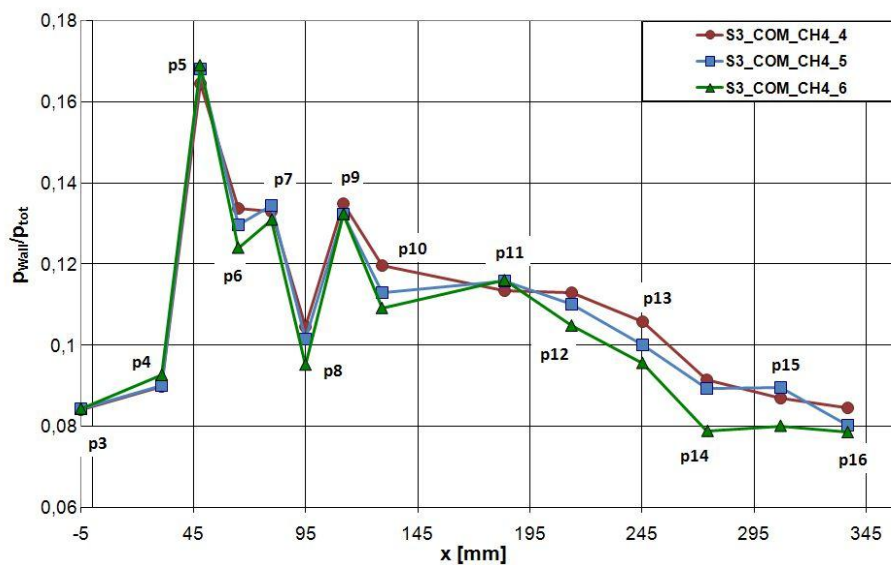


Figure 4.38 Wall static pressure distribution for supersonic methane flames stabilized with Strut 3 using a near stoichiometric pilot flame and for increasing amount of injected CH₄.

The performance of the supersonic flames stabilized at the optimal pilot conditions identified for Strut 1 and Strut 3 will be compared to conclude the discussion of the results for single-stage combustion. The data is listed in Table 4.8. For comparable M_{Exit} , at low methane mass flow rates the performance of Strut 1 is higher when considering the total pressure losses and combustion heat release. This is likely due to the fact that when a little amount of fuel is injected the degree of mixing with the supersonic airflow has the main influence on the combustor performance. Although a major limitation of the present injector systems is the mixing effectiveness,

which puts a constraint on the maximum amount of methane that can be burnt, the trailing edge of Strut 1 is designed to promote mixing instead of flame holding. Thus, at methane flow rates for which homogeneous mixing can still be achieved with the current injection configurations, Strut 1 shows a higher combustion heat release because of the higher mixing level compared to Strut 3. However, the flame holding characteristics of Strut 3 become more advantageous for increasing methane flow rates. Since a considerable amount of fuel remains confined in the central layer as discussed in Section 4.2, the overall performance takes advantage of a stable and stretched ignition interface. At $\dot{m}_{CH_4} = 3\text{g/s}$ the performance of both struts is comparable, while at $\dot{m}_{CH_4} = 4.5\text{g/s}$ heat released when using Strut 3 is 60% higher than with Strut 1. As evincible from the Hugoniot curve, the higher heat release is accompanied by a lower exit Mach number for Strut 3. It also follows that the total pressure losses are higher due to the higher degree of reaction.

| Flame [-] | ϕ_P [-] | \dot{m}_{CH_4} [g/s] | ΔH_{tot} [kJ] | Δp_{tot} [MPa] | M_{Exit} [-] |
|--------------|-----------------|---------------------------|--------------------------|---------------------------|-------------------|
| S1_CH4_4 | 1.48 | 1.5 | 205.5 | 0.57 | 1.62 |
| S3_CH4_4 | 0.97 | 1.5 | 171.5 | 0.64 | 1.65 |
| S1_CH4_5 | 1.48 | 3.0 | 250.2 | 0.65 | 1.61 |
| S3_CH4_5 | 0.97 | 3.0 | 245.5 | 0.65 | 1.61 |
| S1_CH4_6 | 1.48 | 4.5 | 71.9 | 0.43 | 1.86 |
| S3_CH4_6 | 0.97 | 4.5 | 113.8 | 0.63 | 1.71 |

Table 4.8 Performance comparison of the supersonic methane flames stabilized with a rich pilot flame using Strut 1 and with a near stoichiometric pilot flame using Strut 3.

4.2.3 Conclusion

Supersonic flame stabilization has been investigated using both Strut 1 and Strut 3 and for different pilot flame conditions. In general, both struts have proven to sustain supersonic combustion of methane at all pilot conditions tested. Optimal pilot flame operative conditions have been identified for each strut based on the overall performance (combustion heat release, total pressure drop and Mach number at the combustor exit). However, Strut 3 appears to be more advantageous for the geometries and the fuelling configurations studied. This conclusion is mainly driven by the considerations that the combustion process is more stable and requires a lower amount of pilot fuel if using Strut 3, while the other performance features are comparable for both struts.

A series of tests has been performed at lower stagnation temperature (650K) and pressure (0.75MPa) whilst maintaining the inlet Mach number (M_{cc}). Additionally, tests were carried out continuously varying the stagnation temperature from 1000K to 650K and stagnation pressure from 0.94MPa to 0.75MPa, to investigate the flame stability during transition from a simulated flight Mach number of 4.25 to 3.25. With both struts it was possible to demonstrate the feasibility of supersonic combustion under conditions that are more severe in relation to flame ignition and stabilization. Hence, the designs proved to be robust for operation across the mid-speed flight regime [70].

However, a major limitation of the current injection system has emerged during the study. Both struts do not support sufficient mixing of the main fuel, which remains confined near the strut wake, leading to flow stratification. The confinement of fuel and highly reactive combustion products into the central layer limits the amount of methane that can react in the present combustor and hence the overall equivalence ratio at which the combustor can operate.

4.3 Two-Stage Injection

To enhance mixing in the combustion chamber and increase the overall equivalence ratio, the strut has been combined with a cavity injector, as described in Section 3.2.3. Preliminary tests have been carried out with additional injection of methane at an injection temperature $T_{CH_4_Cavity}$ of about 260K to reduce the thermal load on the combustor bottom wall. The changes in the mixing and combustion processes have been monitored by measuring the wall pressure distribution while varying the amount of methane injected through the strut and through the cavity, and by collecting gas sampling data at the combustor exit.

| Strut [-] | Φ_P [-] | \dot{m}_{CH_4} [g/s] | $\dot{m}_{CH_4_Cavity}$ [g/s] | $T_{CH_4_Cavity}$ [K] | Labelling [-] |
|--------------|-----------------|---------------------------|-----------------------------------|---------------------------|------------------|
| Strut 1 | 1.48 | 1.5 | 0 | – | CAVITY_1 |
| Strut 1 | 1.48 | 1.5 | 2 | 260 | CAVITY_2 |
| Strut 1 | 1.48 | 1.5 | 8.6 | 260 | CAVITY_3 |

Table 4.9 Summary of the testing conditions for staged injection with Strut 1.

The wall static pressure distribution reported in Figure 4.39 refers to the injection of 1.5g/s of CH₄ through the strut and of 2g/s and 8.6g/s through the cavity, as listed in Table 4.9. The pressure p_c is detected by an additional static pressure tap on the cavity floor, as specified in Table 3.3. Because of the fuel injection in the diverging section, a first wall pressure peak appears immediately downstream of the cavity; the value of the wall static pressure increases with the amount of injected fuel. For higher amounts of CH₄, a second peak appears further downstream, suggesting a weak heat release through combustion. However, the results of the gas sampling measurements indicate that most of the CH₄ leaves the combustor unburned and that the available combustor length is too short for a sensible amount of fuel to mix and react.

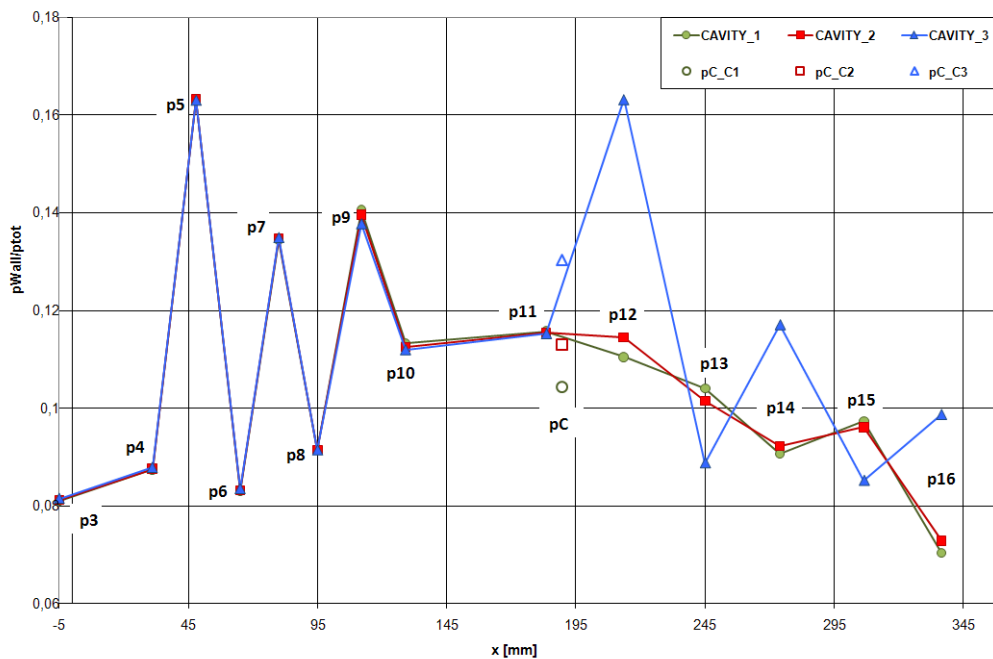


Figure 4.39 Wall static pressure distribution for staged injection with Strut 1 using a rich pilot flame and for increasing amount of CH₄ injected through the cavity.

Further tests have been conducted with methane pre-heating up to 440K prior to injection through the cavity to estimate the influence of $T_{CH_4_Cavity}$ on the mixture ignition. The wall pressure distribution did not show major differences compared to the case at low $T_{CH_4_Cavity}$, which suggests two conclusions. First, the pressure peak detected at p_{14} is due to reflection of the shock originated by the methane jet upstream of the cavity rather than to combustion of part of the fuel. In fact, if the peak of p_{14} detected at 260K were due to weak combustion, increasing the fuel injection temperature would further support combustion and intensify the heat release, which in turn would lead to a higher value of the wall static pressure at p_{14} . Second, the lack of

reaction of the fuel jet with the surrounding supersonic flow indicates that the two streams do not sufficiently mix. Indeed, the flame visualizations of Figure 4.40 confirm that the CH_4 jet penetrates into the combustor, but does not mix with the air and the combustion products. Instead, the flame stabilized by the first injection stage is turned upwards by the impinging CH_4 jet, as visible in the second window.

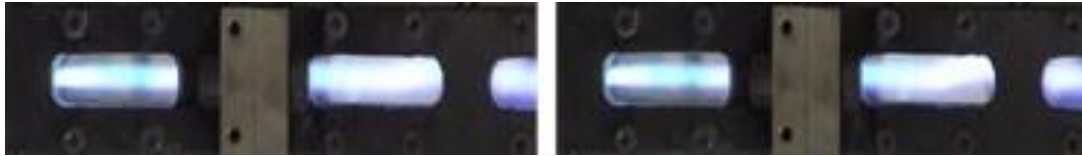


Figure 4.40 Side view of a $\text{CH}_4 = 1.5\text{g/s}$ supersonic methane flame with additional injection of methane through the cavity. Left: $\text{CH}_4_{\text{Cavity}} = 2\text{g/s}$; right $\text{CH}_4_{\text{Cavity}} = 8.6\text{g/s}$.

Similar tests have been performed with Strut 3, to assess whether the geometry of the first stage influences the mixing and combustion processes in the diverging section. The corresponding wall pressure distribution is presented in Figure 4.41 for the conditions summarized in Table 4.10.

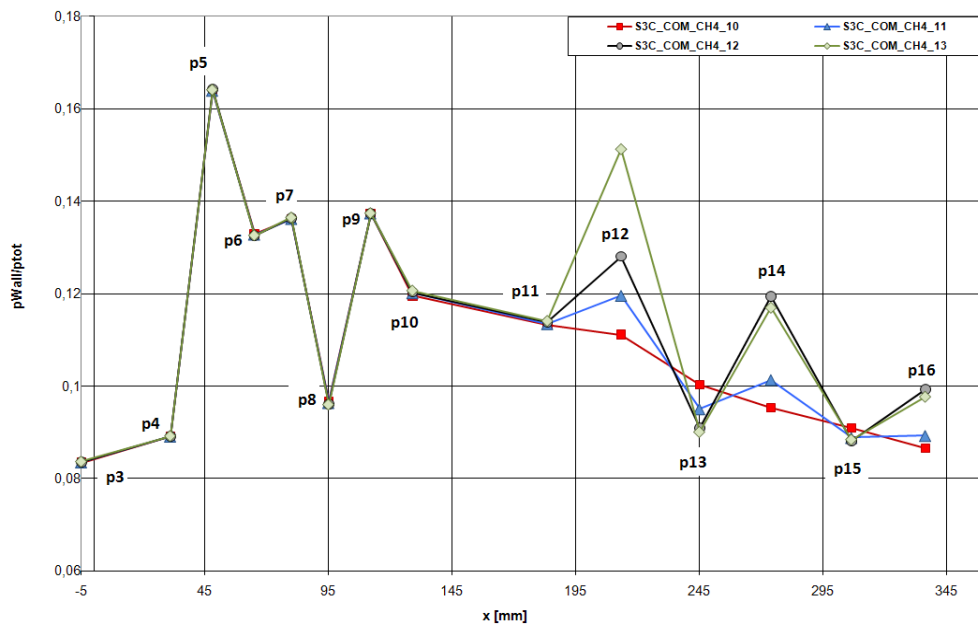


Figure 4.41 Wall static pressure distribution for staged injection with Strut 3 using a rich pilot flame and for increasing amount of CH_4 injected through the cavity.

The static pressure data and the results of the gas chromatographic analysis confirm the same behaviour as for Strut 1 for additional CH_4 injection through the cavity. The lack of combustion of the second-stage fuel is due to poor mixing of the jet with the supersonic airflow. Moreover, the presence of combustion products from the first stage reduces the amount of oxidizer available for the additional fuel, which exits the combustor unburned.

| Strut [-] | Φ_p [-] | \dot{m}_{CH_4} [g/s] | $\dot{m}_{CH_4,Cavity}$ [g/s] | $T_{CH_4,Cavity}$ [K] | Labelling [-] |
|--------------|-----------------|---------------------------|----------------------------------|--------------------------|------------------|
| Strut 3 | 0.97 | 2 | 0 | – | S3C_COM_CH4_10 |
| Strut 3 | 0.97 | 2 | 3 | 260 | S3C_COM_CH4_11 |
| Strut 3 | 0.97 | 2 | 5 | 260 | S3C_COM_CH4_12 |
| Strut 3 | 0.97 | 2 | 7 | 260 | S3C_COM_CH4_13 |

Table 4.10 Summary of the testing conditions for staged injection with Strut 3.

4.3.1 Conclusion

The introduction of a cavity injector in the diverging section of the combustion chamber did not lead to the anticipated results. All experimental data suggest that the CH₄ jet does not penetrate into the supersonic flow, but that it does not mix with the hot gases produced by the flame stabilized through the first stage. The jet appears to modify the flame direction because of the different pressures and temperatures of the gases and an additional layer of CH₄-rich flow can be observed. Due to time constraints, further investigation and improvement of the two-stage injection system could not be carried out in the course of this study. However, further development of the staged injection is recommended to achieve enhancement of the combustor equivalence ratio and improve the overall level of performance.

4.4 Summary

The experimental results produced in the course of this study have been discussed starting from those concerning the stabilization of the pilot flame. The present injectors have been compared to the ones designed and tested in previous years at LFA [11]. The major modifications leading to the elimination of the flame holder used in the past have been discussed along with the ignition, combustion behaviour, and the aerodynamic performance. Three strut injectors have been analysed, each presenting unique design characteristics that are reflected into the experimental findings. The two struts that proved to be suitable for pilot flame stabilization have been further discussed with respect to the stabilization of a supersonic methane flame. Finally, the results of the implementation of a second stage cavity injector have been presented.

5 Conclusion

Airbreathing ramjet and scramjet engines have been recently considered as possible means of providing safe and affordable access to space. Dual-mode scramjets are at the core of concepts for both single-stage-to-orbit and two-stage-to-orbit systems that aim to take advantage of the potential performance gains over conventional rocket-propelled vehicles. The use of supersonic combustion in non-conventional airbreathing engines becomes necessary at flight Mach numbers of approximately five. At those speeds the deceleration of the incoming airflow to subsonic conditions is accompanied by prohibitive losses leading to a drop in performance. One of the key aspects of scramjet engines development is to guarantee efficient energy conversion in the combustor, which goes along with the optimization of the basic physical processes governing fuel injection, mixing and combustion. The design of suitable fuel injection and flame stabilization systems is particularly challenging and has been addressed in this study.

The experimental investigations have been conducted in a subscale, direct connected combustor at an entrance Mach number of 2.2 and a total temperature up to 1000K. Such conditions are below the self-ignition capability of the mixture and a focused laser beam has been used as an external ignition source. The ignition and stabilization behaviour of a strut injection system positioned in the constant cross-area section of the combustor has been studied first, and three different struts have been compared with respect to their capability of stabilizing a pilot flame, which was then used to ignite the main, supersonic combustion. Finally, the strut injectors have been studied in combination with a wall-mounted cavity implemented in the diverging section of the combustor.

Two of the three struts proved to be capable of stabilizing a hydrogen pilot flame in the recirculation zone generated in their wake. The third strut did not support ignition due to the fact that it was designed for the pilot fuel and oxidizer not to converge into one spot. This was found to be a requisite to achieve successful ignition, for it allows forming an ignitable mixture in the location to which the laser spark will be focused. Mixture ignition and pilot flame stabilization have been obtained with both other struts using either air or oxygen as pilot oxidizer. Stoichiometric pilot

conditions have been identified as optimal to guarantee self-sustainment of the pilot flame without depending on the entrainment of air into the wake from the main supersonic flow. The new strut geometries reduced the aerodynamic losses and supported flame stabilization without introducing any additional flame holders, which was the case for the systems previously studied at LFA [11]. This was achieved by reducing the overall injector length. With the shorter struts the ignition point in which the pilot fuel and oxidizer jets converge is located further upstream and is no longer affected by the reflection of the shock generated at the leading edge of the strut. Thus, the flame kernels can form and grow stably without flame holder. A further reduction of the total pressure losses has been obtained by decreasing the thickness of the injectors, which led to a lower aerodynamic blockage of the combustion chamber.

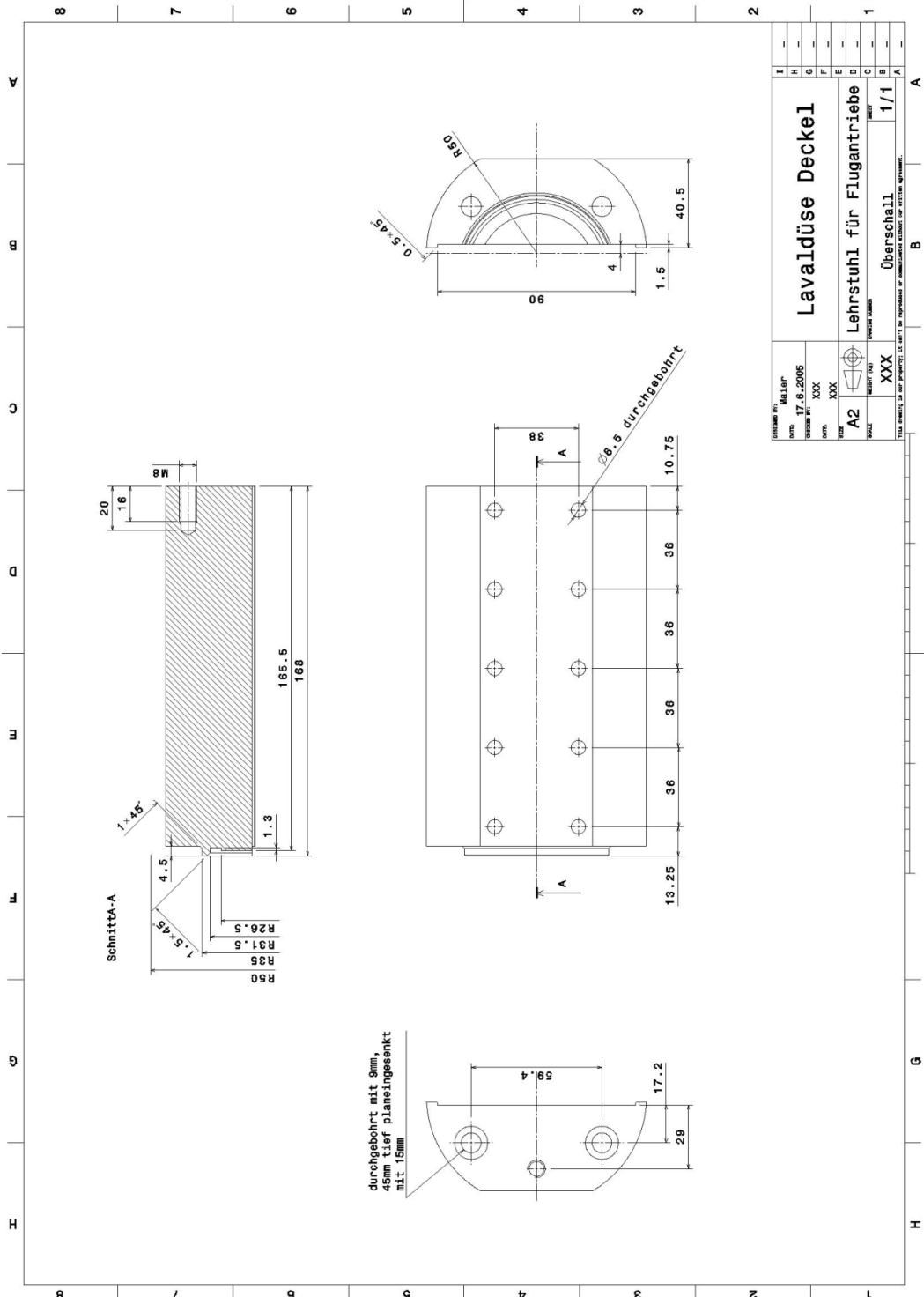
Due to test bed constraints, only hydrogen-oxygen pilot flames have been further considered for stabilization of the main combustion. In general, both struts stabilized a supersonic methane flame under different conditions and at near stoichiometric values of the pilot equivalence ratio. However, the amount of injected methane could not be increased over a certain threshold due to low mixing between the fuel and the supersonic air in the (y,z)-plane. This leads to a stratification of the combustor flow and combustion occurs mainly in the central layer inside and close to the strut wake. Herein the total pressure losses are greatest and the exit Mach number minimal at values of 1.6 to 1.9 depending on the operative conditions.

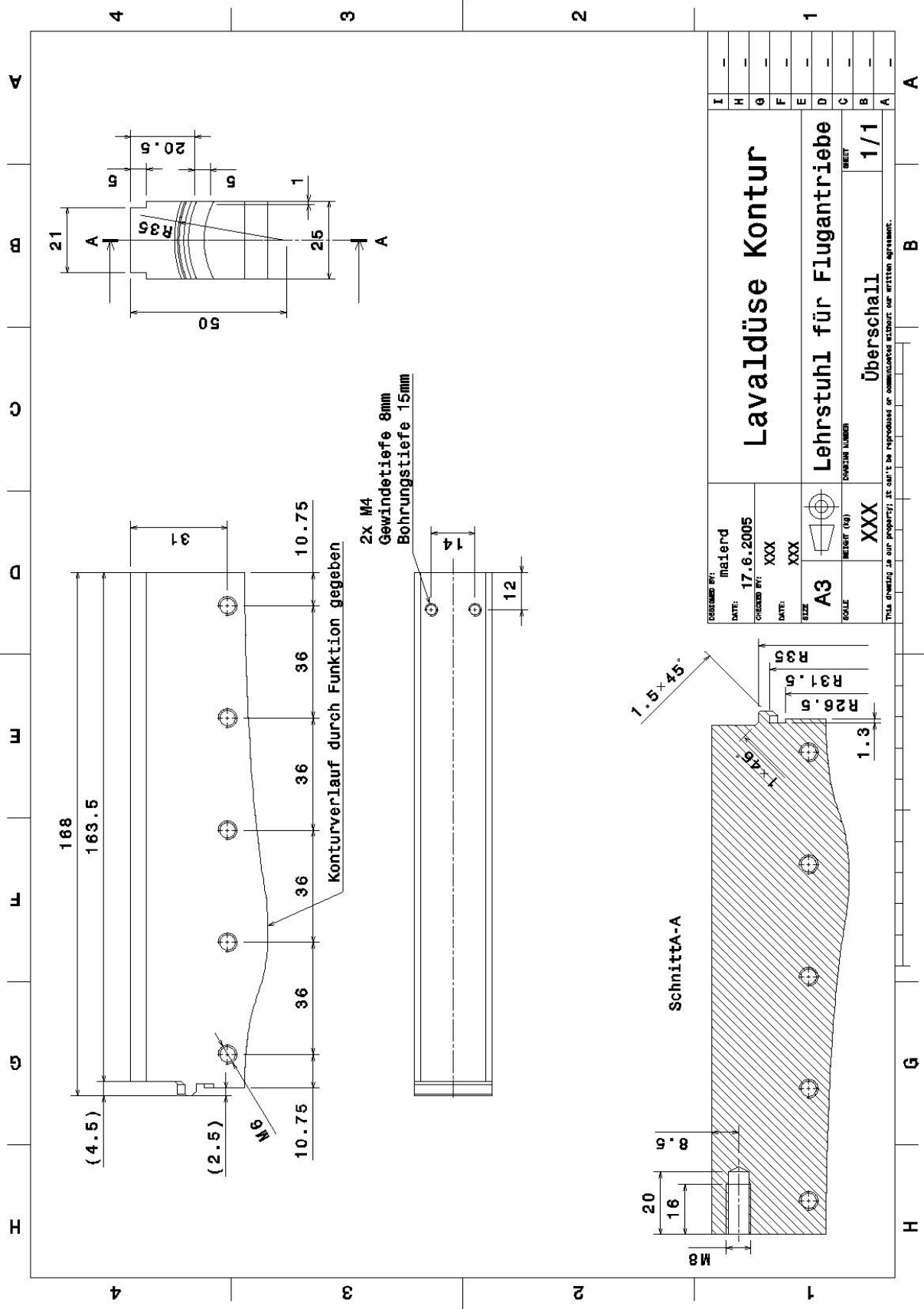
Strut 1 and Strut 3 have been designed to promote mixing and flame holding, respectively. As a result, combustion with Strut 1 occurs in a weak regime downstream of the strut and becomes stronger only in the divergent. The highest combustion heat release is obtained at slightly rich values of the pilot equivalence ratio where the ignition interface is stretched and a higher amount of methane can react before leaving the combustor. Instead, Strut 3 anchors the flame in the recess at its trailing edge and the aerodynamic losses are fairly insensitive to the amount of injected methane. The total pressure losses are mainly controlled by the recirculation zone and remain constant at approximately 0.64MPa. The greatest combustion heat release has been obtained at stoichiometric pilot conditions. Thus, Strut 3 is superior to Strut 1 for the geometries and at the fuelling configurations studied, for the combustion process is more stable and requires a lower amount of pilot fuel, while the other performance is comparable for both struts.

The combination of both struts with the wall-mounted cavity injector did not provide the expected performance improvement. The injected methane did not mix with the supersonic flow, independent of the injection temperature in the tested range (260K to 440K) and on the geometry of the first stage injector (Strut 1 or Strut 3). Thus no successful ignition of the second stage fuel could be achieved and further optimization of the injection strategy in the divergent is recommended to enhance the combustor equivalence ratio and improve the overall performance.

Appendix A Technical Drawings

A.1 Laval Nozzle





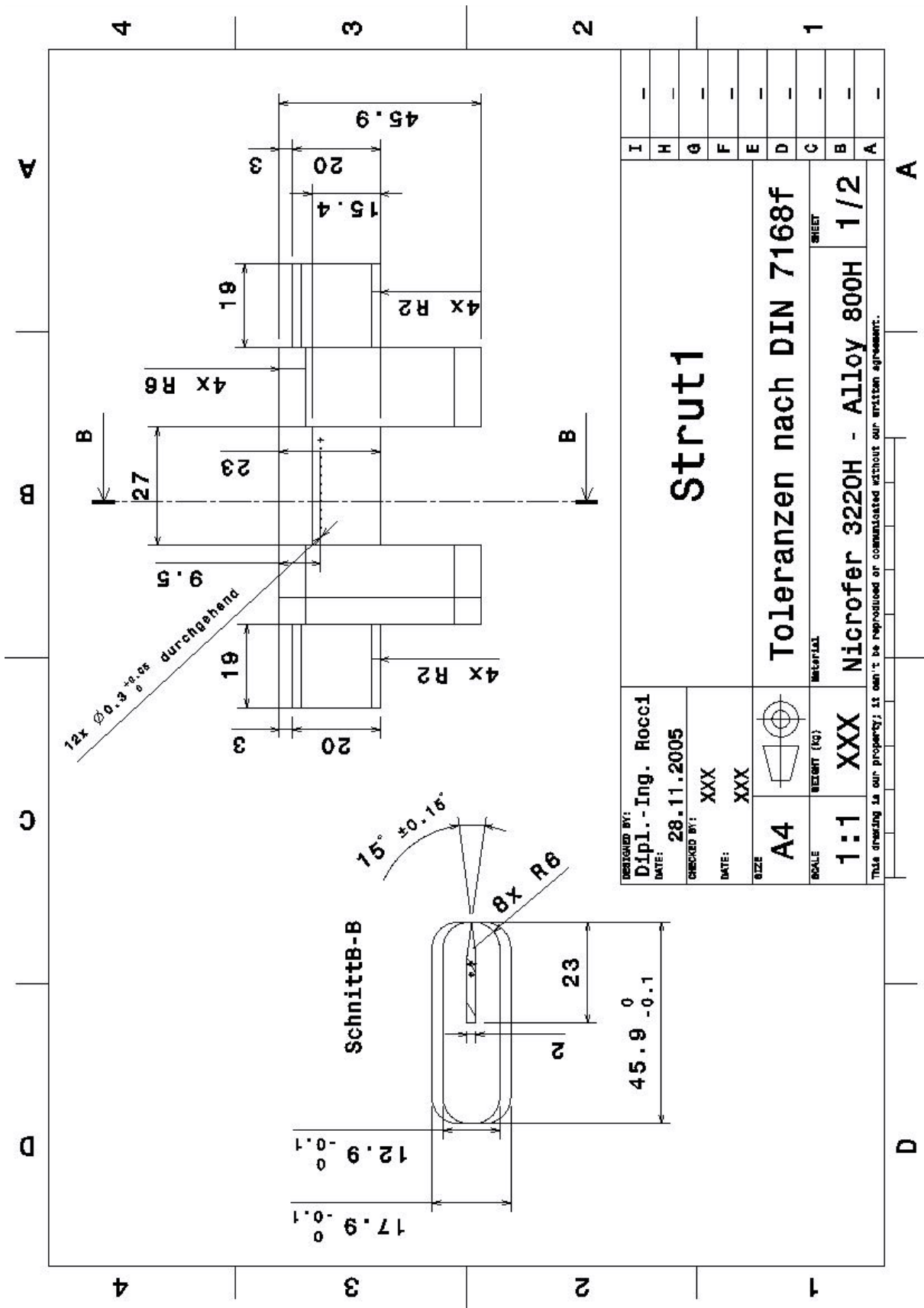
2x M4
Gewindetiefe 8mm
Bohrungstiefe 15mm

Konturverlauf durch Funktion gegeben

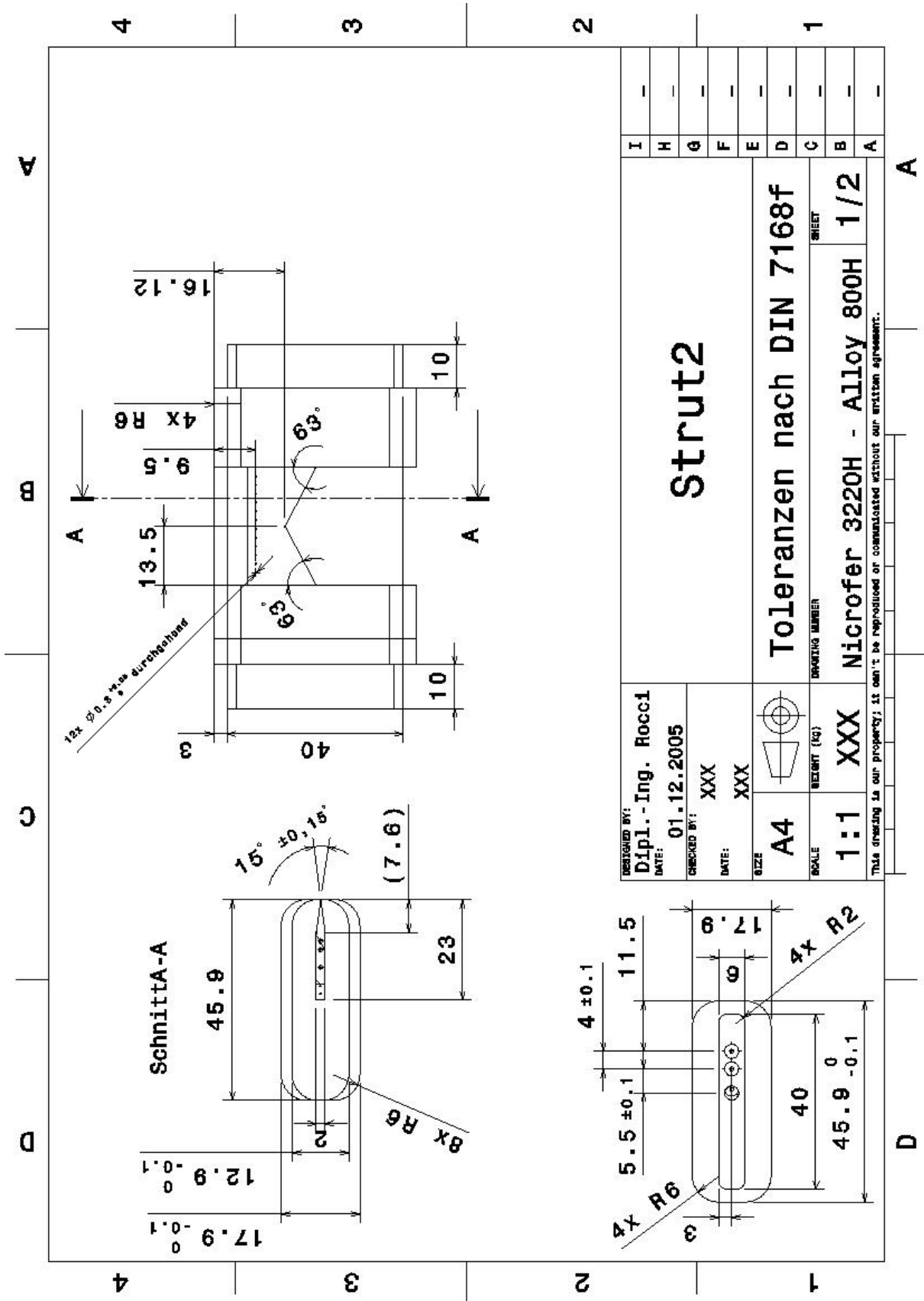
| | |
|---|--|
| PREPARED BY: malederd DATE: 17.6.2005 CHECKED BY: XXX DATE: XXX SIZE: A3 SCALE: 1:1 SHEET NUMBER: 1/1 | Lavaldüse Kontur Lehrstuhl für Flugantriebe ÜBERSCHALL |
|---|--|

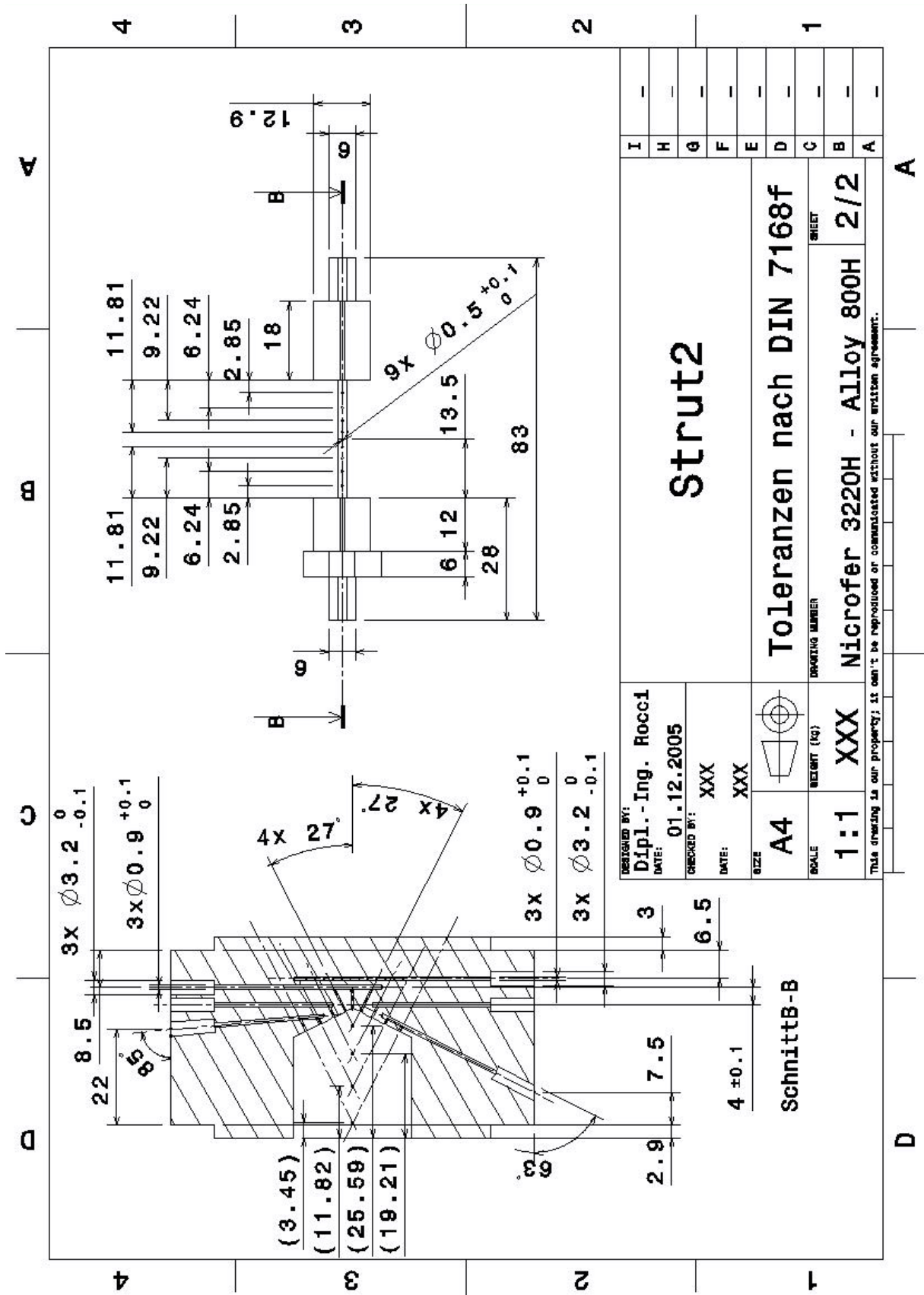
THIS DRAWING IS OUR PROPERTY. IT CAN'T BE REPRODUCED OR COMMUNICATED WITHOUT OUR WRITTEN AGREEMENT.

A.2 Strut 1

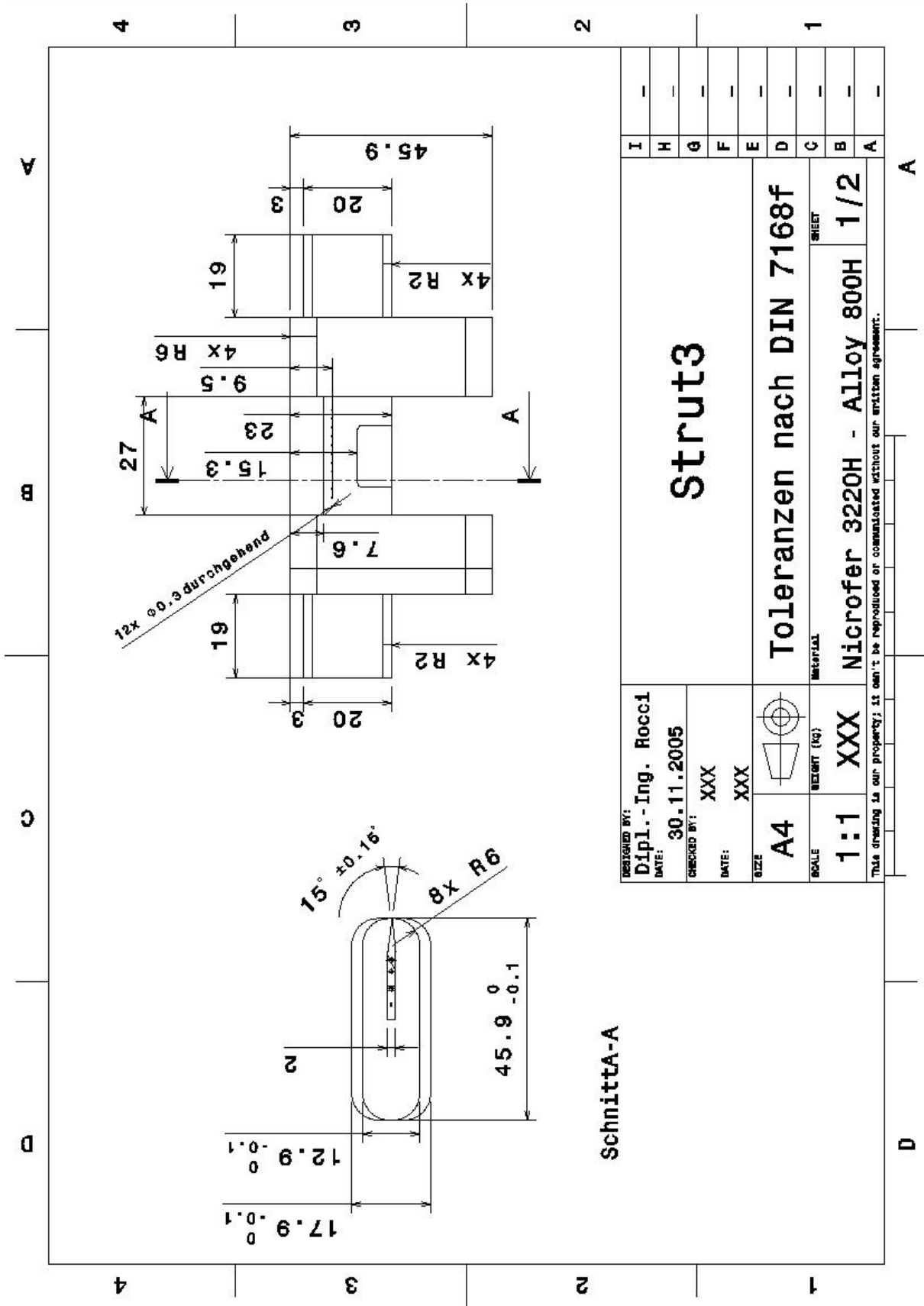


A.3 Strut 2

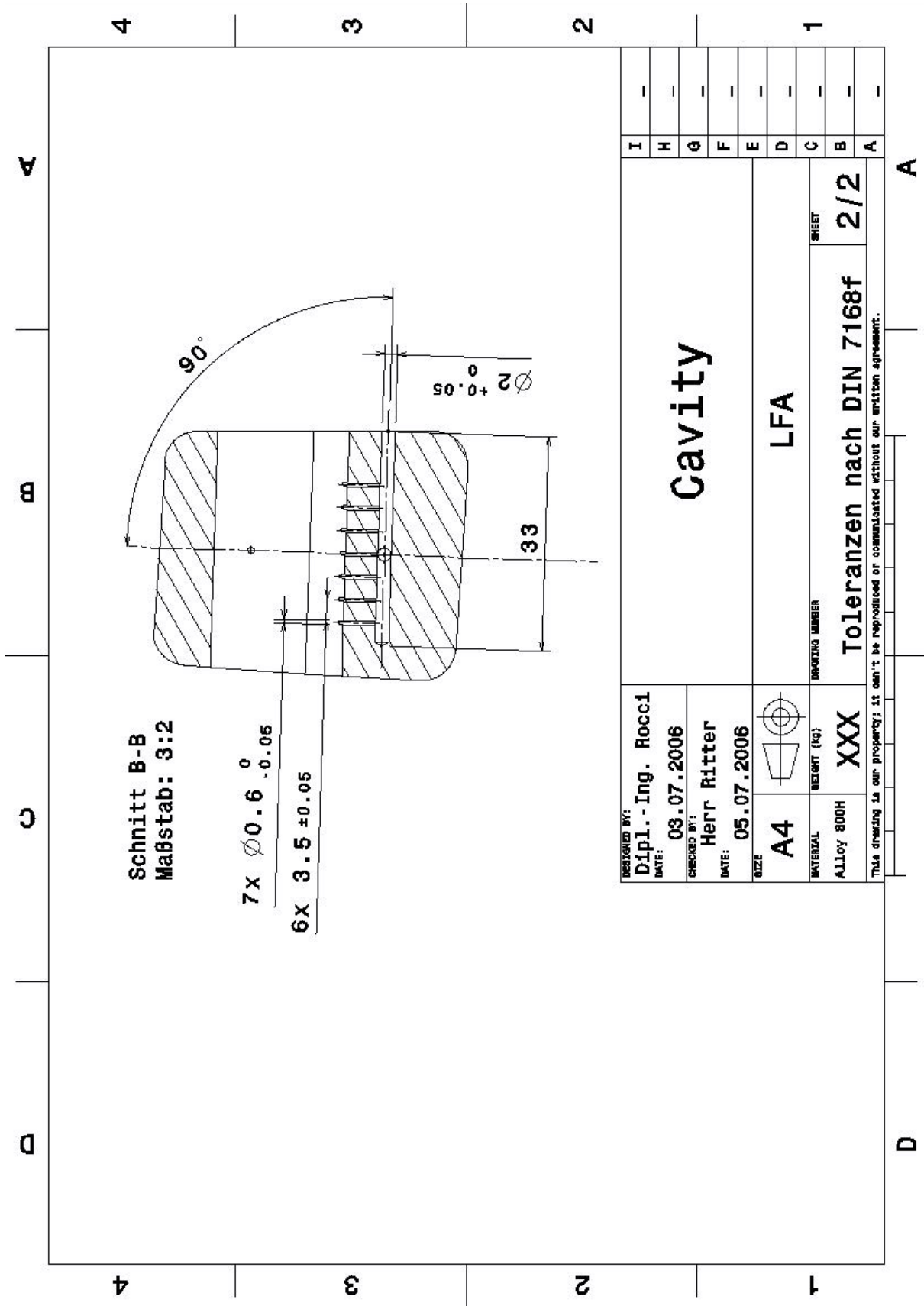


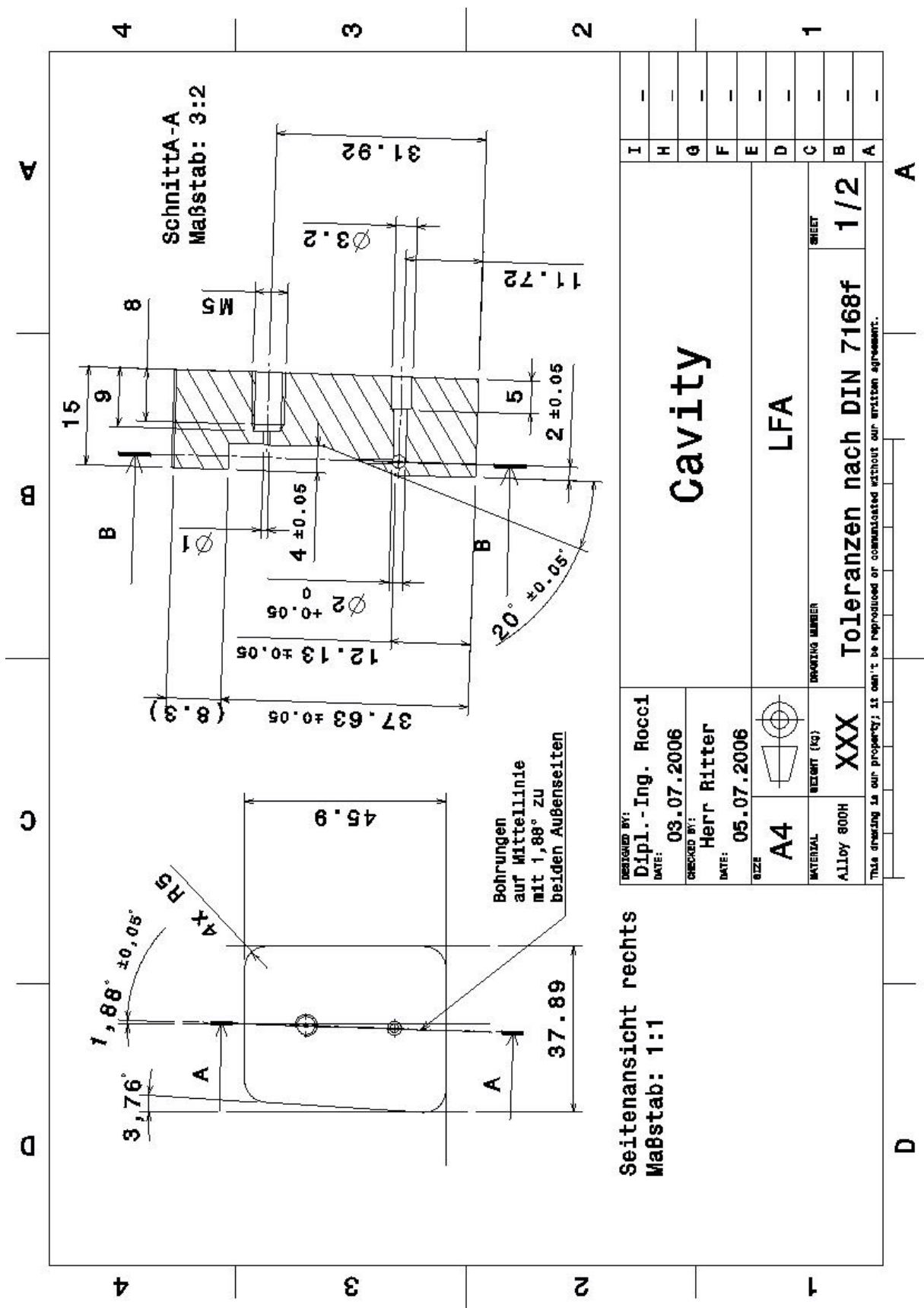



A.4 Strut 3



A.5 Cavity

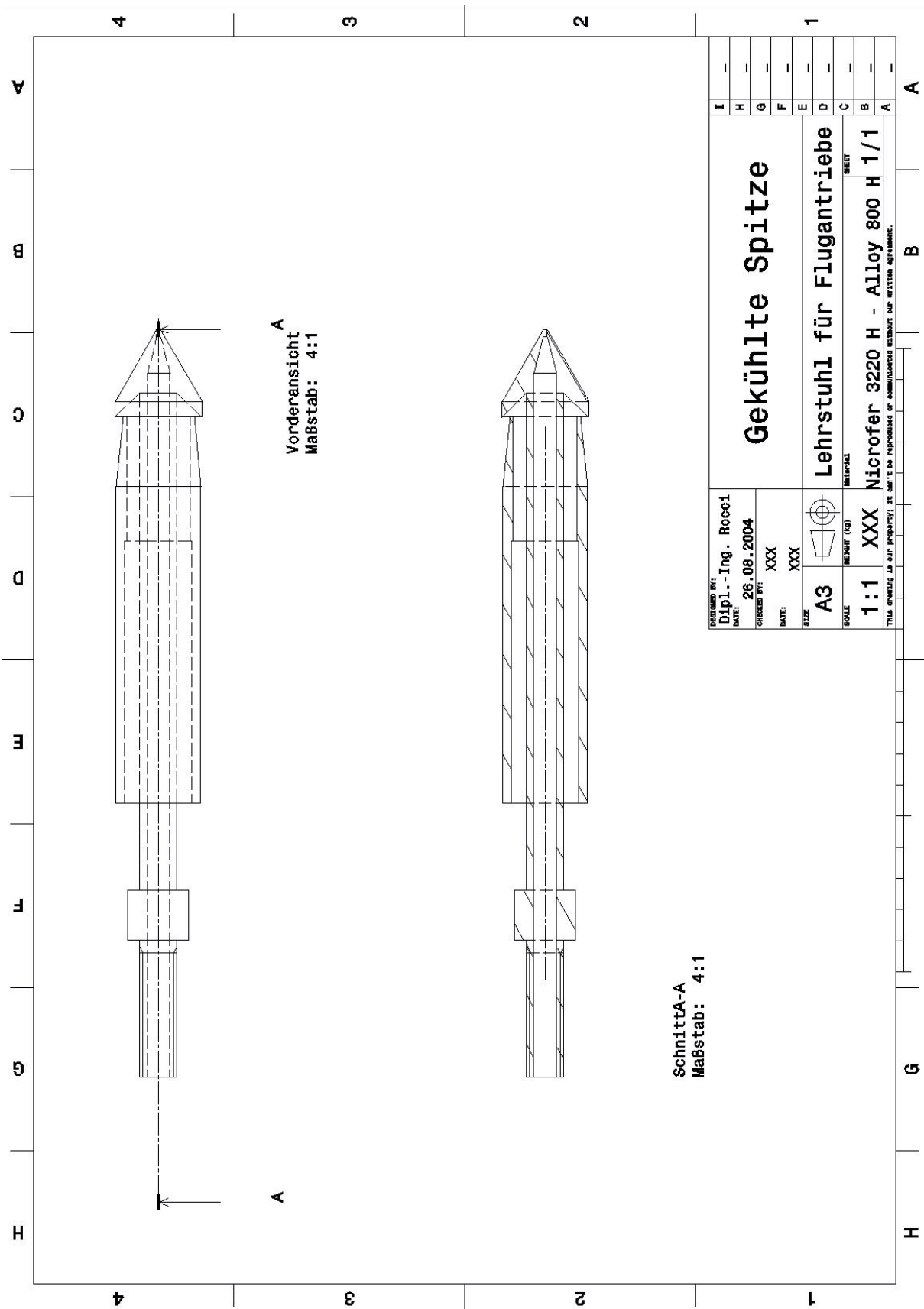


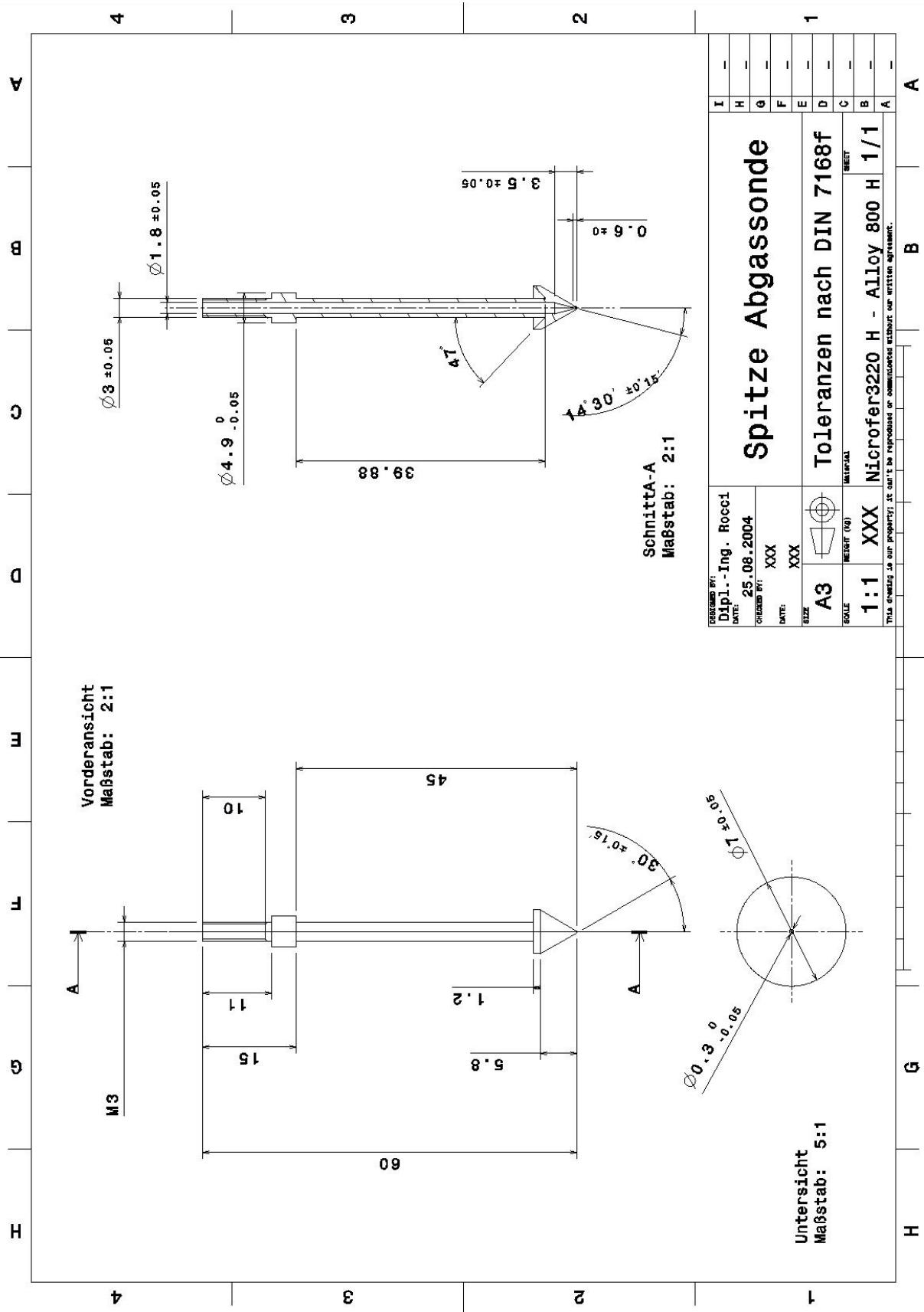


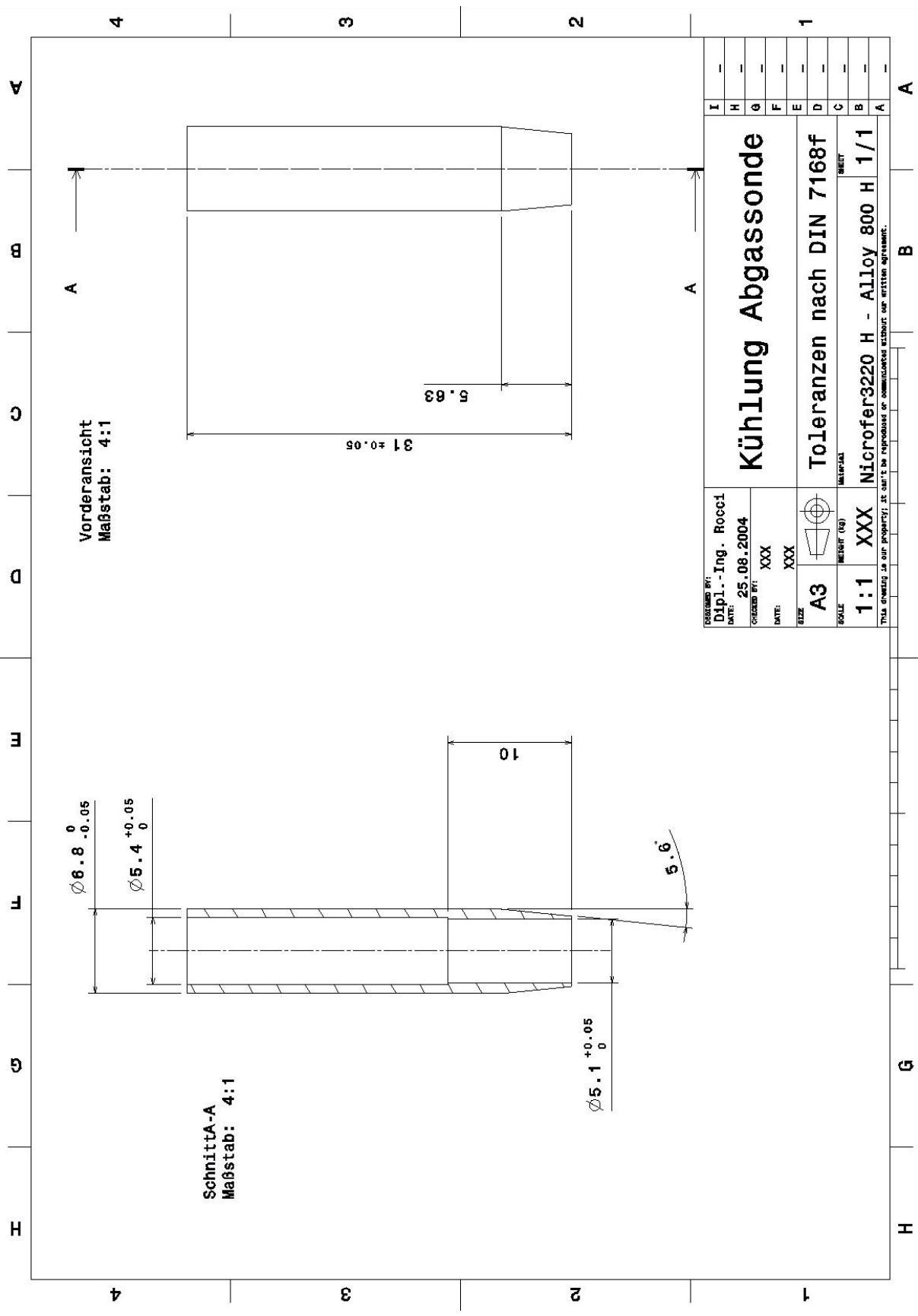
| | | |
|---|-------------------------------|---|
| DESIGNED BY: Dipl.-Ing. Rocci | DATE: 03.07.2006 |  DRAWING NUMBER |
| CHECKED BY: Herr Ritter | DATE: 05.07.2006 | |
| SIZE A4 | MATERIAL ALLOY 800H | SEALING (SQ) XXX |
| MATERIAL ALLOY 800H | | DRAWING NUMBER LFA |
| TOLERANZEN NACH DIN 7168f | | SHEET 1/2 |

This drawing is our property; it can't be reproduced or communicated without our written agreement.

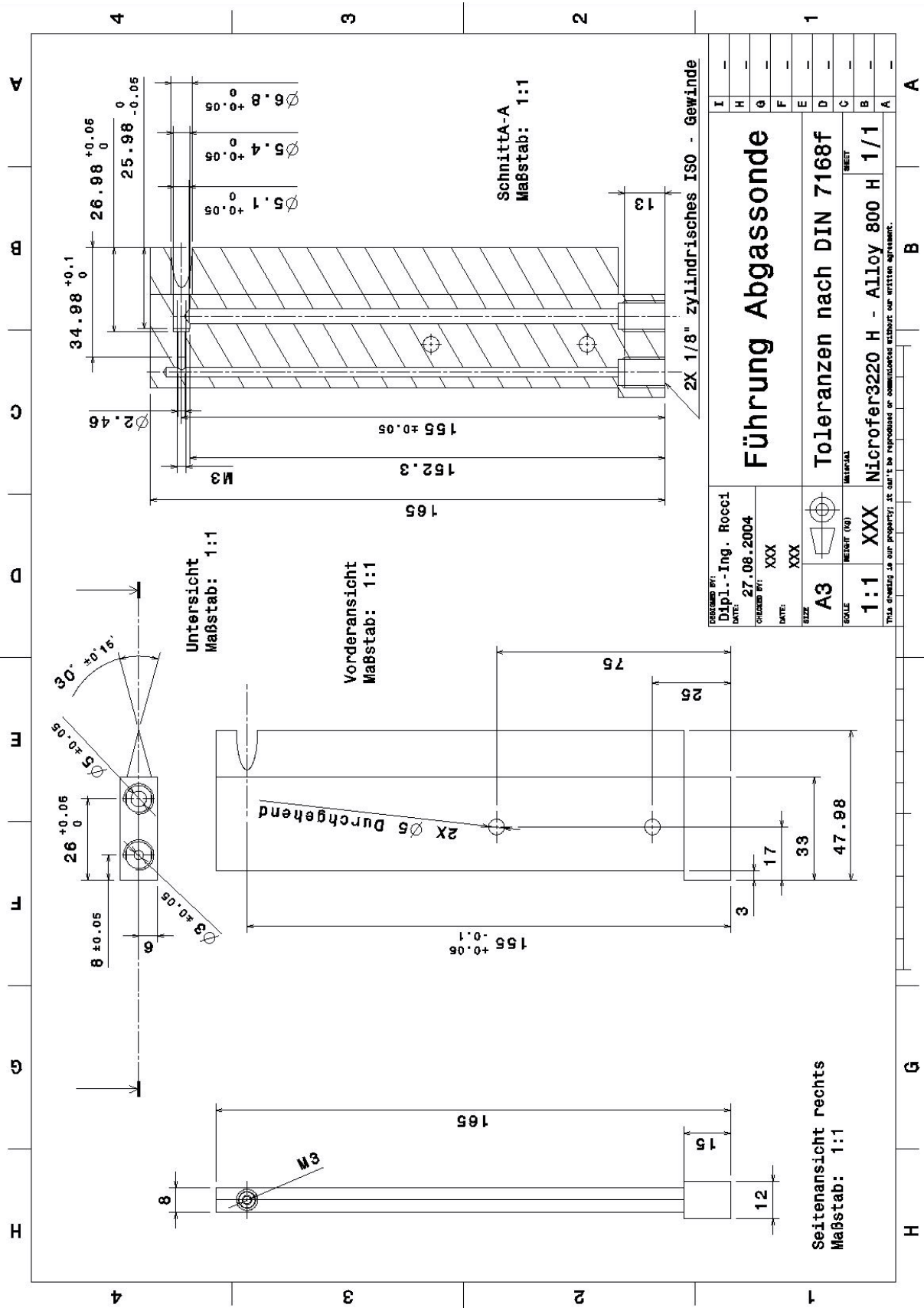
A.6 Gas Sampling and Total Pressure Probe







| | | | | | | | | |
|---|------------------|------------|-----------|---------------------------|------------|------------|----------------------------|--|
| DESIGNER: Dipl.-Ing. Rocci | DATE: 25.08.2004 | CHIEF: XXX | DATE: XXX | SIZE: A3 | SCALE: 1:1 | SHEET: XXX | TOLERANCES: nach DIN 7168f | MATERIAL: Microfer3220 H - Alloy 800 H |
| Kühlung Abgassonde | | | | Toleranzen nach DIN 7168f | | 1/1 | | |
| This drawing is our property; it can't be reproduced or communicated without our written agreement. | | | | | | | | |



| | | | | | | | | | | | | | | | | | | | | | | | | | |
|---|---------------------|------------------|--------------|---|---------------|--|---|---|---|---|---|---|---|---|---|---|---|---|---|---|---|---|---|---|---|
| DESIGNER BY: Dipl.-Ing. Rocci | DATE: 27.08.2004 | ORDER BY: XXX | DATE: XXX | SIZE: A3 | SCALE: 1:1 | TOLERANCES: Toleranzen nach DIN 7168f | MATERIAL: Microfer3220 H - Alloy 800 H | | | | | | | | | | | | | | | | | | |
| THIS DRAWING IS OUR PROPERTY. IT CAN'T BE REPRODUCED OR COMMUNICATED WITHOUT OUR WRITTEN AGREEMENT. | | | | <table border="1"> <tr><td>I</td><td>-</td></tr> <tr><td>H</td><td>-</td></tr> <tr><td>G</td><td>-</td></tr> <tr><td>F</td><td>-</td></tr> <tr><td>E</td><td>-</td></tr> <tr><td>D</td><td>-</td></tr> <tr><td>C</td><td>-</td></tr> <tr><td>B</td><td>-</td></tr> <tr><td>A</td><td>-</td></tr> </table> | | | | I | - | H | - | G | - | F | - | E | - | D | - | C | - | B | - | A | - |
| I | - | | | | | | | | | | | | | | | | | | | | | | | | |
| H | - | | | | | | | | | | | | | | | | | | | | | | | | |
| G | - | | | | | | | | | | | | | | | | | | | | | | | | |
| F | - | | | | | | | | | | | | | | | | | | | | | | | | |
| E | - | | | | | | | | | | | | | | | | | | | | | | | | |
| D | - | | | | | | | | | | | | | | | | | | | | | | | | |
| C | - | | | | | | | | | | | | | | | | | | | | | | | | |
| B | - | | | | | | | | | | | | | | | | | | | | | | | | |
| A | - | | | | | | | | | | | | | | | | | | | | | | | | |

Appendix B Experimental Runs Summary

| Test | Labelling | Configuration | Conditions | Main Air | Pilot H2 | Pilot Air | Pilot O2 | Strut CH4 | Cavity CH4 |
|------|-------------|---------------|-------------------------|----------|----------|-----------|----------|-----------|------------|
| [-] | [-] | [-] | [-] | [g/s] | [mg/s] | [bar] | [bar] | [g/s] | [g/s] |
| 1 | S1_FOFF1 | Strut 1 | Fuel Off | 360 | | | | | |
| 1 | S1_FON_PF1 | Strut 1 | Fuel On Pilot Flame | 360 | 100 | | | | |
| 1 | S1_FON_PF2 | Strut 1 | Fuel On Pilot Flame | 360 | 150 | | | | |
| 1 | S1_FON_PF3 | Strut 1 | Fuel On Pilot Flame | 360 | 200 | | | | |
| 1 | S1_FON_PF4 | Strut 1 | Fuel On Pilot Flame | 360 | 250 | | | | |
| 1 | S1_FON_PF5 | Strut 1 | Fuel On Pilot Flame Air | 360 | 250 | 2 | | | |
| 1 | S1_FON_PF6 | Strut 1 | Fuel On Pilot Flame Air | 360 | 200 | 2 | | | |
| 1 | S1_FON_PF7 | Strut 1 | Fuel On Pilot Flame Air | 360 | 150 | 2 | | | |
| 1 | S1_FON_PF8 | Strut 1 | Fuel On Pilot Flame Air | 360 | 100 | 2 | | | |
| 1 | S1_FON_PF9 | Strut 1 | Fuel On Pilot Flame Air | 360 | 100 | 4 | | | |
| 1 | S1_FON_PF10 | Strut 1 | Fuel On Pilot Flame Air | 360 | 150 | 4 | | | |
| 1 | S1_FON_PF11 | Strut 1 | Fuel On Pilot Flame Air | 360 | 200 | 4 | | | |
| 1 | S1_FON_PF12 | Strut 1 | Fuel On Pilot Flame Air | 360 | 250 | 4 | | | |
| 1 | S1_FON_PF13 | Strut 1 | Fuel On Pilot Flame Air | 360 | 250 | 6 | | | |
| 1 | S1_FON_PF14 | Strut 1 | Fuel On Pilot Flame Air | 360 | 200 | 6 | | | |
| 1 | S1_FON_PF15 | Strut 1 | Fuel On Pilot Flame Air | 360 | 150 | 6 | | | |
| 1 | S1_FON_PF16 | Strut 1 | Fuel On Pilot Flame Air | 360 | 100 | 6 | | | |
| 1 | S1_FON_PF17 | Strut 1 | Fuel On Pilot Flame O2 | 360 | 100 | | 2 | | |
| 1 | S1_FON_PF18 | Strut 1 | Fuel On Pilot Flame O2 | 360 | 150 | | 2 | | |
| 1 | S1_FON_PF19 | Strut 1 | Fuel On Pilot Flame O2 | 360 | 200 | | 2 | | |
| 1 | S1_FON_PF20 | Strut 1 | Fuel On Pilot Flame O2 | 360 | 250 | | 2 | | |

| Test | Labelling | Configuration | Conditions | Main Air | Pilot H2 | Pilot Air | Pilot O2 | Strut CH4 | Cavity CH4 |
|------|-------------|---------------|----------------------------|----------|----------|-----------|----------|-----------|------------|
| [-] | [-] | [-] | [-] | [g/s] | [mg/s] | [bar] | [bar] | [g/s] | [g/s] |
| 1 | S1_FON_PF21 | Strut 1 | Fuel On Pilot Flame O2 | 360 | 250 | | 4 | | |
| 1 | S1_FON_PF22 | Strut 1 | Fuel On Pilot Flame O2 | 360 | 200 | | 4 | | |
| 1 | S1_FON_PF23 | Strut 1 | Fuel On Pilot Flame O2 | 360 | 150 | | 4 | | |
| 1 | S1_FON_PF24 | Strut 1 | Fuel On Pilot Flame O2 | 360 | 100 | | 4 | | |
| 1 | S1_FON_PF25 | Strut 1 | Fuel On Pilot Flame O2 | 360 | 100 | | 6 | | |
| 1 | S1_FON_PF26 | Strut 1 | Fuel On Pilot Flame O2 | 360 | 150 | | 6 | | |
| 1 | S1_FON_PF27 | Strut 1 | Fuel On Pilot Flame O2 | 360 | 200 | | 6 | | |
| 1 | S1_FON_PF28 | Strut 1 | Fuel On Pilot Flame O2 | 360 | 250 | | 6 | | |
| 1 | S1_COM_PF1 | Strut 1 | Combustion Pilot Flame | 360 | 100 | | | | |
| 1 | S1_COM_PF2 | Strut 1 | Combustion Pilot Flame | 360 | 150 | | | | |
| 1 | S1_COM_PF3 | Strut 1 | Combustion Pilot Flame | 360 | 200 | | | | |
| 1 | S1_COM_PF4 | Strut 1 | Combustion Pilot Flame | 360 | 250 | | | | |
| 1 | S1_COM_PF5 | Strut 1 | Combustion Pilot Flame Air | 360 | 250 | 2 | | | |
| 1 | S1_COM_PF6 | Strut 1 | Combustion Pilot Flame Air | 360 | 200 | 2 | | | |
| 1 | S1_COM_PF7 | Strut 1 | Combustion Pilot Flame Air | 360 | 150 | 2 | | | |
| 1 | S1_COM_PF8 | Strut 1 | Combustion Pilot Flame Air | 360 | 100 | 2 | | | |
| 1 | S1_COM_PF9 | Strut 1 | Combustion Pilot Flame Air | 360 | 100 | 4 | | | |
| 1 | S1_COM_PF10 | Strut 1 | Combustion Pilot Flame Air | 360 | 150 | 4 | | | |
| 1 | S1_COM_PF11 | Strut 1 | Combustion Pilot Flame Air | 360 | 200 | 4 | | | |
| 1 | S1_COM_PF12 | Strut 1 | Combustion Pilot Flame Air | 360 | 250 | 4 | | | |
| 1 | S1_COM_PF13 | Strut 1 | Combustion Pilot Flame Air | 360 | 250 | 6 | | | |
| 1 | S1_COM_PF14 | Strut 1 | Combustion Pilot Flame Air | 360 | 200 | 6 | | | |
| 1 | S1_COM_PF15 | Strut 1 | Combustion Pilot Flame Air | 360 | 150 | 6 | | | |
| 1 | S1_COM_PF16 | Strut 1 | Combustion Pilot Flame Air | 360 | 100 | 6 | | | |
| 1 | S1_COM_PF17 | Strut 1 | Combustion Pilot Flame O2 | 360 | 100 | | 2 | | |
| 1 | S1_COM_PF18 | Strut 1 | Combustion Pilot Flame O2 | 360 | 150 | | 2 | | |
| 1 | S1_COM_PF19 | Strut 1 | Combustion Pilot Flame O2 | 360 | 200 | | 2 | | |

| Test | Labelling | Configuration | Conditions | Main Air | Pilot H2 | Pilot Air | Pilot O2 | Strut CH4 | Cavity CH4 |
|------|-------------|---------------|----------------------------|----------|----------|-----------|----------|-----------|------------|
| [-] | [-] | [-] | [-] | [g/s] | [mg/s] | [bar] | [bar] | [g/s] | [g/s] |
| 1 | S1_COM_PF20 | Strut 1 | Combustion Pilot Flame O2 | 360 | 250 | | 2 | | |
| 1 | S1_COM_PF21 | Strut 1 | Combustion Pilot Flame O2 | 360 | 250 | | 4 | | |
| 1 | S1_COM_PF22 | Strut 1 | Combustion Pilot Flame O2 | 360 | 200 | | 4 | | |
| 1 | S1_COM_PF23 | Strut 1 | Combustion Pilot Flame O2 | 360 | 150 | | 4 | | |
| 1 | S1_COM_PF24 | Strut 1 | Combustion Pilot Flame O2 | 360 | 100 | | 4 | | |
| 1 | S1_COM_PF25 | Strut 1 | Combustion Pilot Flame O2 | 360 | 100 | | 6 | | |
| 1 | S1_COM_PF26 | Strut 1 | Combustion Pilot Flame O2 | 360 | 150 | | 6 | | |
| 1 | S1_COM_PF27 | Strut 1 | Combustion Pilot Flame O2 | 360 | 200 | | 6 | | |
| 1 | S1_COM_PF28 | Strut 1 | Combustion Pilot Flame O2 | 360 | 250 | | 6 | | |
| 2 | S1_FOFF2 | Strut 1 | Fuel Off | 345 | | | | | |
| 2 | S1_FON_PF29 | Strut 1 | Fuel On Pilot Flame | 345 | 150 | | | | |
| 2 | S1_FON_PF30 | Strut 1 | Fuel On Pilot Flame | 345 | 200 | | | | |
| 2 | S1_FON_PF31 | Strut 1 | Fuel On Pilot Flame Air | 345 | 200 | 2.35 | | | |
| 2 | S1_FON_PF32 | Strut 1 | Fuel On Pilot Flame Air | 345 | 150 | 2.35 | | | |
| 2 | S1_FON_PF33 | Strut 1 | Fuel On Pilot Flame Air | 345 | 150 | 4 | | | |
| 2 | S1_FON_PF34 | Strut 1 | Fuel On Pilot Flame Air | 345 | 200 | 4 | | | |
| 2 | S1_FON_PF35 | Strut 1 | Fuel On Pilot Flame O2 | 345 | 150 | | 2 | | |
| 2 | S1_FON_PF36 | Strut 1 | Fuel On Pilot Flame O2 | 345 | 200 | | 2 | | |
| 2 | S1_FON_PF37 | Strut 1 | Fuel On Pilot Flame O2 | 345 | 200 | | 3.40 | | |
| 2 | S1_FON_PF38 | Strut 1 | Fuel On Pilot Flame O2 | 345 | 150 | | 3.40 | | |
| 2 | S1_COM_PF29 | Strut 1 | Combustion Pilot Flame | 345 | 150 | | | | |
| 2 | S1_COM_PF30 | Strut 1 | Combustion Pilot Flame | 345 | 200 | | | | |
| 2 | S1_COM_PF31 | Strut 1 | Combustion Pilot Flame Air | 345 | 200 | 2.35 | | | |
| 2 | S1_COM_PF32 | Strut 1 | Combustion Pilot Flame Air | 345 | 150 | 2.35 | | | |
| 2 | S1_COM_PF33 | Strut 1 | Combustion Pilot Flame Air | 345 | 150 | 4 | | | |
| 2 | S1_COM_PF34 | Strut 1 | Combustion Pilot Flame Air | 345 | 200 | 4 | | | |
| 2 | S1_COM_PF35 | Strut 1 | Combustion Pilot Flame O2 | 345 | 150 | | 2 | | |

| Test | Labelling | Configuration | Conditions | Main Air | Pilot H2 | Pilot Air | Pilot O2 | Strut CH4 | Cavity CH4 |
|------|--------------|---------------|----------------------------------|----------|----------|-----------|----------|-----------|------------|
| [-] | [-] | [-] | [-] | [g/s] | [mg/s] | [bar] | [bar] | [g/s] | [g/s] |
| 2 | S1_COM_PF36 | Strut 1 | Combustion Pilot Flame O2 | 345 | 200 | | 2 | | |
| 2 | S1_COM_PF37 | Strut 1 | Combustion Pilot Flame O2 | 345 | 200 | | 3.40 | | |
| 2 | S1_COM_PF38 | Strut 1 | Combustion Pilot Flame O2 | 345 | 150 | | 3.40 | | |
| 3 | S1_FOFF3 | Strut 1 | Fuel Off | 345 | | | | | |
| 3 | S1_FON_PF39 | Strut 1 | Fuel On Pilot Flame O2 | 345 | 100 | | 7 | | |
| 3 | S1_FON_PF40 | Strut 1 | Fuel On Pilot Flame O2 | 345 | 150 | | 7 | | |
| 3 | S1_FON_PF41 | Strut 1 | Fuel On Pilot Flame Air | 345 | 100 | 8 | | | |
| 3 | S1_FON_CH4_1 | Strut 1 | Fuel On Pilot Flame O2 + CH4 | 345 | 100 | | 7 | 1.5 | |
| 3 | S1_FON_CH4_2 | Strut 1 | Fuel On Pilot Flame O2 + CH4 | 345 | 100 | | 7 | 3 | |
| 3 | S1_FON_CH4_3 | Strut 1 | Fuel On Pilot Flame O2 + CH4 | 345 | 100 | | 7 | 4.5 | |
| 3 | S1_FON_CH4_4 | Strut 1 | Fuel On Pilot Flame O2 + CH4 | 345 | 150 | | 7 | 1.5 | |
| 3 | S1_FON_CH4_5 | Strut 1 | Fuel On Pilot Flame O2 + CH4 | 345 | 150 | | 7 | 3 | |
| 3 | S1_FON_CH4_6 | Strut 1 | Fuel On Pilot Flame O2 + CH4 | 345 | 150 | | 7 | 4.5 | |
| 3 | S1_FON_CH4_7 | Strut 1 | Fuel On Pilot Flame Air + CH4 | 345 | 100 | 8 | | 1.5 | |
| 3 | S1_FON_CH4_8 | Strut 1 | Fuel On Pilot Flame Air + CH4 | 345 | 100 | 8 | | 3 | |
| 3 | S1_FON_CH4_9 | Strut 1 | Fuel On Pilot Flame Air + CH4 | 345 | 100 | 8 | | 4.5 | |
| 3 | S1_COM_PF39 | Strut 1 | Combustion Pilot Flame O2 | 345 | 100 | | 7 | | |
| 3 | S1_COM_PF40 | Strut 1 | Combustion Pilot Flame O2 | 345 | 150 | | 7 | | |
| 3 | S1_COM_PF41 | Strut 1 | Combustion Pilot Flame Air | 345 | 100 | 8 | | | |
| 3 | S1_COM_CH4_1 | Strut 1 | Combustion Pilot Flame O2 + CH4 | 345 | 100 | | 7 | 1.5 | |
| 3 | S1_COM_CH4_2 | Strut 1 | Combustion Pilot Flame O2 + CH4 | 345 | 100 | | 7 | 3 | |
| 3 | S1_COM_CH4_3 | Strut 1 | Combustion Pilot Flame O2 + CH4 | 345 | 100 | | 7 | 4.5 | |
| 3 | S1_COM_CH4_4 | Strut 1 | Combustion Pilot Flame O2 + CH4 | 345 | 150 | | 7 | 1.5 | |
| 3 | S1_COM_CH4_5 | Strut 1 | Combustion Pilot Flame O2 + CH4 | 345 | 150 | | 7 | 3 | |
| 3 | S1_COM_CH4_6 | Strut 1 | Combustion Pilot Flame O2 + CH4 | 345 | 150 | | 7 | 4.5 | |
| 3 | S1_COM_CH4_7 | Strut 1 | Combustion Pilot Flame Air + CH4 | 345 | 100 | 8 | | 1.5 | |
| 3 | S1_COM_CH4_8 | Strut 1 | Combustion Pilot Flame Air + CH4 | 345 | 100 | 8 | | 3 | |

| Test | Labelling | Configuration | Conditions | Main Air | Pilot H2 | Pilot Air | Pilot O2 | Strut CH4 | Cavity CH4 |
|------|---------------|---------------|----------------------------------|----------|----------|-----------|----------|-----------|------------|
| [-] | [-] | [-] | [-] | [g/s] | [mg/s] | [bar] | [bar] | [g/s] | [g/s] |
| 3 | S1_COM_CH4_9 | Strut 1 | Combustion Pilot Flame Air + CH4 | 345 | 100 | 8 | | 4.5 | |
| 4 | S1_FOFF4 | Strut 1 | Fuel Off | 345 | | | | | |
| 4 | S1_FON_PF41 | Strut 1 | Fuel On Pilot Flame Air + CH4 | 345 | 100 | | 7 | | |
| 4 | S1_FON_PF42 | Strut 1 | Fuel On Pilot Flame Air + CH4 | 345 | 150 | | 7 | | |
| 4 | S1_FON_CH4_10 | Strut 1 | Fuel On Pilot Flame O2 + CH4 | 345 | 100 | | 7 | 1.5 | |
| 4 | S1_FON_CH4_11 | Strut 1 | Fuel On Pilot Flame O2 + CH4 | 345 | 100 | | 7 | 3 | |
| 4 | S1_FON_CH4_12 | Strut 1 | Fuel On Pilot Flame O2 + CH4 | 345 | 100 | | 7 | 4.5 | |
| 4 | S1_FON_CH4_13 | Strut 1 | Fuel On Pilot Flame O2 + CH4 | 345 | 150 | | 7 | 1.5 | |
| 4 | S1_FON_CH4_14 | Strut 1 | Fuel On Pilot Flame O2 + CH4 | 345 | 150 | | 7 | 3 | |
| 4 | S1_FON_CH4_15 | Strut 1 | Fuel On Pilot Flame O2 + CH4 | 345 | 150 | | 7 | 4.5 | |
| 4 | S1_COM_PF41 | Strut 1 | Combustion Pilot Flame Air + CH4 | 345 | 100 | | 7 | | |
| 4 | S1_COM_PF42 | Strut 1 | Combustion Pilot Flame Air + CH4 | 345 | 150 | | 7 | | |
| 4 | S1_COM_CH4_10 | Strut 1 | Combustion Pilot Flame O2 + CH4 | 345 | 100 | | 7 | 1.5 | |
| 4 | S1_COM_CH4_11 | Strut 1 | Combustion Pilot Flame O2 + CH4 | 345 | 100 | | 7 | 3 | |
| 4 | S1_COM_CH4_12 | Strut 1 | Combustion Pilot Flame O2 + CH4 | 345 | 100 | | 7 | 4.5 | |
| 4 | S1_COM_CH4_13 | Strut 1 | Combustion Pilot Flame O2 + CH4 | 345 | 150 | | 7 | 1.5 | |
| 4 | S1_COM_CH4_14 | Strut 1 | Combustion Pilot Flame O2 + CH4 | 345 | 150 | | 7 | 3 | |
| 4 | S1_COM_CH4_15 | Strut 1 | Combustion Pilot Flame O2 + CH4 | 345 | 150 | | 7 | 4.5 | |
| 5 | S2_FOFF1 | Strut 2 | Fuel Off | 345 | | | | | |
| 5 | S2_FON_PF1 | Strut 2 | Fuel On Pilot Flame O2 | 345 | 100 | | 7 | | |
| 5 | S2_FON_PF2 | Strut 2 | Fuel On Pilot Flame O2 | 345 | 150 | | 7 | | |
| 5 | S2_FON_PF3 | Strut 2 | Fuel On Pilot Flame Air | 345 | 100 | 8 | | | |
| 5 | S2_FON_CH4_1 | Strut 2 | Fuel On Pilot Flame O2 + CH4 | 345 | 100 | | 7 | 1.5 | |
| 5 | S2_FON_CH4_2 | Strut 2 | Fuel On Pilot Flame O2 + CH4 | 345 | 100 | | 7 | 3 | |
| 5 | S2_FON_CH4_3 | Strut 2 | Fuel On Pilot Flame O2 + CH4 | 345 | 100 | | 7 | 4.5 | |
| 5 | S2_FON_CH4_4 | Strut 2 | Fuel On Pilot Flame O2 + CH4 | 345 | 150 | | 7 | 1.5 | |
| 5 | S2_FON_CH4_5 | Strut 2 | Fuel On Pilot Flame O2 + CH4 | 345 | 150 | | 7 | 3 | |

| Test | Labelling | Configuration | Conditions | Main Air | Pilot H2 | Pilot Air | Pilot O2 | Strut CH4 | Cavity CH4 |
|------|---------------|---------------|----------------------------------|----------|----------|-----------|----------|-----------|------------|
| [-] | [-] | [-] | [-] | [g/s] | [mg/s] | [bar] | [bar] | [g/s] | [g/s] |
| 5 | S2_FON_CH4_6 | Strut 2 | Fuel On Pilot Flame O2 + CH4 | 345 | 150 | | 7 | 4.5 | |
| 5 | S2_FON_CH4_7 | Strut 2 | Fuel On Pilot Flame Air + CH4 | 345 | 100 | 8 | | 1.5 | |
| 5 | S2_FON_CH4_8 | Strut 2 | Fuel On Pilot Flame Air + CH4 | 345 | 100 | 8 | | 3 | |
| 5 | S2_FON_CH4_9 | Strut 2 | Fuel On Pilot Flame Air + CH4 | 345 | 100 | 8 | | 4.5 | |
| 5 | S2_COM_PF1 | Strut 2 | Combustion Pilot Flame O2 | 345 | 100 | | 7 | | |
| 5 | S2_COM_PF2 | Strut 2 | Combustion Pilot Flame O2 | 345 | 150 | | 7 | | |
| 5 | S2_COM_PF3 | Strut 2 | Combustion Pilot Flame Air | 345 | 100 | 8 | | | |
| 5 | S2_COM_CH4_1 | Strut 2 | Combustion Pilot Flame O2 + CH4 | 345 | 100 | | 7 | 1.5 | |
| 5 | S2_COM_CH4_2 | Strut 2 | Combustion Pilot Flame O2 + CH4 | 345 | 100 | | 7 | 3 | |
| 5 | S2_COM_CH4_3 | Strut 2 | Combustion Pilot Flame O2 + CH4 | 345 | 100 | | 7 | 4.5 | |
| 5 | S2_COM_CH4_4 | Strut 2 | Combustion Pilot Flame O2 + CH4 | 345 | 150 | | 7 | 1.5 | |
| 5 | S2_COM_CH4_5 | Strut 2 | Combustion Pilot Flame O2 + CH4 | 345 | 150 | | 7 | 3 | |
| 5 | S2_COM_CH4_6 | Strut 2 | Combustion Pilot Flame O2 + CH4 | 345 | 150 | | 7 | 4.5 | |
| 5 | S2_COM_CH4_7 | Strut 2 | Combustion Pilot Flame Air + CH4 | 345 | 100 | 8 | | 1.5 | |
| 5 | S2_COM_CH4_8 | Strut 2 | Combustion Pilot Flame Air + CH4 | 345 | 100 | 8 | | 3 | |
| 5 | S2_COM_CH4_9 | Strut 2 | Combustion Pilot Flame Air + CH4 | 345 | 100 | 8 | | 4.5 | |
| 6 | S2_FOFF2 | Strut 2 | Fuel Off | 345 | | | | | |
| 6 | S2_FON_PF4 | Strut 2 | Fuel On Pilot Flame O2 + CH4 | 345 | 100 | | 7 | | |
| 6 | S2_FON_PF5 | Strut 2 | Fuel On Pilot Flame O2 + CH4 | 345 | 150 | | 7 | | |
| 6 | S2_FON_CH4_10 | Strut 2 | Fuel On Pilot Flame O2 + CH4 | 345 | 100 | | 7 | 1.5 | |
| 6 | S2_FON_CH4_11 | Strut 2 | Fuel On Pilot Flame O2 + CH4 | 345 | 100 | | 7 | 3 | |
| 6 | S2_FON_CH4_12 | Strut 2 | Fuel On Pilot Flame O2 + CH4 | 345 | 100 | | 7 | 4.5 | |
| 6 | S2_FON_CH4_13 | Strut 2 | Fuel On Pilot Flame O2 + CH4 | 345 | 150 | | 7 | 1.5 | |
| 6 | S2_FON_CH4_14 | Strut 2 | Fuel On Pilot Flame O2 + CH4 | 345 | 150 | | 7 | 3 | |
| 6 | S2_FON_CH4_15 | Strut 2 | Fuel On Pilot Flame O2 + CH4 | 345 | 150 | | 7 | 4.5 | |
| 6 | S2_COM_PF4 | Strut 2 | Combustion Pilot Flame O2 + CH4 | 345 | 100 | | 7 | | |
| 6 | S2_COM_PF5 | Strut 2 | Combustion Pilot Flame O2 + CH4 | 345 | 150 | | 7 | | |

| Test | Labelling | Configuration | Conditions | Main Air | Pilot H2 | Pilot Air | Pilot O2 | Strut CH4 | Cavity CH4 |
|------|---------------|---------------|---------------------------------|----------|----------|-----------|----------|-----------|------------|
| [-] | [-] | [-] | [-] | [g/s] | [mg/s] | [bar] | [bar] | [g/s] | [g/s] |
| 6 | S2_COM_CH4_10 | Strut 2 | Combustion Pilot Flame O2 + CH4 | 345 | 100 | | 7 | 1.5 | |
| 6 | S2_COM_CH4_11 | Strut 2 | Combustion Pilot Flame O2 + CH4 | 345 | 100 | | 7 | 3 | |
| 6 | S2_COM_CH4_12 | Strut 2 | Combustion Pilot Flame O2 + CH4 | 345 | 100 | | 7 | 4.5 | |
| 6 | S2_COM_CH4_13 | Strut 2 | Combustion Pilot Flame O2 + CH4 | 345 | 150 | | 7 | 1.5 | |
| 6 | S2_COM_CH4_14 | Strut 2 | Combustion Pilot Flame O2 + CH4 | 345 | 150 | | 7 | 3 | |
| 6 | S2_COM_CH4_15 | Strut 2 | Combustion Pilot Flame O2 + CH4 | 345 | 150 | | 7 | 4.5 | |
| 7 | S3_FOFF1 | Strut 3 | Fuel Off | 345 | | | | | |
| 7 | S3_FON_PF1 | Strut 3 | Fuel On Pilot Flame O2 | 345 | 75 | | 7 | | |
| 7 | S3_FON_PF2 | Strut 3 | Fuel On Pilot Flame O2 | 345 | 100 | | 7 | | |
| 7 | S3_FON_PF3 | Strut 3 | Fuel On Pilot Flame Air | 345 | 100 | 8 | | | |
| 7 | S3_FON_CH4_1 | Strut 3 | Fuel On Pilot Flame O2 + CH4 | 345 | 75 | | 7 | 1.5 | |
| 7 | S3_FON_CH4_2 | Strut 3 | Fuel On Pilot Flame O2 + CH4 | 345 | 75 | | 7 | 3 | |
| 7 | S3_FON_CH4_3 | Strut 3 | Fuel On Pilot Flame O2 + CH4 | 345 | 75 | | 7 | 4.5 | |
| 7 | S3_FON_CH4_4 | Strut 3 | Fuel On Pilot Flame O2 + CH4 | 345 | 100 | | 7 | 1.5 | |
| 7 | S3_FON_CH4_5 | Strut 3 | Fuel On Pilot Flame O2 + CH4 | 345 | 100 | | 7 | 3 | |
| 7 | S3_FON_CH4_6 | Strut 3 | Fuel On Pilot Flame O2 + CH4 | 345 | 100 | | 7 | 4.5 | |
| 7 | S3_FON_CH4_7 | Strut 3 | Fuel On Pilot Flame Air + CH4 | 345 | 100 | 8 | | 1.5 | |
| 7 | S3_FON_CH4_8 | Strut 3 | Fuel On Pilot Flame Air + CH4 | 345 | 100 | 8 | | 3 | |
| 7 | S3_FON_CH4_9 | Strut 3 | Fuel On Pilot Flame Air + CH4 | 345 | 100 | 8 | | 4.5 | |
| 7 | S3_COM_PF1 | Strut 3 | Combustion Pilot Flame O2 | 345 | 75 | | 7 | | |
| 7 | S3_COM_PF2 | Strut 3 | Combustion Pilot Flame O2 | 345 | 100 | | 7 | | |
| 7 | S3_COM_PF3 | Strut 3 | Combustion Pilot Flame Air | 345 | 100 | 8 | | | |
| 7 | S3_COM_CH4_1 | Strut 3 | Combustion Pilot Flame O2 + CH4 | 345 | 75 | | 7 | 1.5 | |
| 7 | S3_COM_CH4_2 | Strut 3 | Combustion Pilot Flame O2 + CH4 | 345 | 75 | | 7 | 3 | |
| 7 | S3_COM_CH4_3 | Strut 3 | Combustion Pilot Flame O2 + CH4 | 345 | 75 | | 7 | 4.5 | |
| 7 | S3_COM_CH4_4 | Strut 3 | Combustion Pilot Flame O2 + CH4 | 345 | 100 | | 7 | 1.5 | |
| 7 | S3_COM_CH4_5 | Strut 3 | Combustion Pilot Flame O2 + CH4 | 345 | 100 | | 7 | 3 | |

| Test | Labelling | Configuration | Conditions | Main Air | Pilot H2 | Pilot Air | Pilot O2 | Strut CH4 | Cavity CH4 |
|------|---------------|------------------|----------------------------------|----------|----------|-----------|----------|-----------|------------|
| [-] | [-] | [-] | [-] | [g/s] | [mg/s] | [bar] | [bar] | [g/s] | [g/s] |
| 7 | S3_COM_CH4_6 | Strut 3 | Combustion Pilot Flame O2 + CH4 | 345 | 100 | | 7 | 4.5 | |
| 7 | S3_COM_CH4_7 | Strut 3 | Combustion Pilot Flame Air + CH4 | 345 | 100 | 8 | | 1.5 | |
| 7 | S3_COM_CH4_8 | Strut 3 | Combustion Pilot Flame Air + CH4 | 345 | 100 | 8 | | 3 | |
| 7 | S3_COM_CH4_9 | Strut 3 | Combustion Pilot Flame Air + CH4 | 345 | 100 | 8 | | 4.5 | |
| 8 | S3_FOFF2 | Strut 3 | Fuel Off | 345 | | | | | |
| 8 | S3_FON_PF4 | Strut 3 | Fuel On Pilot Flame O2 + CH4 | 345 | 75 | | 7 | | |
| 8 | S3_FON_PF5 | Strut 3 | Fuel On Pilot Flame O2 + CH4 | 345 | 100 | | 7 | | |
| 8 | S3_FON_CH4_10 | Strut 3 | Fuel On Pilot Flame O2 + CH4 | 345 | 75 | | 7 | 1.5 | |
| 8 | S3_FON_CH4_11 | Strut 3 | Fuel On Pilot Flame O2 + CH4 | 345 | 75 | | 7 | 3 | |
| 8 | S3_FON_CH4_12 | Strut 3 | Fuel On Pilot Flame O2 + CH4 | 345 | 75 | | 7 | 4.5 | |
| 8 | S3_FON_CH4_13 | Strut 3 | Fuel On Pilot Flame O2 + CH4 | 345 | 100 | | 7 | 1.5 | |
| 8 | S3_FON_CH4_14 | Strut 3 | Fuel On Pilot Flame O2 + CH4 | 345 | 100 | | 7 | 3 | |
| 8 | S3_FON_CH4_15 | Strut 3 | Fuel On Pilot Flame O2 + CH4 | 345 | 100 | | 7 | 4.5 | |
| 8 | S3_COM_PF4 | Strut 3 | Combustion Pilot Flame O2 + CH4 | 345 | 75 | | 7 | | |
| 8 | S3_COM_PF5 | Strut 3 | Combustion Pilot Flame O2 + CH4 | 345 | 100 | | 7 | | |
| 8 | S3_COM_CH4_10 | Strut 3 | Combustion Pilot Flame O2 + CH4 | 345 | 75 | | 7 | 1.5 | |
| 8 | S3_COM_CH4_11 | Strut 3 | Combustion Pilot Flame O2 + CH4 | 345 | 75 | | 7 | 3 | |
| 8 | S3_COM_CH4_12 | Strut 3 | Combustion Pilot Flame O2 + CH4 | 345 | 75 | | 7 | 4.5 | |
| 8 | S3_COM_CH4_13 | Strut 3 | Combustion Pilot Flame O2 + CH4 | 345 | 100 | | 7 | 1.5 | |
| 8 | S3_COM_CH4_14 | Strut 3 | Combustion Pilot Flame O2 + CH4 | 345 | 100 | | 7 | 3 | |
| 8 | S3_COM_CH4_15 | Strut 3 | Combustion Pilot Flame O2 + CH4 | 345 | 100 | | 7 | 4.5 | |
| 9 | S1C_FOFF1 | Strut 1 + Cavity | Fuel Off | 360 | | | | | |
| 9 | S1C_FON_PF_1 | Strut 1 + Cavity | Fuel On Pilot Flame O2 | 360 | 100 | | 7 | | |
| 9 | S1C_FON_CH4_1 | Strut 1 + Cavity | Fuel On Pilot Flame O2 + CH4 | 360 | 100 | | 7 | | 3 |
| 9 | S1C_FON_CH4_2 | Strut 1 + Cavity | Fuel On Pilot Flame O2 + CH4 | 360 | 100 | | 7 | | 5 |
| 9 | S1C_FON_CH4_3 | Strut 1 + Cavity | Fuel On Pilot Flame O2 + CH4 | 360 | 100 | | 7 | | 7 |
| 9 | S1C_FON_CH4_4 | Strut 1 + Cavity | Fuel On Pilot Flame O2 + CH4 | 360 | 100 | | 7 | 2 | 0 |

| Test | Labelling | Configuration | Conditions | Main Air | Pilot H2 | Pilot Air | Pilot O2 | Strut CH4 | Cavity CH4 |
|------|----------------|------------------|---------------------------------|----------|----------|-----------|----------|-----------|------------|
| [-] | [-] | [-] | [-] | [g/s] | [mg/s] | [bar] | [bar] | [g/s] | [g/s] |
| 9 | S1C_FON_CH4_5 | Strut 1 + Cavity | Fuel On Pilot Flame O2 + CH4 | 360 | 100 | | 7 | 2 | 3 |
| 9 | S1C_FON_CH4_6 | Strut 1 + Cavity | Fuel On Pilot Flame O2 + CH4 | 360 | 100 | | 7 | 2 | 5 |
| 9 | S1C_FON_CH4_7 | Strut 1 + Cavity | Fuel On Pilot Flame O2 + CH4 | 360 | 100 | | 7 | 2 | 7 |
| 9 | S1C_COM_PF_1 | Strut 1 + Cavity | Fuel On Pilot Flame O2 | 360 | 100 | | 7 | | |
| 9 | S1C_COM_CH4_1 | Strut 1 + Cavity | Combustion Pilot Flame O2 + CH4 | 360 | 100 | | 7 | | 3 |
| 9 | S1C_COM_CH4_2 | Strut 1 + Cavity | Combustion Pilot Flame O2 + CH4 | 360 | 100 | | 7 | | 5 |
| 9 | S1C_COM_CH4_3 | Strut 1 + Cavity | Combustion Pilot Flame O2 + CH4 | 360 | 100 | | 7 | | 7 |
| 9 | S1C_COM_CH4_4 | Strut 1 + Cavity | Combustion Pilot Flame O2 + CH4 | 360 | 100 | | 7 | 2 | 0 |
| 9 | S1C_COM_CH4_5 | Strut 1 + Cavity | Combustion Pilot Flame O2 + CH4 | 360 | 100 | | 7 | 2 | 3 |
| 9 | S1C_COM_CH4_6 | Strut 1 + Cavity | Combustion Pilot Flame O2 + CH4 | 360 | 100 | | 7 | 2 | 5 |
| 9 | S1C_COM_CH4_7 | Strut 1 + Cavity | Combustion Pilot Flame O2 + CH4 | 360 | 100 | | 7 | 2 | 7 |
| 10 | S1C_FOFF2 | Strut 1 + Cavity | Fuel Off | 360 | | | | | |
| 10 | S1C_FON_PF_2 | Strut 1 + Cavity | Fuel On Pilot Flame O2 | 360 | 100 | | 7 | | |
| 10 | S1C_FON_CH4_8 | Strut 1 + Cavity | Fuel On Pilot Flame O2 + CH4 | 360 | 100 | | 7 | | 3 |
| 10 | S1C_FON_CH4_9 | Strut 1 + Cavity | Fuel On Pilot Flame O2 + CH4 | 360 | 100 | | 7 | | 5 |
| 10 | S1C_FON_CH4_10 | Strut 1 + Cavity | Fuel On Pilot Flame O2 + CH4 | 360 | 100 | | 7 | | 7 |
| 10 | S1C_FON_CH4_11 | Strut 1 + Cavity | Fuel On Pilot Flame O2 + CH4 | 360 | 100 | | 7 | 2 | 0 |
| 10 | S1C_FON_CH4_12 | Strut 1 + Cavity | Fuel On Pilot Flame O2 + CH4 | 360 | 100 | | 7 | 2 | 3 |
| 10 | S1C_FON_CH4_13 | Strut 1 + Cavity | Fuel On Pilot Flame O2 + CH4 | 360 | 100 | | 7 | 2 | 5 |
| 10 | S1C_FON_CH4_14 | Strut 1 + Cavity | Fuel On Pilot Flame O2 + CH4 | 360 | 100 | | 7 | 2 | 7 |
| 10 | S1C_COM_PF_2 | Strut 1 + Cavity | Fuel On Pilot Flame O2 | 360 | 100 | | 7 | | |
| 10 | S1C_COM_CH4_8 | Strut 1 + Cavity | Combustion Pilot Flame O2 + CH4 | 360 | 100 | | 7 | | 3 |
| 10 | S1C_COM_CH4_9 | Strut 1 + Cavity | Combustion Pilot Flame O2 + CH4 | 360 | 100 | | 7 | | 5 |
| 10 | S1C_COM_CH4_10 | Strut 1 + Cavity | Combustion Pilot Flame O2 + CH4 | 360 | 100 | | 7 | | 7 |
| 10 | S1C_COM_CH4_11 | Strut 1 + Cavity | Combustion Pilot Flame O2 + CH4 | 360 | 100 | | 7 | 2 | 0 |
| 10 | S1C_COM_CH4_12 | Strut 1 + Cavity | Combustion Pilot Flame O2 + CH4 | 360 | 100 | | 7 | 2 | 3 |
| 10 | S1C_COM_CH4_13 | Strut 1 + Cavity | Combustion Pilot Flame O2 + CH4 | 360 | 100 | | 7 | 2 | 5 |

| Test | Labelling | Configuration | Conditions | Main Air | Pilot H2 | Pilot Air | Pilot O2 | Strut CH4 | Cavity CH4 |
|------|----------------|------------------|---------------------------------|----------|----------|-----------|----------|-----------|------------|
| [-] | [-] | [-] | [-] | [g/s] | [mg/s] | [bar] | [bar] | [g/s] | [g/s] |
| 10 | S1C_COM_CH4_14 | Strut 1 + Cavity | Combustion Pilot Flame O2 + CH4 | 360 | 100 | | 7 | 2 | 7 |
| 11 | S3C_FOFF1 | Strut 3 + Cavity | Fuel Off | 360 | | | | | |
| 11 | S3C_FON_PF_1 | Strut 3 + Cavity | Fuel On Pilot Flame O2 | 360 | 100 | | 7 | | |
| 11 | S3C_FON_CH4_1 | Strut 3 + Cavity | Fuel On Pilot Flame O2 + CH4 | 360 | 100 | | 7 | | 3 |
| 11 | S3C_FON_CH4_2 | Strut 3 + Cavity | Fuel On Pilot Flame O2 + CH4 | 360 | 100 | | 7 | | 5 |
| 11 | S3C_FON_CH4_3 | Strut 3 + Cavity | Fuel On Pilot Flame O2 + CH4 | 360 | 100 | | 7 | | 7 |
| 11 | S3C_FON_CH4_4 | Strut 3 + Cavity | Fuel On Pilot Flame O2 + CH4 | 360 | 100 | | 7 | 2 | 3 |
| 11 | S3C_FON_CH4_5 | Strut 3 + Cavity | Fuel On Pilot Flame O2 + CH4 | 360 | 100 | | 7 | 2 | 5 |
| 11 | S3C_FON_CH4_6 | Strut 3 + Cavity | Fuel On Pilot Flame O2 + CH4 | 360 | 100 | | 7 | 2 | 7 |
| 11 | S3C_COM_PF_1 | Strut 3 + Cavity | Fuel On Pilot Flame O2 | 360 | 100 | | 7 | | |
| 11 | S3C_COM_CH4_1 | Strut 3 + Cavity | Combustion Pilot Flame O2 + CH4 | 360 | 100 | | 7 | | 3 |
| 11 | S3C_COM_CH4_2 | Strut 3 + Cavity | Combustion Pilot Flame O2 + CH4 | 360 | 100 | | 7 | | 5 |
| 11 | S3C_COM_CH4_3 | Strut 3 + Cavity | Combustion Pilot Flame O2 + CH4 | 360 | 100 | | 7 | | 7 |
| 11 | S3C_COM_CH4_4 | Strut 3 + Cavity | Combustion Pilot Flame O2 + CH4 | 360 | 100 | | 7 | 2 | 3 |
| 11 | S3C_COM_CH4_5 | Strut 3 + Cavity | Combustion Pilot Flame O2 + CH4 | 360 | 100 | | 7 | 2 | 5 |
| 11 | S3C_COM_CH4_6 | Strut 3 + Cavity | Combustion Pilot Flame O2 + CH4 | 360 | 100 | | 7 | 2 | 7 |
| 12 | S3C_FOFF2 | Strut 3 + Cavity | Fuel Off | 360 | | | | | |
| 12 | S3C_FON_PF_2 | Strut 3 + Cavity | Fuel On Pilot Flame O2 | 360 | 100 | | 7 | | |
| 12 | S3C_FON_CH4_7 | Strut 3 + Cavity | Fuel On Pilot Flame O2 + CH4 | 360 | 100 | | 7 | | 3 |
| 12 | S3C_FON_CH4_8 | Strut 3 + Cavity | Fuel On Pilot Flame O2 + CH4 | 360 | 100 | | 7 | | 5 |
| 12 | S3C_FON_CH4_9 | Strut 3 + Cavity | Fuel On Pilot Flame O2 + CH4 | 360 | 100 | | 7 | | 7 |
| 12 | S3C_FON_CH4_10 | Strut 3 + Cavity | Fuel On Pilot Flame O2 + CH4 | 360 | 100 | | 7 | 2 | 0 |
| 12 | S3C_FON_CH4_11 | Strut 3 + Cavity | Fuel On Pilot Flame O2 + CH4 | 360 | 100 | | 7 | 2 | 3 |
| 12 | S3C_FON_CH4_12 | Strut 3 + Cavity | Fuel On Pilot Flame O2 + CH4 | 360 | 100 | | 7 | 2 | 5 |
| 12 | S3C_FON_CH4_13 | Strut 3 + Cavity | Fuel On Pilot Flame O2 + CH4 | 360 | 100 | | 7 | 2 | 7 |
| 12 | S3C_COM_PF_2 | Strut 3 + Cavity | Combustion Pilot Flame O2 | 360 | 100 | | 7 | | |
| 12 | S3C_COM_CH4_7 | Strut 3 + Cavity | Combustion Pilot Flame O2 + CH4 | 360 | 100 | | 7 | | 3 |

| Test | Labelling | Configuration | Conditions | Main Air | Pilot H2 | Pilot Air | Pilot O2 | Strut CH4 | Cavity CH4 |
|-------------|------------------|----------------------|---------------------------------|-----------------|-----------------|------------------|-----------------|------------------|-------------------|
| [-] | [-] | [-] | [-] | [g/s] | [mg/s] | [bar] | [bar] | [g/s] | [g/s] |
| 12 | S3C_COM_CH4_8 | Strut 3 + Cavity | Combustion Pilot Flame O2 + CH4 | 360 | 100 | | 7 | | 5 |
| 12 | S3C_COM_CH4_9 | Strut 3 + Cavity | Combustion Pilot Flame O2 + CH4 | 360 | 100 | | 7 | | 7 |
| 12 | S3C_COM_CH4_10 | Strut 3 + Cavity | Combustion Pilot Flame O2 + CH4 | 360 | 100 | | 7 | 2 | 0 |
| 12 | S3C_COM_CH4_11 | Strut 3 + Cavity | Combustion Pilot Flame O2 + CH4 | 360 | 100 | | 7 | 2 | 3 |
| 12 | S3C_COM_CH4_12 | Strut 3 + Cavity | Combustion Pilot Flame O2 + CH4 | 360 | 100 | | 7 | 2 | 5 |
| 12 | S3C_COM_CH4_13 | Strut 3 + Cavity | Combustion Pilot Flame O2 + CH4 | 360 | 100 | | 7 | 2 | 7 |

Bibliography

- [1] G.Y. Anderson, C.R. McClinton, J.P. Weidner
Scramjet Performance
Chapter 6 in *Scramjet Propulsion - AIAA Progress in Astronautics and Aeronautics*,
Vol. 189, Ed. E.T. Curran, S.N.B. Murthy, 2000
- [2] J.D. Anderson Jr.
Hypersonic and High Temperature Gas Dynamics
AIAA, 2000
- [3] J.D. Anderson Jr.
Modern Compressible Flow
McGraw Hill Inc., New York, 1982
- [4] T. Arai, H. Sugiyama, N. Uno
Mixing Enhancement by Normal Gas Injection in Supersonic Mixing Layer
Chapter 5.1 in *Proceedings of the IUTAM Symposium on Combustion in Supersonic Flows*,
Kluwer Academic Publishers, Ed. M. Champion, B. Deshaies, pp. 301-308, 1997
- [5] F. Bartlmä
Gasdynamik der Verbrennung
Springer, 1975
- [6] A. Ben-Yakar, R.K. Hanson
Cavity Flameholders for Ignition and Flame Stabilization in Scramjet: An Overview
AIAA Journal of Propulsion and Power, Vol. 17, No. 4, pp. 869-877, 2001
- [7] J.J. Bertin
Hypersonic Aerothermodynamics
AIAA Education Series, 1994
- [8] F.S. Billig
Combustion Processes in Supersonic Flow
AIAA journal of Propulsion and Power, Vol. 4, No. 3, May-June 1988
- [9] F.S. Billig
Research on Supersonic Combustion
AIAA Journal of Propulsion and Power, Vol. 9, No. 4, July-August 1993

- [10] A. Brandstetter
Auslegung und Konstruktion einer Modellbrennkammer zur Untersuchung der Wasserstoffverbrennung in Überschallströmungen
DGLR Jahrestagung, DGLR-JT-99-186, 1999
- [11] A. Brandstetter
Betriebsverhalten einer Dual-Modus-SCRamjet-Modellbrennkammer mit Wasserstoffverbrennung
Ph.D. Thesis, Lehrstuhl für Flugantriebe, Technische Universität München, 2004
- [12] U. Busse
Messtechnik an den Prüfständen des Lehrstuhls für Flugantriebe
Internal Report, Lehrstuhl für Flugantriebe, Technische Universität München, 2009
- [13] Ch.E. Cockrell Jr., A.H. Auslender, R.W. Guy, Ch.R. McClinton, S.S. Welch
Technology Roadmap for Dual-Mode Scramjet Propulsion to Support Space-Access Vision Vehicle Development
11th AIAA/AAAF International Space Planes and Hypersonic Systems and Technologies Conference, Orléans, France; AIAA-2002-5188, 2002
- [14] M.B. Colket, L.J. Spadaccini
Scramjet Fuels Autoignition Study
AIAA Journal of Propulsion and Power, Vol. 17, No. 2, pp. 315-323, 2001
- [15] R.A. Cox, J.A. Cole
Chemical Aspects of the Autoignition of Hydrocarbon-Air Mixtures
Combustion and Flame, Vol. 60, pp. 109-123, The Combustion Institute, Elsevier Science Inc. Publisher, 1985
- [16] W. Demtröder
Laser Spectroscopy
Springer, 1996
- [17] P.E. Dimotakis
Turbulent Free Shear Layer Mixing and Combustion
Chapter 5 in *High-Speed Flight Propulsion Systems - AIAA Progress in Astronautics and Aeronautics*, Vol. 137, Ed. S.N.B. Murthy, E.T. Curran, 1991
- [18] J.P. Drummond
Enhancement of Mixing and Reaction in High-Speed Combustor Flowfields
Advanced Computation and Analysis of Combustion, INAS Publishers, Ed. G.D. Roy, S.M. Frolov, and P. Givi, Moscow, Russia, pp. 238-251, 1997

- [20] A.C. Eckbreth
Laser Diagnostics for Combustion, temperature and Species
Gordon and Breach, 1996
- [21] J.S. Fox
Visualization and Instantaneous Planar Laser-Induced Fluorescence Imaging Techniques Developed and Applied to Turbulent Flows
Ph.D. thesis, Australian National university, 2003
- [22] U. Gaisbauer, B. Weigand, B. Reinartz, H.-P. Kau
Aero-Thermodynamical Design of a Scramjet for Future Space Transportation Systems: The Graduate School 1095/1 Funded by the "Deutsche Forschungsgemeinschaft" (DFG)
18th International Symposium on Air-Breathing Engines, Beijing, China; ISABE-2007-1131, 2007
- [23] E. George, P. Magre, V. Sabel'nikov
Self-Ignition of Hydrogen-Hydrocarbons Mixtures in a Hot Supersonic Confined Coflow of Air
13th AIAA/CIRA International Space Planes and Hypersonic Systems and Technologies Conference, Capua, Italy; AIAA-2005-3393, 2005
- [24] M.R. Gruber, J.M. Donbar, C.D. Carter, K.-Y. Hsu
Mixing and Combustion Studies Using Cavity-Based Flameholders in a Supersonic Flow
AIAA Journal of Propulsion and Power, Vol. 20, No. 5, pp. 769-778, 2004
- [25] C. Gruenig, V. Avrashkov, F. Mayinger
Fuel Injection into a Supersonic Airflow by Means of Pylons
AIAA Journal of Propulsion and Power, Vol. 16, No. 1, pp. 29-34, 2000
- [26] R.P. Hallion
The Hypersonic Revolution, Vol. I: From Max Valier to Project Prime, 1924-1967
Aeronautical Systems Division, Wright-Patterson AFB, OH, 1987
- [27] R.P. Hallion
The Hypersonic Revolution, Vol. II: From Scramjet to the National Aero-Space Plane, 1964-1986
Aeronautical Systems Division, Wright-Patterson AFB, OH, 1987
- [28] B. Han, C.J. Sung, M. Nishioka
Effect of Vitiating Air on Hydrogen Ignition in a Supersonic Laminar Mixing Layer
Combustion Science and Technology, Vol. 176, No. 3, pp. 305-330, 2004

- [30] W.H. Heiser, D.T. Pratt
Hypersonic Airbreathing Propulsion
AIAA Education Series, 1994
- [31] E.H. Hirschel
Viscous Effects
Chapter 12 in *Space Course 1991*, pp. 12-1 to 12-35, Aachen, Germany, 1991
- [32] R. Hömig, D. Theisen, R. Fink, G. Kappler
Experimental Investigation of a SCRAMJET Model Combustor with Injection through a Swept Ramp using Laser Induced Fluorescence with Tunable Excimer Lasers
26th Symposium on Combustion, The Combustion Institute, Napoli, Italy, 1996
- [33] R. Hömig, D. Theisen, R. Fink, G. Kappler, D. Rist, P. Andresen
Diagnostic of Non-Reacting Supersonic Flows in a SCRAMJET Model Combustor using Non-Intrusive Spectroscopic Methods
4th International Symposium on Special Topics in Chemical Propulsion, Stockholm, 1996
- [34] P.W. Huber, C.J. Schexnayder Jr., C.R. McClinton
Criteria for Self-Ignition of Supersonic Hydrogen-Air Mixtures
NASA Technical Paper TP-1457, 1979
- [35] C.J. Jachimowski
An Analysis of Combustion Studies in Shock Expansion Tunnels and Reflected Shock Tunnels
NASA Technical Paper TP-3224, 1992
- [36] D. Kors
Design Considerations for Combined Air-Breathing-Rocket Propulsion Systems
2nd AIAA International Aerospace Planes Conference, Orlando, FL, USA; AIAA-1990-5216, 1990
- [37] P. Kutschenreuther
Supersonic Flow Combustors
Chapter 8 in *Scramjet Propulsion - AIAA Progress in Astronautics and Aeronautics*, Vol. 189, Ed. E.T. Curran, S.N.B. Murthy, 2000
- [38] S. Lenz, M. Hornung, W. Staudacher
Conceptual Design of Winged Reusable Two-Stage-To-Orbit Space Transport Systems
Chapter 5.3.1 in *Basic Research and Technologies for Two-Stage-to-Orbit Vehicles* WILEY-VCH and DFG, Ed. D. Jacob, G. Sachs and S. Wagner, 2005

- [40] D. Maier, S. Kirstein, T. Fuhrmann, S. Rocci Denis, A. Hupfer, H.-P. Kau
Scramjet Research Activities at the Institute of Flight Propulsion of the Technische Universitaet Muenchen
 6th European Symposium on Aerothermodynamics for Space Vehicles, Versailles, France, 2008
- [41] C. Manfretti, J. Sender, M. Oswald
Theoretical and Experimental Discours on Laser Ignition in Liquid Rocket Engines
 The 27th International Symposium on Space Technology and Science, Tsukuba, Japan, 2009-a-07, 2009
- [42] T. Mathur, M. Gruber, K. Jackson, J. Donbar, W. Donaldson, T. Jackson, F. Billig
Supersonic Combustion Experiments with a Cavity-Based Fuel Injector
 AIAA Journal of Propulsion and Power, Vol. 17, No. 6, pp. 1305-1312, 2001
- [43] T. Mitani, M. Takahashi, S. Tomioka, T. Hiraiwa, K. Tani
Analysis and Application of Gas Sampling to Scramjet Engine Testing
 AIAA Journal of Propulsion and Power, Vol. 15, No. 4, pp. 572-577, 1999
- [44] T. Mitani
Ignition Problems in Scramjet Testing
 Combustion and Flame, Vol. 101, pp. 347-359, The Combustion Institute, Elsevier Science Inc. Publisher, 1995
- [45] T. Mitani, N. Kinzei, G. Masuya
Mach 2.5 Experiments of Reaction Quenching in Gas Sampling for Scramjet Engines
 27th International Symposium on Combustion, The Combustion Institute, pp. 2151-2156, 1998
- [46] T. Mitani, M. Takahashi, S. Tomioka, T. Hiraiwa, K. Tani
Measurements of Scramjet Engine Performance by Gas Sampling
 8th AIAA International Space Planes and Hypersonic Systems and Technologies Conference, Norfolk, VA, USA; A98-27876 06-15, 1998
- [47] T. Mitani, N. Chinzei, T. Kanda
Reaction and Mixing-Controlled Combustion in Scramjet Engines
 AIAA Journal of Propulsion and Power, Vol. 17, No. 2, pp. 308-314, 2001
- [48] S.N.B. Murthy
Basic Performance Assessment of Scram Combustors
 Chapter 10 in *Scramjet Propulsion - AIAA Progress in Astronautics and Aeronautics*, Vol. 189, Ed. E.T. Curran, S.N.B. Murthy, 2000

- [50] A.J. Neely, C. Riley, R.R. Boyce, N.R. Mudford, A.F.P. Houwing, M.R. Gruber
Hydrocarbon and Hydrogen-Fuelled Scramjet Cavity Flameholder Performance at High Flight Mach Numbers
12th AIAA International Space Planes and Hypersonic Systems and Technologies Conference, Norfolk, VA, USA; AIAA-2003-6989, 2003
- [51] T. Niioka, K. Terada, H. Kobayashi, S. Hasegawa
Flame Stabilization Characteristics of Strut Divided into Two Parts in Supersonic Airflow
AIAA Journal of Propulsion and Power, Vol. 11, No. 1, pp. 112-116, 1995
- [52] J. Odam
Scramjet Experiments using Radical Farming
Ph.D. Thesis, University of Queensland, 2004
- [53] P.J. Ortwerth
Scramjet Flowpath Integration
Chapter 17 in *Scramjet Propulsion - AIAA Progress in Astronautics and Aeronautics*, Vol. 189, Ed. E.T. Curran, S.N.B. Murthy, 2000
- [54] A. Paull, R.J. Stalker
Scramjet Testing in the T3 and T4 Hypersonic Impulse Facilities
Chapter 1 in *Scramjet Propulsion - AIAA Progress in Astronautics and Aeronautics*, Vol. 189, Ed. E.T. Curran, S.N.B. Murthy, 2000
- [55] F.P. Povinelli, L.A. Povinelli
Correlation of Secondary Sonic and Supersonic Gaseous Jet Penetration into Supersonic Crossflows
NASA Technical Note TN D-6370, 1971
- [56] B. Reim
Visualization and Pressure Measurements of Supersonic Swept Cavity Flows
Master Thesis, Institute for Flight Propulsion, TUM and School of Aerospace, Civil and Mechanical Engineering, ADFA, UNSW, 2005
- [57] S. Rocci Denis, A. Brandstetter and H.-P. Kau
Experimental Study on Transition between Ramjet and Scramjet Modes in a Dual-Mode Combustor
12th AIAA International Space Planes and Hypersonic Systems and Technologies Conference, Norfolk, VA, USA; AIAA-2003-7048, 2003
- [58] S. Rocci Denis, A. Brandstetter, D. Rist, H.-P. Kau
Combustion Stability of a Dual-Mode Scramjet Configuration - Configuration with Strut Injector
Chapter 5.3.1 in *Basic Research and Technologies for Two-Stage-to-Orbit Vehicles* WILEY-VCH and DFG, Ed. D. Jacob, G. Sachs and S. Wagner, 2005

- [59] S. Rocci Denis, D. Maier, W. Erhard and H.-P. Kau
Catalytic Pre-Heating of Air for Free Stream Investigations on Combustion Stability for a Specific SCRamjet Configuration
 17th International Symposium on Air-Breathing Engines, Munich, Germany; ISABE 2005-1234, 2005
- [60] S. Rocci Denis, D. Maier, W. Erhard and H.-P. Kau
Free Stream Investigations on Methane Combustion in a Supersonic Air Flow
 13th AIAA/CIRA International Space Planes and Hypersonic Systems and Technologies Conference, Capua, Italy; AIAA-2005-3314
- [61] M. Samimy, H.L. Petrie, A.L. Addy
Study of Turbulent Reattaching Free Shear Layers
 AIAA Journal, Vol. 24, No. 2, pp. 261-267, 1986
- [62] C. Schmutzler
Inbetriebnahme eines PLIF-Lasermesssystems zur Bestimmung und Visualisierung der Verbrennungszonen in einer Überschallbrennkammer
 Master Thesis, Institute for Flight Propulsion, TUM, 2006
- [63] I. Stozt
Flow and Combustion Studies on a Cavity Flame-Holder Scramjet
 Master Thesis, Institute for Flight Propulsion, TUM and School of Aerospace, Civil and Mechanical Engineering, ADFA, UNSW, 2004
- [64] J. Tauer, H. Kofler, E. Wintner
Laser-Initiated Ignition
 Laser & Photon, Rev. 4, No. 1, pp. 99-122, 2010
- [65] K. Terao
Irreversible Phenomena - Ignitions, Combustion and Detonation Waves
 Springer, 2007
- [66] J.M. Tishkoff, J. P. Drummond, T. Edwards, A.S. Nejad
Future Directions of Supersonic Combustion Research: Air Force/NASA Workshop on Supersonic Combustion
 35th Aerospace Meeting and Exhibit, Reno, NV, USA; AIAA-1997-1017, 1997
- [67] S. Tomioka
Personal Communication
 2005
- [68] S. Tomioka, A. Murakami, K. Kudo, T. Mitani
Combustion Tests of a Staged Supersonic Combustor with a Strut
 AIAA Journal of Propulsion and Power, Vol. 17, No. 2, pp. 293-300, 2001

- [69] S.R. Turns
An Introduction to Combustion - Concepts and Applications
McGraw Hill, 2000
- [70] D.M. Van Wie
Scramjet Inlets
Chapter 7 in *Scramjet Propulsion - AIAA Progress in Astronautics and Aeronautics*,
Vol. 189, Ed. E.T. Curran, S.N.B. Murthy, 2000
- [71] D.M. Van Wie, S.M. D'Alessio, M.E. White
Hypersonic Airbreathing Propulsion
Johns Hopkins APL Technical Digest, Volume 26, Number 4, 2005
- [72] B. Weigand, U. Gaisbauer, H.-P. Kau, B. Reinartz, W. Schröder
*Das Graduierten Kolleg 1095/1: „Aerothermodynamische Auslegung eines
Scramjet-Antriebssystems für zukünftige Raumtransportsysteme“*
Deutsche Luft- und Raumfahrtkongress 2006, Braunschweig, Germany;
DGLR-2006-127, 2006
- [73] A. Yesil
Numerical Simulation of a Supersonic Combustion Chamber
Term Thesis, Institute for Flight Propulsion, TUM, 2007
- [74] X. Zahng, A. Rona, J.A. Edwards
*The Effect of Trailing Edge Geometry on Cavity Flow Oscillation Driven by
Supersonic Shear Layer*
Aeronautical Journal, pp. 129-136, 1998